RADIATION BACKGROUND INVESTIGATIONS FOR ENVIRONMENTAL AND RARE DECAY STUDIES

DOCTORAL THESIS

SWATI THAKUR

DEPARTMENT OF PHYSICS
INDIAN INSTITUTE OF TECHNOLOGY ROPAR
RUPNAGAR, PUNJAB 140001, INDIA

NOVEMBER 2023

Radiation Background Investigations for Environmental and Rare Decay Studies

A Thesis Submitted

in Partial Fulfillment of the Requirements

for the Degree of

DOCTOR OF PHILOSOPHY

by

Swati Thakur

(2017PHZ0004)

DEPARTMENT OF PHYSICS

INDIAN INSTITUTE OF TECHNOLOGY ROPAR

NOVEMBER 2023

Swati Thakur
Radiation Background Investigations for Environmental and Rare Decay Studies

to my Family and Friends

Declaration of Originality

I, hereby, declare that the work presented in this thesis entitled **“Radiation Background Investigations for Environmental and Rare Decay Studies”** has been solely authored by me. It presents the result of my own independent investigation/research conducted during the time period from **August 2017** to **June 2023** under the supervision of **Prof. Pushpendra P. Singh** of IIT Ropar, and **Prof. V. Nanal** of TIFR Mumbai. To the best of my knowledge, it is an original work, both in terms of research content and narrative, and has not been submitted or accepted elsewhere, in part or in full, for the award of any degree, diploma, fellowship, associateship, or similar title of any university or institution. Further, due credit has been attributed to the relevant state-of-the-art and collaborations, if any, with appropriate citations and acknowledgments in line with established ethical norms and practices. I also declare that any idea/data/fact/source stated in my thesis has not been fabricated/ falsified/ misrepresented. All the principles of academic honesty and integrity have been followed. I fully understand that if the thesis is found to be unoriginal, fabricated, or plagiarized, the Institute reserves the right to withdraw the thesis from its archive and revoke the associated Degree conferred. Additionally, the Institute also reserves the right to appraise all concerned sections of society of the matter for their information and necessary action (if any). If accepted, I, hereby, consent for my thesis to be available online in the Institute’s Open Access repository, inter-library loan, and the title & abstract to be made available to outside organizations.

Swati

Swati Thakur
2017PHZ0004 / Ph.D.

Department of Physics
Indian Institute of Technology Ropar
Rupnagar, Punjab 140001

Acknowledgements

I intend to take this opportunity to express gratitude to my Ph.D. advisors, Prof. V. Nanal and Dr. Pushpendra P. Singh. I acknowledge Prof. V. Nanal for her significant & effective supervision and timely recommendations on various aspects of this thesis. Her guidance, perseverance, and support, made it possible to get through tough yet interesting situations. Her unrelenting efforts and passion have greatly impacted and motivated me to do successful investigations. I especially thank Dr. Pushpendra P. Singh for investing great confidence in me and giving me the fortitude to take on difficult challenges. I appreciate you for encouraging me to maintain calm and perseverance through more setbacks than victories. Our conversations on different issues at times inspired me to obtain desired progress and helped me get through some challenging times while working on my Ph.D. thesis.

I express my deep respect to Prof. R. G. Pillay for numerous stimulating discussions, critical comments, and encouragement during the entire course of this work. Those discussions always helped me to feel excited about research and motivated to learn more. I sincerely thank Prof. S. K. Dhiman for his help in collecting the rock samples from the Aut tunnel.

The Ministry of Education (MoE), Government of India, and the National Mission on Interdisciplinary Cyber-Physical Systems (NM - ICPS), Department of Science & Technology (DST), Government of India, through the Technology Innovation Hub - AWaDH at the Indian Institute of Technology Ropar, are gratefully acknowledged for the Ph. D. fellowship. I thank TIFR Mumbai for enabling me with financial support to conduct the experiments, simulations, and analysis for this thesis.

My gratitude to the present and former TIN.TIN and INO collaborators at TIFR, Dr. A. Mazumdar, Dr. H. Krishnamoorthy, G. Gupta, V. Vatsa, and Dr. A. Reza, with whose support this work has been accomplished. I thank Dr. A. Bhatt for his assistance and valuable discussions regarding the simulations, and Mr. G. Gupta for being so nice and helping me during my TIFR visits. I would like to extend my thankfulness to Mr. Mahesh Pose, Mr. Mallikarjunachary, and Mr. Kiran Divekar for their help and support for the experimental measurements, and to the Pelletron-Linac Facility staff for providing high-quality beams during the neutron activation experiments.

I thank my doctoral committee, Dr. Shubhrangshu Dasgupta (Chairperson), Dr. Subhendu Sarkar, Dr. Sourav Bhattacharya, and Dr. Yashveer Singh for regularly monitoring the progress of my work and providing invaluable suggestions towards the improvement of the thesis. I sincerely acknowledge Prof. H. J. Wollersheim for teaching the basics of nuclear physics and acquainting me to the world of nuclear detectors and instrumentation during my early Ph.D. days. I thank my colleagues at the Department of Physics for their support, Mr. Sahil Kapoor, Mr. Satish, and Ms. Athira for assisting me in utilizing all the facilities available in the department, and Mr. Anshu Vaid for all the help and motivation during this journey.

I thank my former group members, Dr. Rudra N. Sahoo, Dr. Pawan Kumar, Dr. Arshiya Sood, and Dr. Malika Kaushik, for their helpful advice, and the present members for so much warmth and positivity all around. I would especially mention Priyanka for being the best confidant and accomplice one could ask for, and Sanjeet and Soni for their help with the experiments conducted for this thesis. Arzoo, Riya, and Piyush need special mention for making my stay at IIT Ropar enjoyable. Dr. Navneet Singh and Dr. Kapil Garg are the best connections I made during my Ph.D. journey. I remember each and everyone with whom I met or interacted; thank you all for making IIT Ropar a happy place to live and learn.

I am immensely grateful to my family for always believing in me and wishing for my success. I would never have made it to this point in my life without the boundless love and encouragement of my papa and mumma. Thank you for holding me and praying for me in silence. I wish to acknowledge my beloved grandparents, your prayer for me was what sustained me this far. I express my heartfelt to the best person I know - my sister, Shikha, for being my pillar of support and staying by my side, come what maybe. I thank my jiju, Saurabh, for his support over the years.

I wish to shower my love on my adorable niece - Kaushiki, my constant source of happiness and laughter. She made the most challenging pandemic days the happiest ones, filled with pure joy and positivity. Finally, I would like to thank God for letting me through all the difficulties.

Certificate

This is to certify that the thesis entitled **Radiation Background Investigations for Environmental and Rare Decay Studies**, submitted by **Swati Thakur** (2017PHZ0004) for the award of the degree of **Doctor of Philosophy** of the Indian Institute of Technology Ropar, is a record of bonafide research work carried out under my guidance and supervision. To the best of my knowledge and belief, the work presented in this thesis is original and has not been submitted, either in part or full, for the award of any other degree, diploma, fellowship, associateship, or similar title of any university or institution.

In my opinion, the thesis has reached the standard of fulfilling the requirements of the regulations relating to the Degree.

Dr. Pushpendra P. Singh
Department of Physics
Indian Institute of Technology Ropar
Rupnagar, Punjab - 140 001, India

Prof. V. Nanal
Department of Nuclear and Atomic Physics
Tata Institute of Fundamental Research
Mumbai - 400 005, India

June 2023

Lay Summary

Experimental searches for rare decay processes seek evidence with elusive event rates buried under interfering radiation background environment. For these searches, these events are similar to that of looking for a needle (rare decay event signal) in a haystack (interfering radiation background). Note that the rare event experiments use highly sensitive detectors which detect signals from rare events and also from overlapping radiation backgrounds. In order to distinguish the rare event signals from relatively significant radiation backgrounds contribution, a comprehensive knowledge of the quantum of radiation background is essential. Developing dedicated low background measurement setups for accurately investigating interfering background radiations is crucial for reaching adequate sensitivity levels. The work presented in this thesis investigates various aspects of low-level but interfering radiation background, the natural radioactivities in rock samples from BWH and Aut regions, and feasibility studies relevant to environmental radioactivity and rare decay searches.

In order to achieve high sensitivity for investigating low-level ambient and environmental radioactivity, a low background setup ILM (IIT Ropar Low-background Measurement setup) is being set up at ground level at the Indian Institute of Technology Ropar in India. In this thesis, the development of ILM-0, a demonstrator of ILM, is presented. The suitability of the setup has been investigated by studying various soil and rock samples collected from different locations in Rupnagar and Aut regions, respectively. Additionally, the work presented in this thesis has been supported with the relevant Monte Carlo simulation performed using a GEANT4 package employing configurations of 2/4 HPGe detectors with a relative efficiency of ~33%. This was done to optimize the source-detectors configuration and to investigate the rare decay of ^{96}Zr and other exotic decay modes in ^{112}Sn or ^{106}Cd isotopes.

In India, the scientific community is looking for a suitable site to set up an underground laboratory to perform rare decay experiments in a relatively low or minimal background radiation environment. Some of the potential sites for an underground laboratory that are being investigated at present are Bodi West Hills (BWH) and Aut tunnel in Himachal Pradesh. In order to ascertain natural background radiation levels originating from the surrounding rocks of the sites, feasibility studies have been initiated by measuring the low background radiations originating from the rock samples. This thesis presents extensive radiopurity studies of rock samples collected from the Aut tunnel in Himachal Pradesh and their comparison with Bodi West Hills (BWH) rock samples. The comparison of radiation background levels suggests that the Aut tunnel region in Himachal Pradesh is equally suitable as that of Bodi West Hills (BWH), a designated site for the India-based Neutrino Observatory (INO) in the state of Tamil Nadu for an underground laboratory for rare decay investigations. To supplement the information from the experiments mentioned above, the impact of long-lived neutron-induced activities on the Aut and BWH rock samples has been investigated, as the neutron background can be the limiting factor for the low background experiments to achieve desirable sensitivity.

Abstract

Studies of low-level environmental radioactivity and experiments to investigate solar neutrino, dark matter (DM), double beta decay (DBD), and rare nuclear decays ($T_{1/2} > 10^{18}$ years) have minimal event rates, which require stringent background conditions and thereby makes most of the experimental search challenging. Given the rare nature of the processes, it is necessary to perform a detailed study of natural background radiation to investigate the sensitivity of the measurement and plan its reduction for different targeted experiments. For exploring the background issues related to rare event searches, the development of dedicated low background measurement setups is crucial to reaching adequate sensitivity levels. The present thesis investigates various aspects of radiogenic background relevant to low-level environmental radioactivity and rare decay searches employing single or combinations of low background HPGe spectrometers.

A low background setup ILM (IIT Ropar Low-background Measurement setup) above ground is being set up at IIT Ropar in India for rare decay studies. As of now, ILM-0, a demonstrator of ILM, has been achieved, which consists of a carbon-loaded HPGe detector. The low background HPGe detector has been is characterized using point-like γ-ray sources in a wide energy range of 80-1408 keV at IIT Ropar. A preliminary detector model has been developed using the GEANT4 simulation package to estimate the photopeak efficiency of an HPGe detector employed in the setup. The present model shows an average relative deviation of $\sim$10%, and the experimental setup has shown improved measurement sensitivity for counting environmental samples and quantifying radionuclides. Investigations of specific activity and its variation in soil samples from the arable lands in the Ropar district of Punjab state in India have been carried out.

As a part of this thesis, feasibility studies have been carried out to investigate the single beta and double beta decay modes in ^{96}Zr and ^{112}Sn isotopes, respectively. The physics simulations have been performed using a GEANT4 simulation package employing 2/4 HPGe detectors ($\sim$33% R.E.) to optimize the source configuration for rare decay experiments. For the β decay of ^{96}Zr, the results suggest that $\sim$70 g of 50% enriched source will yield mass efficiency of $\sim$12-20 g-% for 568-1091 keV gamma-ray pair in the ^{96}Nb decay cascade, comparable to the Finch *et al.* (Nucl. Instrum. Methods A, 806, 70, 2016). The feasibility study of positron double beta decay modes involving simultaneous emission of 2/4 gamma rays of 511 keV in ^{112}Sn (EC-β^+) and ^{106}Cd ($\beta^+\beta^+$) has been performed using a coincidence setup of two HPGe detectors. To estimate the sensitivity to search for $\beta^+\beta^+$/ECβ^+ processes in ^{112}Sn, the ambient background has been measured with moderate Pb shielding around the coincidence setup of two low background HPGe detectors in the laboratory of TIFR, Mumbai at the sea level. The coincident detection of the 511 keV pair significantly improves the background in the region of interest. From background measurements with $\sim$40 g of ^{nat}Sn, the sensitivity for $T_{1/2}^{\beta^+\beta^+}$ (^{106}Cd) and $T_{1/2}^{EC-\beta^+}$ (^{112}Sn) is estimated to be $\sim 10^{19}$ - 10^{20} y for 1 y of measurement time with enriched samples (90%).

Efforts are underway in India to set up an underground laboratory for planning the low background experiments. In order to support these efforts, the radiopurity studies of rock samples from the Aut tunnel have been carried out using the TiLES at TIFR, Mumbai. The findings of the present studies were compared with the Bodi West Hills (BWH) of the Theni district in Madurai, Tamil Nadu. Compared with BWH rock, the Aut rock appears to have a lesser amount of ^{232}Th and a somewhat higher amount of ^{238}U. It has been found that the concentration of ^{40}K in Aut rock was observed to be lower by a factor of ~ 1000 as compared to the BWH rock samples. It is noted that the Aut rock trace impurity concentrations were considerably lower than the respective worldwide average values. Overall, the ambient gamma-ray background at Aut is expected to be lower than at the BWH site, indicating the suitability of the site for low background experiments.

In order to assess the impact of the long-lived neutron-induced activities, fast neutron activation experiments have been carried out on the Aut and BWH rock samples. Irradiations were carried out at BARC-TIFR Pelletron Linac Facility, Mumbai, at two incident proton energies, 12 and 22 MeV, to cover a broader energy range and compare the yield of the observed products on neutron energy. Neutron activation studies of Aut rock have revealed mostly short-lived activity. The fast neutron activation studies of both Aut and BWH rock samples have indicated the presence of long-lived activities like ^{54}Mn (0.855 y) and ^{22}Na (2.60 y). Still, the resultant gamma-ray energies are lower than 1500 keV, and no significant long-lived contributions at $E > 2$ MeV were observed. The low energy neutron flux arising due to spontaneous fission and (α,n) reactions, dominated by ^{238}U, is expected to be around 3×10^{-6} n cm^{-2} s^{-1}, which is similar to other underground laboratories. The Aut site is expected to have lower ambient gamma-ray background than the BWH, while the low-energy neutron background is expected to be similar. From the radioactive background investigations, Aut appears to be a good site for building an underground laboratory for rare decay studies.

Keywords: Gamma ray spectroscopy; low background radiations; HPGe detector; environmental radioactivity; background for rare decays; (neutrinoless) double beta decay; GEANT4 simulation; neutron activation

List of Publications

Journal

1. **Swati Thakur**, A. Mazumdar, Nishant Jangid, V. Vatsa, M.S. Pose, S. Mallikarjunachary, S. Pal, V. Nanal, R.G. Pillay, P.K. Raina, Pushpendra P. Singh and S.K. Dhiman (2022) Radiopurity studies of a rock sample from the Aut region, *Nuclear Instruments and Methods A*, **1038**, 166892

2. **Swati Thakur**, V. Nanal, Pushpendra P. Singh, R. G. Pillay, H. Krishnamoorthy, A. Mazumdar, A. Reza, P. K. Raina and V. Vatsa (2022), Simulation studies for source optimization in ^{96}Zr β decay, *Il nuovo cimento C* **45**, 1-5

3. **Swati Thakur**, A. Mazumdar, R. Shah, V. Vatsa, V. Nanal, M.S. Pose, Pushpendra P. Singh, P.K. Raina, R.G. Pillay (2021), Background Estimation Studies for Positron Double Beta Decay, *arXiv preprint arXiv:2111.08825* (Accepted in AIP Publishing Conf. Proc.)

4. Malika Kaushik, G. Gupta, S.K. Pandit, V.V. Parkar, **Swati Thakur**, V. Nanal, A. Shrivastava, R.G. Pillay, H. Krishnamoorthy, K. Mahata, S. Pal, C.S. Palshetkar, K. Ramachandran, Pushpendra P. Singh (2021), Neutron transfer in ^{9}Be$+^{159}$Tb system, *European Physical Journal A*, **57**, 320

5. Malika Kaushik, S.K. Pandit, V.V. Parkar, G. Gupta, **Swati Thakur**, V. Nanal, H. Krishnamoorthy, A. Shrivastava, C.S. Palshetkar, K. Mahata, K. Ramachandran, S. Pal, R.G. Pillay, Pushpendra P. Singh (2021), Investigating neutron transfer in the ^{9}Be $+^{197}$ Au system, *Physical Review C*, **104**, 024615

6. Arshiya Sood, **Swati Thakur**, Arzoo Sharma, Vijay R Sharma, Abhishek Yadav, Manoj K Sharma, B P Singh, R Kumar, R K Bhowmik and Pushpendra P Singh (2020), Disentangling complete and incomplete fusion events in ^{12}C $+^{169}$ Tm reaction by spin-distribution measurements, *Journal of Physics G: Nuclear and Particle Physics*, **48**, 025105

7. Malika Kaushik, G. Gupta, **Swati Thakur**, H. Krishnamoorthy, Pushpendra P. Singh, V. V. Parkar, V. Nanal, A. Shrivastava, R. G. Pillay, K. Mahata, K. Ramachandran, S. Pal, C. S. Palshetkar, S. K. Pandit (2020), Fusion of the Borromean nucleus ^{9}Be with a ^{197}Au target at near-barrier energies, *Physical Review C*, **101**, 034611

8. Rudra N. Sahoo, Malika Kaushik, Arshiya Sood, Pawan Kumar, **Swati Thakur**, Arzoo Sharma, Pushpendra P. Singh, Md. Moin Shaikh, Rohan Biswas, Manoj K. Sharma, Abhishek Yadav, J. Gehlot, S. Nath, N. Madhvan (2020), Role of neutron transfer in sub-barrier fusion, *Physical Review C*, **102**, 024615

9. Rudra N. Sahoo, Malika Kaushik, Arshiya Sood, Pawan Kumar, Arzoo Sharma, **Swati Thakur**, Pushpendra P. Singh, P. K. Raina, Rohan Biswas, J. Gehlot, S. Nath, N. Madhavan, Abhishek Yadav, Md. Moin Shaikh, Manoj K. Sharma, Nabendu K. Deb, Anjali Rani, A. Banerjee, Unnati Gupta, B. J. Roy, B. P. Singh, R. Prasad (2020), Examining the Role of Transfer in Sub-barrier Fusion Enhancement: ^{35,37}Cl $+^{130}$ Te

Systems *Proc. 13th Int. Conf. on Nucleus-Nucleus Collision, JPS Conf. Proc.* **32**, 010016

10. Rudra N. Sahoo, Malika Kaushik, Arshiya Sood, Pawan Kumar, Arzoo Sharma, **Swati Thakur**, Pushpendra P. Singh, P. K. Raina, Md. Moin Shaikh, Rohan Biswas, Abhishek Yadav, J. Gehlot, S. Nath, N. Madhavan, V. Srivastava, Manoj K. Sharma, B. P. Singh, R. Prasad, Anjali Rani, A. Banerjee, Unnati Gupta, Nabendu K. Deb, B. J. Roy (2019), Sub-barrier fusion in the $^{37}\mathrm{Cl} +^{130}$ Te, *Physical Review C*, **99**, 024607

11. Mohd. Shuaib, Vijay R. Sharma, Abhishek Yadav, **Swati Thakur**, Manoj Kumar Sharma, Ishfaq Majeed, Mahesh Kumar, Pushpendra P. Singh, Devendra P. Singh, R. Kumar, R. P. Singh, S. Muralithar, B. P. Singh, and R. Prasad (2019), Mass and isotopic yield distributions of fission-like events in the $^{19}\mathrm{F} +^{169}$ Tm system at low energies, *Physical Review C*, **99**, 024617

Conference Proceedings

1. **S. Thakur**, A. Mazumdar, V. Vatsa, M.S. Pose, S. Mallikarjunachary, S. Pal, V. Nanal, P.P. Singh, R.G. Pillay, and P.K. Raina (2022), Neutron induced activation studies for low background experiments, *Proceedings of the DAE Symp. on Nucl. Phys.* **65**, 810

2. **Swati Thakur**, H. Krishnamoorthy, V. Nanal, Pushpendra P. Singh, R.G. Pillay (2019), Performance study of low background co-axial HPGe detector, *Proceedings of the DAE Symp. on Nucl. Phys.* **64**, 992

3. Malika Kaushik, G. Gupta, **S. Thakur**, H. Krishnamoorthy, Pushpendra P. Singh, V.V. Parkar, V. Nanal, A. Shrivastava, R.G. Pillay, K. Mahata, K. Ramachandran, S. Pal, C.S. Palshetkar, S.K. Pandit (2019), Fusion Suppression in $^{9}\mathrm{Be} +^{197}$ Au reaction, *Proceedings of the DAE Symp. on Nucl. Phys.* **64**, 513

4. Malika Kaushik, G. Gupta, **Swati Thakur**, H. Krishnamoorthy, V. Nanal, A. Shrivastava, Pushpendra P. Singh, R. G. Pillay, C. S. Palshetkar, K. Mahata, K. Ramachandran, S. Pal, S. K. Pandit, V.V. Parkar (2018), Study of fusion and direct reaction at near barrier energies in $^{9}\mathrm{Be} +^{197}$ Au, *Proceedings of the DAE Symp. on Nucl. Phys.* **63**, 598

5. G. Gupta, Malika Kaushik, **Swati Thakur**, H. Krishnamoorthy, V. Nanal, A. Shrivastava, Pushpendra P. Singh, R.G. Pillay, C.S. Palshetkar, K. Mahata, K. Ramachandran, S. Pal, S. Pandit, V.V. Parkar (2018), Complete Fusion in $^{9}\mathrm{Be} +^{159}$ Tb at near barrier energies *Proceedings of the DAE Symp. on Nucl. Phys.* **63**, 650

6. Mohd. Shuaib, ,Vijay R. Sharma, Abhishek Yadav, **Swati Thakur**, Ishfaq Majeed, Mahesh Kumar, Manoj Kumar Sharma, Pushpendra P. Singh, Unnati Gupta, Devendra P. Singh, R. Kumar, R. P. Singh, S. Muralithar, B. P. Singh, and R. Prasad (2018), Measurement and analysis of mass distribution of fission like events in $^{19}\mathrm{F} +^{169}$ Tm system at low energies, *Proceedings of the DAE Symp. on Nucl. Phys.* **63**, 570

7. Rudra N. Sahoo, Malika Kaushik, Arshiya Sood, Pawan Kumar, Arzoo Sharma, **Swati Thakur**, Pushpendra P. Singh, P. K. Raina, Rohan Biswas, Abhishek Yadav, J.

Gehlot, S. Nath, N. Madhavan, Md. Moin Shaikh, Manoj K. Sharma, B. J. Roy, Anjali Rani, A. Banerjee, Unnati Gupta, Nabendu K. Deb, B. P. Singh, R. Prasad (2018), Effect of coupling on sub-barrier fusion: The case of ^{37}Cl $+^{130}$ Te Systems *Proceedings of the DAE Symp. on Nucl. Phys.* **63**, 492

Notations and Abbreviations

The list of notations and abbreviations used in this thesis are summarised here.

Symbol	
$2\nu\beta\beta$	Two neutrino double beta decay
$0\nu\beta\beta$	Neutrinoless double beta decay
t_{c}	Cooldown time after neutron irradiation
t	Counting period of the gamma ray spectrum
γ-ray	Gamma-ray
E_γ	energies of γ-ray/γ-lines
I_γ	Absolute intensity of a γ-ray
N_γ	Number of counts in the photo-peak
λ	Decay constant
ϵ_γ	Photo-peak efficiency of the detector for the characteristic γ-ray
$T_{1/2}$	Half-life of a nucleus

Abbreviations	
NDBD	Neutrinoless double beta decay
TiLES	Tifr Low background Experimental Setup
TIN.TIN	The INdia-based TIN detector
MC	Monte Carlo
BWH	Bodi West Hills
CL	Confidence Level
DPP	Digital Pulse Processing
FWHM	Full Width at Half Maximum
HDPE	High Density PolyEthylene
INO	India-based Neutrino Observatory
LAMPS	Linux Advanced Multi-Parameter System
PSD	Pulse Shape Discrimination
ROI	Region Of Interest
SIMS	secondary ion mass spectroscopy
ICPMS	Inductively Coupled Plasma Mass Spectrometry
BARC	Bhabha Atomic Research Centre
CAMAC	Computer Aided Measurement And Control
DAQ	Data Acquisition System
R.E.	Relative Efficiency
g.s.	ground state
HPGe	High Purity Germanium
keV	Kilo Electron Volt
MeV	Mega Electron Volt
7N purity	purity at the level of 99.99999%
PLF	Pelletron Linac Facility
TIFR	Tata Institute of Fundamental Research
ENDF	Evaluated Nuclear Data File

Contents

List of Figures

List of Tables

Chapter 1

Introduction

Background radiations have been ubiquitous since the formation of the earth. Studies on the natural radioactive background have been ongoing for several decades and have radically impacted the developments in science & technology [7, 8]. The presence of natural radionuclides in the environment is usually in very low concentration and is a continuous source of radiation exposure. The natural radioelements, such as; potassium, uranium, and thorium, are inhomogeneously distributed. Therefore, determining the quantum of natural radioactivity in the environment originating from these nuclei and establishing their distribution patterns has attracted much attention worldwide. Comprehensive research on traditional environmental radioactivity dealing with radiation monitoring and its risk to human health is extensively available in literature [9, 10]. Some aspects of environmental radioactivity deal with very low concentrations, such as; the fallout of nuclear tests, radioactive waste, radioactive tracers, activation experiments, potable water, marine samples, etc. [11–15]. There is a continuous need for technological advancements in radiation background studies that can considerably improve the sensitivity below the level accessible with commercial equipments [16, 17]. Apart from environmental sciences, some areas of fundamental physics, such as; nuclear physics, astrophysics, biological sciences, and other fields of national security, require the measurement of very low-level background radiation. However, the background radiation measurements and techniques deployed to satisfy adequate sensitivity levels are purpose-dependent and vary in different experiments [17, 18]. The need to achieve high sensitivity has led to the development of low background counting facilities employing state-of-the-art detection systems [19] for solar neutrino [20], dark matter (DM) [21], double beta decay (DBD) [22], rare nuclear decays [23] ($T_{1/2} > 10^{15}$ years) experiments, which have meager event rates and require to measure ultra-low background radiation levels. The key challenge in such measurements is to use the potential of low background to unprecedented levels. Before actual data taking, investigation and estimation of all the individual contributions to the background at these locations are essential to address the issue of its reduction most effectively.

The following sections discuss different aspects of radiation background and their reduction techniques. The need for low radioactive background with a particular emphasis on environmental radioactivity and rare event studies, such as; DBD, positron DBD and forbidden single β decay searches, are examined. A brief overview of gamma ray background in various operational underground laboratories, background rate achieved in pioneer experiments, and some of the low background gamma ray facilities is presented regarding low-level radioactivity measurements.

1.1 Sources of low background radiations

The most common source of radiation background concerning low-level radioactivity measurements is broadly classified into cosmic radiation, terrestrial radiation emitted from naturally occurring radionuclides, and neutron background. All of these are sources of radiation background and can significantly influence any sensitive nuclear measurement and, therefore, necessary to be investigated. This section briefly describes various sources of background radiations encountered in rare decay nuclear experiments.

1.1.1 Cosmic rays and associated processes

Earth's atmosphere is continuously bombarded with high-energy primary cosmic rays originating from the cosmos. The primary interaction of these cosmic rays with the atmosphere produces a shower of secondary radiations in the form of neutrons and protons of various energies, which in turn produce a variety of radionuclides through nuclear reactions with nitrogen, oxygen, and other nuclei present in the atmosphere and other processes. The secondary cosmic ray particles, such as; muons produced via cosmic ray interactions in the upper atmosphere, are highly penetrating and thus interact directly with the detector volume or create secondary particles via hadronic or electromagnetic interactions in surrounding materials. The interaction of cosmic rays may cause delayed events by activation of detector materials and producing cosmogenic radioactive isotopes such as ^{11}C, ^{56}Co, ^{60}Co, ^{68}Ge and ^{22}Na, having a longer half-life and could raise the background levels at the energy region relevant for rare physics processes [24–26]. The cosmic-muon flux is dominated at surface laboratories by approximately 1 $\mathrm{min}^{-1}\mathrm{cm}^{-2}$ [27]. Due to overburden depth, the deep underground laboratories can suppress the primary cosmic ray flux by several orders of magnitude. However, muon-induced neutrons are most challenging to mitigate even in underground laboratories [28].

1.1.2 Natural radioactivity

Natural radioactivity represents one of the main backgrounds in the search for rare decay processes. Most of the natural background contribution arises from the primordial radionuclides of the uranium series (^{238}U to ^{206}Pb), thorium series (^{232}Th to ^{209}Pb), actinium series (^{235}U to ^{207}Pb) and potassium (^{40}K) with $T_{1/2} \sim 10^8 - 10^{10}$ years. These naturally occurring radioisotopes exist at trace levels in the earth's crust. The predominant isotopes (natural abundance of more than 99%) with their decay chains are shown in figure 1.1, 1.2. The decay products of each isotope of these series emit many α, β, and γ rays. Due to the short range of α and β particles, the dominant background comes from the gamma radiations emitted from the decay products of natural radioactive chains of ^{238}U and ^{232}Th. For example, the high energy intense γ-ray of 2615 keV from ^{208}Tl in the ^{232}Th decay chain, 2448 keV from ^{214}Bi (^{222}Rn progeny) lies above the Q-value for several possible isotopes of DBD. Another potential background from the ^{238}U decay chain whose progeny ^{214}Bi emits γ-rays at many different energies out to 3184 keV and β electron with an energy up to 3270 keV. However, the most significant natural contributor to low energy background is Radon gas which has three short-lived isotopes, namely, ^{222}Rn ($T_{1/2}$ = 3.8 d), ^{220}Rn ($T_{1/2}$ = 55.6 s),

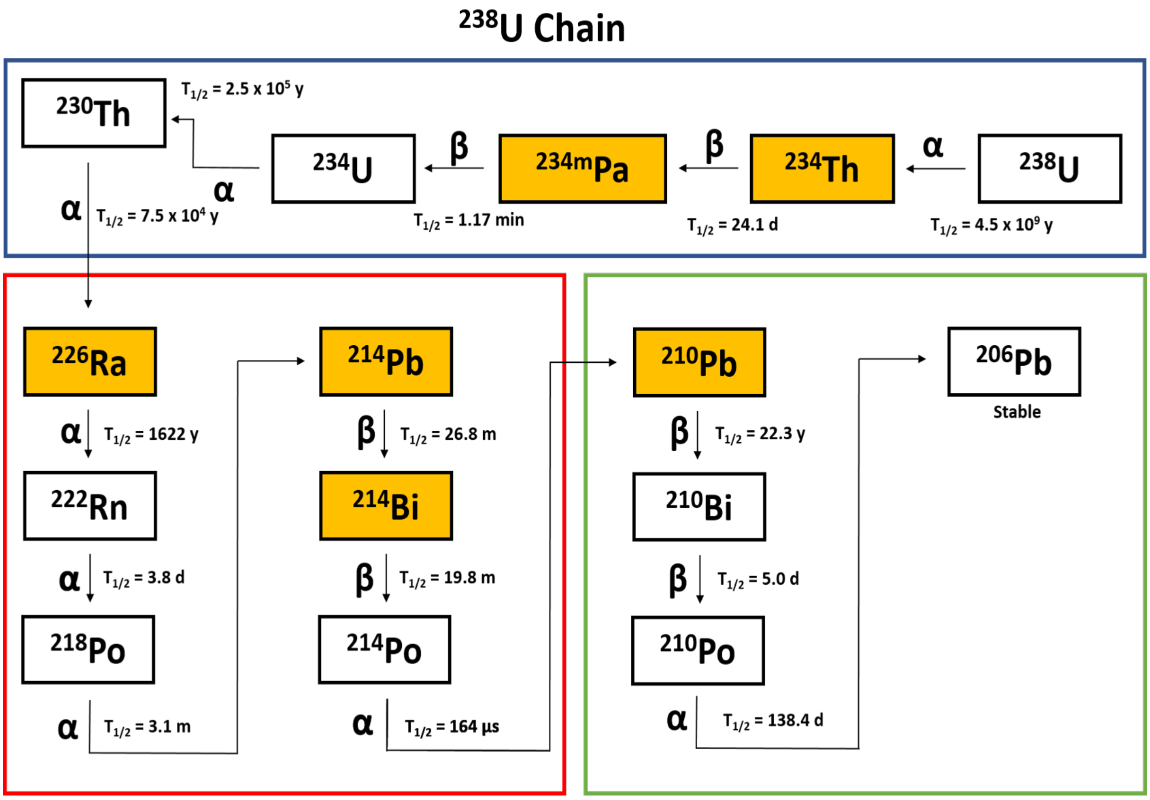

Figure 1.1: The decay sequence from ^{238}U to ^{206}Pb. The γ-ray emitting radionuclides with a high intensity ($\geq$5%) photons from a given decay are also highlighted (in yellow).

^{219}Rn (T$_{1/2}$ = 3.96 s) produced in the uranium decay series. It is always in underground tunnels or mines and seeps from rocks, concrete, and detector construction materials [29]. Bremsstrahlung arising from the ^{238}U and ^{232}Th α and β emitting isotopes and ^{210}Pb (T$_{1/2}$ = 22.3 y) from the environmental ^{222}Rn can contaminate the surface/volume of the detector and contributes to the background. The contaminated surface can contribute to additional β and γ-ray events. Surface alpha background from ^{210}Po can be a dominant contributor to the background for direct DM experiments. Above 2600 keV, most environmental and material radioactivity from β and γ contributions tend to vanish. However, α remains the chief source of radioactive background.

1.1.3 Neutron background

Neutrons coming from the spontaneous fission of U and Th in the rock and surrounding materials significantly contribute to the rare decay experiments. In addition, the α particles emitted from the decay of intermediate radioisotopes in the U, Th decay chains can react with lighter nuclei in the rock structures to produce neutrons via (α,n) reactions. The main worries are the production of muon-induced secondary neutrons of very high energy up to $\sim$10 GeV. These additional neutrons can be produced via several processes, such as muons capture in nuclei, muon-induced spallation reactions, and muon-induced hadronic and electromagnetic showers. Thermalization and capture of neutrons or inelastic scattering

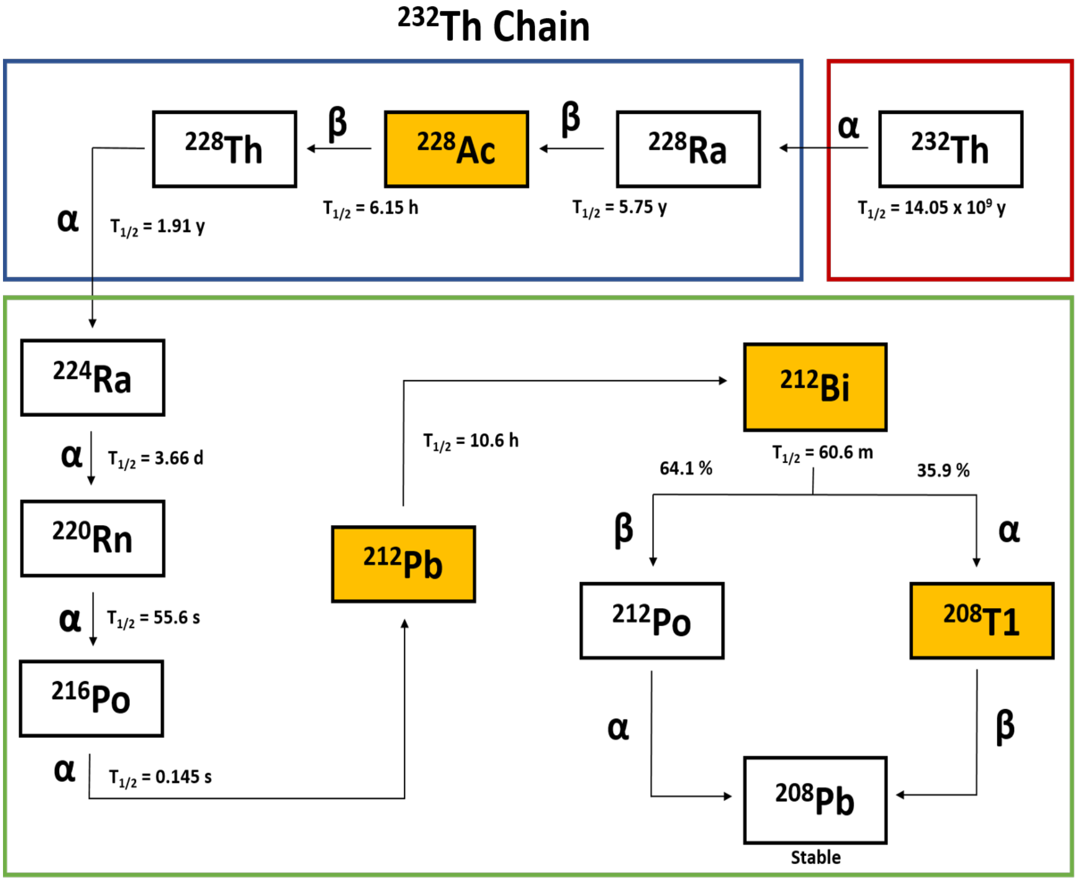

Figure 1.2: The decay sequence from ^{232}Th to ^{208}Pb. The γ-ray emitting radionuclides with a high intensity ($\geq$5%) photons from a given decay are also highlighted (in yellow).

in the materials surrounding the detector produce additional gamma ray background and act as a potential source of background in DBD decay experiments. Another background source is the production of cosmogenic radioisotopes in detector or shielding material by neutron activation during handling, transport, or storage.

1.2 Radiation background reduction techniques

After understanding the primary sources of background and their contributions to the detector counting rates, rejection of the background entangling the expected signal is one of the primary goals of low background experiments. Studies of various background rejection techniques are ever-evolving to reduce all potential sources of radioactive background to the lowest possible level. This section briefly discusses the technical effort and strategies to minimize background encountered in various experiments and their implication on the results. It will be helpful in the construction of the background model to prepare the final design of the experiment. The selection of radiopure materials for detection construction is crucial for the low background experiments. Although detectors used for these experiments are mostly installed in underground sites, which strongly reduces the cosmic ray flux, activation can occur during the manufacturing and transportation of the detectors to the underground laboratory. The contamination can arise from impurities present in the raw material or introduced during manufacturing. To reduce the introduction of the contamination of radioactive isotopes, the production and handling of detector components should happen underground. Further, minimizing contamination in the detector's active volume and the surrounding shield materials is essential. The most common shielding materials around detector setups are lead, steel, copper, etc. The most relevant contribution is from the ^{210}Pb and ^{232}Th intrinsic impurities present in the shielding. For example, the steel cryostat with internal Cu shield used in GERDA [30] is procured from selected low background austenitic steel; crystals are enclosed in ultra-pure (^{238}U, ^{232}Th <0.3 μBq/Kg) electroformed Cu in MAJORANA DEMONSTRATOR (MJD) [31], ancient lead (^{210}Pb $<$ mBq/kg) obtained from a sunk Roman ship is used in CUORE. The best upper limits obtained with the modern germanium spectrometers for lead are tens of μBq/kg.

The dominating component of the main spectrometer background in the KATRIN experiment is related to α decays in the spectrometer walls, causing neutral particles to propagate into the spectrometer volume [32]. In a bolometric experiment like CUORE [33], the degraded α's from the surface of TeO_2 crystals, inert materials facing the crystals and mostly copper frames form the most pernicious source of background and therefore, requested low background levels concerning radioactive impurities should be typically below 10^{-13} g/g. The KamLAND-Zen experiment intended to investigate the neutrinoless double beta decay (NDBD) in ^{136}Xe using a xenon-loaded liquid scintillator (LS) detector has the huge spherical outer balloon ultra-clean (^{238}U: 3.5×10^{-18} g/g, ^{232}Th: 5.2×10^{-17} g/g) active shield with negligible external γ ray backgrounds [34].

As an example, for the HPGe detector setup, the GeMPI III-spectrometer failed to reach the sensitivity of GeMPI, which is the most sensitive gamma ray spectrometer available for routine material screening, due to an anthropogenic activity from ^{207}Bi ($T_{1/2} = 31.55$ y) contamination of few mBq within the cryostat of the detector [35]. The case of the DarkSide-50 experiment uses Liquid argon (LAr) for direct detection of DM searches. However, the presence of atmospheric argon produces ^{39}Ar ($T_{1/2} = 239$ y) typically via ^{40}Ar(n,2n)^{39}Ar reaction with an activity of 1 Bq/Kg [36]. Therefore, reducing ^{39}Ar background and ultra-pure argon are crucial requirements to improve the sensitivity of WIMP (Weakly Interacting Massive Particle) dark matter direct detection searches. In the XENONnT experiment for dark matter searches, an extensive material screening program, cleanliness procedures to surface contamination of detector, and ^{222}Rn mitigation using novel radon distillation system is expected to achieve the target activity of 1 μBq/kg [37].

1.2.1 Passive shielding

Several detection systems are surrounded by a low-activity passive shield of lead (5-15 cm) and copper (5-10 cm) to reduce the external gamma ray background. These systems are often implemented by passive graded shielding in the order of increasing atomic number (Z). In MJD, all crystals are enclosed in ultra-pure, electroformed copper cryostats, further enclosed in a graded passive shielding of Cu and Pb. Outside this bulk, high-Z shielding is a layer of hydrogenous material (polyethylene and borated polyethylene) as neutron moderator [31]. Careful consideration must be given to the effects of inadequate shielding material and dimensions, as they can become a source of secondary radioactivity and often prove very difficult to reduce or eliminate. The cosmic muon interactions become more critical for high-Z targets such as Pb and Cu, which can produce secondary particles in the detector vicinity and the shielding material itself. Therefore, a thicker shield may not be reasonable and should be optimized to significantly reduce gamma radiation from environmental radionuclides distributed in the detector surroundings, simultaneously providing an acceptable number of muon-induced background events. The ultra-pure water or liquid cryogen may also allow the shielding medium to be a passive shield against external radiation and an active veto for rejecting cosmic muons and muon-induced particles. Ultra-low background facilities such as XENONnT, GeMPI, GeTHU, CUORE, etc., are equipped with these types of shielding.

1.2.2 Active shielding

As mentioned earlier, the above-ground laboratories are dominated by the cosmic ray flux and the shower of secondary particles generated; hence the low background experiments are primarily housed in the deep underground site where the cosmic ray muons are significantly suppressed. A typical overburden or underground depth of 1 km can reduce the muon flux by six orders of magnitude compared to the sea level. Therefore, the depth of the facility is vital in determining the types of physics that an experiment can address. Figure 1.3 shows the depth of various underground sites, along with the Cosmic ray muon flux. The units of meter water equivalent (m.w.e) is to denote depth.

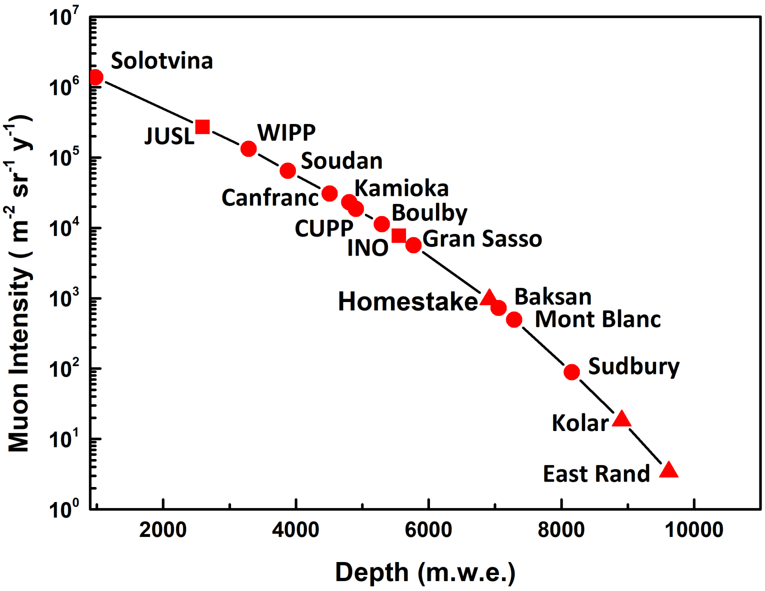

Figure 1.3: The expected total muon intensity as a function of depth with new (square), current (circles) and closed (triangles) underground laboratories. Figure adapted from [1].

Active shields are the additional detectors such as NaI(Tl), CsI, BGO, or plastic scintillator, usually placed as the outer shields of the detector setup for active muon veto in anticoincidence mode. Its purpose is to reduce the detector background induced by the nuclear interaction of cosmic rays with passive shieldings and primary detectors. Generally, ultra-pure water or liquid scintillator tanks serve as Cherenkov's medium for muon veto and can act as neutron shields. Apart from a radiopure detector setup, passive shielding, and an active muon veto, radon protection of the sample chamber is needed to reduce the contribution of airborne background from a radioactive noble gas ^{222}Rn, which is a progeny of ^{238}U ($T_{1/2}$ = 3.8 d). Various radon abatement techniques are utilized, such as purging boil-off N_2 gas, adsorption-based purification, and various other gas purification methods [38, 39]. XENONnT's demonstrates a novel radon removal system based on cryogenic distillation that will reduce the radon concentration by a factor of three lower than its predecessor XENON1T [37]

1.2.3 Coincidence techniques

Several improvements have been achieved by deploying ultra-pure construction materials in the cryostat and shielding as a part of essential design criteria for low background spectrometers to utilize the full potential of the range of detectors. To achieve the desired measurement sensitivity, the ideal scenario would be a large quantity of enriched source mass, high-efficiency detectors with excellent resolution, and almost zero background conditions (see Eq. 1.6). However, in actual experiments, one of the major challenges in low-level measurement primarily involves reducing background to improve the signal-to-noise ratio while preserving the high signal detection efficiency. In the case of external-source configuration, maximizing the efficiency using a large detector/source mass may provide the most significant gain in sensitivity. On the contrary, background increases with an increase in the size of the detector, or self-absorption increases in the source itself with the source size that limits the achievable sensitivity. Multidimensional gamma ray spectrometry is a powerful technique for studying low-level nuclear measurements. Studies of rare event searches using multiple HPGe detectors operated in coincidence have been extremely useful in diminishing background from ambient radioactivity and a possible way to increase sensitivity, especially when activity from other nuclides in the sample dominates and contributes to the high Compton background [40, 41]. Studying in coincidence allows both the selection of specific events and the rejection of background, providing a better handle in distinguishing the $\beta\beta$ from other single β transitions by detecting their characteristics γ-rays [4]. Various event selection criteria characterize experimental investigations of DBD using TeO_2 bolometers, and enhanced signatures from detecting multiple gammas in cascade are extremely clean and lead to an almost background-free search [42]. MJD uses coincidence techniques and pulse shape analysis to remove background events with multiple energy deposits [43]. References [44–46] gives a recent review of the searches on alternate modes of DBD employing coincidence techniques in scintillators or HPGe detectors.

1.2.4 Particle discrimination and tracking

The DBD events are single-site events and are often localized to a region of a few mm. In contrast, the background events are multi-sited events that are predominantly photon-induced. Therefore, the difference in the time structure of both signals provides a powerful discrimination strategy against various radioactive backgrounds. The recent improvement of pulse shape analysis capability and the development of enriched point-contact Ge detectors has revolutionized the ability to discriminate between backgrounds from γ-rays and $\beta\beta$ signals. The GERDA experiment has demonstrated the powerful and effective pulse shape analysis technique for identifying and removing background events [47]. The double readout strategy of heat and scintillation light in scintillator bolometers provides the particle discrimination between β/γ and α backgrounds, which is the primary source of background in bolometric experiments [48]. The external-source configuration, where the detector and the DBD source are distinct, offers the possibility of superior tracking and effective background rejection. For instance, SuperNEMO is a next-generation DBD experiment that uses a tracking plus calorimetry detection technique which allows full topological reconstruction of events resulting in powerful background rejection [49]. The gamma radiation detection using highly segmented position-sensitive germanium detectors like AGATA provides the three-dimensional position and energy information of individual interactions and implementation of complete reconstruction process [50].

In recent years, in an effort to set up a future rare event searches experiment, various types of background measurements have been carried out at underground laboratories. The measurement of all kinds of backgrounds fully exploits the requirement of ambitious background budgets for various experiments. In this thesis, the underground laboratories are

Table 1.1: Measured natural gamma ray background in the representative underground laboratories worldwide. Fields with (-) indicate that the values are not provided in the listed reference.

Underground site	depth/ overburden ~m.w.e.	Rock type	Rock density g/cm^3	Specific activity ^{238}U (Bq/kg)	Specific activity ^{232}Th (Bq/kg)	Specific activity ^{40}K (Bq/kg)
[51]Boulby (UK)	2800	halite	(-)	0.032 (7)	0.16 (2)	0.036 (3)
		mudstone	(-)	0.57 (2)	0.95 (3)	0.39 (1)
[52]INO (India)	2890	charnockite	(2.89)	1.2 (1)	14.7 (6)	1064 (68)
[53]Callio (Finland)	4100	pyrite	2.8	83 (7)	48 (5)	1513 (333)
[54]LNGS (Italy)	3800	dolomite	2.7	1.8 (1)	1.5 (1)	26 (2)
[55]LSM (France)	4800	calcschist	2.7	11.8 (6)	10.2 (5)	182 (4)
[56]SURF (US)	4300	Homestake	(-)	2.7	1.3	297
[57]CJPL (China)	6720	calcite	(-)	3.95	0.58	4.28

defined as shallow (<500 m) and deep (>500 m), respectively. As aforementioned 1.1.2, the most important sources of gamma ray background inside the deep underground laboratories are decays of primordial radionuclides in parent rock and concrete walls. The overview of gamma ray background in various operational or proposed low-level shallow/deep underground laboratories searching for rare event experiments are discussed. Table 1.1 gathers information on natural gamma ray radioactivity from the surrounding rock samples in some underground laboratories. However, the investigations of the individual contributions to the background are essential for optimizing future shielding techniques using MC simulations and allowing the effective background reduction in the region of interest [58, 59]. The current interest is to build state-of-the-art radiation measurement laboratories located at modest underground depths to explore the full potential present at the shallow depth using various background reduction strategies as discussed in section 1.2. Some of the pioneer experiments with best-achieved background levels are listed in Table 1.2 As mentioned earlier, some specific areas of low background physics involve determining low and trace levels of

Table 1.2: The best background levels (N_{bkg}) achieved by pioneer neutrinoless double beta decay (NDBD) and dark matter (DM) experiments.

Experiment	Main Activity	location	Detector	Achieved N_{bkg} ($keV^{-1}kg^{-1}y^{-1}$)	Reference
KamLAND-Zen	NDBD	Kamioka (Japan)	Scintillator	1.5×10^{-4}	[60]
GERDA	NDBD	LNGS (Italy)	Ge diodes	0.7×10^{-3}	[61]
CUORE	NDBD	LNGS (Italy)	Bolometers	1.4×10^{-2}	[62]
EXO-200	NDBD	WIPP (New Mexico)	LXe TPC	1.7×10^{-3}	[60]
LUX-ZEPLIN (LZ)	DM	SURF (South Dakota)	LXe TPC	$\sim4\times10^{-4}$	[63]
DEAP-3600	DM	SNOLAB (Sudbury)	LAr TPC	$\sim3\times10^{-4}$	[64]
Darkside-50	DM	LNGS (Italy)	LAr TPC	$\sim1\times10^{-3}$	[65]
XENON1T	DM	LNGS (Italy)	LXe TPC	$\sim9\times10^{-3}$	[66]

radioactivity. In such cases, the key point is to achieve very low detection limits. In recent years, low background physics has emerged as a dedicated branch of radioactive background studies involving the measurements in surface and underground laboratories specific to the prerequisite of the experiments. In the following sections, the environmental and rare event studies covering the overview of ongoing physics interests are discussed.

1.3 Environmental radioactivity studies

The origin of low background physics begins deep underground, mainly within the realm of fundamental physics of neutrino interactions. However, other than fundamental physics, many experiments in environmental sciences such as environmental monitoring, waste assay, medical application, Fukushima fallout, surveillance of nuclear activities, homeland security, neutron activation analysis, general gamma ray spectroscopy services, benchmarking of other physical techniques and materials screening are hampered predominantly by background signals and requires low-level of radioactivity. This kind of experiment can also be conducted in similar research facilities due to the versatility of the technique.

Gamma ray spectrometry using HPGe detectors is a non-destructive reliable technique widely applied in qualitative and quantitative analyses of γ-ray emitting isotopes when dealing with environmental radioactivity. The strengths of environmental gamma ray backgrounds strongly depend on the surroundings of the detector, namely the content of radionuclides in the environment (e.g., uranium or thorium in the rock or radon in the air), rather than the depth of the location. The majority of the radionuclides can be attributed to primordial long-lived radioactive nuclides, or their decay chains, as indicated in Figure 1.1, 1.2. The concentration of ^{238}U, ^{232}Th, and ^{40}K in soil, sands, and rocks depend on the local geology and varies greatly at different levels in each region of the world [9]. The radionuclide concentration in such samples possesses very weak activity and, therefore, requires low background contribution to reduce the counts in the detector other than the sample being analyzed. Of particular concern is the long-lived uranium and thorium isotopes that emit relatively high-energy photons, which contribute to serious backgrounds, as mentioned before. In addition, the seasonal, humidity, and temporal variations of the amount of radon in the air can affect the effective background rates and may produce a troublesome background if it reaches the sensitive region of the detector setup. With this caveat in mind, the purpose of such measurements is to investigate the potentialities by improving the detection limits of the main spectrometer, realizing and testing dedicated types of equipment able to deal with demanded sensitivity during construction while paying particular attention to the requirement to achieve as low as possible background rates at the lines of progenies in the decay chains of ^{238}U and ^{232}Th. Environmental measurements are often costly and time-consuming practices, and the analysis of samples at the environmental level is a complicated task due to the inherent complexity in the natural decay chains.

Moreover, low-level activity samples are often counted in the close vicinity of a detector. Accurate determination of radionuclides largely depends on the efficiency calibration of an HPGe gamma ray detector with volume samples. Due to the limited availability of reference radionuclides with the same geometry as the sample and simple gamma ray spectra, the Monte Carlo (MC) studies in gamma ray spectroscopy have been reported as a complementary tool to evaluate the detector response and spectrum prediction for point-like and voluminous samples within a typical error budget below 10%. These advanced gamma ray spectrometry methods often have to deal with practical problems of predominant background peaks, efficiency calibration, monitoring plan design, and data analysis and processing. Significant improvements have been made in the construction of Ge detectors as primary spectrometers for gamma ray spectrometry systems operating above the surface or underground. Dedicated low background spectroscopy systems using large volume Ge detectors have been developed to measure the activities in the level similar to or better than mBq/Kg sensitivity [67]. The desirability of these low-level measurement systems lies in their low detection limits and in analyzing smaller samples with improved accuracy within a shorter period of time.

Keeping in view, the ever-increasing demand for measuring low levels of radioactivity in the diverse area of research, low-background HPGe counting activities employing HPGe detectors are hosted in several laboratories with various depths ranging from ground-level to going deep underground locations. Previously reported low background measurement systems by other researchers [68] have shown that the selection of large-size HPGe detectors, radiopure materials, boil-off nitrogen gas purging, active shielding at ground-level or shallow-location or going deep underground location can lead to effective background reduction in the region of interest. Ultra-low background gamma ray spectrometry is continuously under development with the goal of reaching envisioned sensitivity. The currently operating representative ultra low-level Ge-spectrometry performed in the field of monitoring of environmental samples to contamination control and material assaying for the usage in physics experiments are summarized in Table 1.3. The current state-of-the-art level is accomplished by the most sensitive spectrometer, GeMPI (1 mBq/kg - 10 μBq/kg) especially suited for extraordinarily large sample measurements located in the Low Level Research Facility (LLRF) in the Gran Sasso underground laboratory at a depth of 3500 m w.e. [67]. Another setup of the same design with large N_2-flushed sample chambers and Pb/Cu passive shields, GeMPI III, is situated at the same facility but suffers the ^{207}Bi contamination and therefore, fails to reach the sensitivity of GeMPI available for routine material screening.

In India, efforts are underway to build a cryogenic bolometer detector, TIN.TIN (The INdia based TIN detector), for studying NDBD in ^{124}Sn [76]. To facilitate low background radiopurity measurements and material screening activities in connection with rare event studies [77] for TIN.TIN, the TiLES (Tifr Low background Experimental Setup) has been installed at sea level [2]. The integrated background rate in TiLES is the best possible

Table 1.3: List of the representative laboratories operating underground for low-level environmental radioactivity measurements using low background co-axial germanium spectrometers. Fields with (-) indicate that the values are not provided in the listed reference.

Name (Laboratory)	location	depth m.w.e	detector type	Background rate ($d^{-1}kg^{-1}$) 40-2700 keV	Main activity
IAEA-MEL	CAVE (Monaco)	35	n, p-type coaxial (100%, 170%)	1368, 1632 [69]	Marine radioactivity
PTB	Braunschweig (Germany)	2100	p-type extended range (95%)	26784 [70]	Reference measurements Dosimetry and spectroscopy
Felsenkeller	Dresden (Germany)	110	p-type coaxial (92%)	2938 [14]	Environmental radioactivity
OUL	Komatsu (Japan)	270	p-type coaxial (93%)	788 [71]	Environmental radioactivity
HADES	Mol (Belgium)	500	p-type coaxial	260 [72]	Reference measurements
DLB	Dortmund (Germany)	10	p-type semi coaxial (60%)	3641 [73]	Material screening and environmental analytics
PNNL	Richland (WA, USA)	30	p, n-type coaxial (112%, 97%)	1848, 3984 [74]	International Monitoring
TiLES	TIFR (Mumbai, India)	0	p-type coaxial (70%)	17000 [75]	Radiopurity studies and Material screening*

* for rare decay searches

background level achieved at sea level.

1.4 Studies of Rare events

Rare event searches seek evidence from processes with elusive event rates buried under very high background levels to detect signals of interest. The standard model (SM) of particle physics has successfully understood the basic principles of composition of matter-particle interactions [78]. However, recent studies point towards the missing pieces of the SM. The physics beyond the SM will be required to explain neutrino oscillations and the existence of non-zero neutrino mass. The observation of neutrino oscillations has convincingly shown that neutrinos have a finite mass [79]. However, the oscillation results do not provide information about the absolute neutrino masses and nature of neutrinos, whether a Dirac (particle $\neq$ antiparticle) or a Majorana (particle = antiparticle) character. The Nobel prize-winning neutrino oscillation experiments caused a renaissance of enthusiasm in pursuing physics beyond the SM in studying neutrino properties on many fronts. The tritium beta decay experiment by KATRIN collaboration measures the absolute neutrino mass aiming for a sensitivity of 0.2 eV/c^2 at 90% C.L. The desired sensitivity can only be achieved with a very low background level of 10 mcps in the detector region of interest [32]. The ECHo experiment determines the effective electron neutrino mass of ^{163}Ho from the calorimetric measurement of the electron capture spectrum. The measured background level is about

8×10^{-5} d^{-1}pixel^{-1} [80]. Other experiments like DM [21], proton decay [81], NDBD [22], rare nuclear decays ($T_{1/2} \sim 10^{15} - 10^{20}$ yr) [23], low energy studies of reactions in nuclear astrophysics [82] looks for extremely low event rates. Due to the rare nature of these processes, stringent background conditions are essential to achieve the required sensitivities.

1.4.1 Double beta decay

Double beta decay ($\beta\beta$ or $\beta^-\beta^-$) is a second-order weak process in which a parent nucleus (A, Z) decays to a daughter nucleus (A, Z + 2), along with the emission of two e^- and two $\bar{\nu_e}$. This isobaric transition can occur in neutron-rich nuclei, where β decay is either energy and/or spin forbidden. In 1935, Maria Geoppert-Mayer introduced the possibility of this nuclear interaction [83] often termed as $2\nu\beta\beta$ and can be represented by the following equation:

$$(A, Z) \rightarrow (A, Z + 2) + 2e^- + 2\bar{\nu}_e \tag{1.1}$$

This process is allowed within the SM and is expected to occur in many even-even nuclei. Normal $\beta\beta$ decay (or $2\nu\beta\beta$), conserves the total lepton number and has been experimentally detected in about 12 nuclides with longest half-lives typically 10^{18}–10^{24} yr [44]. In 1937, Majorana theoretically showed that Fermi's theory of β decay remains unchanged even if the neutrino was its own antiparticle [84]. In the same year, Racah put forth a $\beta\beta$ decay sequence [85] where the initial nucleus (A, Z) emits one β particle and goes into a virtual intermediate state (A, Z ± 1) plus an antineutrino. This antineutrino induces the decay of this intermediate nucleus with emission of the another β particle and itself reabsorbed. In 1939, Furry considered the possibility of a $0\nu\beta\beta$ decay following the Racah sequence in which a parent nucleus (A, Z) decays to a daughter nucleus (A, Z + 2) in a single step, without the production of antineutrino in the final state. This process is known as neutrinoless double beta decay and can be written by the following equation as:

$$(A, Z) \rightarrow (A, Z + 2) + 2e^- \tag{1.2}$$

The neutrinoless double beta decay ($0\nu\beta\beta$ or NDBD) process violates the total lepton number by two units ($\Delta L = 2$) and is not allowed within the SM. It is a novel probe to investigate lepton number violation (LNV), and matter-antimatter asymmetry, and perhaps the only practical way to assess the nature of the neutrinos. NDBD has not been observed to date, with a typical half-life limit of $> 10^{26}$, and possible only if neutrinos are Majorana particles with non-zero mass. Elliot *et al.* [86] measured the first direct experimental evidence of $2\nu\beta\beta$ in ^{82}Se using a time projection chamber (TPC). The decay rate (or inverse of half-life) for $2\nu\beta\beta$ can be written as:

$$\frac{1}{T^{2\nu}_{1/2}} = G^{2\nu}(Q_{\beta\beta}, Z)|M^{2\nu}|^2 \tag{1.3}$$

where $G^{2\nu}$ is the phase space factor and can be calculated precisely, the $Q_{\beta\beta}$ is the Q value and $M^{2\nu}$ is the nuclear transition matrix element (NTME) of the transition. For $0\nu\beta\beta$ decay, the decay rate is given by:

$$\frac{1}{T^{0\nu}_{1/2}} = G^{0\nu}|M^{0\nu}|^2(\frac{< m_{\beta\beta} >}{m_e})^2 \tag{1.4}$$

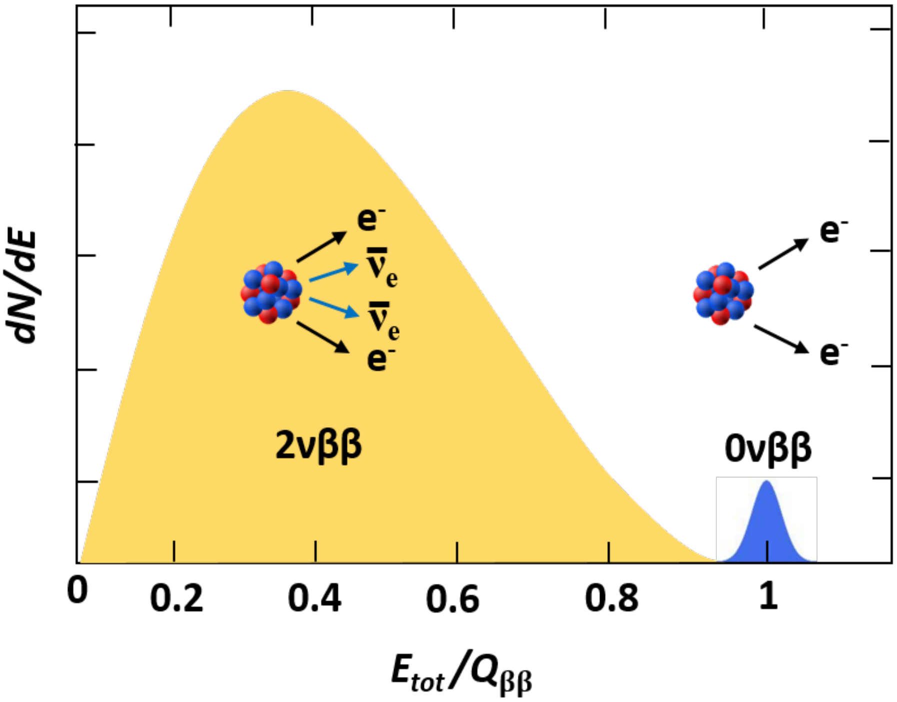

Figure 1.4: Schematic of energy spectra for the $2\nu\beta\beta$ and $0\nu\beta\beta$ processes.

where $G^{0\nu}$ is phase space factor, $M^{0\nu}$ is the NTME for the decay, $< m_{\beta\beta} >$ is the effective neutrino mass and m_e is the electron mass. NDBD mode is sensitive to the neutrino mass and new specific theoretical scenarios. Moreover, the calculations of NTMEs involve several assumptions of many-body techniques and nuclear models and thus add to large theoretical uncertainties. Thus, searches for this type of decay are important for a complete understanding of the DBD process. The experimental signature of observation of the NDBD process is a peak at the Q-value of the decay in the sum energy spectrum of the two emitted electrons. In case if the peak is observed for $0\nu\beta\beta$, the half-life $T^{0\nu}_{1/2}$ can be obtained from the relation:

$$T^{0\nu}_{1/2} = \frac{ln2\ N_A\ M\ \epsilon\ a\ t}{N_{obs}\ W} \tag{1.5}$$

where N_A is Avogadro's number, ϵ is the peak detection efficiency, a is the isotopic abundance in the sample of the mass M, W is the molar mass of the source, N_{obs} is the number of events attributed to $0\nu\beta\beta$ events, and t is the measurement time. If no signal is detected, then the sensitivity of an experiment is usually defined as a lower limit on the half-life of $0\nu\beta\beta$ and can be set as:

$$T^{0\nu}_{1/2} > \frac{ln2\ N_A\ \epsilon\ a}{k_{CL}\ W}\sqrt{\frac{M\ t}{\Delta E\ N_{bkg}}} \tag{1.6}$$

where k_{CL} is the number of standard deviations corresponding to a given confidence level, N_{bkg} is the number of background events normalized to energy unit defined as background index in the region of interest ($kg^{-1}keV^{-1}y^{-1}$) and ΔE is the energy resolution of the detector. The most sensitive NDBD experiments such as GERDA [61], CUORE [62] and KamLAND-Zen [87] quote half-life limits in $\beta^-\beta^-$ at the level of $T_{1/2} > 10^{25} - 10^{26}$ yr, corresponding to Majorana neutrino mass limits in the range $m_{\beta\beta} < 0.04 - 0.3$ eV. Current ongoing projects will probe Majorana neutrino mass in the inverted hierarchy region of $m_{\beta\beta} < 0.01 - 0.05$ eV. The KamLAND-Zen experiment have the best background level of 1.5×10^{-4} kg^{-1} keV^{-1} y^{-1} [60]. Currently, LEGEND [88], a joint collaboration of MJD [89] and GERDA [61], will probe the half-life sensitivity beyond 10^{28} yr with a ton scale HPGe detectors and a background goal of $< 1 \times 10^{-5}$ kg^{-1} keV^{-1} y^{-1} corresponding to a (0.02 - 0.05) eV Majorana neutrino mass.

As pointed out earlier, for the precise measurement of $0\nu\beta\beta$ half-lives, the accurate knowledge of 0ν NTME values is essential. The 2ν NTME calculations can be verified from Eq. 1.3 by measuring the decay rates of $2\nu\beta\beta$ processes in different isotopes. In some model cases, one can consider the 2ν NTME as a test case for the 0ν modes. However, for accurate measurement of effective neutrino mass $m_{\beta\beta}$, it is essential to observe $0\nu\beta\beta$ decay in different nuclei. The precise and unambiguous investigations of $2\nu\beta\beta$ decay are equally important to constrain the different parameters in nuclear models, which can clarify various aspects of $0\nu\beta\beta$ decay and to search for several exotic processes such as neutrino self-interactions [90], right-handed leptonic currents [91], Lorentz and CPT violation [92, 93] and Majoron decay modes [94, 95], etc. Given the significance and the critical role played by $2\nu\beta\beta$ decays, they have been studied in a dozen of DBD nuclei, and the most relevant ongoing experiments based on low background detectors are well documented in [96].

As discussed, similar to DBD negative decay modes, equivalent positive decay modes also exist. In the case of proton-rich nuclei, three kinds of DBD+ modes are kinetically possible such as double positron emission ($2\nu\beta^+\beta^+$), positron emission and electron capture ($2\nu EC\beta^+$) and double electron capture ($2\nu ECEC$), respectively, as shown in following equations,

$$(A, Z) \to (A, Z-2) + 2e^+ + 2\nu_e, \tag{1.7}$$

$$(A, Z) + e^- \to (A, Z-2) + e^+ + 2\nu_e, \tag{1.8}$$

$$(A, Z) + 2e^- \to (A, Z-2) + 2\nu_e. \tag{1.9}$$

There are essentially 34 nuclei where positive modes of DBD can be measured. These processes are strongly disfavoured due to reduced decay energy and available phase space, which further limits the sensitivity of experiments, thereby more challenging to detect. The $2\nu\beta^+\beta^+$, $2\nu EC\beta^+$ modes provide additional experimental signature of 511 keV γ-rays from positrons annihilation, while $2\nu EC\beta^+$ and $2\nu ECEC$ emits characteristic X-rays. The emitted positrons/electrons and gammas can be measured employing coincidence techniques. The $0\nu ECEC$ process is revisited where the rate of $0\nu ECEC$ can experience a resonant enhancement in several nuclides when the initial and final states are energetically degenerate and can approach the sensitivity of the $0\nu\beta^-\beta^-$ mode[97]. These appealing features and continuous advancement in the technology, along with further improvement in the background levels, have renewed interest in studying these other modes of DBD decay using a variety of experimental techniques. The achieved sensitivities reported in the most sensitive experiments for DBD positive modes are modest in the range of $T_{1/2} > 10^{21} - 10^{22}$ yr (see reviews [45, 46]). These experimental tests can provide important complementary information to study the shape of the nucleus and decay modes of other nuclei. They provide information on the dynamics of the DBD decay by undergoing any of these processes both to the ground and the excited states. The $2\nu\beta^+\beta^+$, $2\nu EC\beta^+$ processes have lower decay probability than $2\nu\beta^-\beta^-$ but their investigations can significantly contribute to the clarification of $0\nu\beta\beta$ decay. The collusive information from the study of positive and negative DBD can constrain the theoretical parameters with high confidence. Therefore, studies on other decay modes of DBD decay provide supplementary information about the DBD decay of the parent nuclide and are important from both the experimental and the theoretical sides. The techniques to study DBD can be broadly classified into two categories:

- Active detectors technique (source = detector) - In this technique, the detector is made out of the nuclide of interest. Examples of such detectors are High Purity germanium (HPGe), Cadmium Zinc Telluride (CdZnTe), bolometers (TeO_2), scintillators, liquid noble gas (LXe) detectors, high-pressure gaseous time projection chambers (TPCs), etc.

- Passive detectors technique (source $\neq$ detector) - In this technique, the detector and the source are not the same, and the nuclide of interest is mostly measured by the γ-ray emission of enriched sample material using HPGe detectors. The detectors deployed are generally of larger size.

The listed detection methods are of low background variety and are placed mostly in underground or shallow/deep laboratories. The primary spectrometers are well shielded by composite layers of passive and active shielding as discussed in section 1.2. Quite a large number of $\beta\beta$ decay isotopes have been measured using the above experimental techniques at existing or similar low background installations. In the present thesis, we are interested in the external-source approach, which enables the measurements of multiple DBD nuclei deploying HPGe detectors in single/multi-configuration.

1.4.1.1 Search for positive double beta decay modes (DBD+)

The search for DBD+ is ongoing in several isotopes employing different detector technologies. The most sensitive experiments give modest limits on these processes in the range of about $T_{1/2} \sim 10^{21} - 10^{22}$ yr (for ^{40}Ca, ^{36}Ar, ^{58}Ni, ^{64}Zn, ^{78}Kr, ^{96}Ru, ^{106}Cd, ^{112}Sn, ^{120}Te, ^{124}Xe, ^{126}Xe, ^{130}Ba, and ^{132}Ba). The major direct counting experiments using active and passive detector approaches in various potential isotopes are discussed here.

- **CRESST** (Cryogenic Rare Event Search with Superconducting Thermometers) is a scintillating bolometer based on $CaWO_4$ crystals and installed in LNGS. The detector is surrounded by a passive shield of low background copper (14 cm) and lead (20 cm) thick. The inner shielding assembly is enclosed within a gas-tight radon box that is continuously purged off with N_2 gas. With an exposure of 2 kg.yr, the limit of $T_{1/2}$ on $0\nu ECEC$ decay in ^{180}W and ^{40}Ca has been set to $> 9.4 \times 10^{18}$ yr and $> 1.4 \times 10^{22}$ yr (at 90% C.L.), respectively.

- **COBRA** (Cadmium zinc telluride 0-neutrino double-Beta Research Apparatus) Collaboration uses semiconductor diodes employing CdZnTe crystals that allow for the operation at room temperature. These detectors are arranged in four layers of 16, each with a size of $1 \times 1 \times 1\ cm^3$. They are further surrounded by shielding of ultrapure copper and lead, with an additional layer of borated Polyethelene and an EMI shielding. The setup is continuously flushed with nitrogen for radon removal. CdZnTe contains nine double-beta isotopes: ^{64}Zn, ^{70}Zn, ^{106}Cd, ^{108}Cd, ^{114}Cd, ^{116}Cd, ^{120}Te, ^{128}Te, and

^{130}Te, but the sensitivity that is reached for their DBD+ is often not competitive. The sensitivity for the $2\nu EC\beta^+$ in ^{120}Te is at the level of $> 9.4 \times 10^{15}$ yr (at 90% C.L.) while, the best limit lower limit of ECβ^+ is given by CUORE as $> 2.9 \times 10^{22}$ yr (at 90% C.L.) [98]. This limit is improved by order of magnitude from the existing limits of CUORICINO and CUORE-0 collaborations.

- **CUPID** (CUORE Upgrade with Particle Identification) experiment is an upgrade of CUORE adopting ZnSe crystals using scintillator-bolometric techniques. The first physics run named CUPID-0 has provided the best limit on $0\nu\beta\beta$ (ECβ^+) of ^{64}Zn as $> 1.2 \times 10^{22}$ yr (at 90% C.L.).

An interesting case of ^{106}Cd isotope studied by DAMA and DAMA-INR Kyiv collaborations using ^{106}CdWO$_4$ crystal scintillator detector carried out in LNGS. In later stages, to improve the sensitivity for $\beta^+\beta^+$, the experiment with ^{106}CdWO$_4$ scintillation was operated in coincidence with four HPGe detectors and with two CdWO$_4$ counters. The half-life limits for different channels and modes of the ^{106}Cd double beta decay is at the level of $T_{1/2} \sim 10^{20} - 10^{22}$ yr. The AURORA experiment investigates $0\nu EC\beta+$ in ^{106}Cd and achieved the best limit of $4{\times}10^{21}$ yr (at 90% C.L.) using ^{116}CdWO$_4$ scintillators [99]. The sensitivity has reached the range of theoretical reported values for the decay half-life. The direct observation of $2\nu ECEC$ in ^{124}Xe is reported for the first time with the XENON1T detector utilizing liquid xenon (LXe) and time projection chamber (TPC) experimental technique [100] at LNGS. It contains ∼3 tons of ultrapure liquid xenon (LXe) with 2 tons as the target material in the active volume of the time projection chamber (TPC). The purpose of this detector is to look for dark matter, but due to the presence of tonnes of natural xenon, it is also sensitive to search for NDBD experiments. The recent results measure a half-life of $T_{1/2} = 2.1 \pm 0.2(stat) \pm 0.1(syst) \times 10^{22}$ yr [101]. The limits on $\beta^+\beta^+$ decay of ^{124}Xe are obtained using a high-pressure ionization chamber (HPIC) as $> 2.0 \times 10^{14}$ yr (2ν) and $> 4.2 \times 10^{17}$ yr (0ν), respectively at 68% C.L. [102]. HPGe detectors and low-temperature bolometers appear to be the most suitable detection techniques for $0\nu ECEC$ experiments, with a sensitivity of $T_{1/2} > 10^{25} - 10^{26}$ yr [97].

Several DBD+ emitters are studied utilizing low background germanium spectrometers by passive source techniques. The measurements carried out by the HPGe spectrometers at the SubTErranean Low-Level Assay (STELLA) facility of LNGS [103] by the DAMA-INR Kyiv collaboration holds the most stringent limits for mostly all of the isotopes investigated by this approach. The experimental setups of ultra-low level detector systems with sensitivity down to the μBq/kg level, which allow detection of many DBD+ transitions up to the level of 10^{21} yr [46] in low-scale experiments. Different purification techniques have been developed to reduce sample contamination. There is a great interest in pursuing new double beta decay experiments for lanthanide and rare-earth elements.

1.4.1.2 Search for DBD to excited states of daughter nuclei

DBD decay can also occur in excited states other than the ground state, albeit lower decay rate due to smaller available phase space. The study of DBD decay to excited levels of the daughter nucleus provides a clear signal via accompanying de-excitation γ-rays with characteristic energies along with two emissions of electrons/positrons. The detection of single γ-rays and, in cascade, γ-rays deploying coincidence techniques can help gain more information on the nuclear structure, and effective background reduction can be performed.

The first experimental investigation on $\beta\beta$ decay to the excited levels of ^{76}Ge was reported by E. Fiorini in 1977, studied as a by-product of the main experiment searching for transition to the ground state [104]. Given the merit of these transitions, many experiments of [86, 105–108] have been pursued on many potential $\beta\beta$ candidates by improving the experimental sensitivity and achieved new limits. Reference [106, 109] pointed out the possibility of detecting the γ-rays produced in the de-excitation of the nuclear levels after a $\beta\beta$ decay to excited levels of daughter nuclei in three nuclei: ^{96}Zr, ^{100}Mo, ^{150}Nd and corresponding evaluated half-lives are of the order of ($10^{20}-2\times10^{21}$) yr. The more recent results of deduced half-lives of $\beta\beta$ decay in ^{100}Mo and ^{150}Nd and different nuclei are given in [44] while in ^{96}Zr only a limit is obtained by Finch *et al.* [110] ($T_{1/2} > 3.1\times10^{20}$ yr of 0^+ - 0_1^+ transition). DBD studies of ^{94}Zr (another isotope of Zr) to excited states of ^{94}Mo were carried out using a low background experimental setup TiLES [2] installed in TIFR, Mumbai at sea level in India. The improvement of the half-life limit $T_{1/2} > 3.4\times10^{19}$ yr [77] by a factor of ~4 for 0^+ - 2_1^+ transition was observed than the earlier reported value [105]. Another investigation with a low background setup at the Felsenkeller underground laboratory in Dresden, Germany, has reported the present best lower limit of 5.2×10^{19} yr (90% C.L.) [111].

To date, $\beta\beta$ decay of ^{124}Sn has not been experimentally observed despite the suitability with $Q_{\beta\beta} = 2.23$ MeV and natural isotopic abundance of 5.8% for DBD searches. The best limits obtained for $\beta\beta$ decay of ^{124}Sn to the excited state of ^{124}Te are ~0.8-1.2$\times10^{21}$ yr [112]. ^{124}Sn can be made into low-temperature bolometers, and in experiments with such detectors, measurement accuracy of half-life can reach up to 1-2%. An indigenous effort is underway in India to build the next-generation NDBD experiment TIN.TIN to search for $0\nu\beta\beta$ in ^{124}Sn using a cryogenic bolometer at the India-based Neutrino Observatory (INO) (for details see [113]). ^{112}Sn is another interesting isotope with natural abundance is 0.97% which can undergo $EC\beta^+$ and $ECEC$ processes. Searches have been made on $\beta\beta$ and $ECEC$ decay of ^{112}Sn to excited states, and the best present lower limits are obtained in the range 10^{19}-10^{21} yr [114]. Nevertheless, the positive modes in tin isotopes have not been investigated very well theoretically or experimentally. The Ge based experiments GERDA and MJD have reached a sensitivity at the level of 10^{23}-10^{24} yr for the double beta decay of ^{76}Ge to excited states of the daughter nucleus. MJD has reported the most stringent limits for all the $\beta^-\beta^-$ processes to excited levels for both for 2ν and 0ν modes [115]. CUORE-0 experiment has established the most stringent limit on the decay to the 0_1^+ excited state in ^{130}Xe [116]. As mentioned earlier, many experiments have been carried out at the STELLA facility of LNGS. Some double beta decay processes have been investigated for the first time at STELLA using ultra-low background HPGe spectrometry. For instance, the search for $ECEC$ and $EC\beta^+$ of ^{168}Yb to the ground and excited states of ^{168}Er were achieved in the level of 10^{14}-10^{18} yr [117]. The lower half-life limit of another isotope of ^{162}Er to the ground and excited states of ^{162}Dy were estimated as as 10^{15}-10^{18} yr [118]. The lower limit for the half-life for $ECEC$ and $EC\beta^+$ decay of ^{174}Hf was first measured using ultra-low background HPGe detector at HADES laboratory on the level of 10^{16}-10^{18} yr [119]. However, future large-scale and sensitive measurements are necessary to establish more reliable and precise half-life values and effective nuclear matrix elements.

1.4.1.3 Search for hindered single beta decay

Long-lived nuclei ($T_{1/2} > 10^{10}$ yr) which decay through single α or β decay very often create significant backgrounds in studies of rare events like double beta decay, solar neutrinos or dark matter [23, 120]. Renewed interest in investigations of rare β decays has gained much attention very recently due to the steady improvement in experimental techniques and more sensitive measurements. The forbidden beta decay of ^{187}Re ($T_{1/2} = 4.12\times10^{10}$ yr) and electron capture decay of ^{163}Ho ($T_{1/2} = 4570$ yr) both with low Q-value $\sim$2.5 keV are competitive isotopes planned to be studied by MARE experiment with cryogenic microcalorimeters to measure the electron neutrino mass with sub-eV sensitivity [121]. Recently, β decay of ^{115}In to the first excited state of ^{115}Sn is observed with lowest Q_β ($\sim$155 eV) value known among the observed β decay to-date [122]. The more precise half-life was obtained as $T_{1/2} = 4.3\pm0.5\times10^{20}$ yr using ultra-low HPGe gamma ray spectrometer at the HADES underground laboratory [123]. Another similar β decay of ^{113}Cd isotope is highly forbidden (fourth-fold) and studied with $CdWO_4$ crystal scintillator in LNGS as $T_{1/2} = 8.04\pm0.05 \times 10^{15}$ yr [124]. This is the most precise and the longest observed β decay to date.

Out of 35 DBD isotopes, only two cases of ^{96}Zr and ^{48}Ca are energetically allowed for single β decay but are strongly suppressed due to large spin forbiddenness and hence are long-lived radionuclides. The best experimental limit for ^{48}Ca single β decay is $T_{1/2} > 2.5\times10^{20}$ yr using low background HPGe spectrometer and enriched external source [125]. This observed limit is very close to the theoretically estimated values. However, $\beta\beta$ decay to ^{48}Ti is faster and already observed with $T_{1/2} = 6.4\times10^{19}$ yr [126]. The half-life of single β decay of ^{96}Zr was first established to be $\geq 1.4 \times 10^{18}$ yr by Norman *et al.* [105]. In 1994, Arpesella *et al.* [108] achieved improved limit of $\geq 3.9 \times 10^{19}$ yr and the best lower limit for ^{96}Zr to date. After more than two decades, a study conducted by Finch *et al.* [4] has produced a limit of $T_{1/2} > 2.4\times10^{19}$ yr for ^{96}Zr. In addition, this is the first experimental search to distinguish between the two decay modes of single β and the $\beta\beta$ decay deploying coincidence techniques, but with a slightly less stringent limit than the value given by Arpesella *et al.* [108]. Therefore, detecting single γ-rays or a set of γ-rays for the number of investigated transitions could provide more information about the decay modes and hence have higher discovery potential for the studied nuclei. In addition, synergies of DBD physics with rare β decays are found and require a continued search in the future with large enriched source mass and advanced background reduction techniques.

1.5 Present work

This thesis investigates various low background aspects to explore the improvement in detection sensitivity employing multi-dimensional spectrometers and performing low-level measurements to understand the radiogenic backgrounds, particularly using high purity germanium (HPGe) detectors in connection with rare decay measurements. The characterization of a low background HPGe detector setup and a suite of experimental measurements performed using point-like γ-ray sources in a wide energy range of 80-1408 keV are discussed in the present work. A preliminary detector model has been developed using the GEANT4 simulation package to estimate the photopeak efficiency of an HPGe detector employed in the setup. Investigations of specific activity and its variation in soil samples from the arable lands in the Ropar district of Punjab state in India have been carried out using ILM-0, a demonstrator of low background setup ILM (IIT Ropar Low-background Measurement setup) being developed at IIT Ropar for rare decay studies.

The present interest of chapter 3 is to carry out the feasibility study of an experiment to investigate the single beta and double beta decay modes in ^{96}Zr and ^{112}Sn isotopes, respectively. In order to perform the feasibility studies of rare decays, a set of MC simulations with a 2/4 HPGe detector setup employing the coincidence technique for source optimization, along with the data analysis of the detection efficiencies within the framework of GEANT4 [127] and ROOT [128] are presented. An attempt to study the feasibility of the ^{96}Zr β decay through ^{96}Mo γ-ray cascade using a low background setup of four detectors has been performed. Developing detectors operating in time coincidence is a possible way to increase the sensitivity and specificity in low background gamma ray spectroscopy. Therefore, to estimate the sensitivity to search for $\beta^+\beta^+$/ECβ^+ processes in ^{112}Sn, the ambient background has been measured with moderate Pb shielding around the coincidence setup of two low background HPGe detectors in the laboratory of TIFR, Mumbai at the sea level. The experimental details and data analysis procedures are discussed in the following chapter.

Efforts are underway to set up an underground laboratory for planning the low background experiments in India. The ambient radiation background level in rock samples collected from the Aut site in the eastern Pir Panjal range of the Himalayas, India, has been investigated. Findings of the present studies were compared with the Bodi West Hills (BWH) of the Theni district in Madurai, Tamil Nadu [52, 129]. In order to assess the impact of the long-lived neutron-induced activities, fast neutron activation experiments have been carried out on the Aut and BWH rock samples. Irradiations were carried out at BARC-TIFR Pelletron Linac Facility, Mumbai [5] at two incident proton energies, 12 and 22 MeV, to cover a broader energy range and compare the yield of the observed products on neutron energy.

Chapter 2

Low Background Radiation Measurement Setups

Low background gamma ray spectrometry employing HPGe detectors is a sensitive tool for measuring low radioactivity levels in environmental applications, material screening, and experimental searches for rare decay experiments. A low background measurement setup has been developed at IIT Ropar in Punjab, India, to measure trace natural radioactive elements, with a particular interest in studying radioactivity in soil from different locations of Punjab state. The performance and characterization of low background cryocooled HPGe detector (~33%) have been investigated. A preliminary detector model has been developed using Monte Carlo simulations to determine the detector's response over a wide energy range. The minimum detectable levels of the spectrometer are determined for the environmental soil matrices. The present setup provides improved detection limits of low-level environmental samples and is adequate for environmental radioactivity measurements. The preliminary results of the primordial radionuclide traces at the agricultural test site of Katli village have been investigated. In addition, other low background experimental setups installed at Tata Institute of Fundamental Research (TIFR), Mumbai utilized for measurements reported in this thesis, are also discussed.

2.1 Introduction

The radioactive background at sea level laboratories is dominated by cosmic rays and cosmic ray-induced interactions, primordial radioactivity in the material around the detector setup. As discussed in chapter 1, environmental radioactivity originating from the natural decay chains of ^{238}U, ^{232}Th, and ^{40}K are long-lived ($T_{1/2}$ $\sim$$10^8$ - 10^{10} y) and present in trace amounts at different levels in the earth crust. The gamma ray background from these naturally occurring radionuclides is a significant source of radiation exposure for sea-level laboratories. It is important to assess the background radioactivity as measurements at the environmental level deal with low radioactivity concentration over a wide energy range and involve inherent complexity due to typical interference of natural radionuclides, thereby complicating the measurements. In addition, the gamma ray flux is subject to variation, possibly due to experiment location in the laboratory/site, seasonal fluctuations, the radon concentration near the experimental setup, or unknown systematic uncertainties. Background statistical fluctuations can influence the assessment of peak identification, peak area calculations, energy resolution, confined intervals, and detection limits. For reliable estimation of the radioactive impurities in weak samples, it is necessary to identify and minimize the background to improve the minimum detection limits of the spectrometer. As stated before, the radiopure cryostat with selectively refined detector construction materials and applying passive shielding allows for lower minimum detectable activity and high sample throughput for a specific counting time, which is highly desirable in low background counting applications. Therefore, low background HPGe gamma ray spectrometers play an increasingly important role in investigating trace radioactive element detection [2, 19, 52].

Some areas in Punjab have shown somewhat higher natural radioactivity as compared to the other districts. Although many studies of environmental radioactivity have been reported from different cities of Punjab, very few investigations have been conducted in the Ropar region. In order to study the natural radioactivity levels from different agricultural lands in the Ropar district, a low background measurement setup ILM-0 (IIT Ropar Low-background Measurement setup) was developed and installed in the above-ground laboratory at the Indian Institute of Technology Ropar. This setup intends to study radiation background and radio-purity assessment to conduct low-level environmental radioactivity experiments.

The present chapter describes the characterization of a low background carbon fiber HPGe detector (~33%). A suite of experimental measurements has been performed using point-like gamma ray sources to characterize a low background cryocooled HPGe detector over a wide energy range from 80.9–1408 keV. The performance specifications are successfully tested against the values provided by the manufacturer, such as energy resolution, peak shape, peak-to-Compton ratio (P/C), full energy peak efficiency (FEPE), and figure of merit (FoM). Mono-energetic sources are used for the close scanning of germanium crystal along its parallel and perpendicular axis to test the homogeneity of the detector response over the crystal surface and the possible effect of a weak electrical field. Monte Carlo (MC) simulations using GEANT4 [127] software have been performed in order to estimate the full energy peak efficiency of an HPGe detector. From the literature, it has been observed that the MC simulated efficiencies are often $\geq$10% higher than the measured values, which can be attributed to various factors such as a thicker dead layer, uncertain crystal dimensions, and a weak electrical field [2, 130, 131]. The MC detector model was then optimized by adjusting detector parameters to reproduce experimental efficiency within acceptable uncertainty. The present study focuses on the potential of ILM-0 for environmental studies. Therefore, the ambient gamma ray background and its further reduction using passive shielding around the detector are investigated. The sensitivity of the setup is studied in soil samples from the agricultural test site of Ropar district in Punjab, India. Specific activities and trace impurity concentrations from the primordial radionuclides have been estimated. Additionally, characteristics of other low background experimental setups TiLES [2] and CRADLE [132] installed at sea level in Tata Institute of Fundamental Research (TIFR), Mumbai for radiation background studies related to rare decay searches are also discussed.

2.2 ILM-0

The experimental setup (ILM-0) comprises of p-type co-axial HPGe detector, ORTEC makes (GEM30P4-83-RB) with a measured relative efficiency of 33%. The schematic of the setup is shown in Figure 2.1. The detector crystal ($62\ mm \times 46\ mm$) is mounted inside a low background cryostat of carbon fiber (carbon-composite). The top of the crystal face is 5 mm beneath a 0.9 mm thick carbon fiber entrance window suitable for measurements as low as 10 keV. The rear end of the detector is attached to the ∼150 mm long vertical cold finger connected to the transfer hose of an electro-mechanical cooler (Ortec X-Cooler III) for cooling the detector crystal to liquid nitrogen (LN_2) temperature. The typical cooldown time required by the electro-mechanical cooler is found to be 10-16 hrs. The detector assembly is supported with additional online UPS to protect during utility power failure. This setup is suitable for the underground laboratory by eliminating the need to transport liquid nitrogen. The detector is coupled with the pulse processing electronics and data acquisition system, including a NIM-based high voltage power supply, spectroscopic amplifier, and multichannel analyzer procured from Ortec. The multichannel analyzer records the data using the emulator software Maestro. A list of relevant technical details, along with the associated electronics, are summarized in Table 2.1. It should be mentioned that the shaping time of 6 μs was found to be optimum to minimize the noise. Data have been acquired for at least 10,000 counts for characterization measurements to reduce the statistical error to as

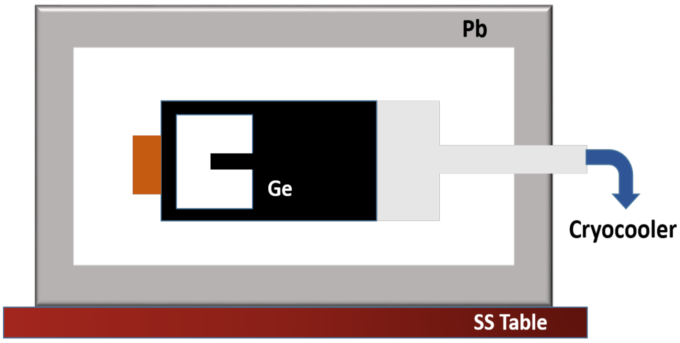

Figure 2.1: Schematic cross-section of the experimental setup of ILM-0 (IIT Ropar Low Background Measurement setup). The setup is mounted on thick stainless steel (SS) table 1 m above the ground.

Table 2.1: Detector specifications used in the measurement setup.

Model	GEM30P4-83-RB
Manufacturer	Ortec
In service since	2017
Capsule type	Pop top
HV Bias	2900 V
Input polarity	+ve
DAQ	Analog
Shaping time	6 μs
Geometry	Closed end
Cryostat type	Vertical dipstick
Cryostat diameter	75 mm
Cryostat height	165 mm

low as 1%. Detector dead time has been monitored throughout the measurement and found to be less than 1%. No significant worsening of energy resolution and shift in energy was observed at different times of long counting measurements. The data of the background spectrum was recorded in a timestamp of 24 h. The raw data is then converted and analyzed using LAMPS [133] software. Each photopeak is fitted to the sum of Gaussian and second-order polynomial for a background to extract the net photopeak area. The scanning of the detector has been carried out using a set of standard sealed disk-type gamma sources of the active diameter of ∼6 mm and thickness of ∼1 mm with absolute strength of gamma sources $\leq$95 kBq within 5% uncertainty. These sources cover a gamma ray energy range from 80.9 keV to 1408 keV, as shown in Table 2.2. Nuclear data such as half-lives and the emission probabilities of the isotopes are obtained from the chart of the radionuclides database of the National Nuclear Data Center [3]. To reduce the scattering effects during the measurements, the detector was placed on the scanning table with adequate clearance around it. The placement of the source was maintained as consistent and repeatable as possible. Specific care has been taken to ensure that the same set of sources is used and that the detector remains in the exact location during the testing and characterization of the setup.

2.2.1 Spectroscopic performance of the detector

The HPGe detector is surrounded by moderate passive shielding with lead bricks of dimensions $22.9cm \times 7.6cm \times 5.1cm$ and mounted on a custom-made stainless steel table, as shown in Figure 2.1. In this arrangement, the detector with a preamplifier is entirely shielded with adequate space for mounting voluminous sources generally used in environmental radioactivity measurements. It should be mentioned that different shapes and configurations of the lead shields were also considered before the final implementation of bricks geometry. The accuracy of the measurements depends profoundly on the performance and stability of the detector and associated electronics. Different characteristics of the HPGe detector, such as energy calibration and resolution, peak shape and peak-to-Compton ratio (P/C), full energy peak efficiency (FEPE), and figure of merit (FoM) are determined as a function of gamma ray energies against the warranted values provided by the manufacturer. The radioactive gamma sources used in the scanning of the detector are given in Table 2.2. For the present HPGe detector, GEM30P4-83-RB, a relative efficiency check at 1332.5 keV from ^{60}Co has been measured according to standard test procedures of IEEE [134]. The photopeak efficiency of the HPGe detector at 1332.5 keV gamma line is given by the ratio of the total counts in the 1332.5 keV peak to the total number of source disintegration during the elapsed time. The time is corrected by the dead time of the amplifier and analyzer. The ratio of the photopeak efficiency of the HPGe detector has been calculated to the efficiency of a 3×3 NaI (Tl) scintillation detector at 25 cm from the endcap face. This ratio presented in percentage is given as the relative efficiency of the detector. The relative efficiency of the detector was found to be 33(0.3)% in the laboratory test, which is 6% lower than the measured value provided by the manufacturer.

Energy linearity and resolution

The HPGe detector has been calibrated using different standard gamma sources and shown in Figure 2.3 (a). The line through the data points represents a fitting function of type Y

Table 2.2: Radioactive gamma ray sources used in the present work.

Sources	Gamma Energy (keV)	Decay mode	Half-life	Branching Ratio (%)
^{109}Cd	88.0	EC	461.4 d	3.64
^{57}Co	122.1	β^-	271.7 d	85.60
	136.5	β^-		10.68
^{133}Ba	80.9	EC	10.5 y	32.90
	276.4			7.160
	302.9			18.34
	356.0			62.05
	383.9			8.940
^{22}Na	511.0	β^+	2.6 y	180.7
	1274.5			99.94
^{137}Cs	661.7	β^-	30.1 y	85.10
^{54}Mn	834.5	EC	312.2 d	99.98
^{65}Zn	1115.5	EC	243.9 d	50.04
^{60}Co	1173.2	β^-	1925.3 d	99.85
	1332.5			99.98
^{152}Eu	121.7	EC	13.5 y	28.53
	244.7	EC		7.550
	344.4	β^-		26.60
	411.1	β^-		2.240
	444.0	EC		0.298
	779.0	β^-		12.93
	867.4	EC		4.230
	964.0	EC		14.51
	1085.8	EC		10.11
	1089.7	β^-		1.734
	1112.1	EC		13.67
	1213.0	EC		1.415
	1299.1	β^-		1.633
	1408.0	EC		20.87

= a + bX, where a = 0.45 ± 0.03 and b = 0.38185 ± 1.59279 $\times 10^{-5}$. As can be noticed from this figure, a good linear relationship with the channel number can be observed. The statistical correlation coefficient is found to be 1 for each measured data point with the detector. The energy resolution measures the width (FWHM) of a single energy peak at a specific energy, usually expressed in keV for germanium detectors. It may be pointed out that the typical energy resolution of NaI and HPGe detectors are found to be 50 keV

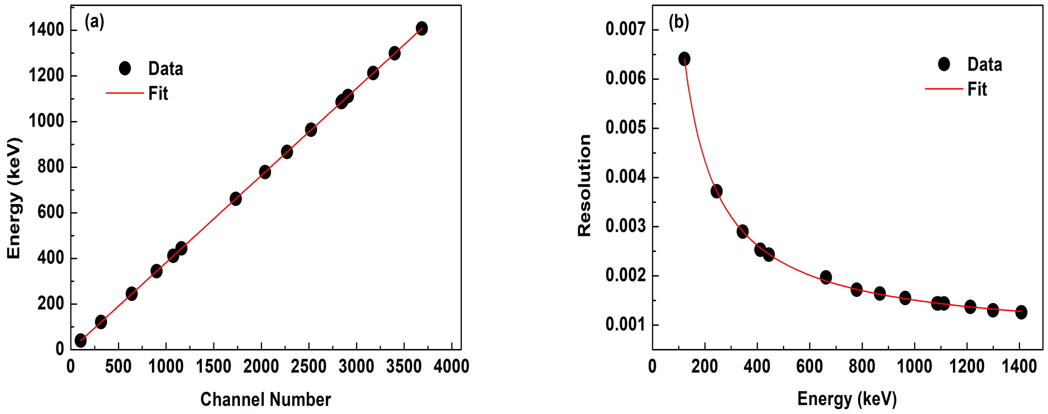

Figure 2.2: Energy calibration and resolution of the HPGe detector are shown in (a) and (b), respectively. The solid line through the data points is the best fit.

and 1.5 keV at 1332.5 keV, respectively [135]. Hence, HPGe is preferred over NaI detectors for high-resolution gamma ray spectroscopy, even though the NaI is likely to have greater counting efficiency. Generally, the energy resolution of a detector is expressed as the ratio of FWHM to the gamma ray energy. The distribution of energy resolution with different gamma rays is shown in Figure 2.3 (b) and fitted to an empirical three-parameter function of type,

$$\mathrm{R} = \frac{\mathrm{A}}{\mathrm{E}^{\mathrm{B}}} + \mathrm{C} \tag{2.1}$$

The best-fit values to the fitted parameters A, B, and C are 0.43 ± 0.03, 0.90 ± 0.01 and $6.42229 \times 10^{-4} \pm 3.43594 \times 10^{-5}$, where A and B are in keV. The typical energy resolution of this detector at 1332.5 keV is 1.72 keV and found to be similar to another LN_2 based HPGe detector of similar relative efficiency present in the laboratory. No worsening of the energy resolution has been observed over the running period of about five years. A typical gamma ray spectra obtained at the distance of 10 cm using ^{152}Eu, ^{57}Co, and ^{60}Co is shown in Figure 2.3.

Peak shape

To check for the worsening of the tail for a specific detector with time is determined by the peak shape. In standard solid detectors, peak shapes play an important role by carrying information regarding increasing demands for reduced minimum detectable activity as it is limited by the extent of the interference of the peaks with each other and peak shape discrimination system (PSD) [50]. The total system resolution was measured following ANSI/IEEE standards [134, 136]. In addition to the FWHM taken at each peak, the full width at one-fifth maximum (FW.2M), full width at one-tenth maximum (FW.1M), and full width at one-fiftieth maximum (FW.02M) were also recorded. The resolution in uncalibrated spectra was also computed manually using the interpolation method using the formula given below.

$$\mathrm{FWHM} = \frac{\Delta \mathrm{E}}{\mathrm{C}_2 \text{ - } \mathrm{C}_1 + 1} \times \mathrm{N}_r \tag{2.2}$$

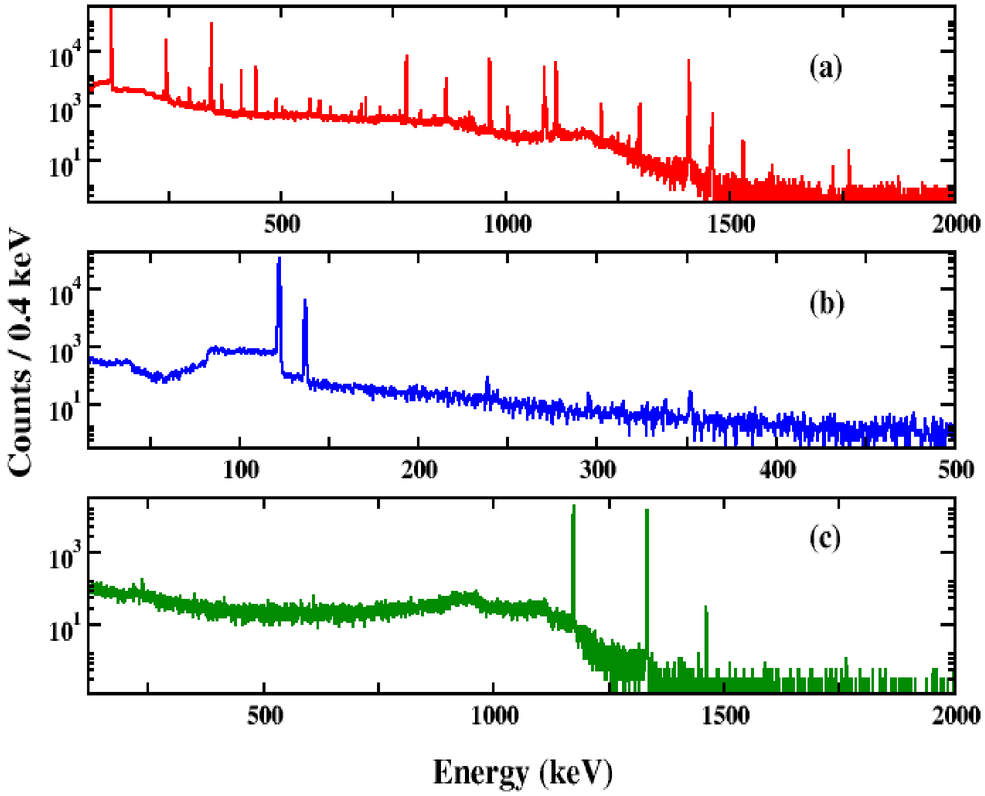

Figure 2.3: Typical gamma ray spectra of (a) ^{152}Eu (red), (b) ^{57}Co (blue) and (c) ^{60}Co (green) at a distance of 10 cm from the top detector face.

where ΔE is the energy difference between two peaks, known as a conversion factor, C_1 and C_2 are the peak positions in terms of a channel. One in the denominator is the uncertainty in channel count. N_r is the width of the selected peak regarding the channel number. A similar approach was adopted to calculate FW.2M, FW.1M, and FW.02M using expressions obtained by linear interpolation. These values lie close to recorded results, indicating excellent accuracy of the acquisition software for peak deconvolution.

Peak-to-Compton ratio

The peak-to-Compton ratio has been measured from the same gamma line, 1332.5 keV, which has been used for the resolution measurement obtained from ^{60}Co source. The peak-to-Compton ratio, as described in the ANSI/IEEE standards [134, 136] can be determined as the ratio of highest peak count at 1332.5 keV to the average counts per channel between 1040 keV to 1096 keV. It may be noted that the region from 1040 keV–1096 keV is a part of the Compton plateau, excluding the edge. This ratio is an analogy to the signal-to-noise ratio. Higher peak-to-Compton values are achieved with better values of energy resolution.

The loss in peak-to-Compton ratio might be attributed to worsened energy resolution of the detection system [137]. Absorber material in the vicinity, i.e., the detector itself, source, presence of ^{40}K from the concrete wall, and flooring, may increase the Compton background. Typical values of the peak-to-Compton ratio for gamma line 1332.5 keV ranges from about 40:1 for a 10% relative efficiency detector (small) to over 90:1 for some very large detectors [135]. The value of this ratio was measured at various axial distances. The mean value of the peak-to-Compton ratio was found to be 62:1, following the manufacturer data.

Full energy peak efficiency

The efficiency calibration of a spectrometer is of great importance in analyzing radionuclides of interest. Physical parameters such as the crystal volume and shape, source dimensions, gamma ray absorption cross-section, attenuation layers in front of the detector, and the distance and position from the source to the detector, determine the efficiency of the detector [130, 138]. Full energy peak efficiency (FEPE), also known as absolute photopeak efficiency, is defined as the ratio of the number of photopeak counts detected to the total number emitted by the source and can be determined according to the following equation:

$$\text{Efficiency} = \frac{\mathrm{N}_\gamma}{\mathrm{A}_\gamma \times \mathrm{I}_\gamma \times \mathrm{t}} \tag{2.3}$$

Where N_γ is the net photopeak area (background subtracted), A_γ is the present activity of source (Bq), I_γ is the gamma ray emission probability, and t is the time elapsed (taking into account the analyzer counting losses). Figure 2.4 shows the efficiency measurements for all the considered gamma ray energies at a distance of 25 cm. The quoted errors may be due to the number of counts in the photopeak (statistical) and source activities (systematic). As shown in Figure 2.4, the solid line through the data points represents the best fit to the

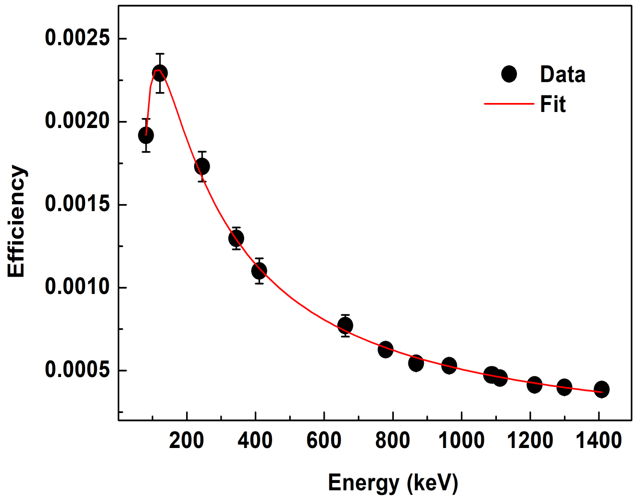

Figure 2.4: Efficiency calibration curve of the HPGe detector at source to detector distance of 25 cm.

data. The efficiency curve is fitted using an inverse square fitting function,

$$\epsilon = \mathrm{A} + \frac{\mathrm{B}}{\mathrm{E}} + \frac{\mathrm{C}}{\mathrm{E}^2} \tag{2.4}$$

where ϵ is the photopeak efficiency, and E is the gamma ray energy. The best-fit values to the fitted parameters A, B, and C are found to be 1.01263 $\times 10^{-5}$ ± 1.23209 $\times 10^{-5}$, 0.5 ± 0.01 and -30 ± 1. The fitting function yields good approximations over different energy ranges and for different crystal sizes. As can be noticed from the figure, some fluctuations in the data points are primarily due to variations in peak shape and low count rates. The HPGe detector has a closed-end coaxial configuration of p-type material and a thick attenuation layer at the detector entrance contact. Correspondingly, the detector's efficiency was found to be less for low energy gamma rays below 80.9 keV as clearly visible in Figure 2.5. The efficiency curve shows a rapid increase from 80.9 keV of ^{133}Ba source, peaks at 121.8 keV of ^{152}Eu, and sharply decreases as a result of an increase in gamma ray energy. This implies that the efficiency is maximum at low energy and decreases exponentially at higher emitted gamma rays consistent with similar detectors by Ortec [139]. The efficiency curve demonstrates the excellent performance of the measurements and analysis applied in this work. Measurement of photopeak efficiencies using the above radioactive sources can help better estimate the detector's active volume and surrounding materials. A detection model is developed using photopeak efficiency measurements with various gamma ray sources described in later sections.

Figure of merit

Striving for large detectors of high efficiency is driven by the fact that one can achieve lower detection limits in low-level measurements. The larger crystals' size has a higher background and a more significant coincidence-summing effect. Thus, the thinner detectors with higher resolution are an alternate choice to achieve low detection limits with high resolution. The detector's Figure of merit (FoM) is obtained from the measured resolution, the peak-to-Compton ratio, and relative efficiency, all at 1332.5 keV [134]. The detector with the largest FoM will have the highest sensitivity (or lowest detection limit) for detecting gamma rays of given energy in the presence of higher energy. In low-level measurements, the FoM is defined as,

$$\text{FoM} = \text{Relative efficiency} \times \sqrt{\frac{\text{peak-to-Compton ratio}}{\text{energy resolution}}} \tag{2.5}$$

The fact that the FWHM is in the denominator implies that reducing the FWHM will improve FoM, and increasing the peak-to-Compton (P/C) ratios will enhance FoM. The FoM values are most helpful in comparing sensitivity measurements using calibration spectra rather than background spectra. This is because the FoM calculation requires peak areas with a high count rate to ensure that the statistical error is small. Generally, the FoM allows a comparison of two detectors from the point of view of their detection limit for one nuclide in the presence of one or more higher-energy nuclides. The FoM for the present HPGe detector was found to be 1.79 for 1332.5 keV.

2.2.2 Characterization of the detector

Radiography with X-rays is used to determine the detector structure and its dimensions. However, an active volume may differ depending upon the electric field configuration inside the crystal [130, 131]. In the present work, radiography was not possible, and hence mono-energetic gamma ray sources were used to scan the crystal in the energy range of 88–1332.5 keV. In order to characterize the detector geometry, three types of scans, namely, 1) Distance scan, 2) Radial scan, and 3) Lateral scan, has been performed around the detector. The scanning schemes of the detector are demonstrated in Figure 2.5. The radial and lateral scans were carried out using ^{57}Co, ^{60}Co, ^{137}Cs, ^{54}Mn, ^{65}Zn and ^{109}Cd gamma sources, see Table 2.2 for the reference energies. The radial scan was performed by moving the source parallel to the top detector face at a distance of 10 mm from the carbon fiber (C-window) endcap in the position steps of 5 mm and covered a range of $\pm$6.5 cm w.r.t. the center of the detector. For the lateral scan, the gamma source was moved parallel to its cylindrical axis at a distance of 10 mm from the side face of the detector in 5 mm steps and covered a range of -2 cm to 6 cm again w.r.t. the top face of the detector (C-window). The distance scan was performed with point-like sources at a regular interval from 5 cm to 30 cm along the detector's symmetry axis away from the C-window of the detector. Typical uncertainty in the positioning of the source in all scans is estimated to be $\leq$1 mm. Given relatively low source strengths, no pileup effects have been observed in the spectra. Errors associated with the photopeak efficiency were computed, including statistical and systematic errors. Typical errors obtained in the present work were estimated to be $\sim$0.2% in radial/lateral scans for $E_\gamma = 88$ keV, $\sim$0.5% for $E_\gamma = 122.1$ keV, $\sim$0.4% for $E_\gamma =$

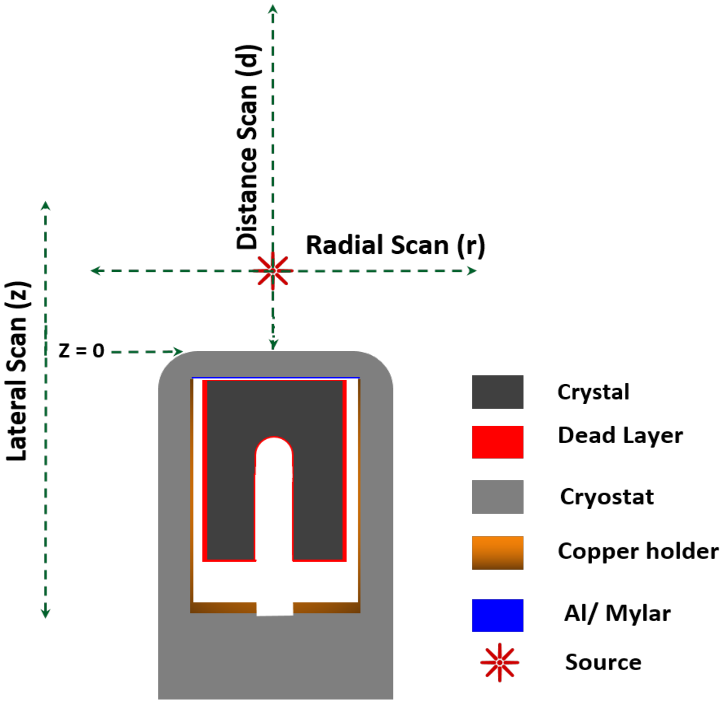

Figure 2.5: A cross-sectional view of the detector with scanning directions indicated.

661.7 keV and ~0.1% for $E_\gamma = 1115.5$ keV. It should be noted that the statistical errors are mainly due to the difference in strengths of various sources and energy-dependent variation in detection efficiency. Similarly, for the axial distances, scan errors in the experiment were ~0.1%. Measurements were also performed with multi-gamma sources such as ^{60}Co, ^{152}Eu and ^{133}Ba at z ≥ 10 cm to ensure that the coincidence summing is negligible.

Scan along the detector surface

The detector's diameter and thickness define the sensitivity. The low-energy gamma rays are sensitive to outer absorbers or dead layers. In contrast, high-energy gamma rays can probe the detector size, while the diameter affects the resolution and the efficiency at a particular detector to source distance. The detector response to different point source placements along the top surface of the detector has been tested. The photopeak efficiency peaks at the center 0 mm and decreases on both sides as we move away. At the center, it drops from 10.75% to 1.94% where the maximum is observed for 122.1 keV and minimum in 1115.5 keV. It falls off quickly at ± 40 mm onward in lower energies than high energy gammas. This may be due to the non-uniformity of the electric field at the corners of the crystal or the non-uniformity of dead layers. This effect is more pronounced in low energies due to less penetration in the crystal. The data was taken at high energy with 1115.5 keV, where the measurements are not strongly affected by dead layers and surrounding materials. An apparent radial symmetry can be observed between the left and right-hand side of the crystal w.r.t its center in all the plots shown in Figure 2.6. It should be mentioned that the

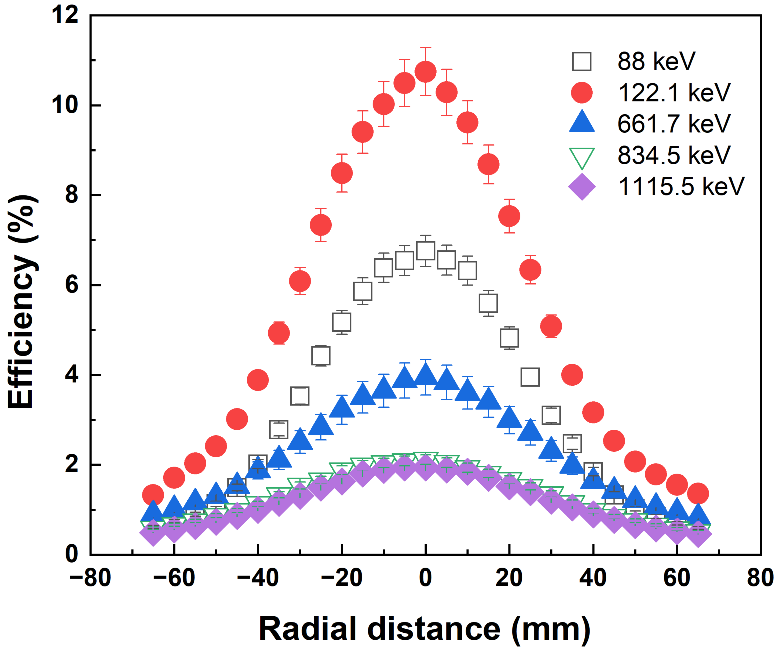

Figure 2.6: Efficiency as a function of radial distance at $z = 10$ mm along the top face of the detector for various gamma ray energies.

highest efficiency is observed at the exact 0 mm of the scan, which highlights the positional accuracy of the measurement. Near the radial extensions probability of Compton scattering starts dominating the photoelectric absorption because of the edge effects.

Scan along the symmetry axis

To look for an efficiency behavior along crystal length, Figure 2.7 shows efficiency curves as a function of lateral distance moved by the sources. If the manufacturer's data is to be trusted, the crystal volume is confined within the copper holder with a crystal length of 46 mm. In figure 2.7, photopeak efficiency starts to increase more quickly between 5–10 mm than at 0 mm; this is because the face of the crystal starts 5–6 mm away from the endcap face of the detector. At 30 mm, efficiency varies from 4.24% to 1.09% where the maximum is observed at 122.1 keV and minimum efficiency is in 1115.5 keV. The efficiency peaks around 30 mm, somewhere middle of the crystal length, and decreases afterward. The efficiency decrease from the highest value at 30 mm is steeper in lower energies, whereas a somewhat gradual fall is observed for higher energies as expected. The percentage decrease in efficiency is more from 50–55 mm than approaching higher distances, according to the manufacturer's stated crystal length. It is to be noticed that the slope to the left of 0 mm is more prominent at lower energies than the corresponding right side, and this marks the presence of a borehole in this coaxial detector geometry. The radial and lateral scans show that efficiency in lateral dimensions is reduced by nearly half compared to the front of the crystal. Therefore, the most suitable source mounting should be done in front of the detector crystal to maximize

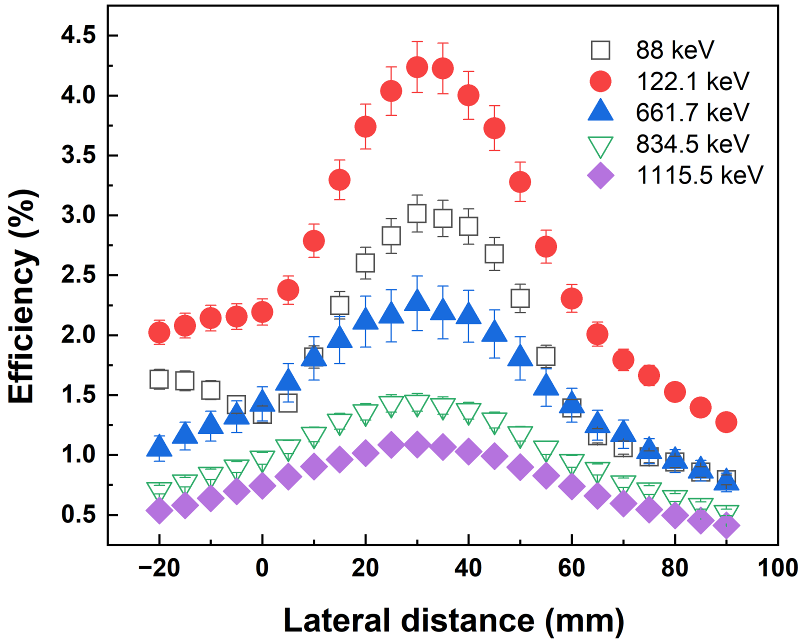

Figure 2.7: Efficiency as a function of lateral distance at $r = 10$ mm along the symmetry axis of the detector for various gamma ray energies.

the overall efficiency. The general nature of the efficiency scans shows the uniformity in the crystal structure and orientation. However, more tests are needed with collimated sources to find the near-exact length of the crystal and the diameter of the crystal.

A distance scan was performed to test the volume effect by choosing different axial distances when performing the measurement. The obtained efficiency range changes from 0.53% to 2.97% where the maximum was achieved for energy 122.1 keV and minimum efficiency is for 1115.5 keV at the closest measured distance. The curve obtained from the distance test is proportional to $1/\mathrm{r}^2$, which is expected by an isotropic source as a distance function. The detector response obtained from measurements can be seen in Figure 2.8. The detector model has been constructed using MC simulations in the GEANT4 framework to extract the photopeak efficiencies. The goodness of simulated results to experimental data is obtained by best-fit values of detector parameters using the below equation:

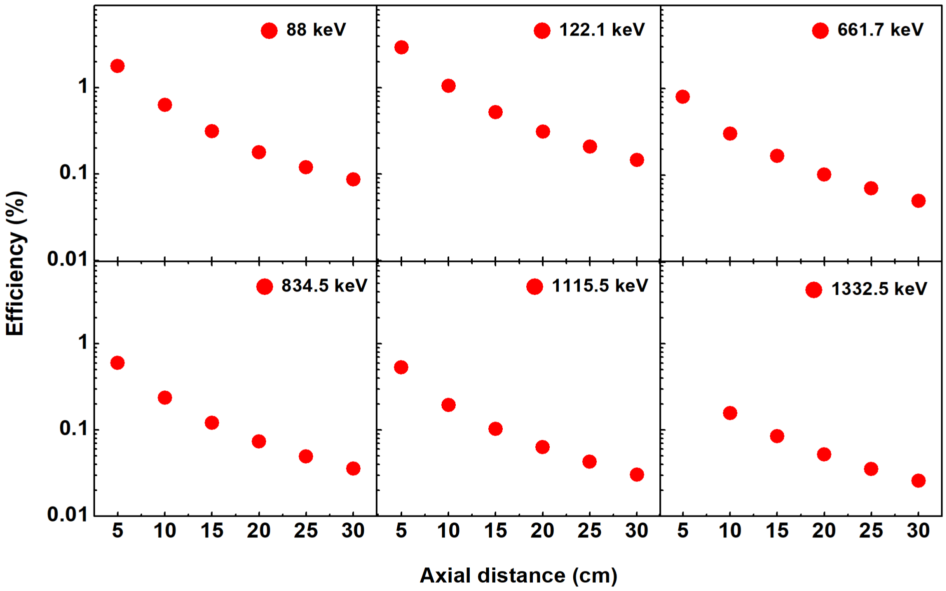

Figure 2.8: Efficiency as a function of axial distance at $z = 5 - 30$ cm from the top face of the detector for various gamma ray energies.

$$\mathrm{R.D.} = \frac{\epsilon_{exp} - \epsilon_{sim}}{\epsilon_{sim}} \tag{2.6}$$

where ϵ_{exp} represents the measured photopeak efficiency and ϵ_{sim} is the corresponding simulated photopeak efficiency for a gamma ray of given energy (E_γ). As mentioned, large discrepancies (10-30%) have been reported in the simulation and experimental data using manufacturer-supplied parameters. The discrepancies calculated in the present study with nominal parameters for E_γ=122.1-1115.5 keV using a distance scan (d) of 5-30 cm, resulted in a significantly large relative deviation (R.D.) of ~27(3)%. Therefore, the MC model has been preliminary optimized by minimizing R.D. to reproduce the experimental data. The initial estimate of the germanium crystal's radius and length were obtained by comparing measured and simulated values at nominal parameters using a ^{60}Co source data at $z = 25$ cm. The detector parameters were optimized to match measured photopeak efficiency data $\epsilon_{exp}(E_\gamma)$. The parameters list with dimensions is summarized in Table 2.3. Simulated photopeak efficiencies, $\epsilon_{sim}(E_\gamma)$, using optimized model agree with $\epsilon_{exp}(E_\gamma)$ within ~10% uncertainty. The simulated results were analyzed in ROOT framework [128].

Table 2.3: Optimized dimensions of HPGe detector.

Parameter	Manufacturer Dimensions (mm)	Optimized Dimensions (mm)
Crystal Radius (R)	31	29(1)
Crystal length (L)	46	42.9(3)
Hole radius (h_r)*	5.55	5.55
Hole depth (h_l)*	33.7	33.7
Top dead layer (t_d)$^{\oplus}$	–	1.2
Side dead layer (t_s)$^{\oplus}$	0.7	1.7
Front gap (g)	4	9(1)
Front carbon fiber*	0.9	0.9
side carbon fiber*	1.6	1.6
Cu cup thickness*	0.8	0.8

*unaltered in simulations, $^{\oplus}$similar to Table 2.8

2.2.3 Radiopurity assessment of soil samples

The ambient background in the laboratory has been measured using an HPGe detector without any shielding at different times since its installation to check for possible changes in the background due to incoming and outgoing materials (for impurity control), daily variations of radon concentration, and aperiodic variations of cosmic rays intensity. From a typical gamma ray background spectrum recorded for 24 h, about 120 gamma lines were identified, emitted from the uranium and thorium decay chains in the room environment around the detector. The most prominent peak of 1460.8 keV is emitted from ^{40}K radionuclide present in the building materials such as concrete walls and flooring. The integral background from energy range of 40 keV to 2700 keV is 5.9×10^5 /kg/hr with a total count rate of 116 counts/sec. Long background measurements were also performed to observe the day-wise variation in the overall background and estimate the statistical fluctuation in the prominent gamma peaks. Most of the variations were attributed to radon dynamics in the laboratory, while the background count rate over the energy region of 40–2700 keV is found to be similar. The spectrometer exhibits good gain stability and negligible calibration drifts (<1 keV) over a long duration of measurements. As a result of lead shielding, the overall background has been significantly reduced from 116 to 2 counts/sec in the energy range of 40-2700 keV. The background rate for 1460.8 keV (^{40}K) and 2614.5 keV (^{208}Tl) lines is 634 and 443 counts/day, respectively. Typical one-day background gamma ray spectra, without and with lead shield, are shown in Figure 2.9. Lead shielding effectively reduces most of the gamma rays from entering the active volume of the detector crystal. At the

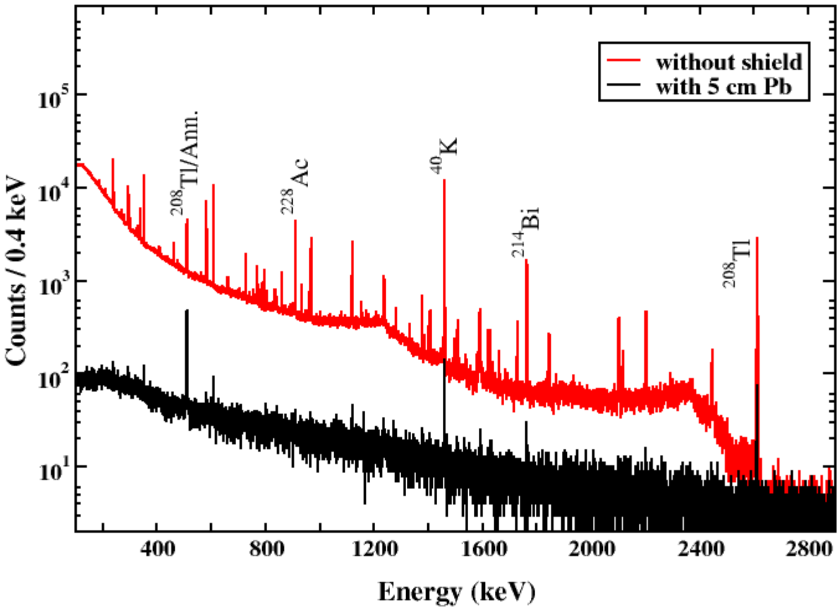

Figure 2.9: Improvement in ILM-0 background with and without Pb shield (t = 1 d).

same time, the reduction ratio of the integration of the count rate depends on the gamma ray energy. The background reduction achieved has been compared with unshielded data for major peaks and various energy ranges. The photopeak intensity reduction of major gamma lines visible in unshielded and shielded setups are given in Table 2.4. For ^{238}U, the activity levels are reduced to 0.5% for ^{214}Bi and ^{214}Pb. In case of ^{232}Th, the ratios fluctuate between 0.2% and 2.5% for ^{208}Tl and 0.6% for ^{228}Ac. Photopeaks of ^{137}Cs and ^{60}Co are not visible in the shielded spectra. The ^{40}K ratio is 1%, and the annihilation peak drops to 20% of its original value without shielding. This procedure allowed diminishing detection limits of many isotopes of interest to be considered for environmental radioactivity. Ambient background in the shielded setup has been counted for a duration of 49 d over a span of 3 months. It should be mentioned that the stability of the energy scale was monitored with background gamma rays such as 1460.8 and 2614.5 keV where calibration with standard sources was only sometimes convenient due to heavy passive shielding. The gamma lines from anthropogenic contamination of ^{137}Cs and ^{60}Co were found below detection limits. In aboveground low-level gamma spectrometry systems, some peaks associated with the activation of germanium and fast neutron scattering in the shielding material occur in the background spectrum. For example, 139.7 keV gamma line comes via neutron-induced process ^{74}Ge(n,γ)^{75}Ge. Two peaks at 569.7 keV and 1063.3 keV from scattering reaction (n,n') on lead were observed. Another gamma ray at 803.3 keV is clearly detectable and corresponds to the de-excitation of ^{206}Pb* which can result from the decay of ^{210}Po or from fast neutron scattering on lead.

An important characteristic to measure the quality of a spectrum in the gamma spectrometric measurements is the Minimum Detectable Activity (A_D) that defines the least

Table 2.4: Observed activity with and without Pb shield along with the reduction factor.

Element	Energy (keV)	Without Shield (X) (counts/day)	With Shield (Y) (counts/day)	Reduction factor Y/X(%)
^{212}Pb	238.6	37812(147)	127(47)	0.34(3)
^{214}Pb	295.3	16937(266)	86(54)	0.51(20)
^{214}Pb	351.9	31365(329)	219(25)	0.70(8)
^{208}Tl/Ann.	511.0	14956(903)	3039(110)	20.32(12)
^{208}Tl	583.2	21159(286)	54(23)	0.25(8)
^{214}Bi	609.3	32746(349)	170(23)	0.52(7)
^{137}Cs	661.7	858(98)	–	–
^{214}Bi	806.4	1084(139)	–	–
^{228}Ac	835.6	1356(133)	–	–
^{228}Ac	911.2	16609(232)	94(28)	0.57(12)
^{214}Bi	1120.3	9411(208)	106(21)	1.13(10)
^{60}Co	1173.2	654(130)	–	–
^{60}Co	1332.5	464(87)	–	–
^{40}K	1460.8	61137(834)	700(37)	1.14(4)
^{214}Bi	1764.5	8916(154)	199(33)	2.23(21)
^{208}Tl	2614.5	19101(400)	469(31)	2.64(8)

amount of activity in the sample to quantify the radiation level slightly above the unavoidable background. Shorter measurement times and higher background radiation levels would increase the $\mathrm{A_D}$ and reduce the sensitivity of all detectors. The detector efficiency significantly affects the detection levels. In addition to the detection efficiency, amount of sample, measurement time, and photon emission probability, the $\mathrm{A_D}$ in gamma spectrometry depends on the background level at a specific energy. These background events mainly come from three primary reasons: the sample itself, the Compton continuum, and natural radioactivity. The $\mathrm{A_D}$ in Bq/kg at a given gamma ray energy is calculated by the Curie method [140] and given by:

$$\mathrm{A_D} = \frac{\mathrm{N_D}}{\mathrm{I_\gamma \times m \times \epsilon_\gamma \times t}} \tag{2.7}$$

Where $\mathrm{N_D} = 2.7 + 4.65\,\sigma_\mathrm{B}$ is minimum detectable counts and σ_B is the standard deviation in the background counts, I_γ is the branching ratio of the gamma ray, ϵ_γ is the photopeak detection efficiency computed using GEANT4 simulation, m is the mass of the sample and t is the counting time. In order to determine the detection limit of ILM-0 for low activity measurements, $\mathrm{A_D}$ in soil matrices were computed from the minimum detectable counts ($\mathrm{N_D}$) using the Eq. 2.7. $\mathrm{A_D}$ is calculated for several radionuclides often encountered in the environmental samples from which the most dominating ones are shown in Table 2.5.

Table 2.5: Estimated sensitivity of the setup.

Parent radionuclide	Daughter radionuclide	Energy (keV)	N_D (counts/day)	A_D (Bq/kg)
^{238}U	^{214}Pb	238.6	81	5
^{232}Th	^{212}Pb	295.3	66	1
^{40}K		1460.8	129	53

Sub-surface soil samples (30 cm depth) were collected randomly from the agricultural test site of the Ropar region. The type of soil is clay loam with a composition listed in table 2.6. Samples were oven dried (110°C), fine powered, and then sieved through a 150 μm mesh. Each sample was packed and sealed in a cylindrical polypropylene container of ~3.5 cm dia. and ~2.2 cm high and stored for stabilization. The smaller sample geometries are desirable over voluminous sample geometries because the attenuation of gamma rays within the sample matrix is negligible. A total of 10 soil samples, average mass $\langle$m$\rangle$~20 g, were counted in compact geometry for 24 hours. The mean soil density $\langle\rho\rangle$, as packed in the container, is ~1.3 g/cm^3 with an overall variation of ~10%. In close counting geometry, coincident summing affects the observed photopeak yield [52]. The present analysis considered gamma rays with no summing to estimate activities. ϵ_{sim} were obtained with the optimized model for 10^6 events uniformly distributed within the sample and the same counting geometry kept during the measurement. To enhance the detection efficiency, the samples were mounted in the front of the detector face and confined within 60% of the radial extensions to avoid edge effects. The effect of the elemental composition and sample density were taken into account. The estimated variation in ϵ_{sim} is about 1% due to 10% density variation in the sample. The $\epsilon_{sim}(E_\gamma)$ for gamma rays 238.6, 295.3 and 1460.8 keV are 6.66(9)%, 5.41(7)% and 1.31(1)%, respectively. Figure 2.10 compares typical one-day spectra of background and soil samples.

Table 2.6: Typical clay loam composition of Ropar district taken from [6].

Compound	Mass fraction	Compound	Mass fraction
SiO_2	0.5890	K_2O	0.0325
Al_2O_3	0.1625	Na_2O	0.0235
Fe_2O_3	0.1340	MgO	0.0135
CaO	0.0360	TiO_2	0.0090

Most of the gamma rays were visible from the uranium and thorium decay chains, but only a few could be considered for trace impurity analysis, particularly with lower statistical error (<5%) and higher intensity. Some of the gamma rays are mixed from different radionuclides - for instance, the observed gamma line at 242.6 keV has a contribution from ^{214}Pb in ^{238}U decay chain (242.0 keV) and ^{224}Ra in ^{232}Th decay chain (241.9 keV), similarly for 351.9 keV (^{214}Pb, ^{211}Bi), 185.9 keV (^{226}Ra, ^{235}U), etc. Hence, only those gamma rays which could be unambiguously assigned to a particular nuclide were considered in further

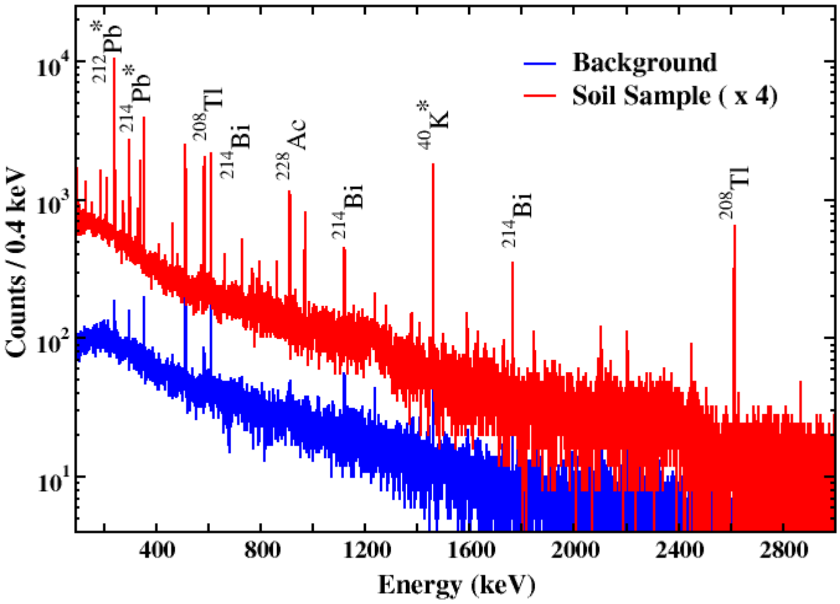

Figure 2.10: A typical gamma ray spectra of soil sample (red line) and ambient background (blue line) (t=1 d). The gamma rays of interest are indicated (*) in the spectra.

analysis. Nuclides in natural radioactive decay chains were considered to be in secular equilibrium, and the gamma lines emitted with negligible coincidence summing were chosen as mentioned above. The specific activities were estimated from the measured photopeak yield after background correction, defined as activity per unit mass A_γ corresponding to a given transition of the radionuclide was determined using.

$$\mathrm{A}_\gamma = \frac{\mathrm{N}_\gamma}{\mathrm{I}_\gamma \times \mathrm{m} \times \epsilon_\gamma \times \mathrm{t}} \tag{2.8}$$

Where N_γ is the net observed counts in the photopeak after correcting for the ambient background. The observed specific activity of primordial radionuclides estimated for ^{238}U, ^{232}Th, and ^{40}K ranged between 32 – 67, 66 – 107, 590 – 860 with a mean specific activity of 50, 85 and 670 Bq/kg, respectively. The measured activity of ^{238}U and ^{232}Th showed a consistent distribution of primordial radionuclides among all the soil samples, while a somewhat large scatter is observed in ^{40}K data. To extract the trace impurity concentrations of the parent radionuclides (^{232}Th and ^{238}U), the atomic fraction $\mathrm{A_T}$ of the trace radioimpurity in the soil sample was computed using

$$\mathrm{A_T} = \frac{\mathrm{A}_\gamma \times \mathrm{M}}{\lambda \times \mathrm{N_A}} \tag{2.9}$$

Where M is the molar mass (in g/mole), λ is the decay constant (in s^{-1}), and $\mathrm{N_A}$ is Avogadro's number. Correspondingly, the observed trace impurity content of ^{238}U, ^{232}Th and ^{40}K were estimated to be 4.0(8), 21(3) and 2.5(3) ppm, repsectively. The estimation of the elemental concentration of potassium was found to be higher, which can be due to extraneous factors like the use of potassium-based fertilizers and chemicals.

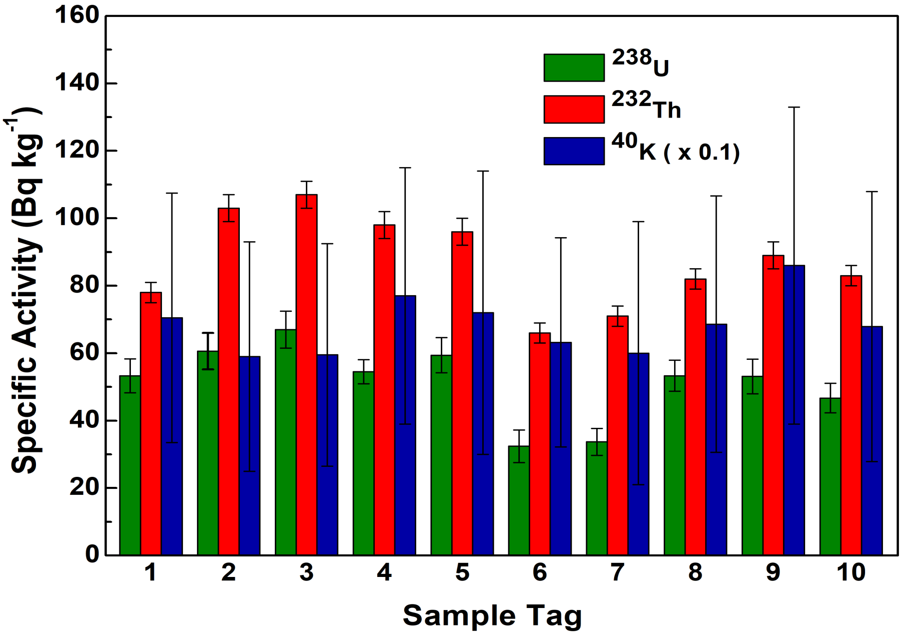

Figure 2.11: Observed specific activity in soil samples.

2.3 TiLES

The TiLES consists of a ~ 70% R.E. coaxial p-type high-purity Germanium (HPGe) detector (Ortec, Model no GEM75-95-LB-C-HJ) in a passive shielding of 10 cm thick low activity Pb (< 0.3 Bq/kg of ^{210}Pb) and 5 cm oxygen-free high thermal conductivity Cu, inside. The setup is enclosed in a Radon exclusion box with continuous dry nitrogen (N_2) flushing at an over-pressure of ~8 mbar. It is further surrounded by plastic scintillators for cosmic muon veto (see Figure 2.12). TiLES data acquisition system is based on a CAEN N6724 digitizer (14-bit, 100 MS/s). The energy calibration was done with standard gamma ray sources, and the resolution was measured to be 2.6 keV at 1408 keV. The efficiency of TiLES was measured using ^{152}Eu gamma ray source and calculated using Eq. 2.3 as shown in Figure 2.13. The optimized geometry of TiLES [2] has been utilized to simulate the detector response. Figure 2.14 shows significant improvement in measured background spectra with the presence of mainly ^{232}Th, ^{40}K radioactivity and impurities such as ^{137}Cs, ^{60}Co. The background spectra were reduced by ~50% in the region of 200–3000 keV by adding three plastic scintillators to the setup. TiLES was further upgraded with one more plastic scintillator and ~9 mm thick perspex box surrounding the HPGe detector for N_2 flushing, which have shown a reduction in the background level by ~39% in the energy range of 40-2700 keV [75]. The photopeaks of 1460.8 keV and 2614.5 keV were not affected after the shield upgrade. The integrated background rate over the energy range of 40–2700 keV is 1.7×10^4 d^{-1}kg^{-1} and the sensitivity achieved for ^{232}Th and ^{40}K are 1 mBq/g and 2 mBq/g, respectively. The detailed performance of TiLES and the effective Monte Carlo

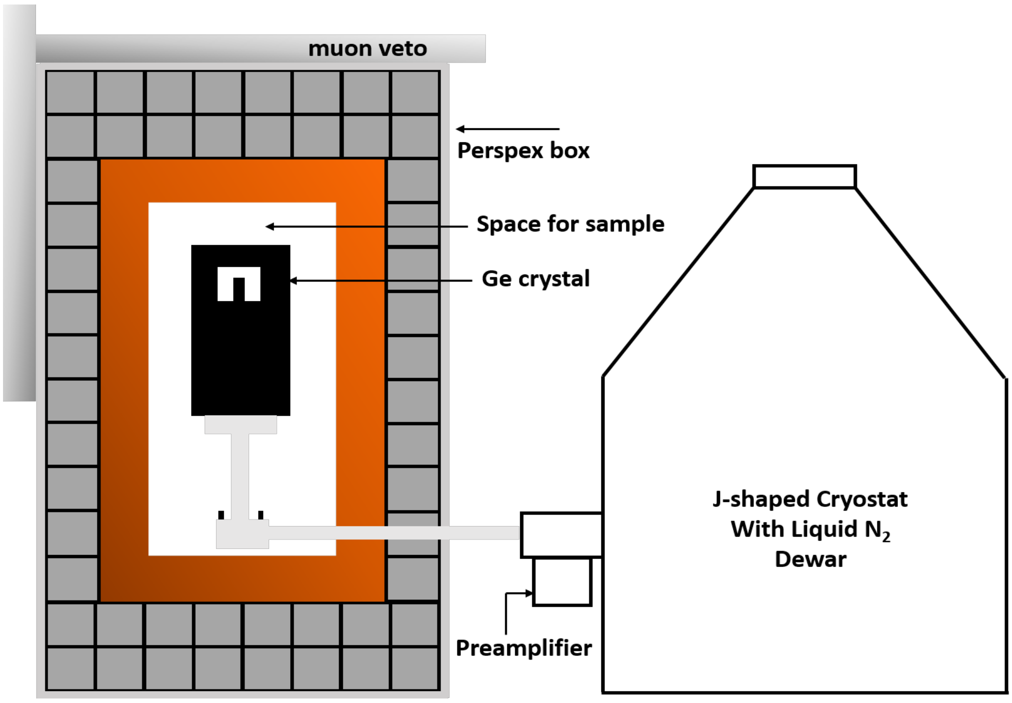

Figure 2.12: A schematic diagram of TiLES cross-sectional view surrounded with inner Cu shields (5 cm) and outer Pb shields (10 cm) enclosed in a perspex box and muon veto. The integral cryostat system is also shown.

model is reported in reference [2]. The setup has been extensively used to qualify and screen radio-pure materials for the TINTIN bolometer. TiLES background rate is the best possible achieved background at sea level.

Table 2.7: Optimized dimensions of TiLES.

Parameter	Optimized Dimensions (mm)
Crystal Radius (R)	37.6(3)
Crystal length (L)	54.0(9)
Hole radius (h_r)	7.5(6)
Hole depth (h_l)	44(1)
Top dead layer (t_d)	1.04(2)
Side dead layer (t_s)	1.26(2)
Bottom dead layer (t_b)	9(1)
Front gap (g)	5.0(7)
Front carbon fiber	0.9
side carbon fiber	1.8
Cu cup thickness	0.8

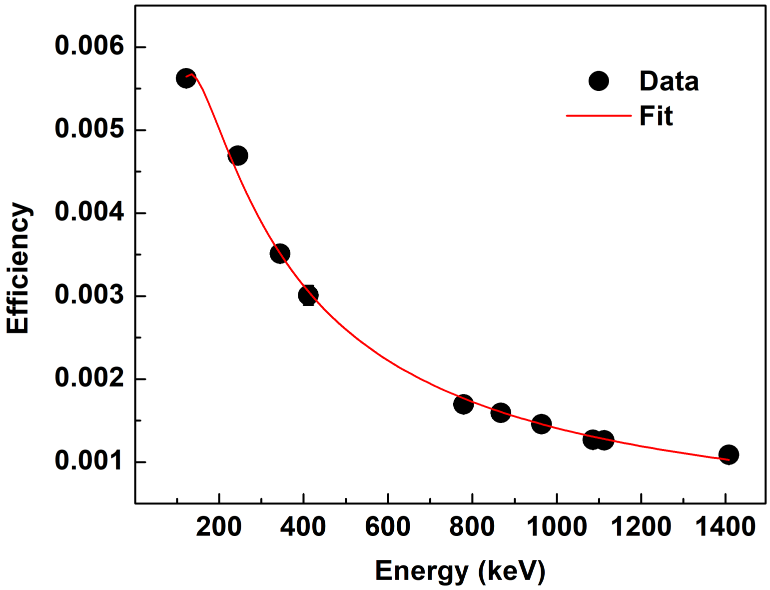

Figure 2.13: TiLES efficiency curve at 10 cm.

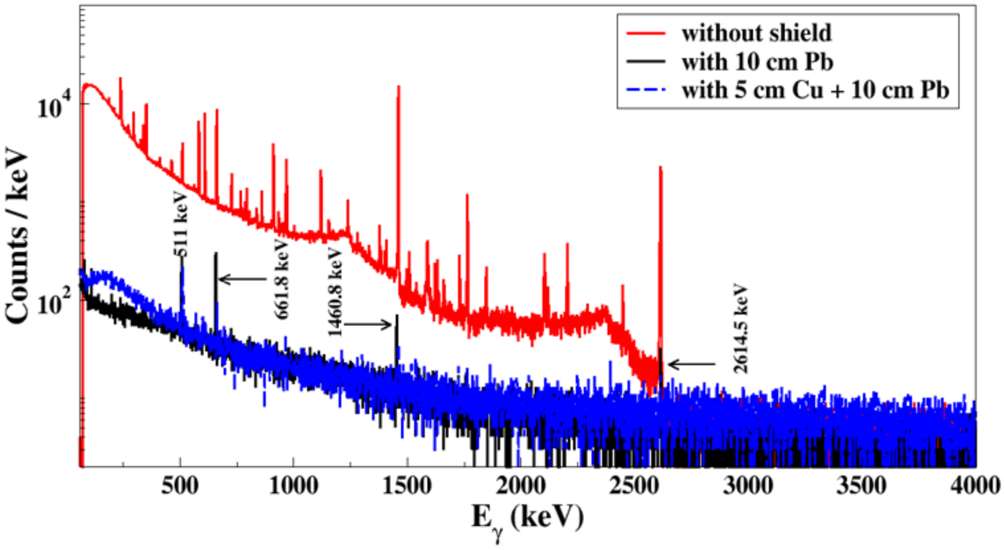

Figure 2.14: Improvement in TiLES background with passive shielding of ultra-pure Cu and Pb (t = 1 d) adapted from [2]

2.4 CRADLE (D1-D2)

Another low background setup, CRADLE, is installed at sea level in TIFR, Mumbai. CRADLE consists of low background cryocooled p-type coaxial HPGe detectors (Ortec, model no GEM30P4-83-RB) similar to the IIT Ropar detector. The D1-D2 coincidence setup has been made of two identical CRADLE detectors. The detectors have ∼33% R.E. and a carbon fiber housing with a thin 0.9 mm entrance window. The D1-D2 detectors are mounted in a compact geometry to maximize counting efficiency, facing each other at a distance of about 2.5 cm, surrounded by two layers of passive shielding with 5 cm thick low activity lead (< 0.3 Bq/kg of ^{210}Pb) inside and 5 cm thick (< 21 Bq/kg of ^{210}Pb) outside, see Figure 2.17. Additionally, it has a provision for an annular anti-Compton shield and an active muon veto. Data were acquired using a CAEN DT6724 digitizer (14-bit, 100 MS/s) and recorded separately (time stamp and energy) for each detector on an event-by-event basis. The detector resolution was measured to be ∼3 keV at 1332.5 keV. The efficiency of CRADLE was obtained using ^{152}Eu gamma ray source and calculated using Eq. 2.3 as shown in see Figure 2.15. The reduction of integral background achieved in single CRADLE detector D1 was 4.3 × 10^3 /kg/hr in the energy range of 40 keV to 2700 keV. The gamma rays in the ambient background due to annihilation radiation at 511 keV, ^{137}Cs at 661.6 keV, ^{40}K, at 1460.8 keV and ^{208}Tl at 2614.5 keV can be clearly seen in Figure 2.16. It has been extensively utilized for low background measurements and radiopurity assessment of materials for rare decay studies. The detailed measurements were carried out with detector D1 using mono-energetic point+extended sources, and an optimized geometrical model of the detector was obtained [132]. As both D1 and D2 are expected to be identical, the optimized geometry of D1 was adopted to simulate the photopeak efficiency of both the detectors (D1 and D2) as given in Table 2.8. The $\gamma - \gamma$ coincidence spectra were generated using C++ based offline analysis in ROOT within the coincidence time window of $\pm 1\,\mu$s. The ambient background measured for a period of 27 days in the close counting geometry is shown in Figure 2.18. It is worth mentioning that the simultaneous detection of two gamma rays in the D1-D2 setup has significantly reduced the majority of radiation background compared to TiLES. Correlated positron annihilation gamma lines and high energy background lines of 1460.8 and 2614.5 keV are visible from the Compton scattered photons creating double triggers in both the detectors and appearing as a diagonal line. It should be mentioned that

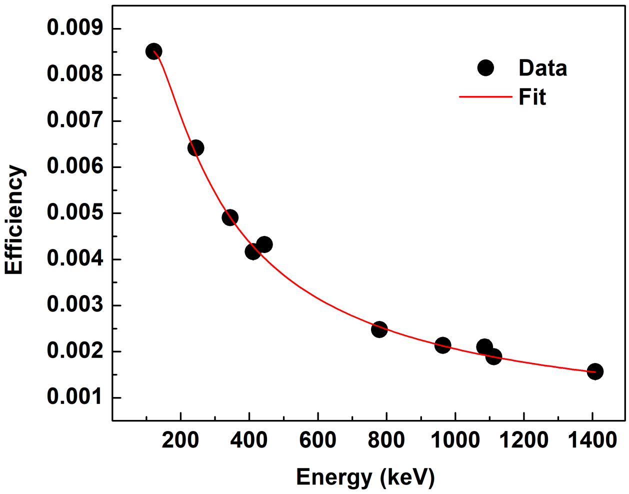

Figure 2.15: CRADLE efficiency curve at 10 cm.

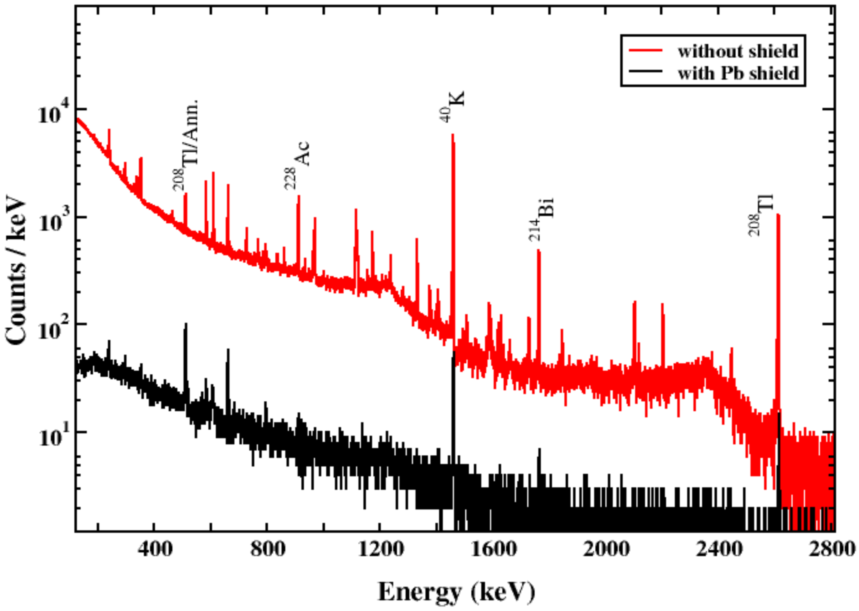

Figure 2.16: Improvement in CRADLE background with and without two layers of ultra-pure and moderate Pb shield (t = 0.5 d).

Table 2.8: Optimized dimensions of CRADLE.

Parameter	Optimized Dimensions (mm)
Crystal Radius (R)	27.7(5)
Crystal length (L)	55.0(5)
Hole radius (h_r)	4.35
Hole depth (h_l)	45.6
Top dead layer (t_d)	1.2(1)
Side dead layer (t_s)	1.7(2)
Bottom dead layer (t_b)	4.7(5)
Front gap (g)	7(1)
Front carbon fiber	0.9
side carbon fiber	1.6
Cu cup thickness	3.0

$\gamma - \gamma$ coincidence counting is profitable only if a radionuclide of interest undergoes a gamma cascade. Therefore, this setup has been utilized in $\gamma - \gamma$ coincidence measurements for various environmental matrices and feasibility studies related to rare decay investigations,

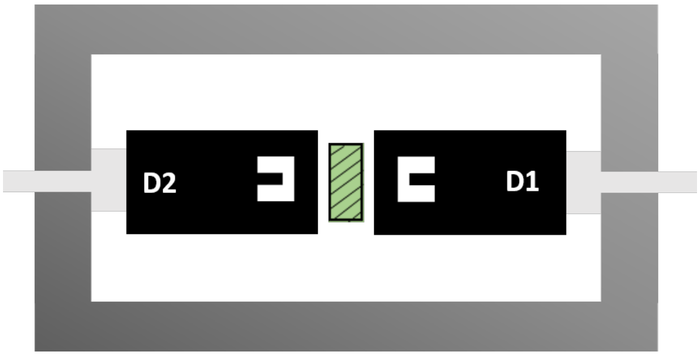

Figure 2.17: A low background D1-D2 coincidence setup. The schematic shows the cross-sectional view of two cryocooled HPGe detectors covered by the lead shielding arrangement.

as discussed in the next chapter.

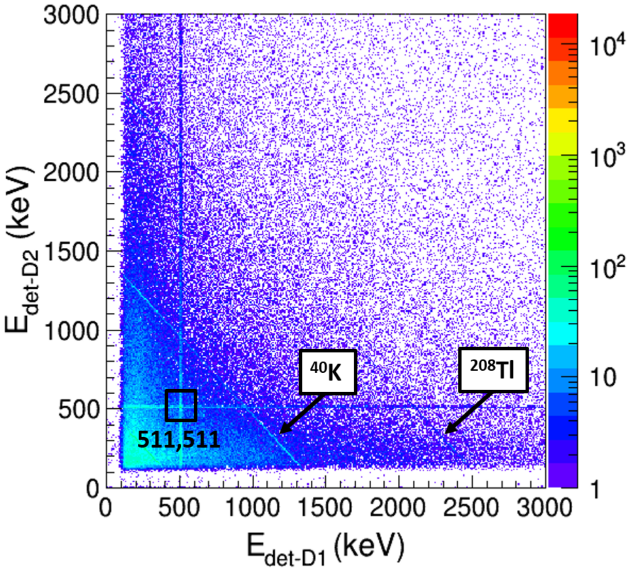

Figure 2.18: Ambient coincident background using D1-D2 setup (t=27 d).

2.5 Summary

A moderately shielded low background counting facility has been set up at IIT Ropar to study environmental radioactivity. The trace concentration of radioactive elements has been estimated in 10 soil samples from the agricultural test site of Katli village in Ropar with ILM-0. The studied site has mean specific activity of 50, 85, and 670 Bq/kg for ^{238}U, ^{232}Th, and ^{40}K, respectively. While ^{238}U and ^{232}Th activities among the samples are consistent within overall uncertainty, ^{40}K shows a somewhat more significant variation. However, for any conclusive evidence of radiation levels, more samples must be studied from different districts of Punjab. Efforts are underway to augment the setup with low-activity lead shields and plastic veto detectors to improve the sensitivity for studies relevant to rare decay searches. The characteristics of low background setups TiLES and CRADLE (D1-D2) used in this thesis are discussed.

Chapter 3

Simulation for Rare Decay Studies Employing Gamma Coincidences

The study of neutrinoless double beta decay has attracted much attention as it can provide valuable information about the neutrino's mass and nature. Double beta decay (DBD) is also interesting in nuclear physics. DBD has been observed in about a dozen nuclei; on the contrary, highly forbidden rare beta decays and positron double beta decays ($\beta^+\beta^+$/ECβ^+) continue to be elusive. These rare decays have recently gained interest to study in increasingly low background conditions. An attempt to study the feasibility of rare decays searches for single β decay of ^{96}Zr and $\beta^+\beta^+$/ECβ^+ in ^{106}Cd/^{112}Sn was carried out by using low background high purity Ge (HPGe) detectors (~33% R.E.) employing the coincidence technique.

3.1 Introduction

Recent neutrino oscillation experiments have boosted the worldwide interest in the search for neutrinoless double beta decay (NDBD) with increased sensitivity [22]. The neutrinoless double beta decay provides a unique probe to study the mass and nature of the neutrino. Investigation of rare single β decays, particularly the study of rare and highly forbidden beta decays, is also an active research topic. The single β decay provides one of the most direct tests for theoretical models describing the underlying mechanism of neutrinoless $\beta\beta$ decays. In addition, the study of rare single β decays is particularly interesting for nuclides which create a significant background in the rare event searches [23, 120]. The nucleus ^{96}Zr is one of the two double β decay (DBD) candidates, where single β decay is spin forbidden. Hence, single β decay and $\beta\beta$ decay modes are feasible with a comparable half-life. Generally, if $Q_{\beta\beta}$ is sufficiently large, then the DBD to excited states are feasible and can be studied via de-exciting gamma rays [108, 109]. For ^{96}Zr, $Q_{\beta\beta}$ is 3.35 MeV and DBD to excited states of ^{96}Mo has been studied with the current best limit of $T_{1/2} > 3.1 \times 10^{20}$ yr at 90% confidence level (C.L.) [110]. For the β decay in ^{96}Zr, the Q_β is relatively small (164 keV) and is dominated by the decay to the 5^+ excited state of the daughter nucleus ^{96}Nb at 44.2 keV. The theoretically estimated half-life of this transition is $T_{1/2} = 2.4 \times 10^{20}$ yr [141]. The daughter nucleus ^{96}Nb further β decays to ^{96}Mo with a half-life of 23.35 h (almost instantaneously compared to the parent decay). In the case of ^{96}Nb, similar to ^{96}Zr, the β decay to excited states of ^{96}Mo is more probable because of spin and can be studied by de-exciting gamma rays. There have been some attempts to measure the half-life for ^{96}Zr β decay [4, 105, 108, 109, 142, 143]. Although Mayer *et al.* [143] geochemically reported the most recent limit of $T_{1/2} \geq 6.2 \times 10^{19}$ yr for the single β decay of ^{96}Zr, the best limit established from the direct experiment is $T_{1/2} > 3.8 \times 10^{19}$ yr at 90% confidence level [108]. One of the major challenges in a rare β decay study is to improve the sensitivity, which primarily involves the reduction of background to improve the signal-to-noise ratio. Also, the natural isotopic abundance of ^{96}Zr is rather small (2.8%). Recently, an improved lower limit for $T_{1/2}$ of DBD of ^{94}Zr to excited states of ^{94}Mo has been reported using low background setup TiLES [2, 77].

To date, $\beta^-\beta^-$ decays have the largest expected rates and are described as the most promising mode of DBD. $\beta\beta$ in some of the nuclei can undergo $\beta^+\beta^+$, ECβ^+, ECEC processes and are mostly hindered due to lower effective Q-value [46]. The search for positive decay modes $\beta^+\beta^+$/ECβ^+ continues to be elusive and poses a great experimental challenge. However, investigations of other modes of $\beta\beta$ could help in the exact calculations of the nuclear dynamics of the nuclei undergoing $\beta\beta$ decay due to their different decay topologies. An important experimental signature of the decay modes involving positrons like ECβ^+ and $\beta^+\beta^+$ is the simultaneous emission of pair(s) of 511 keV gamma rays. Hence, the coincident detection of 511 keV gamma rays can significantly improve the measurement sensitivity. However, since 511 keV gamma rays can also originate from many other processes, it is important to understand and discriminate against the background originating from trace impurities in the source, detector, and surrounding materials and from cosmic muon-induced reactions.

The present work has developed a multi-detector setup using Monte Carlo simulations in GEANT4. A feasibility study of the ^{96}Zr β decay through ^{96}Mo gamma-ray cascade using a low background setup of four detectors is carried out employing the coincidence technique for background reduction. The results are compared with coincidence measurements of Finch *et al.* [4] with a two-detector setup. Another feasibility study was carried out to estimate the sensitivity of the half-life measurement for positron DBD modes using a coincidence setup. Simulations are performed to optimize the source-detector configuration to maximize the mass efficiency product ($M\epsilon_c$). Background measurements are carried out using a coincidence setup of two high-purity Ge (HPGe) detectors (~33%) with moderate lead shielding. Both ambient background and background with natural tin (^{nat}Sn) sample of mass ~40 g were measured. The background in the coincidence setup, especially in the region of interest around 511 keV is compared with that from the low background counting setup TiLES [2]. The sensitivity for $T_{1/2}$ measurement of ECβ^+ in ^{112}Sn and $\beta^+\beta^+$ in ^{106}Cd is estimated using the measured background and simulated coincidence efficiency. Measures for improvement in the background are also discussed.

3.2 Proposed rare decay studies through gamma cascade

For single β decay in ^{96}Zr, it can be seen from Figure 3.1 that the most probable channel of β decay populates 5^+ state of ^{96}Mo, leading to a cascade of gamma rays. There are 3 prominent cascades of three gamma rays each, listed in Table 3.1. As multiple gamma rays are emitted in a given cascade, it is possible to employ the coincidence technique. In the case of positron DBD, the experimental signature of the decay modes involving positrons like EC-β^+ and $\beta^+\beta^+$ is the simultaneous emission of pair(s) of 511 keV gamma rays produced by annihilation. Hence, the following three cases are considered for the present study:

- $^{96}Zr \xrightarrow{\beta^-} {}^{96}Nb \xrightarrow{\beta^-} {}^{96}Mo(5^+)$ in ^{nat}Zr matrix.
- EC-β^+ in ^{112}Sn - it generates 2 gamma-rays of 511 keV (1 correlated pair from same vertex in the ^{nat}Sn matrix).
- $\beta^+\beta^+$ in ^{106}Cd - it generates 4 gamma-rays of 511 keV (2 correlated pair from same vertex in the ^{nat}Cd matrix).

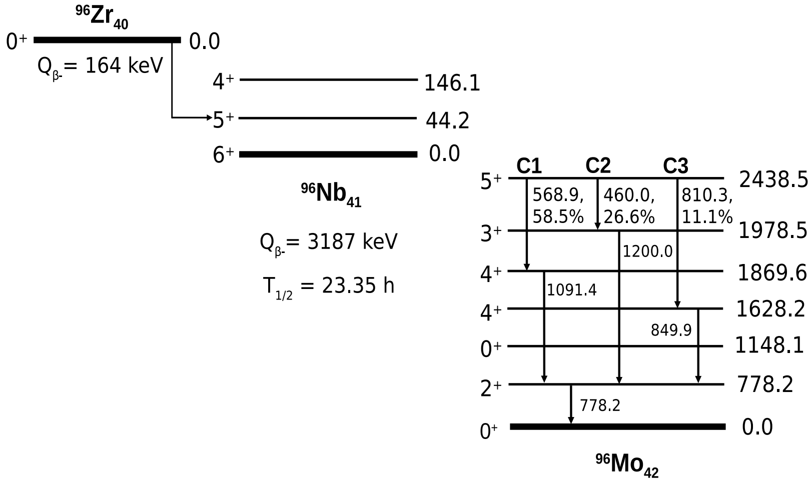

Figure 3.1: A schematic representation of β decay in ^{96}Zr and ^{96}Nb (energy values are in keV) [3].

Table 3.1: The decay cascade in ^{96}Mo with corresponding branching ratios f$_b$ [3] of the first gamma ray in the cascade.

Cascade No.	Decay Sequence	f$_b$ %	γ_1 (keV)	γ_2 (keV)	γ_3 (keV)
C1	$5_0^+ \to 4_1^+ \to 2_0^+ \to 0_0^+$	51.5	568.9	1091.3	778.2
C2	$5_0^+ \to 3_0^+ \to 2_0^+ \to 0_0^+$	18.8	460.0	1200.0	778.2
C3	$5_0^+ \to 4_0^+ \to 2_0^+ \to 0_0^+$	11.3	810.8	849.9	778.2

3.3 Simulation studies

3.3.1 4HPGeSim

A simulation program has been developed using the GEANT4 (v10.05) [127]. A momentum-correlated pair of 511 keV, or two randomly oriented gamma rays from a chosen cascade (C1, C2, or C3) are generated from a given vertex uniformly distributed within the source and detected in the HPGe detectors. A setup with 4 identical HPGe detectors, with a relative efficiency of about 33%, arranged in a plane, is considered in the present study. The dimensions of source plates (and consequently source mass) and their positioning w.r.t the detectors are varied to find the optimum configuration to yield the maximum mass efficiency ($M\epsilon_c$) - the product of the source mass and the coincidence photopeak efficiency. The modular architecture of the GEANT4 toolkit allows the user to build customized applications, including all the functionalities, such as geometry, the particles, and all their interactions with matter. A simulation code for GEANT4-based simulation has some basic structure, including detector and source geometry, particle generator, physics list, stepping/event action, and data structure. Figure 3.2 shows a detector configuration comprising two HPGe detectors for front source mounting (D1, D4) and for side source mounting (D1, D2). The geometry of HPGe detectors is taken to be similar to that of the CRADLE detector at TIFR [132] and relevant parameters are listed in Table 2. The source plates are considered to be either box or cylinder-shaped. The sources of ^{nat}Sn or ^{nat}Zr are implemented from the predefined material database of GEANT4 without any specific isotopic composition. The effect of isotopic enrichment is taken care of by appropriately scaling the number of events generated with the desired fraction while retaining the natural material properties

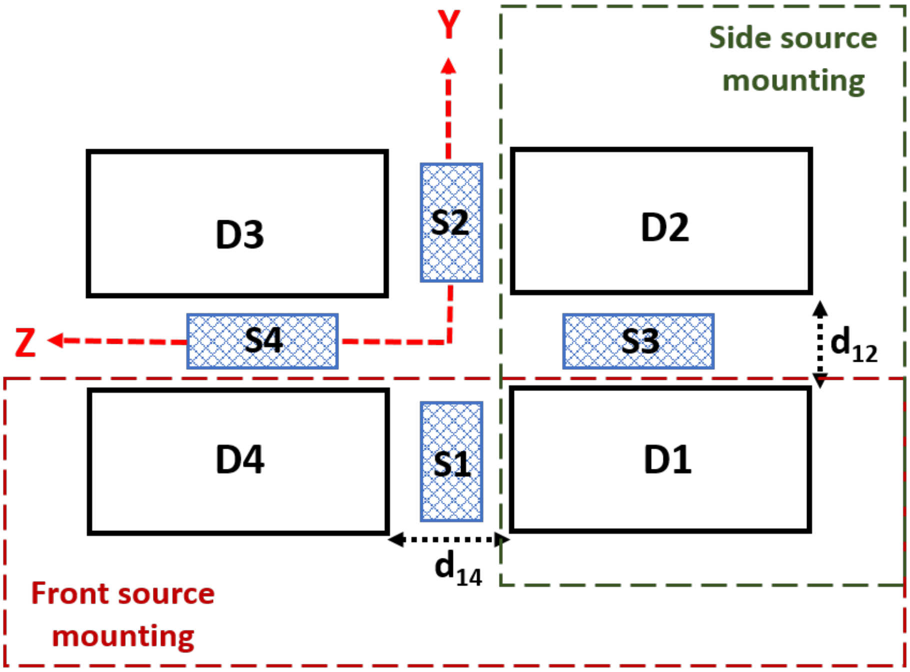

Figure 3.2: A schematic of 4 detectors setup showing front source mounting (D1, D4) and side source mounting (D1, D2). The coordinate frame is shown for reference.

of the source. Thus, throughout the text "x% enrichment" refers to the isotopic faction of interest to be ~x%. The different geometrical parameters, such as detector dimensions, the separation between the detector and source plates, source material, source dimensions, the shape of the source plates, etc., can be changed through configuration card files. This facilitates the easy control to switch ON/OFF any detectors or sources and the choice of the source material without altering the main code. The number of generated gamma rays and their energies are also available as input parameters in the cards. These configuration card files are implemented in the simulation code using libconfig++ libraries. The simulation code directory contains the set of config files in which the commands can be modified to change the geometrical parameters within some bounds.

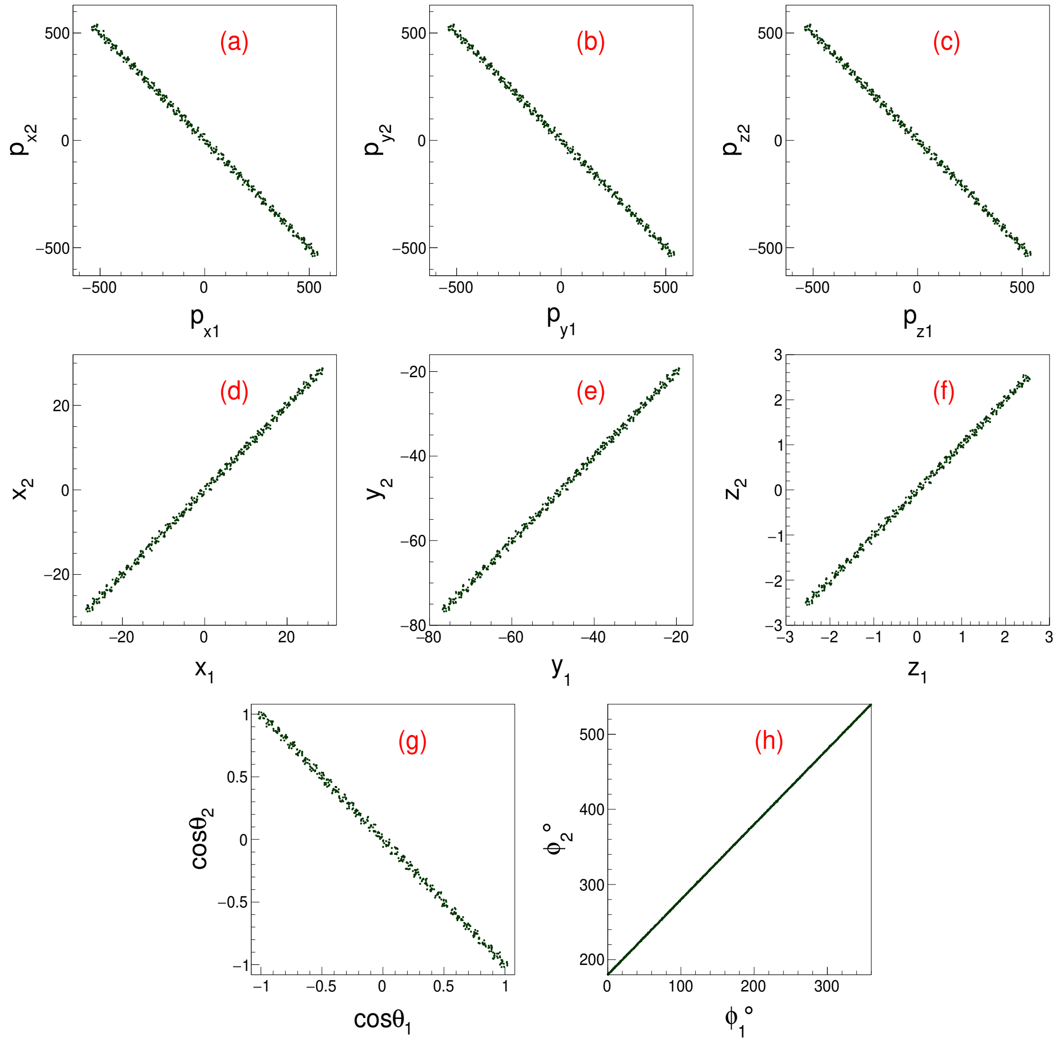

Figure 3.3: Primary particle distribution of two correlated 511 keV gamma-rays generated at the same vertex. The panels (a)-(c) show linear momenta (keV/c) correlation, (d)-(f) show position (mm) correlation, and (g)-(h) show angular correlation.

As mentioned, the gamma rays are generated from vertices uniformly distributed over the source's entire volume in the given geometry. Two modes are employed in the simulations,

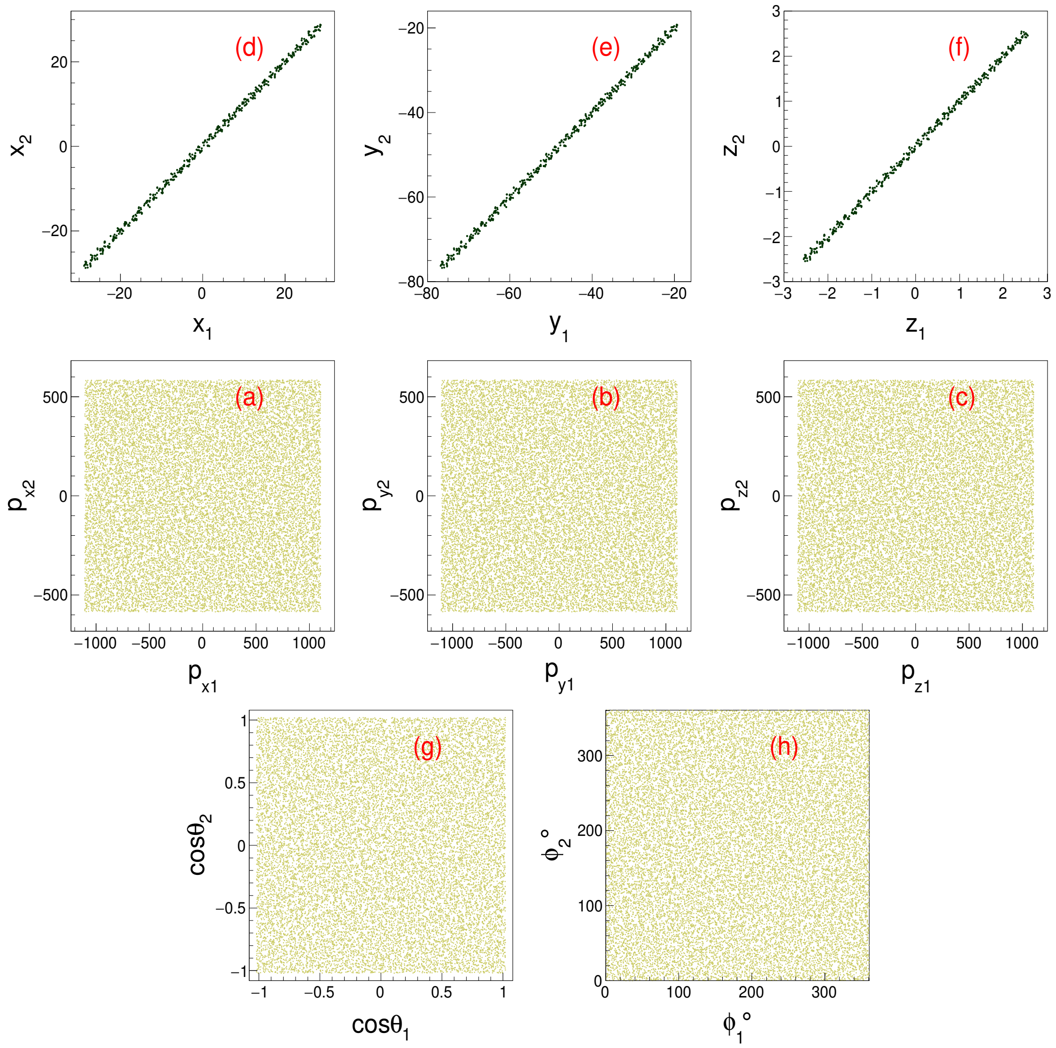

Figure 3.4: same as Figure 3.3, for two randomly generated gamma-rays of $E\gamma = 568$, 1091 keV.

namely:

- same vertex, with equal and opposite momentum, $E\gamma = 511$ keV (for pair production from positron annihilation),

- same vertex, no angular correlation, Eγ corresponding to specific transitions (see Table 3.1, for ^{96}Mo Cascade)

The program and the detector geometry in the program have been verified for both configurations mentioned above. Typical examples of momentum, position, and angular correlation for different gamma ray pairs are shown in Figure 3.3 and Figure 3.4. It is evident from the figures that annihilation gamma rays show an expected correlation in position and momentum, while no momentum correlation is observed for gamma rays of the ^{96}Mo decay cascade. For the simulation in GEANT4, the interactions of the particles and the generation of the secondary particles need to be specified. In the present study, the default electromagnetic interactions have been incorporated [144].

In the GEANT4 framework, the energy deposited by the particle at each step can be tracked. After each event, the energy deposited in each detector element is collected and stored. The total energy deposited in each detector (E_{dep}) is folded by a Gaussian function

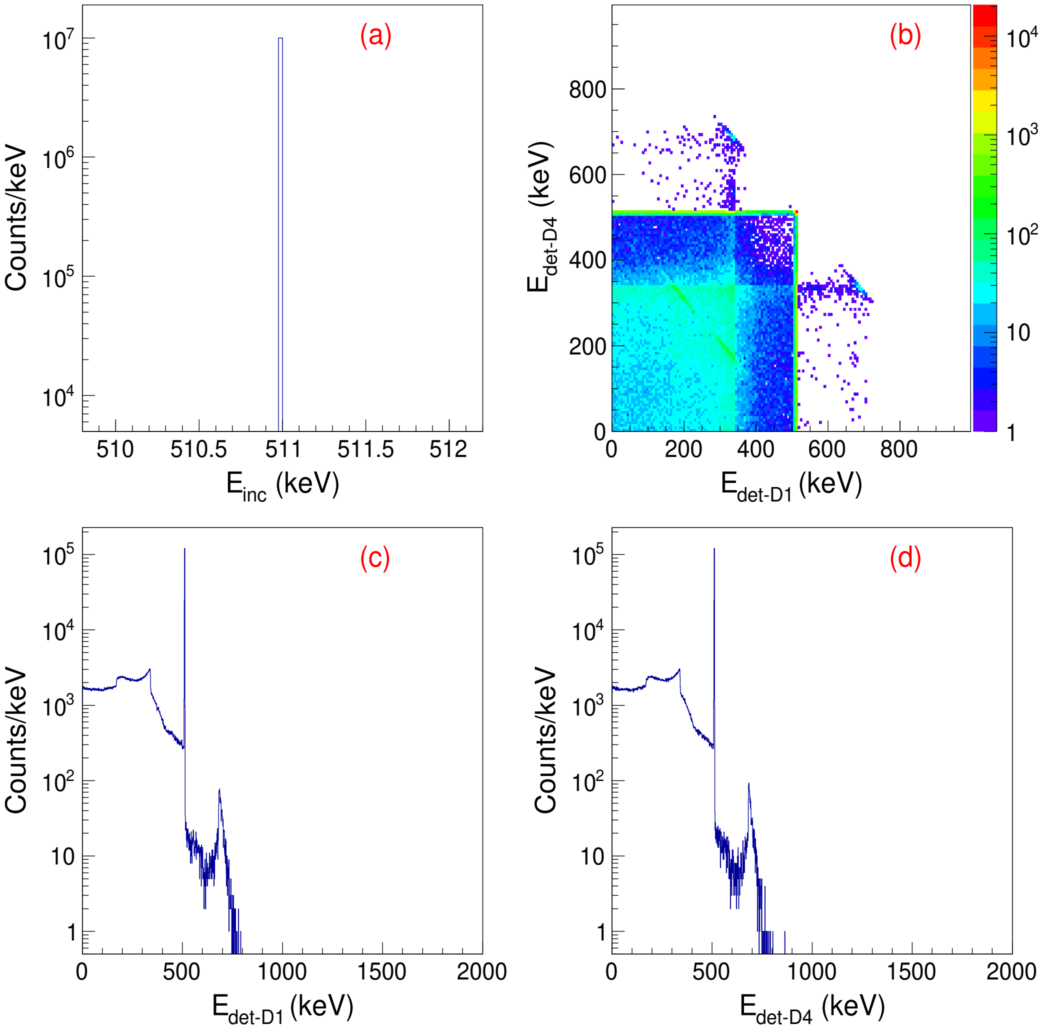

Figure 3.5: Detected energy spectra for two correlated 511 keV gamma-rays generated at the same point :(a) the incident energy spectrum, (b) two-dimensional spectrum of the detected energy in detector D1 and detector D4, (c) and (d) show the singles energy spectra in D1 and D4, respectively.

to account for the detector resolution, and the energy detected (E_{det}) is obtained. The resolution R(E), defined as FWHM/E, given by Eqn. 3.1, is incorporated in the present analysis.

$$R(E) = \frac{3.43}{E^{1.11}} \tag{3.1}$$

It should be mentioned this function gives an approximate description of the measured resolution data of the CRADLE detector in the energy range of 121–1408 keV, with CAEN

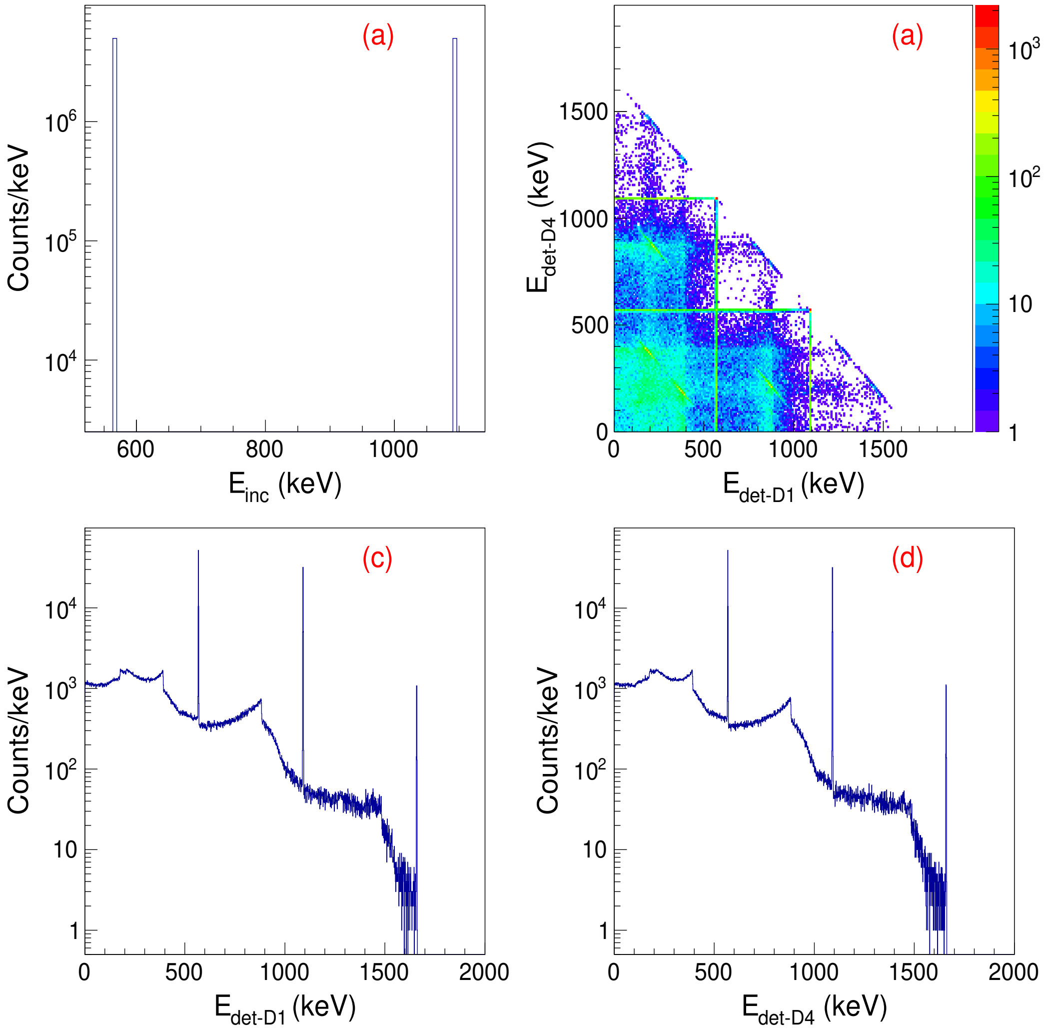

Figure 3.6: same as Figure 3.5 for two randomly generated gamma rays of $E\gamma = 568$, 1091 keV.

N6724 digitizer. The histograms of incident energy (E_{inc}) and energy detected in the detectors (E_{det}) are shown in Figure 3.5 and Figure 3.6. It should be mentioned that the summing contributions from backscattered/incident gamma rays are negligible in both cases. The simulation output is stored in Trees and Histograms in a ROOT file. The parameters stored are event number, momenta, and vertices of the gamma rays generated, the energy detected in each detector (E_{det-D1}, E_{det-D4}, etc.). All the data is stored in a single ROOT Tree [128], which can be used for further analysis.

3.3.2 Analysis of simulation data

An offline analysis program is developed in the ROOT framework to extract photopeak efficiencies in singles and coincidence spectra. In singles spectra, the photopeak is fitted by a sum of Gaussian peaks with a quadratic background. The fit region window is chosen to be ± 4 keV. The efficiency ϵ is computed as

$$\epsilon_i = N_i/N_{gen} \tag{3.2}$$

Where N_i is the area under the Gaussian fitted peak after the background correction in the detector i and N_{gen} is the total generated events. The coincidence counts (N_{coinc}) in the region of interest are extracted from the two-dimensional correlation plots of detected energy E_i vs E_j (e.g. see Figure 3.5 (b) and Figure 3.6 (b)). The energy spectrum E_i (E_j) is projected for a suitable gate covering the photopeak region in E_j (E_i). The gate widths are chosen to be ±4 keV, as in the case of singles spectra. The chance contribution to the coincidence photopeak is also estimated with an appropriate gate, as shown in Figure 3.7. (Note: the gate chosen from the left side somewhat overestimates the background.) The

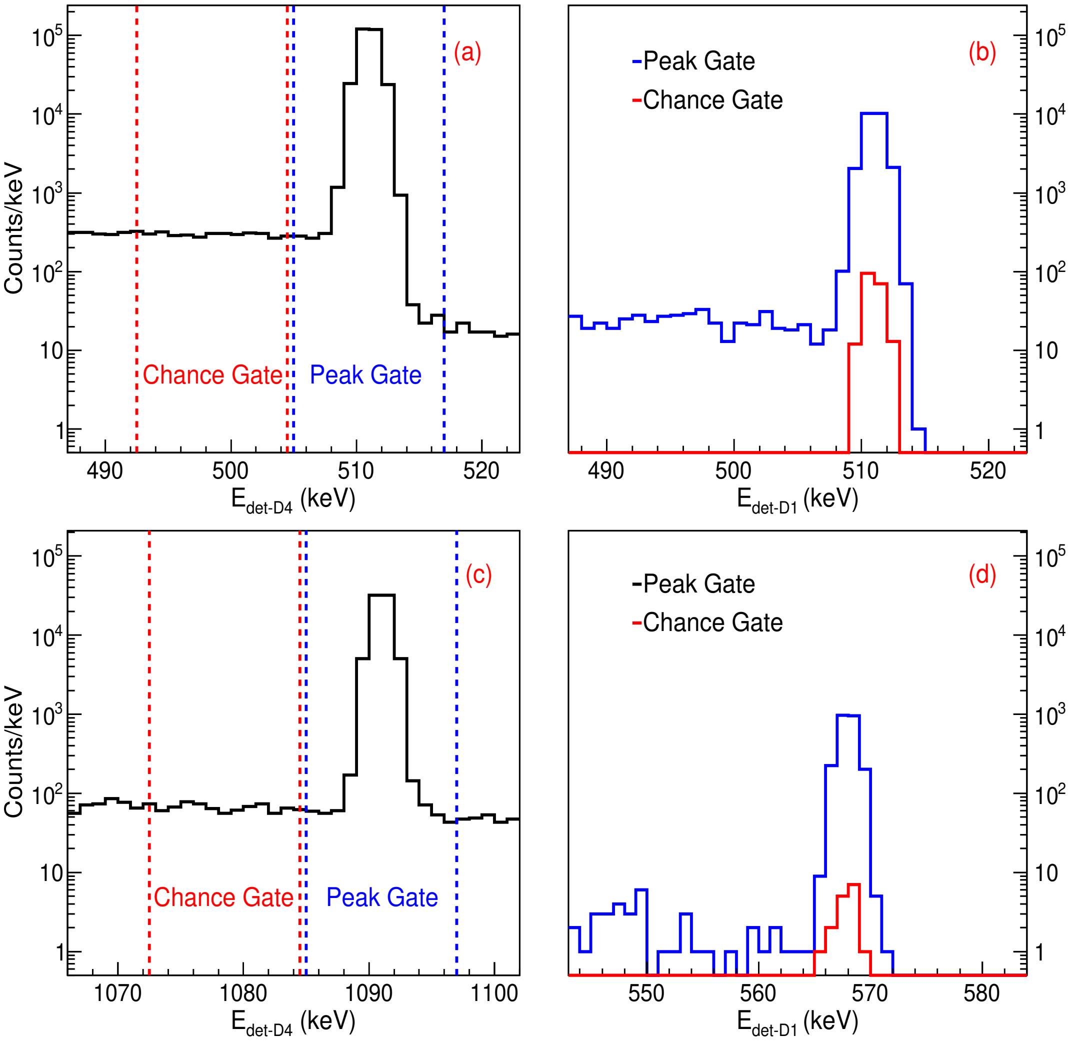

Figure 3.7: Typical projections of 2D spectra of D1-D4 detectors: panels (a) and (b) refer to positron DBD ($E_\gamma = 511$ keV), while (c) and (d) refer to ^{96}Zr β decay ($E_\gamma = 1091$ keV). Panels (a) and (c) show the peak and chance gates in energy spectra in D4, and corresponding energy spectra in D1 are shown in panels (b) and (d), respectively.

net coincidence counts $N_{c,ij}$ is obtained after proper background and chance correction. The coincidence efficiency for D1-D4 and D1-D2 configurations as shown in Figure 3.2 are computed as

$$\epsilon_{c,ij} = N_{c,ij}/N_{gen}, \tag{3.3}$$

Further, considering $\gamma_i - \gamma_j$ (i.e., γ_i in D4 and γ_j in D1) and $\gamma_j - \gamma_i$ (i.e., γ_j in D4 and γ_i in D1) combinations, total coincidence efficiency is defined as

$$\epsilon_c = \epsilon_{c,ij} + \epsilon_{c,ji} \tag{3.4}$$

In the rare decay experiment, the quantity of interest is the net expected event rate, which is often quoted in terms of Mϵ_c product. The Mϵ_c product is defined as

$$M\epsilon_c = f\ M_0\ \epsilon_c, \tag{3.5}$$

Where M_0 is the total mass of the source, f is a fraction of the isotope of interest, and ϵ_c is the total coincidence efficiency in the given setup. It should be noted that with increasing thickness, the attenuation of emitted gamma rays within the source becomes increasingly important. Hence, the source geometry must be optimized to maximize the net event rate.

3.4 Mass efficiency optimization

Initially, Mϵ_c is optimized for a two detector setup D1-D4 and D1-D2 for front and side source geometry, respectively (see Figure 3.2). For the front source, the thickness t of the source varies, keeping the cross-sectional area of $(l \times w)$ constant. The ϵ_c is computed for different configurations involving the constant and variable distance between the detectors (d_{14}). For the side source, thickness t and width w vary, keeping l constant. Distance between detectors d_{12} is fixed at $t + 10$ mm. The effect of variation of l is also investigated separately.

3.4.1 Mϵ_c optimization for ^{96}Zr β decay

Simulation studies have been performed in ^{96}Zr β decay for source optimization of ^{nat}Zr foils. Amongst all 3 possible $\gamma - \gamma$ combinations in the most dominant cascade C1 (see Fig. 3.1), 568-1091 keV pair is expected to give a cleaner identification of the decayed branch. Hence the source geometry optimization has been done for this pair. The Mϵ_c together with the coincidence efficiency and singles efficiency for 568-1091 keV gamma pair are plotted in the Figures 3.8 to 3.9 for front and side sources.

It is seen from Figure 3.8 that the optimum thickness for the front source is about 10 mm. In Figure 3.9, it is observed that both singles and coincidence efficiencies show minimal variation with the source width. Consequently, Mϵ_c indicates a continuous gradual increase. To understand this, the source strip of given thickness can be segmented into smaller pixels of 2.5 mm × 2.5 mm along the length (Z-axis) and width (X-axis) (see Figure 3.2), where each cell can be approximated as a point source. The $\epsilon(Z)$ can be obtained from $\epsilon(X, Z)$ by summing over all pixels along X and are shown in Figure 3.10 (a) and (b) for 568 and 1091 keV. As expected, the efficiency peaks around the detector center. The singles efficiency is nearly constant for $w =$ 5-20 mm and decreases for larger widths.

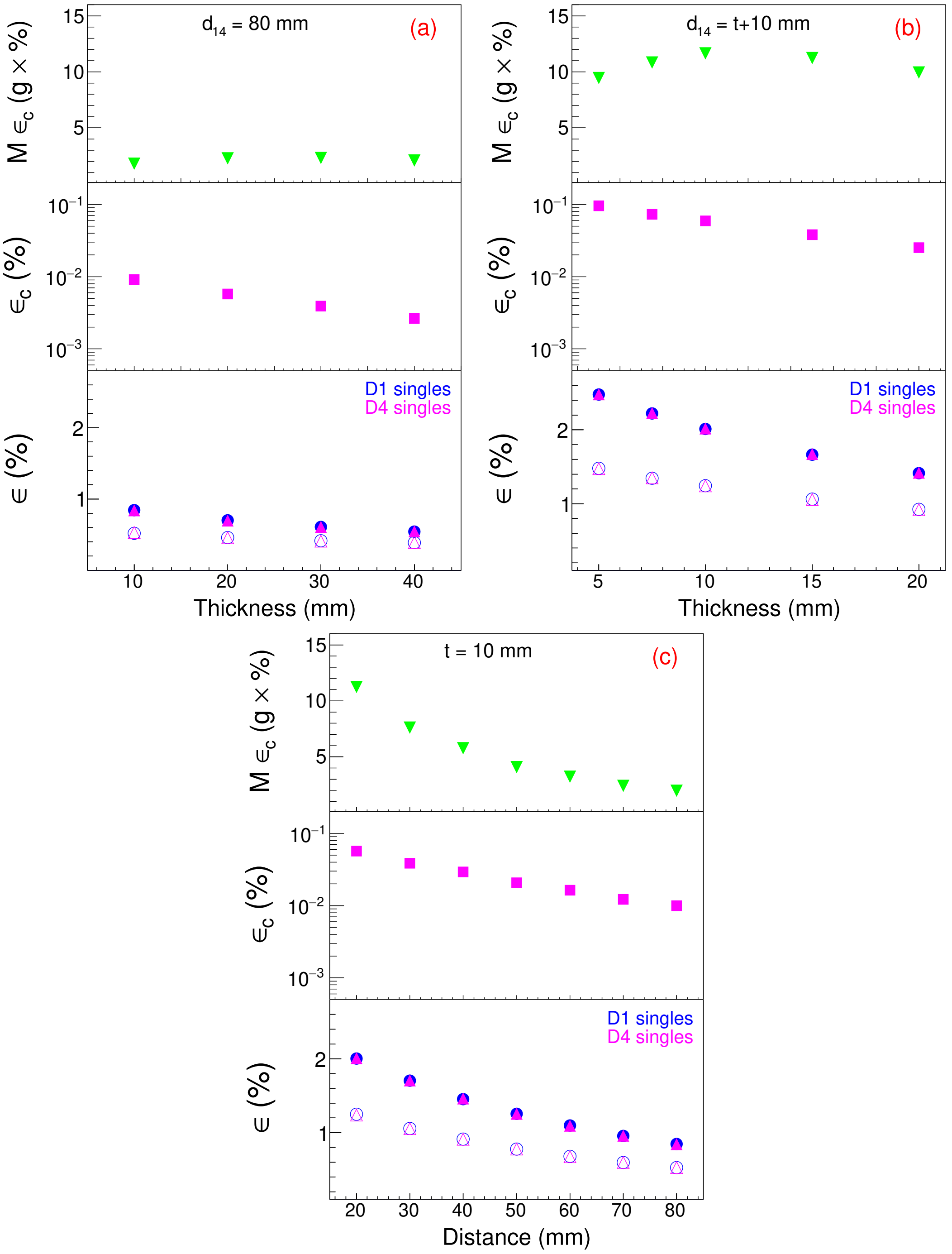

Figure 3.8: Simulated Mϵ_c for coincident detection of 568 and 1091 keV gamma-rays generated in Zr sample ($55\ mm \times 55\ mm \times t\ mm$), mounted between the front faces of detectors D1 and D4: (a) as a function t for fixed $d_{14} = 80\,$mm, (b) as a function t with $d_{14} =$ t+10 mm and (c) as a function of d_{14} for fixed $t = 10\,$mm. Each panel's top, middle, and bottom subpanels show $M\epsilon_c$, ϵ_c, and $\epsilon_1(\epsilon_4)$, respectively.

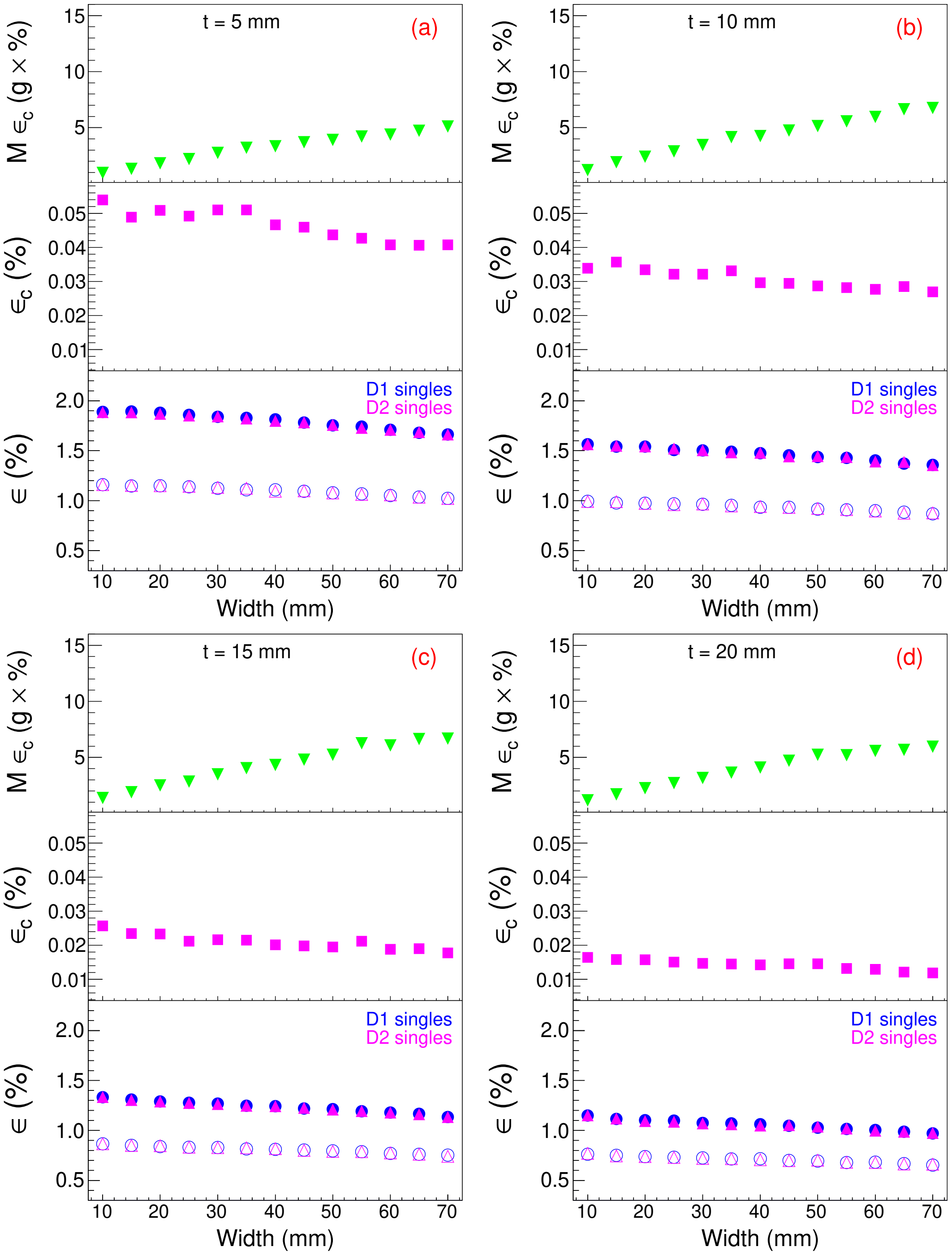

Figure 3.9: Simulated $M\epsilon_c$ for coincident detection of 568, 1091 keV gamma-rays generated in Zr sample ($55\ mm \times w\ mm \times t\ mm$) mounted between detectors sides, as a function of source width (w) for different thickness: a) t = 5 mm, b) t = 10 mm, c) t = 15 mm and d) t = 20 mm. Subpanels have a similar convention as in Figure 3.8.

In Figure 3.10, the percent change in integral under each curve from w = 5-40 mm is about 4% whereas from w = 5-70 mm it is about 11%. This percent change in the integral obtained from the Figure 3.10 is reflected in the singles efficiency data of Figure 3.9. From both these figures (Figure 3.9 and Figure 3.10), it is evident that increasing the width beyond $w \sim 30$ mm does not result in a significant gain in $M\epsilon_c$ and hence w_{opt} is taken to be 30 mm. The effect of variation in the length of the source is checked in coarse steps

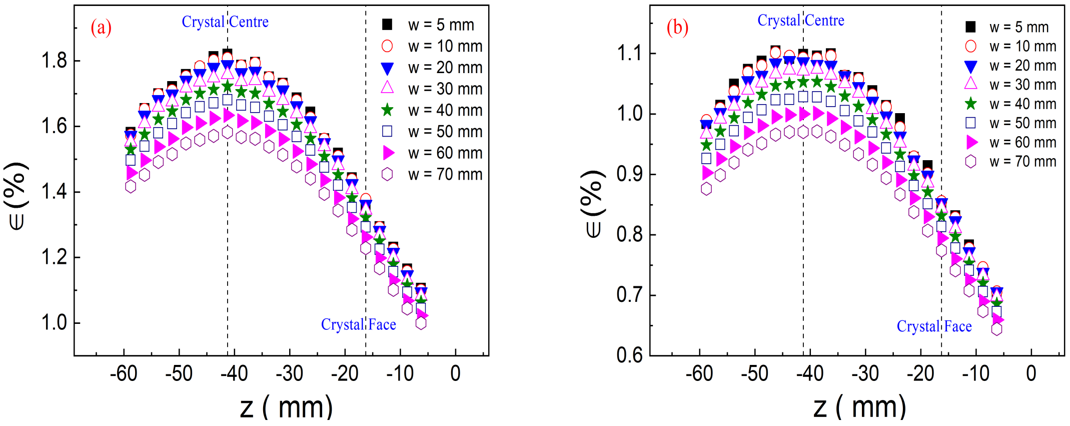

Figure 3.10: The simulated photopeak efficiency $\epsilon(Z)$ for different source widths for (a) Eγ = 568 and (b) Eγ = 1091 keV. The source is positioned in side mounting as shown in Figure 3.2.

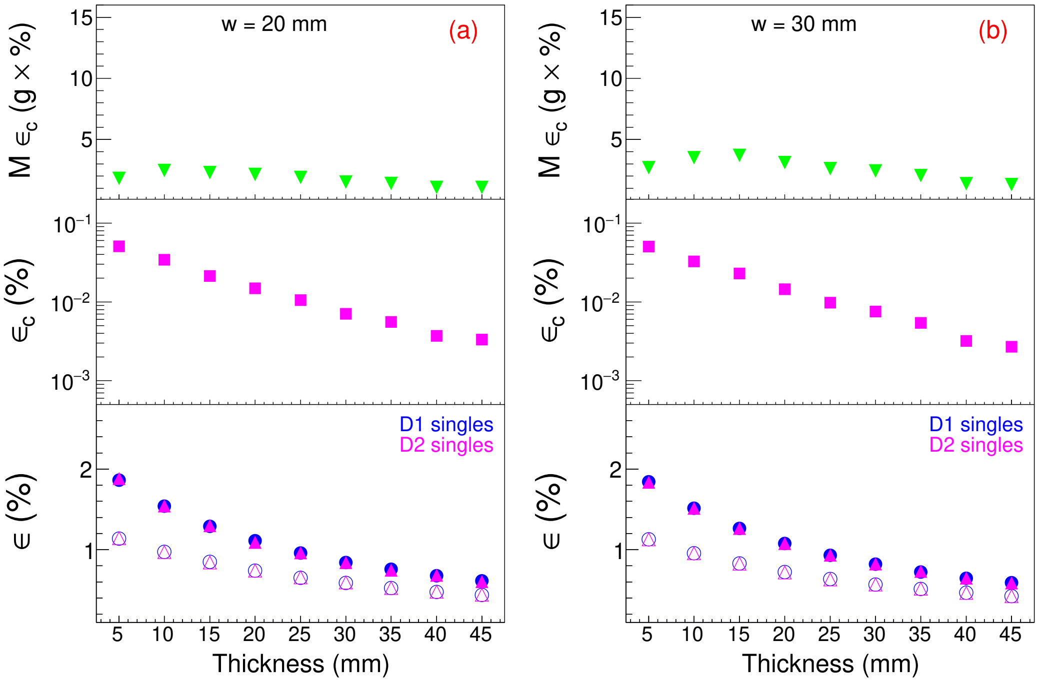

Figure 3.11: Same as Figure 3.9 for the Zr sample ($55\ mm \times w\ mm \times t\ mm$) a) w = 20 mm and b) w = 30 mm

.

and results are shown in Table 3.2. The variation of $M\epsilon_c$ with length (l) in the range 40 to

55 mm shows a linear trend and hence the optimal source length (l_{opt}) is taken to be 55 mm same as the crystal length.

Table 3.2: The Mϵ_c for different l of the source for 568-1091 keV gamma-rays.

Source Position	t (mm)	w (mm)	l (mm)	M (g)	Mϵ_c (g-%)
front	10	55	55	196.9	11.65
	10	40	40	104.2	7.77
side	10	30	55	107.4	3.50
	10	30	40	78.1	2.91

The Mϵ_c for the other two gamma-ray pairs in the C1 cascade, namely, 778-1091 and 568-778 keV as a function of source thickness are plotted in Figures 3.12 to 3.13 for front and side sources, respectively. For 778-1091 keV pair, as energy is higher, the optimal thickness is somewhat higher than 10 mm. Although the highest Mϵ_c is observed for the 568-778 keV pair, the background in the relevant region will be a crucial factor in the actual experiment. Results for the coincidence efficiencies ϵ_{12} (side-to-side detectors) and ϵ_{14} (face-to-face detectors) and corresponding Mϵ_c in Zr matrix with different enrichment factors are summarized in Table 3.3. As expected for the given source mass, the side configuration yields lower efficiency (half) compared to the optimal front configuration. The optimal

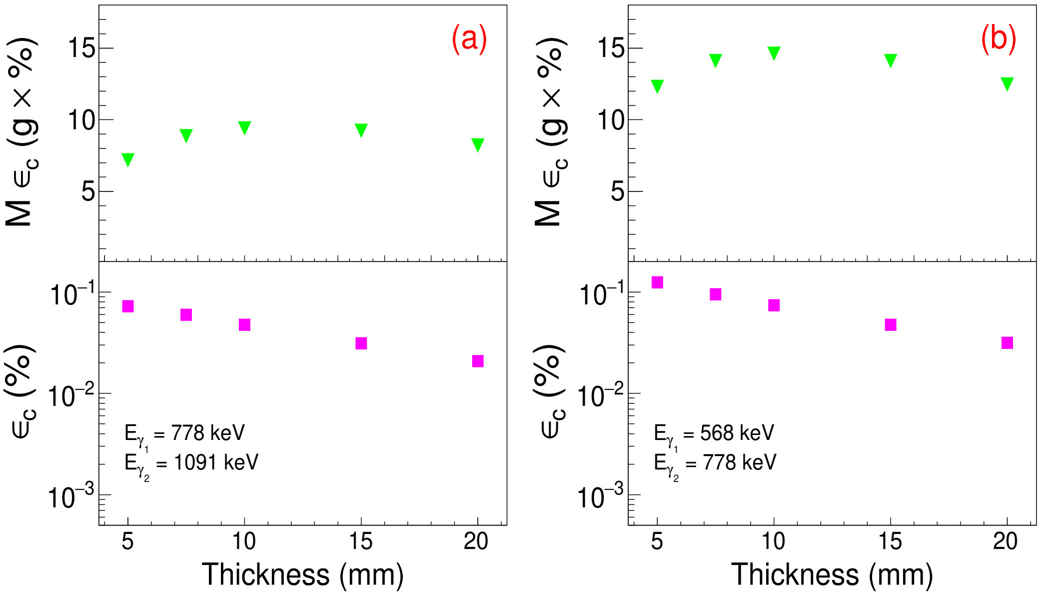

Figure 3.12: Simulated Mϵ_c for coincident detection of gamma-rays generated in Zr sample ($55\ mm \times 55\ mm \times t\ mm$), mounted between the front faces of detectors D1 and D4, as a function t with d_{14} = t+10 mm : a) 778-1091 keV and b) 568-778 keV. The top and bottom subpanels show $M\epsilon_c$ and ϵ_c, respectively.

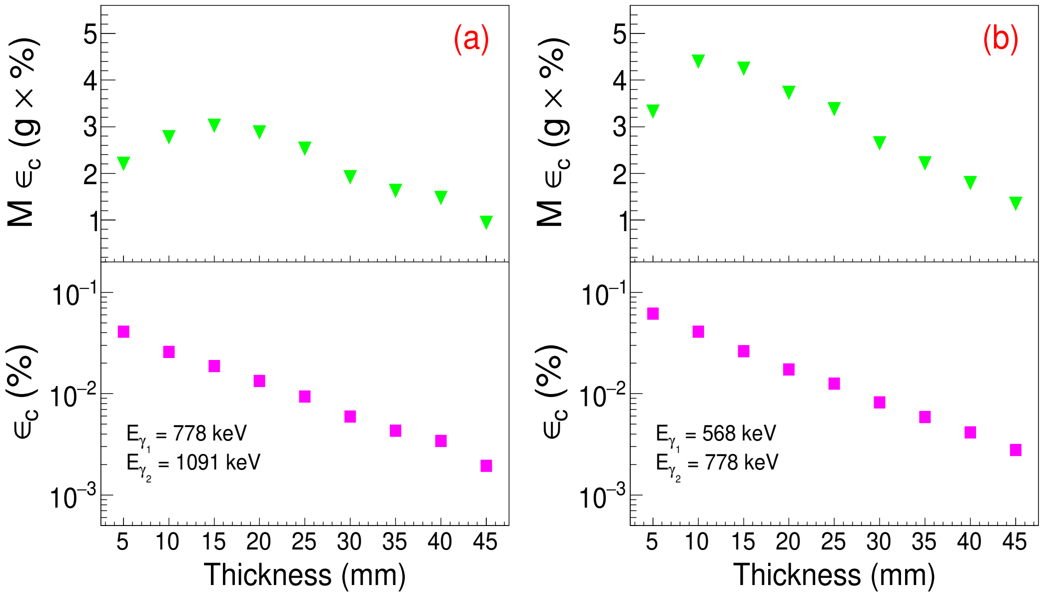

Figure 3.13: Simulated Mϵ_c for coincident detection of gamma-rays generated in Zr sample (55 $mm \times w\ mm \times t\ mm$) mounted between detector sides at w = 30 mm: a) 778-1091 keV and b) 568-778 keV. Subpanels have a similar convention as in Figure 3.12.

side source dimensions for all 3 pairs of C1 cascade are: l_{opt} = 55 mm, w_{opt} = 30 mm and t_{opt} = 10 mm. Among the three possible gamma-ray pairs in the C1 cascade, the best Mϵ_c values are obtained for 568-778 keV pair. Thus, the optimal source dimensions for 2 detector setup are 55 mm×55 mm×10 mm and 55 mm×30 mm×10 mm for the front and side source, respectively. The four detector setup uses these optimum source dimensions to estimate the sensitivity for ^{96}Zr β decay.

Table 3.3: Summary of the source optimization for ^{96}Zr - total mass of the Zr source (M), coincidence efficiency ϵ_c, effective mass M$_1$ of ^{96}Zr (with ~2.8% natural abundance) and corresponding effective mass efficiency M$_1\epsilon_c$, effective mass M$_2$ of ^{96}Zr (with ~50% enrichment) and M$_2\epsilon_c$ are listed.

Source position	Eγ (keV)	Optimum size ($t\ mm \times w\ mm \times l\ mm$)	M (g)	ϵ_c (%)	M$_1$ (g)	M$_1\epsilon_c$ (g-%)	M$_2$ (g)	M$_2\epsilon_c$ (g-%)
front	568, 1091	10 × 55 × 55	196.9	0.05918	5.5	0.326	98.5	5.82
side		10 × 30 × 55	107.4	0.03262	3.0	0.098	53.7	1.75
front	778, 1091	10 × 55 × 55	196.9	0.04766	5.5	0.263	98.5	4.69
side		10 × 30 × 55	107.4	0.02580	3.0	0.078	53.7	1.38
front	568, 778	10 × 55 × 55	196.9	0.07418	5.5	0.409	98.5	7.30
side		10 × 30 × 55	107.4	0.04092	3.0	0.123	53.7	2.19

3.4.1.1 Comparison of optimal Mϵ_c with earlier measurements

To compare the present $M\epsilon_c^{opt}$ with the earlier measurement of Finch et al. [4], $M\epsilon_c$ is estimated for 568-1091 keV gamma ray pair for the reference source-detector geometry. The source-detector geometry in the reference work has been constructed in GEANT4, as shown in Figure 3.14. It consists of two coaxial HPGe detectors mounted face-to-face at a distance of 12 mm. The crystal size ∼88 mm (dia) × 50 mm and 2.54 mm thick front magnesium window are taken from the reference [145]. All other parameters are generated assuming construction similar to the CRADLE, i.e., the separation between crystal and container, dead layers, etc. Simulations are also done assuming ∼0.9 mm carbon front window. A cylindrical source of mass ∼36.8 g with ∼50% enrichment and ∼60 mm dia×2 mm size is considered, giving M_{ref} ∼18 g of ^{96}Zr similar to that of [4]. The coincidence efficiencies of 568 and 1091 keV gamma-ray pair for the reference geometry [4] and the present set (D1-D4) are compared. As can be seen from Table 3.4, a significantly large quantity of the Zr source will be needed to achieve Mϵ_c similar to earlier measurements with the present set of detectors. The coincidence efficiencies of a hypothetical point source are also simulated for comparison. It should be mentioned that the measured best reported limit so far on $T_{1/2}$ of ^{96}Zr employed about 19 g of ZrO_2 powder with 57.3% enrichment for singles gamma ray measurement, resulting in Mϵ of ∼37 g-% [108]. The loss in the coincidence efficiency due to the small crystal size in the present geometry (as discussed in the previous section) can be partially recovered by employing four HPGe detectors. It is also expected that higher granularity will help in background improvement. The proposed source-detector configuration

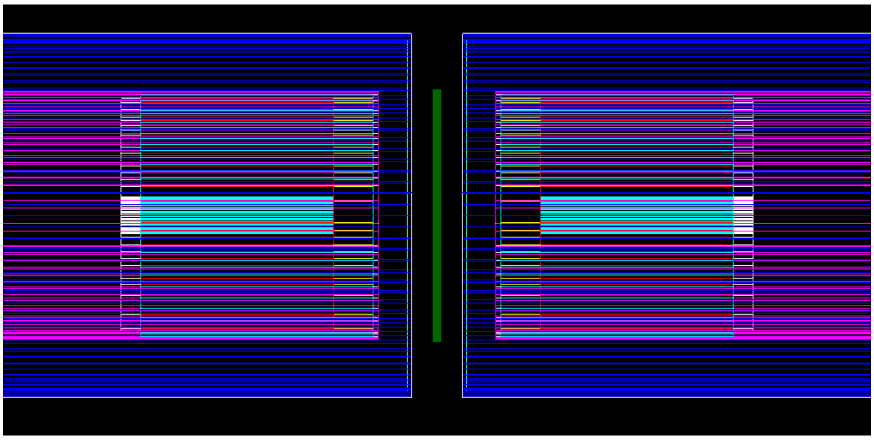

Figure 3.14: The detector-source geometry described in Finch *et al.* [4].

Table 3.4: A Comparison of Mϵ_c (568,1091 keV) for D1-D4 and Ref. [4] setup, ($f = 50\,\%$).

Crystal Size	Front window (mm)	Source Size	d (mm)	ϵ_c %	M (g)	Mϵ_c (g-%)
88 mm (dia)×50 mm	2.54	60 mm (dia)×2 mm	12	0.65	18	12
55 mm (dia)×55 mm	0.90	55 mm×55 mm×2 mm	12	0.12	20	2

is shown in Figure 3.2. The total mass is configured in four sources - S1+S2 (front sources) and S3+S4 (side sources) for the four detector setup. Initially, the respective optimum source dimensions obtained in the two detector geometry for the front (55 mm×55 mm) and side sources (55 mm×30 mm) are employed, and sources are positioned symmetrically w.r.t detector crystal for better solid angle coverage. Simulations are done for two different thicknesses, namely, t = 5 mm and t = 10 mm with inter detector gap (d) of 7 mm and 12 mm, respectively. It may be noted that reducing thickness t from 10 mm to 5 mm, permits d_{14} = 7 mm, which yields $\sim$60% gain in ϵ_c. Thus, even though there is a mass decrease of 50 %, only $\sim$20% decrease is observed in the total Mϵ_c. The four detector configurations with t = 5 mm for front and side sources will result in 70% higher Mϵ_c (see Table 3.3), but still, considerably large mass $\sim$152 g of ^{96}Zr will be needed. Hence, further mass optimization needs to be considered. As mentioned earlier, the dominant contribution comes from sources in the front. So in the first step, only front sources S1 and S2 are employed, and the cross-sectional area of the source ($l \times w$) is varied, maintaining t_0 = 5 mm and d = 7 mm to obtain the optimal front source mass (M$_f$). In the second step, a fraction of M$_f$ (30-60 %) is distributed as side sources S3 and S4. Similar to the first case, t_0 and d are kept as 5 mm and 7 mm, respectively, and ($l \times w$) is varied, keeping M$_f$ fixed ($l <$ crystal length, to avoid edge effects). The estimated net Mϵ_c in zirconium matrix with $\sim$50% enrichment are listed in Table 3.5. It can be seen that initially the Mϵ_c values increase rapidly with l, w ($\sim$20 %), but beyond 50×50 increase is not significant ($\sim$12%). The source size of l_{opt} = 40 mm, w_{opt} = 40 mm, with effective mass (M) of 52 g ($\sim 3M_{ref}$) yields Mϵ_c similar to earlier coincidence measurement (see Table 3.3). It should be mentioned that Mϵ_c is also computed for the disk shape source, but the observed values of Mϵ_c are smaller than those for the cuboidal source geometry for the given mass.

Table 3.5: Summary of the mass optimization in 4 detector geometry with only front sources ($l \times w \times t$) for 568-1091 keV gamma-rays, assuming $\sim$ 50% enrichment.

Source size $l \times w \times 5$ (mm^3)	ϵ_c (%)	M (g)	Mϵ_c (g-%)
35×35	0.260	40	10.4
40×40	0.243	52	12.6
45×45	0.226	66	14.9
50×50	0.213	81	17.3
55×55	0.197	98	19.4

In the second case, additional side sources comprising approximately 30%, 40% and 60% fraction of the optimal front source mass (i.e., M$_f$ $\sim$ 52 g) were employed. The source length l was constrained to be smaller than the crystal length (55 mm) to avoid edge effects of the crystal. The estimated net Mϵ_c in zirconium matrix with $\sim$50% enrichment are given in Table 3.6. It can be seen that Mϵ_c is not very sensitive to l and w in the range of l = 25-35 mm and w = 18-25 mm. In this case, too, for $M_s > 0.3M_f$, no significant gain is observed in Mϵ_c. Thus, the proposed optimal side source dimensions are : l_{opt} = 30 mm, w_{opt} = 20 mm, t_{opt} = 5 mm with a total mass equal to 40% of M$_f$. The optimal

Table 3.6: Summary of the mass optimization in 4 detector geometry with side sources ($l \times w \times 5$, Mass M$_s$) for 568-1091 keV gamma-rays, for a different fraction x%$\sim$ M$_s/M_f$ ($=$52 g), assuming $\sim$ 50% enrichment.

Source size $l \times w \times 5$ (mm^3)	x %	M$_s$ (g)	M (g)	ϵ_c (%)	Mϵ_c (g-%)
50×10	30	16	68	0.208	17.1
25×20				0.211	17.4
40×15	40	19	71	0.206	17.6
30×20		19	71	0.209	17.8
25×25		20	72	0.209	18.0
35×18		20	72	0.209	18.0
50×20	60	32	84	0.192	18.9
45×22		32	84	0.192	18.9

configuration for t = 5 mm is obtained as M_{eff} $\sim$72 g) with M$_s$ $\sim$ 40% of M$_f$. The cross-sectional dimensions (l_{opt}, w_{opt}) are 40 mm×40 mm for the front source and 30 mm×20 mm for the side source. Figure 3.2 shows source and detector configuration. The M$\epsilon_c(\gamma_1, \gamma_2)$ in Zr matrix with $\sim$50% enrichment are estimated for different gamma ray pairs in C1 cascade for the above optimal source configuration, and results are given in Table 3.7. With respect to Mϵ_c (568-1091), Mϵ_c (568-778) is about 30% higher, while Mϵ_c (778-1091) is about 20% lower. Although higher granularity in the four detector setup is expected to improve the background and reduce the pileup, these effects cannot be quantified at this stage.

Table 3.7: M$\epsilon_c(\gamma_1, \gamma_2)$ in optimal source configuration (M_{eff} $\sim$72 g) in 4 detector geometry.

Eγ (keV)	ϵ_c (%)	Mϵ_c (g-%)
568, 1091	0.216	15.4
568, 778	0.279	20.0
778, 1091	0.172	12.3

3.4.2 Mϵ_c optimization (ECβ^+) in ^{112}Sn

The Mϵ_c (with f = 1) and coincidence efficiency for a pair of 511 keV gamma-rays are plotted in Figures 3.15 to 3.17. It can be seen that the optimum thickness is $\sim$10 mm for both front and side sources. It can be seen that the optimum thickness is $\sim$10 mm for both front and side sources. The estimated net Mϵ_c in the tin matrix for different isotopic enrichment (i.e., for different f) are listed in Table 3.8. The simulation results with tin showed that 55 mm×55 mm source of 10 mm thickness yields maximum Mϵ_c. The net Mϵ_c

is estimated in the tin matrix for different isotopic enrichment (i.e., for different f), and it was found that very good Mϵ_c can be achieved with about 50% enriched ^{112}Sn.

Table 3.8: Summary of the source optimization for ^{112}Sn - total mass of the Sn source (M), coincidence efficiency (ϵ_c), effective mass M$_1$ of ^{112}Sn (with ~0.97% natural abundance) and corresponding effective mass efficiency M$_1\epsilon_c$, effective mass M$_2$ of ^{112}Sn (with ~50% enrichment) and M$_2\epsilon_c$ are listed.

Source position	Optimum size (t $mm \times w$ $mm \times l$ mm)	M (g)	ϵ_c (%)	M$_1$ (g)	M$_1\epsilon_c$ (g-%)	M$_2$ (g)	M$_2\epsilon_c$ (g-%)
front	10 × 55 × 55	221.1	0.31	2.1	0.65	110.5	34.2
side	10 × 30 × 55	120.6	0.30	1.1	0.33	60.3	18.0

3.4.3 Mϵ_c optimization ($\beta^+\beta^+$) in ^{106}Cd

For $\beta^+\beta^+$ decay mode, the simulations were extended to two pairs of 511 keV for ^{nat}Cd foils. Results for the coincidence efficiencies and corresponding Mϵ_c in the Zr matrix with different enrichment factors are summarized in Table 3.9.

Table 3.9: Summary of the source optimization for ^{106}Cd - total mass of the Cd source (M), coincidence efficiency (ϵ_c), effective mass M$_1$ of ^{112}Sn (with ~1.25% natural abundance) and corresponding effective mass efficiency M$_1\epsilon_c$, effective mass M$_2$ of ^{106}Cd (with ~50% enrichment) and M$_2\epsilon_c$ are listed.

Source position	Optimum size (t $mm \times w$ $mm \times l$ mm)	M (g)	ϵ_c (%)	M$_1$ (g)	M$_1\epsilon_c$ (g-%)	M$_2$ (g)	M$_2\epsilon_c$ (g-%)
front	10 × 55 × 55	261.4	0.53	3.3	1.7	130.7	69.3
side	10 × 30 × 55	142.6	0.49	1.8	0.9	71.3	34.7

3.5 Background estimation studies for ECβ^+/$\beta^+\beta^+$

A feasibility study for estimating the sensitivity of $\beta^+EC/\beta^+\beta^+$ decay by simultaneous emission of 2/4 511 keV gamma rays with two HPGe detectors has been carried out. In such rare decay search experiments, the mass efficiency product (Mϵ_c) needs to be maximized. The coincident detection efficiency (ϵ_c) of 511 keV gamma rays were simulated using GEANT4. Hence, the source size and mounting geometry were optimized for the present detector setup. The background measurements in coincidence were carried out using a D1-D2 setup with two identical low background cryo-cooled HPGe detectors installed at TIFR, Mumbai (for details, see Chapter 2). The coincident background is estimated at sea level with moderate Pb shielding.

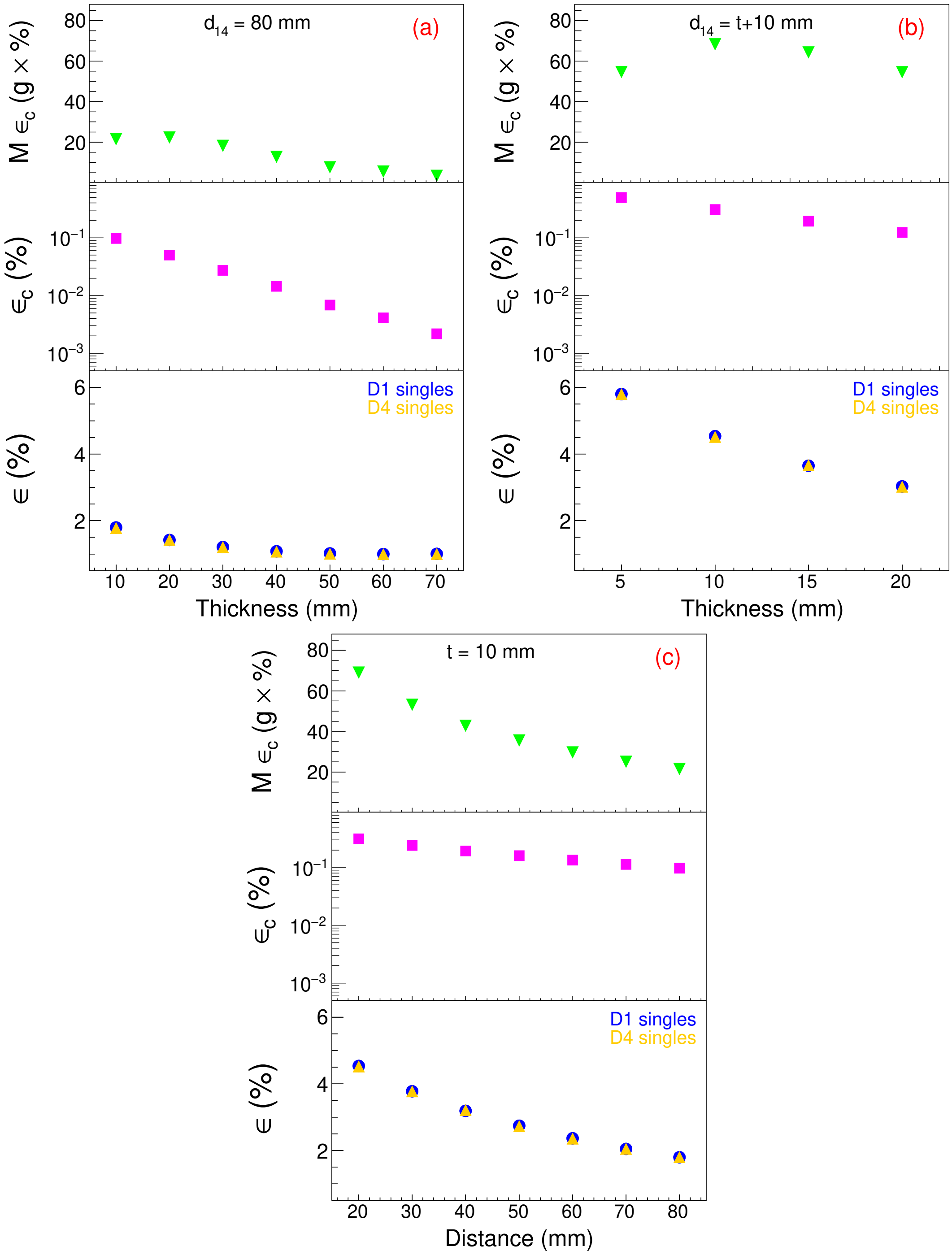

Figure 3.15: Simulated Mϵ_c for coincident detection of two correlated 511 keV gamma-rays generated in Sn sample ($55\ mm \times 55\ mm \times t\ mm$), mounted between the front faces of detectors D1 and D4: (a) as a function t for fixed d_{14} = 80 mm, (b) as a function t with d_{14} = t+10 mm and (c) as a function of d_{14} for fixed t = 10 mm. The top, middle and bottom subpanels in each panel show $M\epsilon_c$, ϵ_c, and $\epsilon_1(\epsilon_4)$, respectively.

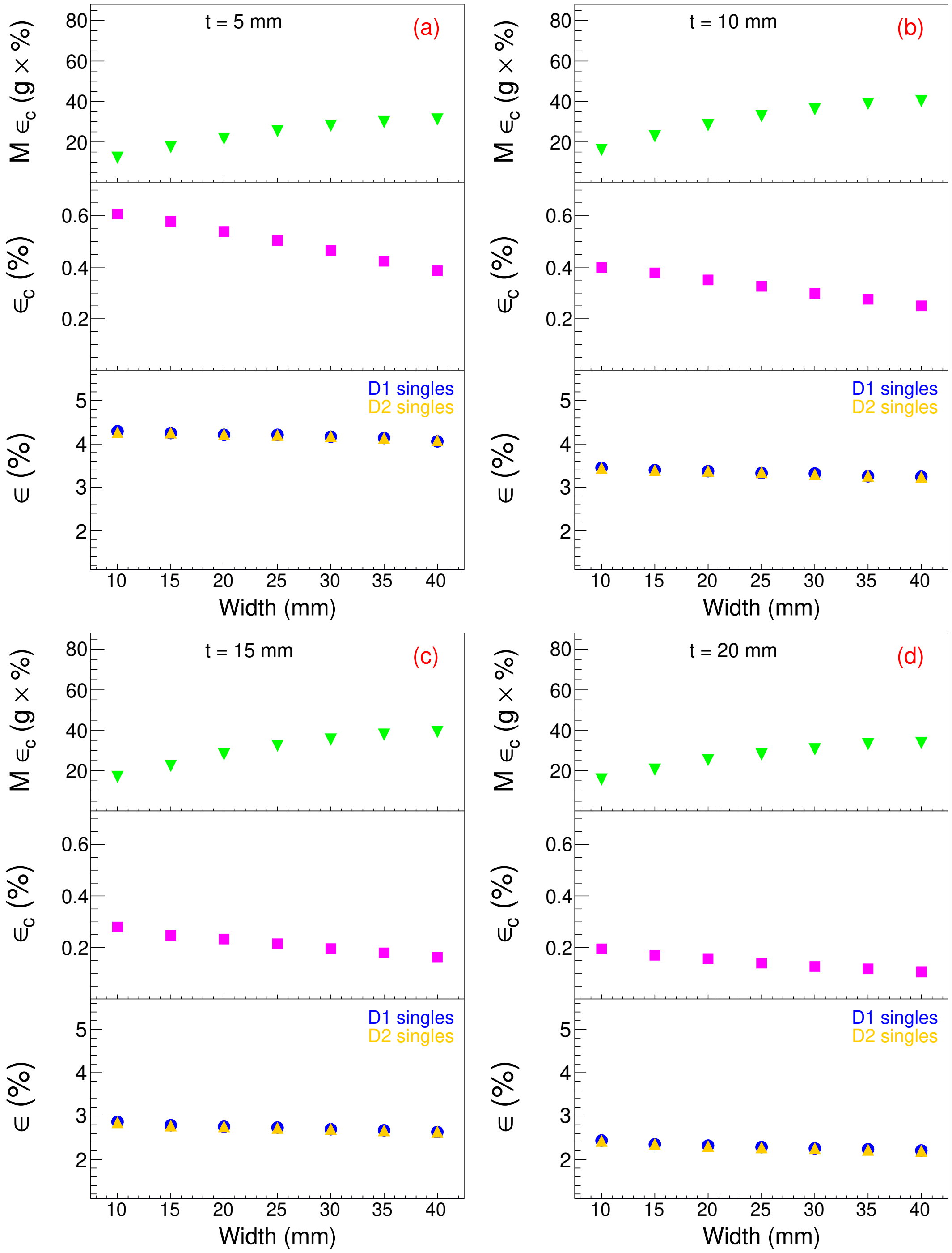

Figure 3.16: Simulated Mϵ_c for coincident detection of two correlated 511 keV gamma-rays generated in Sn sample ($55\ mm \times w\ mm \times t\ mm$) mounted between detectors sides, as a function of source width (w) for different thicknesses: a) t = 5 mm, b) t = 10 mm, c) t = 15 mm and d) t = 20 mm. The top, middle and bottom subpanels in each panel show $M\epsilon_c$, ϵ_c, and $\epsilon_1(\epsilon_2)$, respectively.

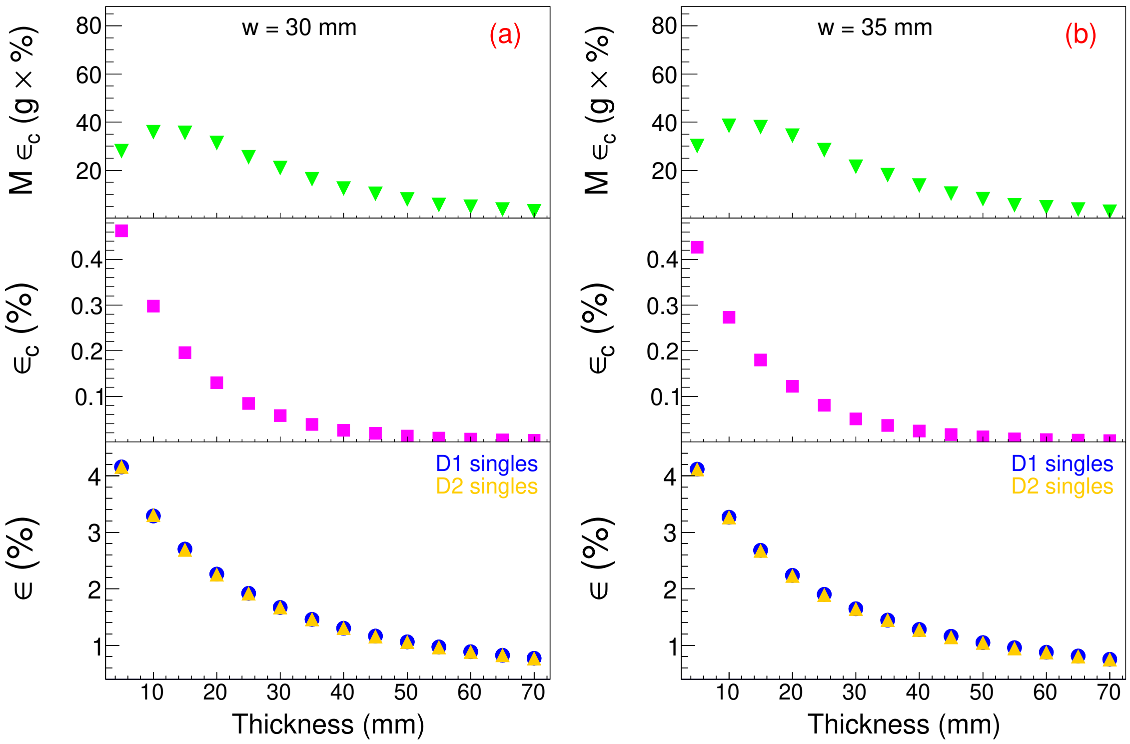

Figure 3.17: Same as Figure 3.16 for the Sn sample ($55\ mm \times w\ mm \times t\ mm$) a) w = 30 mm and b) w = 35 mm

.

3.5.1 Measurement details

Data were acquired using a CAEN DT6724 digitizer (14-bit, 100 MS/s) and recorded separately (time stamp and energy) for each detector on an event-by-event basis. The coincident spectra were generated using offline analysis. The dead time was monitored with a standard 10 Hz pulser and was found to be negligible (< 0.1 %). The resolution of the detector was $\sim$3 keV at 1332 keV. The ambient background was recorded for $\sim$ 27 d, at different times over the period of about 10 months. No measurable drifts were observed in the data. The ^{nat}Sn sample of mass 38.8990 g, in the form of granules (7N purity, Alfa aesar) with an approximate overall size $30\,mm \times 39\,mm \times 6.5\,mm$, was counted in close geometry for t = 77.8 d. Figure 3.18 shows a typical 2-dimensional plot of E_{D1} vs E_{D2} for the coincidence background. Correlated 511 keV lines and high energy background lines (1460, 2615 keV) are clearly visible. The coincidence efficiency (ϵ_c) of D1-D2 detectors for ^{nat}Sn and ^{nat}Cd foils was obtained using a GEANT4 simulation program. A total of 10^6 events of 2 (1) correlated pairs of 511 keV gamma rays were generated at a given vertex for $\beta^+\beta^+$ (EC-β^+). Details of the simulation and source optimization procedure are discussed earlier. It was found that 55 mm×55 mm source of 10 mm thickness yields maximum Mϵ_c. However, with a 5 mm thick source, the detectors can be moved closer (d = 7 mm) and consequently decrease in Mϵ_c is only $\sim$20% even if M is reduced by 50%. This is preferable as the inherent background scales with the mass of the source. Moreover, for the given mass of the source, simulated values of ϵ_c for side configuration yield lower efficiency ($\sim$half) as compared to the front source. Hence, the optimal source geometry is chosen to be $55\,mm \times 55\,mm \times 5\,mm$

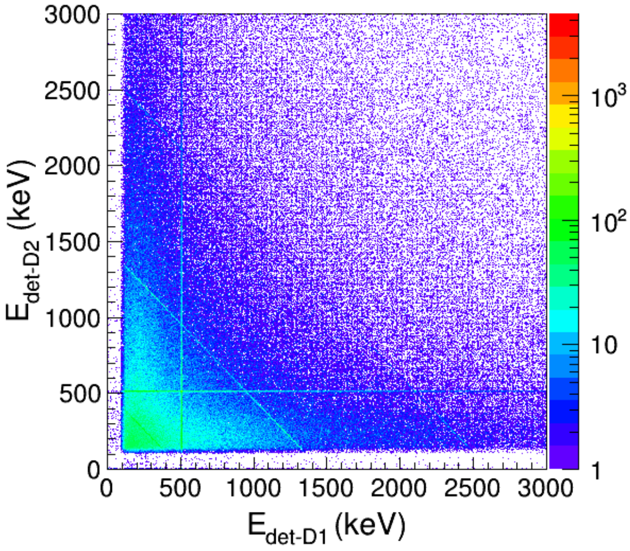

Figure 3.18: Coincident energy spectra of D1-D2 coincidence setup with natural tin sample (t =77.8 d).

foil sandwiched between the front faces of detectors, with separation between detectors d = 7 mm. The simulated values of ϵ_c are given in Table 3.10. Hence, the optimal source geometry is chosen to be $55\,mm \times 55\,mm \times 5\,mm$ foil sandwiched between the front faces of detectors, with separation between detectors d = 7 mm. Further, for β^+EC decay mode, the simulations with optimized source size and similar mounting geometry were adopted using a correlated pair of 511 keV gamma rays for ^{nat}Sn foils.

3.5.2 Analysis and results

The coincidence was performed using offline C++ based algorithms developed in ROOT [128]. The coincidence time window was set to $\pm 1\,\mu$s to ensure that all coincident events were collected and the output was written in a ROOT Tree. The data were analyzed using LAMPS [133]. Figure 3.19 compares the ambient background of D1 in singles and coincidence. It is evident that the coincidence yields significant improvement in the background. In fact, only 511 keV peak survives in the background, albeit with much reduced intensity. The sum energy spectrum ($E_{sum} = E_{D1}+E_{D2}$) is also shown for comparison. It can be seen that while high energy gamma rays like 1460 keV (^{40}K) and 2615 keV (^{208}Tl, originating from ^{232}Th) are visible in sum energy, the overall background is reduced by order of magnitude. For both ambient background and ^{nat}Sn sample, analysis to extract counts in the region of interest (ROI) near 511 keV was done in an identical manner. The chance correction from the time spectrum was found to be negligible. The coincident 511-511 keV events were suitably corrected for underlying Compton chance coincidence. The prompt gated D1 spectrum was generated for the photopeak region (511 ± 5 keV) in D2, while the chance gated spectrum was generated from 5 keV window on the left and right of the photopeak in D2. The observed counts in the ROI for ambient background (i.e., without the sample) are 3 ± 1 cts/d, which is equivalent to 1271 ± 297 cts/y. It should be mentioned that the observed singles count rate for 511 keV gamma ray in low background setup TiLES [2], is

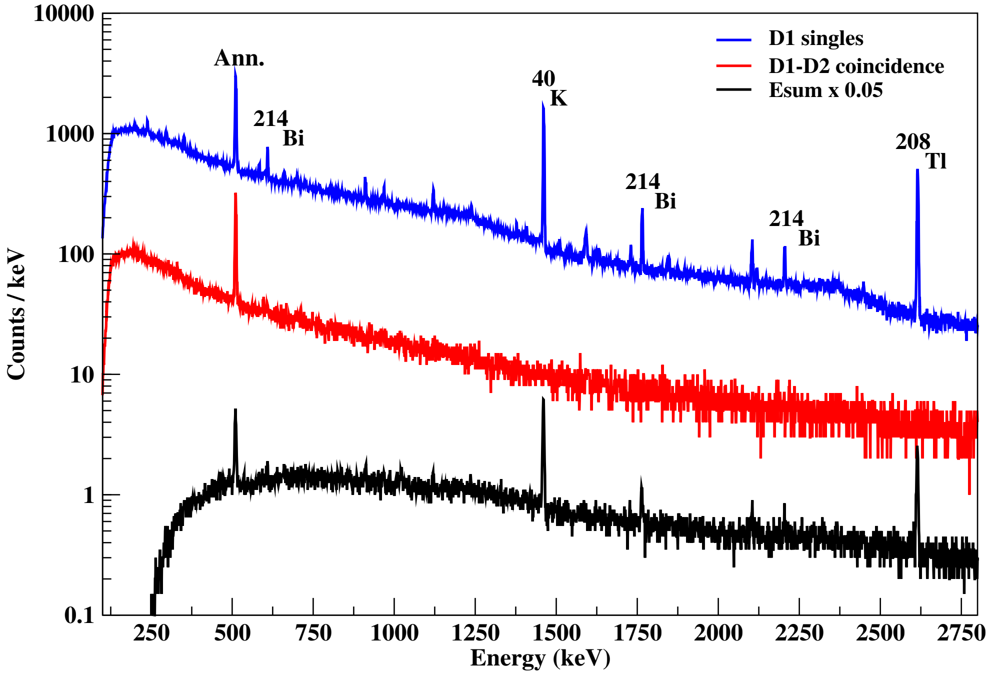

Figure 3.19: A comparison of the ambient background in D1 - singles and coincidence with D2 (i.e. $E_{D2}>0$). Sum energy spectrum $E_{sum}=E_{D1}+E_{D2}$, scaled by an arbitrary factor of 0.05 for better visibility, is also shown for comparison. All spectra have been time normalized to t = 7 d.

680 ± 20 cts/d, which clearly emphasizes improvement with coincident detection. However, higher statistics will be required to study 1022 - 1022 keV correlations. In the presence of ^{nat}Sn (~ 40 g), the background in the ROI was enhanced to 1919 ± 211 cts/y, giving the excess of 2 ± 1 cts/(keV.g.y) with ^{nat}Sn. In the absence of a positive signal, based on the present background, a lower limit on the half-life can be estimated using Eq. 3.6.

$$T_{1/2} > \frac{ln2\ N_A\ \epsilon_c\ a}{W\ k_{CL}}\sqrt{\frac{M\ t}{N_{bkg}\ \Delta E}} \tag{3.6}$$

where N_A is Avogadro's number, ϵ_c is the coincidence detection efficiency of a gamma ray, a is the isotopic abundance of the sample, W is the molar mass of the sample, M is the sample mass, t is the time of measurement (in y), N_{bkg} is the background index (in cts/(keV.g.y)), ΔE is the energy window defining the signal region of D1-D2 setup and k_{CL} is the number of standard deviations corresponding to a given confidence interval (C.L.). If one considers only the background from the source, N_{bkg} is estimated to be 2 ± 1 cts/(keV.g.y) from the tin data. As mentioned in the previous section, the ϵ_c is obtained from simulations for an optimal source geometry ($55\,mm \times 55\,mm \times 5\,mm$). Using the simulated ϵ_c, the $T_{1/2}$ sensitivity of the present D1-D2 coincidence setup for EC-β^+ in ^{112}Sn and $\beta^+\beta^+$ in ^{106}Cd has been estimated for different enrichment fractions and listed in Table 3.10. The ambient background has contributions from trace radioactive impurities, natural radioactive chains, and cosmic muons as well as muon-induced reactions. The external background can be minimized with suitable shielding. A moderate rock cover of ~ 500 m would suppress the muon flux by ~ 4 orders of magnitude [146]. Thus, the inherent background from the source

Table 3.10: The projected sensitivity for the half-life ($T_{1/2}$) of the present D1-D2 coincidence setup for ^{112}Sn (EC-β^+) and ^{106}Cd ($\beta^+\beta^+$) for $t_{data} = 1$ y. The isotopic abundance (a), total mass (M_0) and coincidence efficiency (ϵ_c) are also listed.

Source	a (%)	ϵ_c (%)	M_0 (g)	$T_{1/2}$ (68% C.L.) (y)	$T_{1/2}$ (90% C.L.) (y)
^{106}Cd	50	1.04	130	5.5×10^{19}	3.4×10^{19}
^{106}Cd	90	1.04	130	1.0×10^{20}	6.2×10^{19}
^{112}Sn	50	0.64	110	2.9×10^{19}	1.8×10^{19}
^{112}Sn	90	0.64	110	5.4×10^{19}	3.3×10^{19}

(trace impurities, neutron-induced reactions) will be a limiting factor; hence, the same has been used in the present estimation. Nevertheless, it is important to reduce the overall background. The use of larger detectors with an annular anti-compton shield would also improve the coincidence efficiency and reduce background [4]. In the present setup, it is proposed to augment the shielding by adding an active veto for muon and increasing passive shield thickness.

The present best limits for $T_{1/2}^{\beta^+\beta^+}$ (^{106}Cd) and $T_{1/2}^{EC-\beta^+}$ (^{112}Sn) are 2.3×10^{21} y [147] and 9.7×10^{19} y [114], respectively. From Table 3.10, it can be seen that an improvement in the background index by about a factor of 5 will be suitable to yield an improved limit for ^{112}Sn, while for ^{106}Cd further measures to improve the signal to noise ratio are essential.

3.6 Summary

The feasibility studies of rare decays like positron double beta decay modes for ^{112}Sn (EC-β^+)/^{106}Cd ($\beta^+\beta^+$) and ^{96}Zr β decay is presented. A simulation program has been developed using the GEANT4 tool to optimize Mϵ_c using a coincidence setup of 2/4 HPGe detectors with extended sources in close counting geometry. The optimization of Mϵ_c for β decay measurement in ^{96}Zr is done for four HPGe detectors (~33% relative efficiency each) setup with extended sources in a close geometry for 568-1091 keV gamma ray pair in the ^{96}Nb decay cascade. It is shown that for ^{96}Zr β decay, even in a four detector configuration, a significantly larger source mass is required to achieve the reported sensitivity. Present simulations for a four detector setup show the optimal source configuration to be 5 mm thick foils with a cross-sectional area of 40 mm×40 mm for front sources and 30 mm×20 mm for side sources. This corresponds to about 72 g of effective mass with 50% enrichment and can yield Mϵ_c of ~12-20 g-% for different gamma ray pairs, which is slightly better than the coincidence measurement reported earlier. The coincident detection efficiency of 511 keV gamma rays for source foil sandwiched between the detectors has been estimated using GEANT4. The source of size $55\,mm \times 55\,mm \times 5\,mm$ (thickness) was found to be optimal for 2 pairs of 511 keV gamma rays. The ambient background of the 2 detector setup with moderate Pb shielding is measured in coincidence mode at sea level. The coincident detection of 511 keV pair significantly improves the background in the region of interest. From background measurements with ~40 g of ^{nat}Sn, the sensitivity for $T_{1/2}^{\beta^+\beta^+}$ (^{106}Cd) and $T_{1/2}^{EC-\beta^+}$ (^{112}Sn) are estimated to be $\sim 10^{19}$ - 10^{20} y for 1 y of measurement time with enriched samples. Thus, coincidence measurements with the present two HPGe detector setup at moderate depth can be used to probe EC-β^+/ $\beta^+\beta^+$.

Chapter 4

Radiopurity Studies of Aut and BWH Rock Samples

Significant efforts are underway in India to set up an underground laboratory for rare event studies like double beta decay, dark matter, etc. In order to plan low background experiments, understanding the radiogenic backgrounds at the site from the surrounding rock is one of the crucial factors. The natural gamma ray background of a rock sample from the potential laboratory site in the Aut region of Himachal Pradesh (India) has been measured using the TIFR low background experimental setup (TiLES). The radiopurity of the Aut rocks was investigated and compared to the samples from BWH (Bodi West Hill), Tamil Nadu (India), the current designated site for the India-based Neutrino Observatory. The radioactivity levels of these rocks from the measured spectra of the natural gamma-ray background are presented.

4.1 Introduction

Recently, experimental investigations of physics beyond the standard model, such as neutrino oscillations, neutrinoless double beta decay (NDBD), dark matter search, etc., have attracted much attention worldwide [22, 148, 149]. These studies for rare events demand stringent background levels. The ultimate background levels (N_{bkg}) achieved in the region of interest are $4.0 \times 10^{-4}\,\mathrm{keV^{-1}kg^{-1}y^{-1}}$ for KamLAND-Zen NDBD experiment [150] and $8.5 \times 10^{-2}\,\mathrm{keVee^{-1}kg^{-1}y^{-1}}$ for XENON1T dark matter experiment [66]. It is important to note that minimizing the ambient background is a crucial aspect of rare event studies. Some of the significant sources of the background radiation are cosmic rays, long-lived primordial radionuclides ($T_{1/2} \sim 10^8$ - 10^{10} y), cosmogenic radionuclides ($T_{1/2} \sim$ days - years) and neutron-induced activity produced in and around the detector [22]. In order to suppress the cosmic muon background (by about 5 - 6 orders of magnitude), these experiments are located in underground laboratories, typically with a rock overburden of more than 500 m. In an underground laboratory, the ambient gamma and neutron background at the site and the background arising from penetrating (high energy) cosmic muons can be the limiting factors for the sensitivity of the experiment.

The gamma-ray background originates from natural radioactivity due to trace elements like ^{40}K, ^{232}Th, ^{235,238}U in the rock, and the neutron-induced activities of the constituents of the rock. The concentrations of these trace elements, and subsequently the associated gamma/neutron backgrounds, are known to exhibit geographical variation depending on local geological conditions. Amongst the natural gamma ray background, high energy γ-rays ($E \geq 2\,\mathrm{MeV}$) produced in the natural radioactivity chains of ^{238}U and ^{232}Th e.g. 2448 keV (^{214}Bi) and 2615 keV (^{208}Tl), respectively, are of significant concern. In India, driven by the interest in rare decay studies, a proposal for an underground laboratory has been initiated. A laboratory with about 1 km rock overburden is proposed in Bodi West Hills (BWH) of the Theni district in Tamil Nadu (Lat. North 9°57'47.65" and Long. East 77°16'22.55") [151]. Also, a small laboratory (approximately 5 m × 5 m × 2.2 m) has been set up at UCIL, Jaduguda, Jharkhand with a rock cover of 555 m inside a Uranium mine [146].

In the present work, another potential site with a reasonable rock overburden (~ 500 m) has been identified in the existing Aut tunnel, Himachal Pradesh (Lat. North 31.725° and Long. East 77.206°) to build an underground nuclear laboratory. In order to assess the feasibility of this site, it is necessary to study the radiogenic background that contributes to the background level for rare event experiments. The radiopurity studies of the Aut rock samples have been carried out using low background gamma-ray spectrometry. The concentrations of trace-level natural radioactive elements are determined and compared with the BWH rock sample data.

4.2 Experimental details

The Aut tunnel is a 2.9 km long tunnel built on the Manali-Chandigarh National Highway at Aut in Himachal Pradesh. The rock samples used in the present study were collected from the Aut tunnel with an average rock overburden of ~ 500 m (see Figure 4.1) and the BWH site (in Reference [151]). The latter sample was bored from a depth of ~ 30 m. The Aut rock is Dolomite type, while the BWH rock is Charnockite with a measured density of $\sim 2.93\,\mathrm{g/cm^3}$ and $\sim 2.89\,\mathrm{g/cm^3}$, respectively are shown in Figure 4.2. Several months after the collection, they were measured using two low background counting setups at TIFR (Mumbai) laboratory at sea level - TiLES (TIFR Low background Experimental Setup) [2] and a coincidence setup of two low background HPGe detectors (D1-D2) [152] described in chapter 2. Details of the samples, namely, type, mass, and counting time, are given in table 4.1. TiLES has a provision to further reduce the ambient background by employing a cosmic muon veto using plastic scintillators and continuous dry nitrogen flushing. However,

Table 4.1: Rock samples information studied in TiLES.

Site	Type	Sample ID	Mass (g)	counting time (days)
BWH	Charnockite	BWH0	32.1	24.9
		BWH1	16.1	11
Aut	Dolomite	AUT0	27.5	23.4
		AUT1	23.9	17.3
		AUT2	22.7	13.7
-	-	BKG	-	69

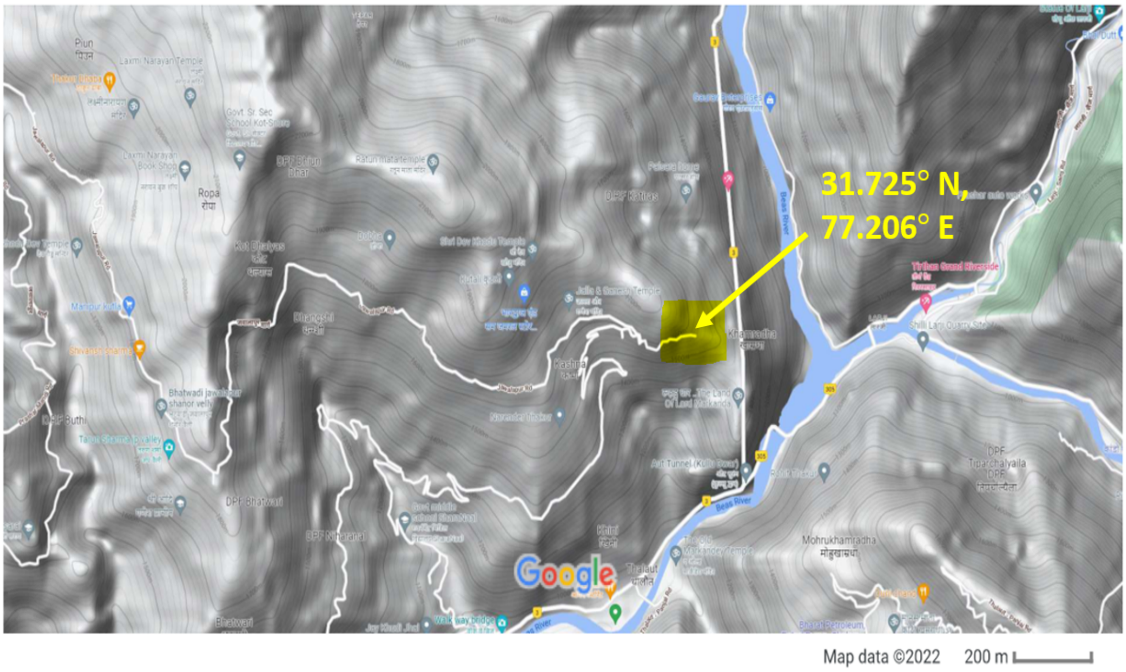

Figure 4.1: A Google map of the study area.

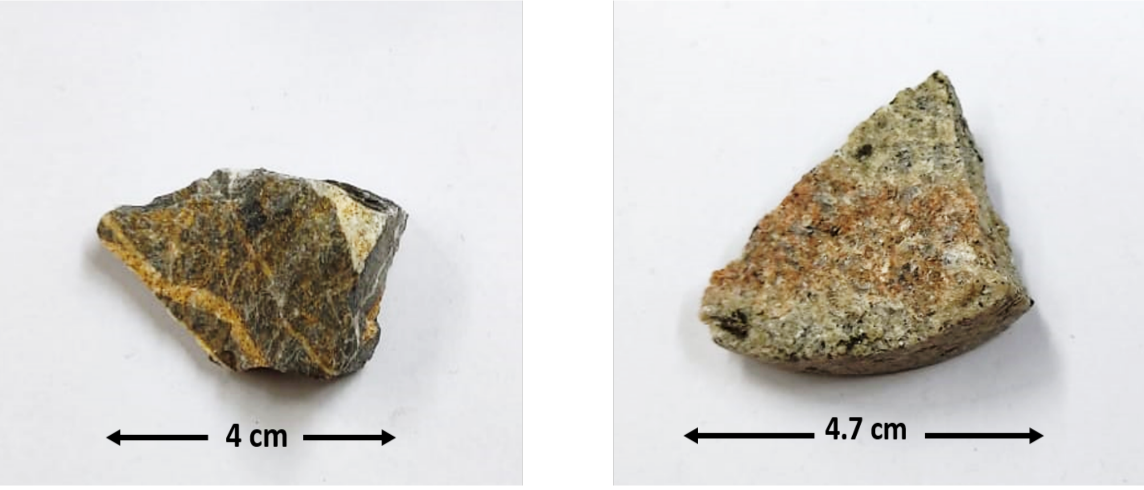

Figure 4.2: Typical images of the rock samples used in this study: On the left from the Aut site. On the right from the BWH site.

the cosmic muon veto and dry nitrogen flushing were not used for the present measurements as the samples had sufficiently high activity compared to the ambient background as well as to facilitate frequent sample changes. The sample was kept at $d \sim 10\,\text{mm}$ from the face of the detector on a perspex plate placed with a thickness of $\sim 1\,\text{mm}$. The sample mounting geometry was kept fixed for all the radiopurity measurements. The optimized geometry of TiLES [2] and D1-D2 [132] has been utilized to simulate the detector response. It should be mentioned that the systematic errors in the simulated efficiencies of the optimized models for TiLES and D1/D2 are 5 %, and 8 %, respectively. Total uncertainties quoted include all contributions: statistical, systematic (due to detector modeling), and coincident summing. Data were recorded using a 14-bit, 100 MHz CAEN 6724 commercial digitizer using the trapezoidal filter for pulse height determination. The digital parameters were optimized to achieve the best energy resolution. For both setups, the optimum trapezoidal filter settings, namely, input signal decay time (T_{decay}), trapezoidal rise time (T_{rise}), and trapezoidal flat top time ($T_{flattop}$) were set at 50 μs, 5.5 μs, and 1.3 μs, respectively. The typical resolution at 1460 keV was $\sim$ 2.6 keV in TiLES and $\sim$ 3.5 keV for D2. In the case of the D1-D2 setup, the data were acquired both in singles and coincidence mode with a timing window of $\pm\,1\,\mu$s. The data were saved and analyzed offline using ROOT [128] and LAMPS [133] software. The energy calibration was obtained using standard gamma-ray sources before the measurement and monitored with known background lines over an energy range of 120 - 2615 keV. The observed drifts were less than 1 keV over an extended period of one year. The dead time was monitored with a standard 10 Hz pulser and was found to be negligible ($<$ 0.1%).

The rock samples were counted in a compact geometry to attain a higher count rate. The photopeak efficiencies (ϵ) for various gamma rays in each rock sample were obtained using the GEANT4-based simulation program [127] for respective counting configurations. Since the rocks were of irregular shape, the geometry of the sample was simulated by approximating the closest regular shapes corresponding to the sample volume. The material composition was implemented by defining the fractional mass for each element, mainly Si, Mg, Ca, C, and O, which is found in terrestrial rocks. Modeling of the geometry of the samples was realized using cuboidal and sector shapes for AUT0 and BWH0 rock samples, respectively, as shown in Figure 4.3. The gamma rays were assumed to originate from trace impurities uniformly distributed within the sample. For each energy, 10^6 (1 M) gamma rays were generated within the sample isotropically, and consequently, statistical errors in simulated photopeak efficiencies were negligible ($<$ 1%). Further, the uncertainties in the detection efficiency due to variations in rock dimensions about mean values were estimated. Since the largest linear

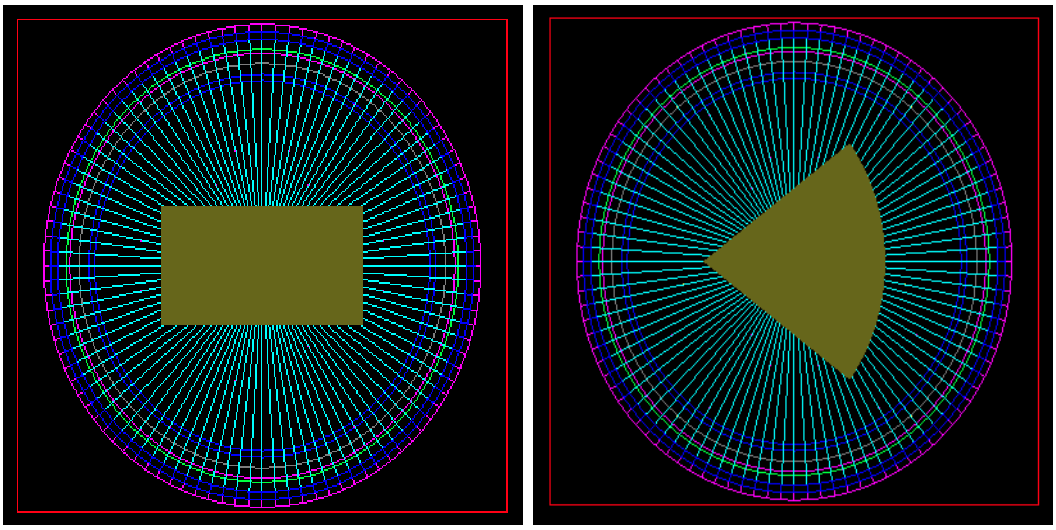

Figure 4.3: Visualization of a top view of the simulated rock geometry in GEANT4. AUT0 (left) and BWH0 (right) are mounted on the perspex plate in the front of HPGe detector.

dimension of both samples was smaller than the detector crystal size, only the variation in thickness is expected to have a pronounced effect on the efficiency, as discussed in chapter 3. The thickness variation over the sample size was found to be 8.1 - 8.6 mm for AUT0 and 9 - 12 mm for BWH0. In the simulation, different shapes were generated corresponding to different thicknesses by appropriately modifying the cross-sectional area to keep the volume constant. The ϵ_γ is taken as an average value of ϵ for different shapes, while the error in the efficiency is calculated as $(\epsilon_{max}$-$\epsilon_{min})/2$. The overall observed spread in efficiency due to shape variation was $< \pm 5\,\%$, for the energy range of interest ($E_\gamma = 186 - 2615\,\mathrm{keV}$). In the first step, a long gamma ray background was measured to examine any difference in the background level prior to and after the measurement of rock samples. Figure 4.4 shows the background measured in TiLES (with the perspex sample mounting plate) for a total duration of 69 d, acquired at different times over a period of about 7 months. Typically, the integrated background count rate (without nitrogen purging and active veto) in the energy range of 40-2700 keV normalized to crystal mass was $7 \times 10^4\,\mathrm{d^{-1}kg^{-1}}$. The ambient gamma ray background has been measured, and the background count rates have been determined to estimate the minimal detected activities (A_D) of several natural radionuclides. The minimum detectable counts (N_D) was estimated using Currie's method [140] as given in

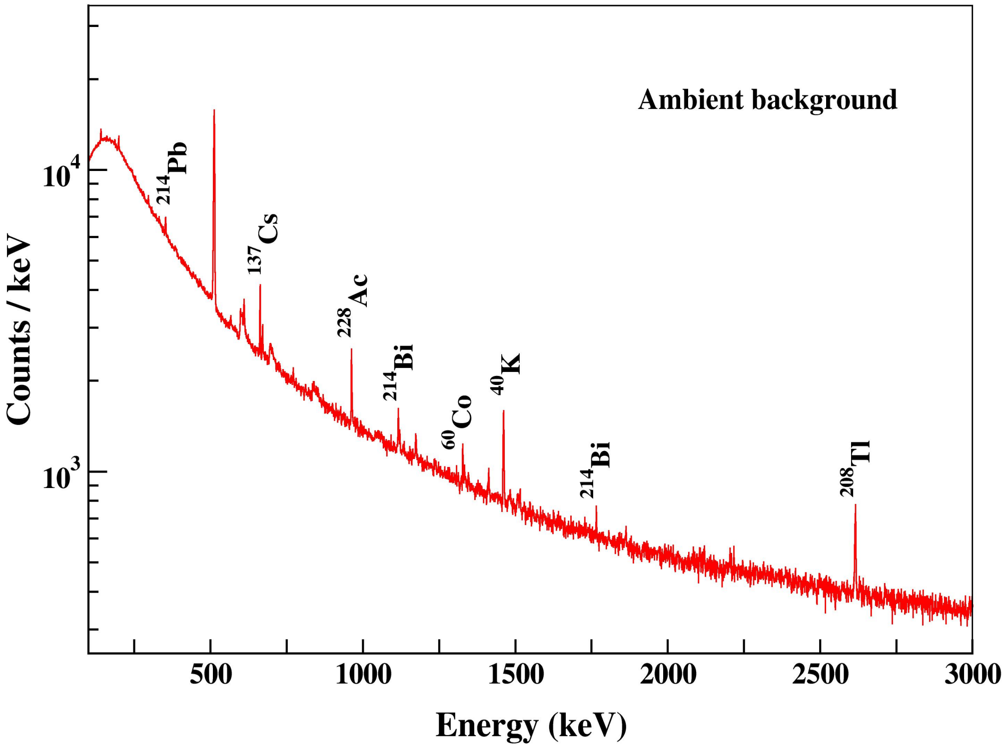

Figure 4.4: A typical γ ray spectrum of the ambient background in the TiLES, where the prominent gamma rays are labeled (counting time $t = 69\,\mathrm{d}$).

Eq. 2. The measured background arises mainly from the radioactivity of ^{232}Th, ^{40}K and impurities such as ^{137}Cs, ^{60}Co. In addition, some gamma rays were observed from the neutron interactions in the germanium crystal.

4.3 Analysis and results

A comparison of gamma ray spectra of the AUT0 and BWH0 rock samples in TiLES is shown in Figure 4.5 along with the ambient background. Compared to the ambient background,

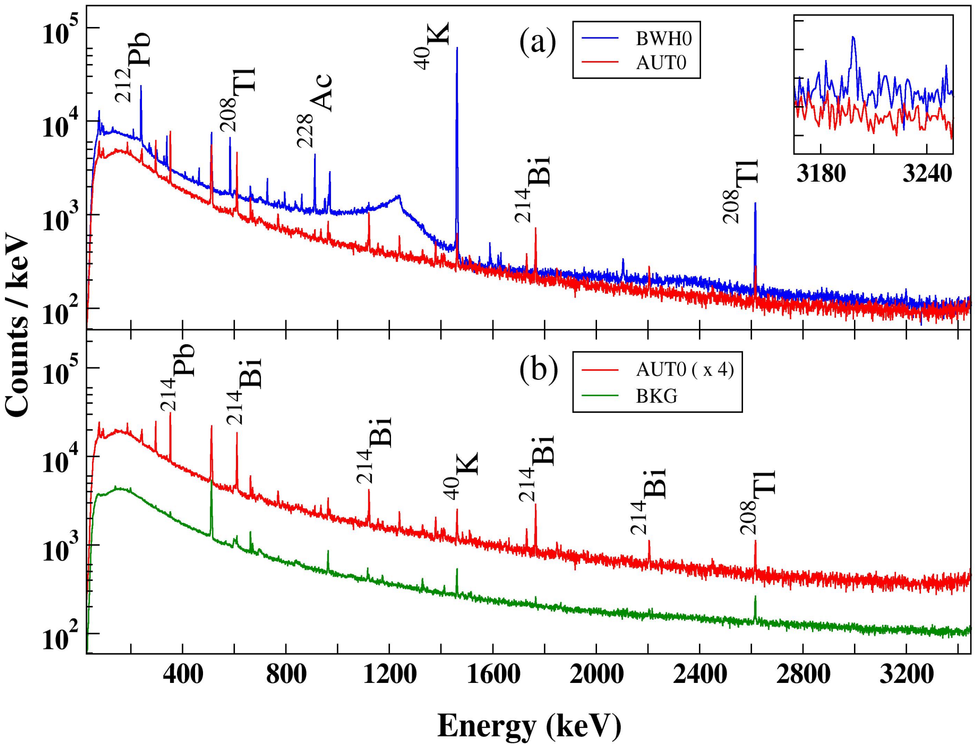

Figure 4.5: Gamma ray spectra measured in TiLES for a) AUT0 (red line) and BWH0 (blue line), b) ambient background (green line) and AUT0, scaled by an arbitrary factor of 4 for better visualization. The inset in the top panel shows the presence of the sum energy peak at 3197.7 keV in the BWH rock. All the spectra are normalized to $t = 23.4$ d.

the rock spectra are dominated by gamma lines from the ^{238}U and ^{232}Th decay chains. The high energy gamma rays from ^{208}Tl (end product in ^{232}Th decay chain) - 2614.5 keV ($I_\gamma = 99.75\,\%$) are of particular concern. A sum energy peak at 3197.7 keV, arising from the coincident summing of 2614.5 and 583.2 keV, is clearly visible in the BWH0 spectrum but not observed in the AUT0 spectrum, thereby revealing the higher amount of ^{208}Tl in the latter. The BWH0 also shows a strong peak at 1460.8 keV, indicating a large amount of

^{40}K in the rock. This also results in a significantly enhanced background at lower energies, $E < 1500$ keV, for the BWH0 as compared to the AUT0. Although many gamma rays from ^{232}Th and ^{238}U decay chains are visible, not all could be considered for trace impurity analysis. Some of the gamma rays are mixed from different radionuclides - for example, the observed gamma line at 242.6 keV has a contribution from ^{214}Pb in ^{238}U decay chain (242.0 keV) and ^{224}Ra in ^{232}Th decay chain (241.9 keV), similarly for 351.9 keV (^{214}Pb, ^{211}Bi), 185.9 keV (^{226}Ra, ^{235}U), etc. It should be mentioned that other samples of Aut rock

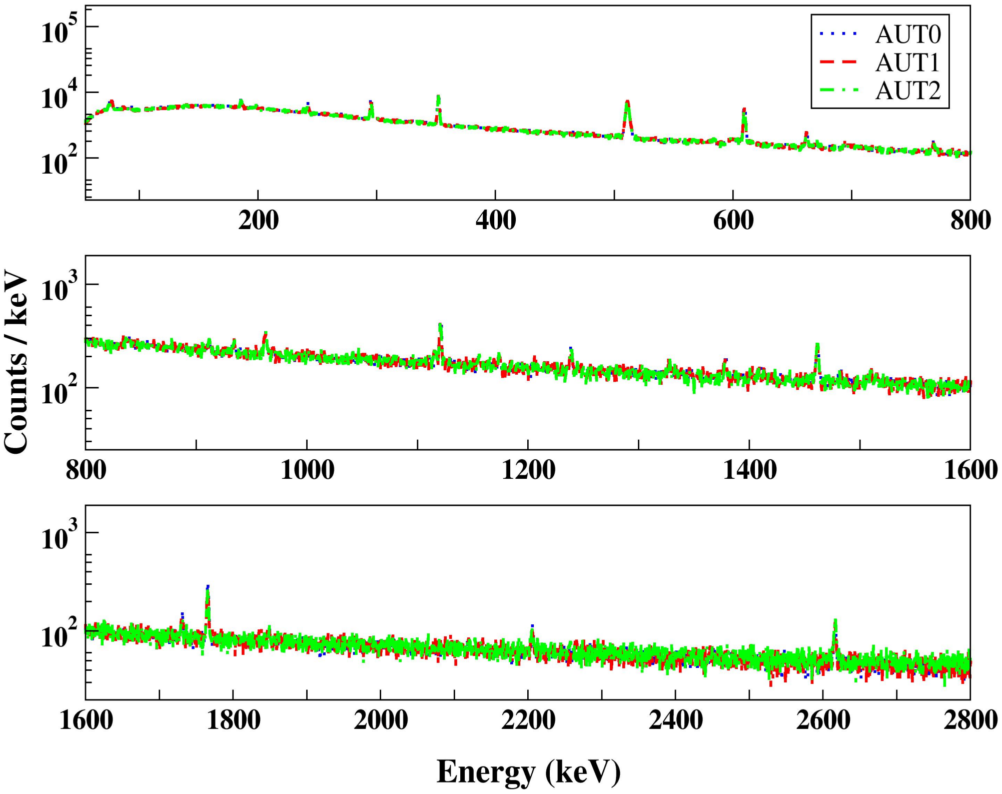

Figure 4.6: Gamma ray spectra of various Aut rock samples measured in TiLES. All the spectra are normalized to $t = 13.7$ d.

were also measured for different counting times as listed in Table 4.1 and shown in Figure 4.6. All samples showed similar background levels and activities within measurement uncertainty. Therefore, the largest Aut rock sample with gamma rays that could be unambiguously assigned to a particular nuclide was considered for further analysis. The photopeaks of interest were fitted with a Gaussian + background (second-order polynomial) to extract the peak area. The specific activity, that is, activity per unit mass A_γ corresponding to a given transition of the radionuclide, was determined using Eq. 2. In a close counting geometry, the coincident summing of multiple gamma rays in the decay cascade is an important aspect that must be considered. Therefore, the branching ratio I_γ of gamma lines was corrected for a coincident summing estimate of 2 gamma cascades and listed in Table 4.2. While detailed simulations are essential for multi-stage decay cascades, a simple estimation can be done for a two gamma cascade $2 \xrightarrow{\gamma_2} 1 \xrightarrow{\gamma_1} 0$ as shown in Figure 4.7. If ϵ_i^{tot} is the total detection probability of γ_i (i.e., Compton and Photopeak), then the loss due to the coincident summing (I_1^{sum}, I_2^{sum}) to the intensity of γ_1 and γ_2 ($I_{\gamma 1}$ and $I_{\gamma 2}$, respectively) can be estimated as

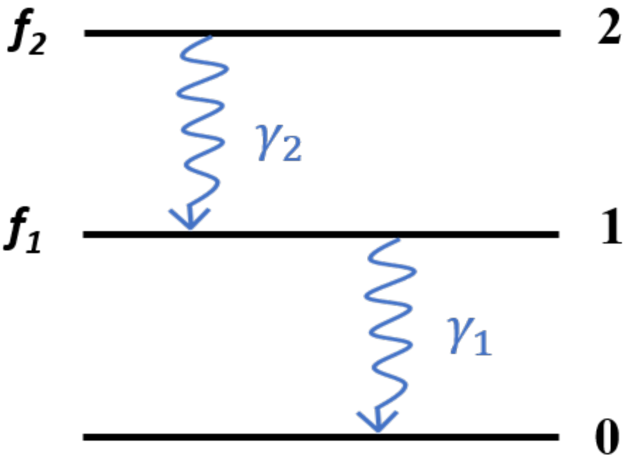

Figure 4.7: Simplified level scheme for two gamma cascades.

$$
\begin{aligned}
I_1^{sum} &= \epsilon_2^{tot} \cdot p_1 \cdot p_2 \cdot f_2, \\
I_2^{sum} &= \epsilon_1^{tot} \cdot p_1 \cdot p_2 \cdot f_2
\end{aligned}
\tag{4.1}
$$

Where p_1 and p_2 are the gamma decay probabilities of levels 1 and 2, respectively, and f_2 is the feeding fraction for level 2. The effective net intensity for γ_i can be written as

$$I_i^{net} = I_{\gamma i} - I_i^{sum}. \tag{4.2}$$

Here, both gamma rays are assumed to be emitted isotropically, neglecting angular correlations. For lines 238.6, 1377.7, 1729.6, 1764.5, 1847.4, and 2204.1 keV top feeding fraction is small, and estimated coincidence correction is small ($<1\%$); therefore, it can be used without summing correction. While 609.3, 911.2, 969.0, and 1120.3 keV has been corrected for coincidence summing. For the simplification, in the case of 609.3 keV, E_{coin} which is taken as the average ($<E>$=1120.3 keV) for all the gamma lines in coincidence with 609.3 keV. All the top feeding has been assigned to it (refer to Table 4.2). However, in the case of 911.2 and 969.0 keV, the entire top feeding is assigned to arise from 463.0 keV, for ease of calculation. It is evident that the coincident summing probability of 3 or more gamma rays is insignificant. However, the complex decay cascades with multiple parallel decay branches are not considered for estimating elemental concentration. The summing correction of each listed gamma line in Table 4.3 was estimated, and coincident summing was neglected if the summing correction was significantly less than the statistical error. For the radiopurity analysis, the summing corrections (wherever applicable) were found to be 4 - 16%. In the cases where no measurable activity could be observed above the ambient background, the upper limit on the specific activity (N_D) was estimated from the minimum detectable counts using Eq. 2.7. The extracted specific activities for the AUT0 and BWH0 samples are listed

Table 4.2: Gamma rays emitted from natural radionuclides in decay cascade.

Nuclide	E_γ (keV)	List of gammas in coincidence
^{212}Pb	238.6	176.68
	295.2	—
^{214}Bi	609.3	1665.9, 806.2, 934.0, 1238.1, 1509.2, 1385.3, 768.4, 1281.0, 1401.5, 1120.3, 1408.0, 1583.2, 1155.6
^{228}Ac	911.2	562.5, 755.3, 154, 674.8, 463.0
	969.0	562.5, 755.3, 154, 674.8, 463.0
^{214}Bi	1120.3	609.3
	1377.7	—
	1729.6	—
	1764.5	—
	1847.4	—
	2204.1	—

in Table 4.3. Due to its small isotopic abundance, the concentration of ^{235}U could not be determined in the present work. The mean specific activity ($< A_\gamma >$) is obtained by a weighted average over measured specific activities of different gamma rays/daughter nuclides in the given decay chain. In order to extract the concentrations of the parent radionuclides (^{232}Th and ^{238}U), the data were analyzed under the assumption of secular equilibrium within samples, the atomic fraction A_T of the trace radio-impurity in the rock sample was computed using Eq. 2.9. For the BWH0 sample, the molar mass was determined from the rock composition obtained from the Secondary Ion Mass Spectroscopy (SIMS) results reported in

Table 4.3: Observed specific activities for different radionuclides in the AUT0 and BWH0 rocks

Parent Radionuclide	Daughter Radionuclide	E_γ	E_{coin}	AUT		BWH	
		(keV)		A_E (mBq/g)	$< A_E >$ (mBq/g)	A_E (mBq/g)	$< A_E >$ (mBq/g)
^{40}K		1460.8	—	<1	<1	1064 (68)	1064 (68)
^{232}Th	^{212}Pb	238.6	—	0.50 (7)	0.50 (6)	15 (1)	14.7 (6)
	^{228}Ac	911.2	463.0	0.5 (2)		15 (1)	
		969.0	463.0	—		14 (1)	
^{238}U	^{214}Pb	295.3	—	8.2 (5)	8.2 (3)	1.2 (2)	1.2 (1)
	^{214}Bi	609.3	1120.3	7.7 (4)		1.5 (2)	
		1120.3	609.3	8.1 (5)		—	
		1377.7	—	12 (2)		—	
		1729.6	—	13 (2)		—	
		1764.5	—	7.8 (7)		0.9(3)	
		1847.5	—	14 (3)		—	
		2204.1	—	10 (1)		—	

Ref. [129]. It should be mentioned that the molar mass of the rock was determined using molecular percentages of individual elements provided by SIMS measurements. Further, in the case of the AUT0 sample, since the rock composition was not available, the molar mass was assumed to be identical to that of the BWH0. This is a reasonable assumption as the molar mass is not expected to vary significantly for different types of rocks. The concentrations of the trace radio-impurities for both the rock samples are listed in Table 4.4. The comparison of trace element concentrations in AUT0 and BWH0 in Table 4.4 shows that the ^{40}K content in the AUT0 is significantly lower by a factor of $\sim$ 1000. The content of ^{232}Th is also lower in the AUT0 by a factor of $\sim$ 28, while that for the ^{238}U is higher by a factor of $\sim$ 7. The concentrations of ^{40}K and ^{232}Th in the BWH0 rock obtained in the present study are similar to earlier reported values [129], namely, 2520 ppb (by SIMS) and 224 ppb (by Inductively Coupled Plasma Mass Spectroscopy, i.e., ICPMS), respectively. However, for ^{238}U, the present value is significantly lower than that reported with ICPMS, namely 60 ppb [129]. It should be pointed out that radiopurity measurements reflect the average over a larger finite sample size as compared to the ICPMS. Hence, the observed difference may arise due to the non-homogeneous distribution of radionuclides within the rock. Measurements also probed the variation in trace impurity content on different BWH/Aut samples from the exact location. While no differences were observed in the spectra at the measured level of sensitivity for three different Aut rock samples ($t \sim 2$ weeks), two BWH rock samples showed $\sim$ 33 % and $\sim$ 17 % variation for ^{232}Th and ^{40}K, respectively.

Table 4.4: Trace radioimpurity concentrations in AUT0 and BWH0 rocks.

Sample	Parent Radionuclide	Concentration (ppb)
AUT0	^{40}K	<2
	^{232}Th	12 (1)
	^{238}U	60 (2)
BWH0	^{40}K	2179 (139)
	^{232}Th	338 (14)
	^{238}U	9 (1)

As a result of lower levels of ^{40}K and ^{232}Th in AUT0, the yield of the high energy gamma rays of 1460.8 keV and 2614.5 keV is significantly reduced as compared to the BWH0. The higher ^{232}Th content in BWH0 is also reflected in the presence of 3197.7 keV gamma ray (see inset of Figure 4.7). The presence of high-energy gamma rays and the corresponding Compton background leads to an overall enhancement in the background at lower energies, i.e., in the region of interest relevant to low background experiments ($E \sim 2\,\text{MeV}$). Thus, the smaller ^{232}Th content in the Aut rock appears to be advantageous.

The observed specific activities in the AUT0 (see Table 4.3) can be compared with those at the well-established underground facility LNGS, which also has dolomitic limestone rock as well as the worldwide average. The measured average specific activities in LNGS [54] are 26 (2) mBq/g for ^{40}K, 1.5 (1.0) mBq/g for ^{232}Th and 1.8 (1.0) mBq/g for ^{238}U. Thus, the Aut rock appears to have lower levels of both ^{40}K and ^{232}Th, while ^{238}U content is somewhat higher. It is important to note that the trace radioactive element content in Aut rock is significantly lower than the worldwide average, namely, 400, 30, and 35 mBq/g for ^{40}K, ^{232}Th and ^{238}U, respectively [9]. The neutron flux at the BWH site is estimated to be 2.76 (47) $\times$ 10^{-6} n cm^{-2} s^{-1} with 60 ppb for ^{238}U and 224 ppb of ^{232}Th [129] trace impurities in the rock. The low energy neutron flux produced by spontaneous fission and (α,n) reactions in the rocks is dominated by ^{238}U. The measured concentration of ^{238}U in the AUT0, 60 (2) ppb, is similar to that used for the neutron flux estimation at the BWH site (namely, 60 ppb). Consequently, the expected neutron flux at the Aut site will be similar to that for the BWH site, i.e., $\sim 3 \times 10^{-6}$ n cm^{-2} s^{-1}. It should be noted that this estimate is comparable to other underground laboratories, although concrete wall contributions will have to be taken into consideration at the actual site. Thus, the Aut site is expected to have an overall lower gamma ray background and similar neutron background as compared to the BWH and subsequently appears to be a suitable site for laboratory from radioactive background considerations.

4.4 Summary

The radiopurity studies of a rock sample from the potential underground laboratory site in the Aut tunnel have been carried out using the TiLES. The concentration of ^{40}K in Aut rock is lower by a factor of $\sim$1000 compared to the BWH rock sample. The rocks that surrounded the Aut site were characterized by very low specific activities of trace impurities ^{232}Th and ^{238}U as 0.50 (6) and 8.2 (3) mBq/g, respectively. Compared with BWH rock, the Aut rock appears to have a lesser amount of ^{232}Th and a somewhat higher amount of ^{238}U. It is important to note that Aut rock trace impurity concentrations are considerably lower than the respective worldwide average values. In general, the results of this study confirm that the ambient gamma ray background level at Aut is expected to be lower than the BWH, and the energy spectrum of background gamma radiation of the Aut site within the studied energy range is defined mainly by the composition of the surrounding rock. Hence, the Act appears to be a suitable site for the laboratory from radioactive background considerations. The obtained results can be used to estimate the background contribution from the Aut cavern for the rare decay experiments.

Chapter 5

Neutron Activation Studies in Aut and BWH Rock Samples

The underground laboratories with sufficient rock coverage provide a low radioactive background to house the rare decay experiments. Production of neutrons in such underground laboratories is the dominant source of background which significantly affects the sensitivity of the experiments. In order to assess the neutron-induced gamma background in rock samples of Aut and BWH sites, fast neutron activation studies have been carried out on both the Aut and BWH rock samples at the Pelletron Linac Facility, Mumbai. Neutron-induced reactions have been investigated, emphasizing long-lived activities, which can be a limiting factor for rare event experiments.

5.1 Introduction

The neutron background is most difficult to suppress due to its extensive energy range and is crucial to understand for reducing the background levels. The origin of neutron background is usually categorized into two primary sources - low energy neutrons ($E_n < 20$ MeV), originating from the spontaneous fission of uranium and (α, n) reactions in the rock, and very high energy neutrons ($E_n > 1$ GeV) produced by muon-induced interactions in the rocks or materials surrounding the detector. For depths from 10 to 100 m of rock overburden, the flux of high energy neutrons is expected to be smaller by a factor of 10^2 - 10^3 as compared to the low energy neutrons [28, 153]. The neutron flux originating from muon-induced interactions is highly penetrating and depth-dependent. However, deploying layers of thicker neutron shielding can reduce the average neutron energy to ≤ 20 MeV, giving rise to a substantial gamma ray flux. The interaction of these secondary lower energy neutrons with detector setup produces high energy gamma rays giving rise to the background for double beta decay experiments [154]. In underground laboratories, the low energy neutron background from the natural radioactivity at the site contributes heavily to the local neutron flux and hence is crucial to understand. The background arising from the inelastic scattering of neutrons (n, n$'\gamma$) and neutron-capture (n, γ) with the detector or surrounding materials can also lead to the production of high-energy gamma rays. The absorbed neutrons can interact within the detector setup, and the subsequent nuclear de-excitation leads to direct energy deposition in the detector, causing significant deterioration of background levels. Neutron background in rare event studies is reported as the main background that can affect the experiments' sensitivity and outcome. Surface exposure of Ge detectors used for double beta decay experiments is a serious concern due to the production of ^{57}Co, ^{54}Mn, ^{65}Zn, ^{60}Co and ^{68}Ge from spallation reactions caused by high energy cosmogenic neutrons at the earth's surface [155]. Radiogenic neutron background is the most irreducible background for direct dark matter detection experiments, which can induce nuclear recoils similar to WIMPs (Weak Interacting Massive Particles) [21]. Any impurities in the detector materials could be potential sources of neutron-induced background. The neutron-activated reaction products can have wide-ranging half-lives ($\sim$ min to $\sim$ years), and the contribution of long-lived activities is difficult to mitigate. Short-lived activities can be avoided by storing the material for prolonged periods in underground locations; however, long-lived activities are highly undesirable. In addition to situating the experiment underground, studying the total neutron flux and contribution of neutron-induced background is essential for the low background experiments. From the results of radioactive contamination and estimation of neutron flux, a shielding strategy can be designed using Monte Carlo simulations to meet the background required for the planned experiment [58, 129, 146]. In the present work, the fast neutron activation studies of the Aut and BWH rock samples have been carried out in the Pelletron Linac Facility, Mumbai, at two irradiation energies of 12 and 22 MeV. It should be mentioned that radio-impurity studies of all pristine rock samples, including the site information, are discussed in chapter 4. The gamma ray spectra of the irradiated sample were investigated using low-level Ge-spectroscopy systems for both short and long-lived activities. In comparison, emphasis has been made on long-lived activities, which can be the limiting factor for the sensitivity of low background experiments. The impact of observed high-energy gamma rays and residual activity after a cooldown time of a month will be discussed. The comparison of neutron-induced specific activity for dominating reaction products in BWH (INO) and Aut rock samples will be presented.

5.2 Experimental details

Neutron activation measurements were performed at the fast neutron irradiation setup at the Pelletron Linac Facility (PLF), Mumbai. The rock sampling information is listed in Table 5.1. Fast neutrons having a broad energy range upto $\sim$ 20 MeV were produced at the irradiation setup of the Pelletron Linac Facility, Mumbai, using ^{9}Be(p,n)^{9}B reaction (Q = -1.85 MeV) with $\sim$ 5 mm thick ^{9}Be target [5]. The maximum proton beam energy (22 MeV) was chosen to cover the energy range of neutron spectra originating from fission and (α,

Table 5.1: Rock samples information counted in low background setups.

Site	Sample	Mass	Setup
Aut	AUT1A	10.6	TiLES
	AUT4E	6.7	TiLES, D1-D2
BWH	BWH2A	8.2	TiLES
	BWH2B	5.5	TiLES, D1-D2

n) reactions in the rocks [129]. Irradiation at lower proton beam energy (12 MeV) was carried out for independent verification of some channels by comparison of relative yields. Although the primary interest in the present work was to study the Aut rock samples, neutron activation for BWH rock was also carried out for comparison at one energy. The neutron flux was estimated using the ^{56}Fe(n,p)^{56}Mn reaction [156]. For this purpose, the ^{nat}Fe foils ($\sim 4.5 - 10$ mg/cm^2) were placed in the front and back of the rock samples during each irradiation. The activity of ^{56}Mn in the irradiated iron foils was extracted from the yield of 846.8 keV gamma ray, which was measured with the D2 or TiLES. The yield for 846.8 keV was corrected for losses due to coincident summing in the detector with 1810.7 keV ($I_\gamma = 26.9\%$) or 2113.1 keV ($I_\gamma = 14.2\%$). The corrections due to coincident summing from other low-intensity gamma rays (branching ratio $< 1.5\%$) are found to be negligible. The energy averaged neutron flux $< \phi_n >$ is obtained using relation

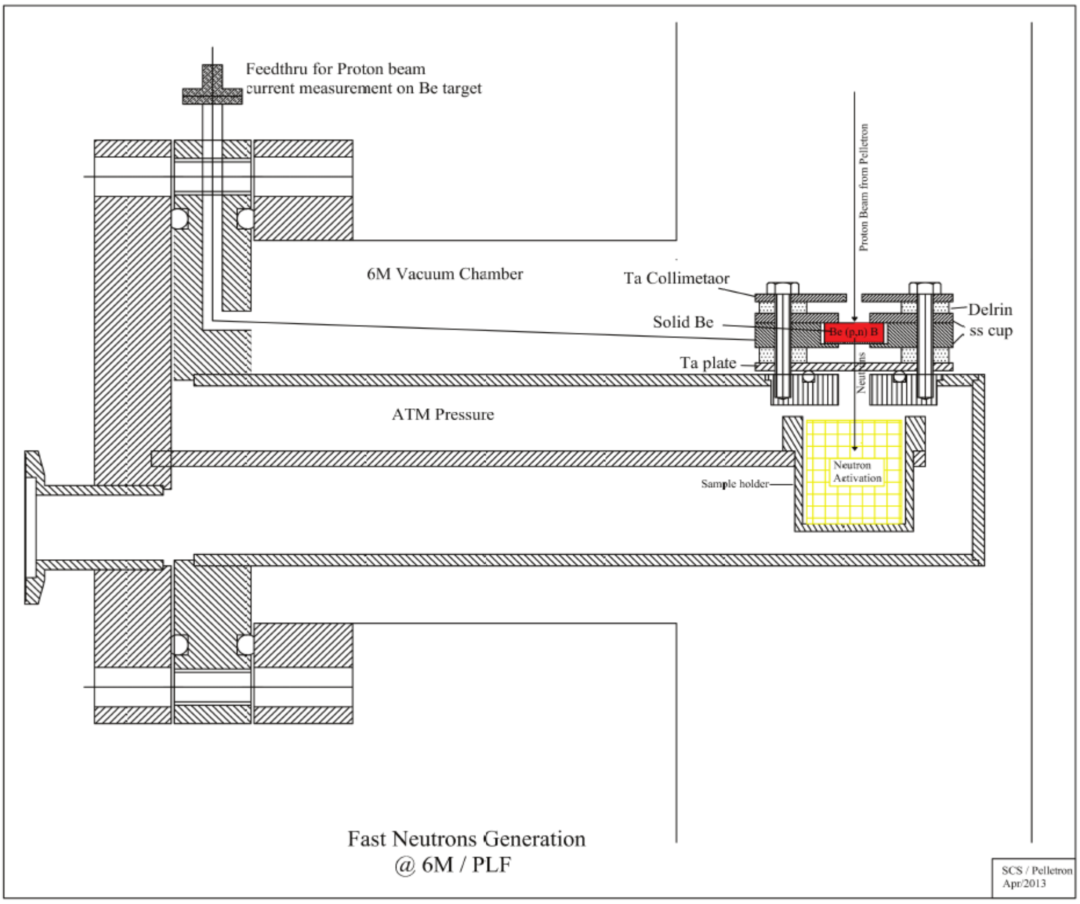

Figure 5.1: A schematic of the neutron irradiation setup shown with solid production target (in red color) and Teflon sample holder (in yellow color) [5].

$$< \phi_n >= \frac{\sum_{E_n} \sigma(E_n)\phi_n(E_n)dE_n}{\sum_{E_n} \sigma(E_n)dE_n} \tag{5.1}$$

where $\sigma(E_n)$ is the neutron-induced reaction cross section and $\phi_n(E_n)$ is the neutron flux per unit energy at E_n. The numerator is derived from the measured ^{56}Mn activity with appropriate corrections for the decay during irradiation and cooldown time. The cross-sections for the ^{56}Fe(n,p)^{56}Mn reaction were taken from the ENDF/B-VIII.0 library [157]. The error in $< \phi_n >$ is largely limited by the statistical error in extracting the 846.8 keV gamma ray yield. It should be noted that the uncertainties in the neutron cross-sections have not been considered in the final errors. Table 5.2 gives the details of the rock samples and irradiation (average proton beam current, irradiation time t_{irr}, etc.) The irradiated rock samples and iron foils were removed from the irradiation setup after a sufficient cool-down time t_c ($\geq$ 1-2 hr). Hence, some of the short-lived activities could not be measured. The offline counting of the irradiated rock samples was carried out in a compact geometry in both setups, and reaction products were identified by their characteristic gamma rays. In the case of low energy irradiation, where both BWH and Aut rock samples were irradiated simultaneously for optimal use of the beam time, priority for counting in the offline setups was given to the irradiated Aut samples. Spectra of rock samples were recorded at different cool-down times (t_c) to track activities with varying half-lives, namely, $\sim$ mins to few $\sim$ days. The gamma ray spectra were measured using two low background counting setups at TIFR (Mumbai) at sea level - TiLES (TIFR Low background Experimental Setup) [2] and a coincidence setup of two low background HPGe detectors (D1-D2) [152] (details are described in chapter 4). The D1-D2 setup was mainly used to detect coincident gamma rays to confirm nuclide identification.

Table 5.2: Details of the irradiation of rock samples together with maximum neutron energy (E_n) and estimated energy averaged neutron flux.

Sample	E_p (MeV)	$< I >$ (nA)	t_{irr} (h)	E_n (MeV)	$< \phi_n >$ (10^6 n cm^{-2} s^{-1} MeV^{-1})
AUT1A	22	136	15.5	19.9	1.9 (2)
AUT4E BWH2B	12	148	16.0	9.9	0.51 (4)

5.3 Analysis and results

Figure 5.2 and 5.3 show gamma ray spectra of the irradiated rocks at $E_p = 22$ and 12 MeV, respectively. Various observed reaction channels such as (n,γ), (n,p), (n,α), and (n,2n) are listed in Table 5.3 together with respective $T_{1/2}$ and prominent gamma rays. The threshold neutron energy E_{th} corresponding to $\sim$ 1 μb cross-section is also listed in the table.

In the AUT1A spectrum, the dominant contribution at small t_c (i.e. $\leq 2-3$ days) comes from the ^{24}Na activity ($T_{1/2} = 15$ h). The high energy gamma rays, namely, 1368.6 keV and 2754.0 keV, and the respective single/double escape peaks are clearly visible in the figure. It is important to note that the associated Compton background also enhances the low-energy background. In addition, single/double escape peaks of ^{24}Na may add up to summed peaks which can contribute to the high energy background depending upon the detector

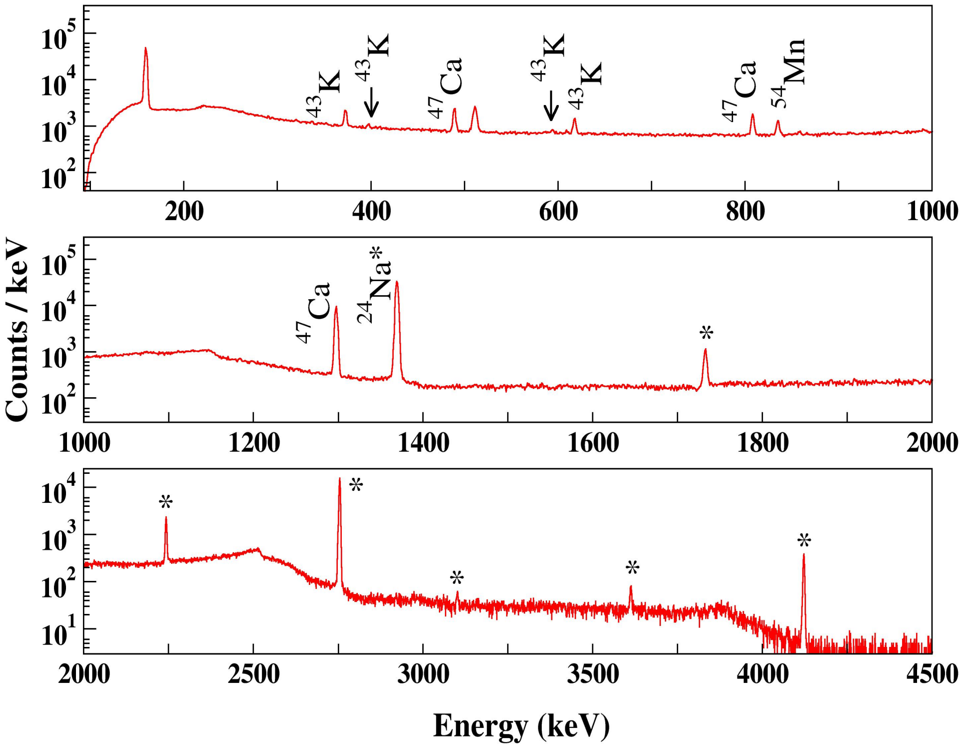

Figure 5.2: Gamma ray spectrum ($t = 1$ d) of the irradiated AUT1A rock ($E_p = 22$ MeV) after $t_c = 5$ d. Various ^{24}Na gamma rays and associated single/double escape peaks are indicated (*).

configuration. The ^{24}Na can be formed either via ^{23}Na(n,γ) or ^{24}Mg(n,p) or ^{27}Al(n,α). With fast neutrons, ^{23}Na(n,γ) is less probable as compared to ^{24}Mg(n,p) or ^{27}Al(n,α). However, the relative contributions of these two channels will depend on the actual rock composition, namely, Al/Mg content. It is seen that the BWH rock contains more aluminum than magnesium (from the SIMS data). The Aut rock also shows the presence of ^{42,43}K and ^{47}Ca originating from the Calcium isotopes present in dolomite rock. These reaction products are relatively short-lived ($T_{1/2} \leq$ few days) and give rise to low energy gamma rays, $E_\gamma < 1300$ keV, during the decay. The long-lived activities ^{22}Na ($T_{1/2} = 2.6$ y) and ^{54}Mn ($T_{1/2} = 0.855$ y) were measured after sufficiently long cool-down time, which ensured that dominant short-lived products have diminished. Further, the identification of long-lived activities ^{22}Na and ^{46}Sc were confirmed by detecting coincident gamma rays in the decay cascade in the D1-D2 setup. The measured half-lives of the reaction products were found to be in good agreement with the reference values [3]. Figure 5.4 shows typical decay curves for a couple of reaction products in the AUT1A sample ($E_p = 22$ MeV).

From the measured yield of the characteristic gamma ray during time t_1 to t_2, the

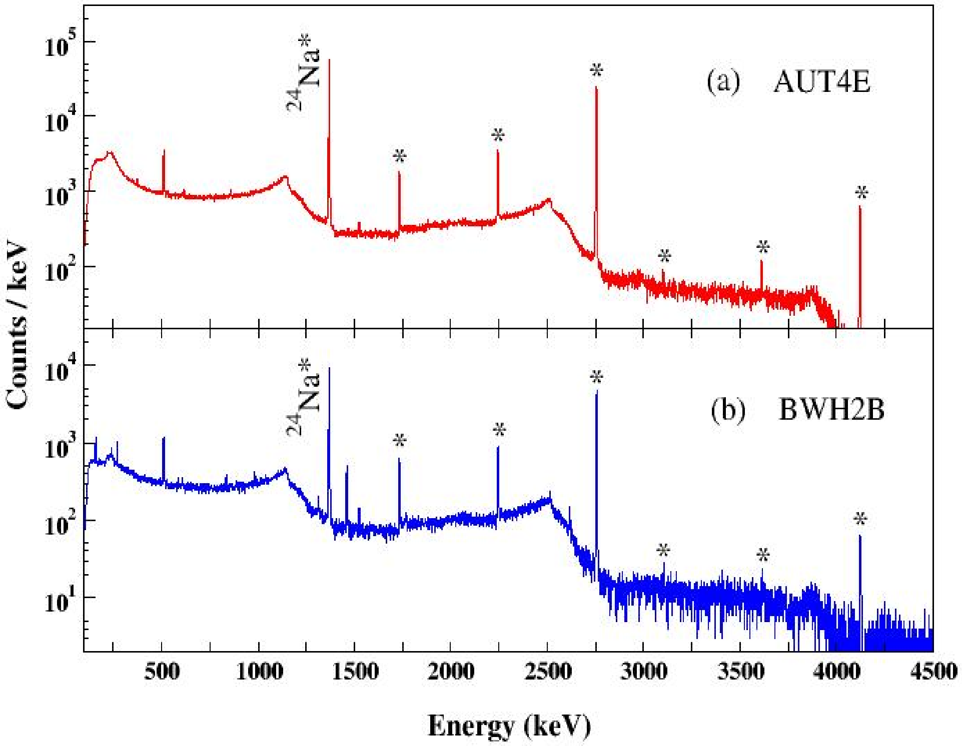

Figure 5.3: Gamma ray spectra ($t = 1$ d) of the irradiated ($E_p = 12$ MeV) rock samples after $t_c = 1.7$ d, (a) AUT4E in TiLES and (b) BWH2B in D1. The * mark has the same meaning as in Figure 5.2.

saturated activity A_∞ [144] (for $t_{irr} \to \infty$) can be obtained as

$$A_\infty = \frac{\lambda N_{obs}}{\epsilon_\gamma I_\gamma^{net}(1 - e^{-\lambda t_{irr}})e^{\lambda t_{irr}}(e^{-\lambda . t_1} - e^{-\lambda . t_2})} \tag{5.2}$$

The saturated activity A_∞ per unit mass has been estimated for the prominent reaction products in the Aut rock and is presented in Table 5.3. The coincident summing corrections have been taken into consideration as samples were counted in the close geometry (see eqn. 4 in chapter 4) and were found to be around 10 - 16% for the nuclides ^{22}Na, ^{24}Na and ^{43}K. The nuclides ^{22}Na and ^{47}Ca are absent in the AUT4E sample, which is irradiated at lower energy ($E_p = 12$ MeV). This is expected as both these nuclides are produced via (n, 2n) reactions, which have higher threshold energies and hence require $E_n > 10$ MeV. The differences in the A_∞ per unit mass at $E_p = 12$ and 22 MeV correspond to contribution from high energy neutrons (i.e. $E_n \sim 10$-20 MeV) and can also be estimated from Table 5.4. It is evident that the production of both ^{24}Na and ^{42,43}K is dominated by high-energy neutrons. It should be mentioned that it is impossible to extract the concentration of the parent nuclides since the

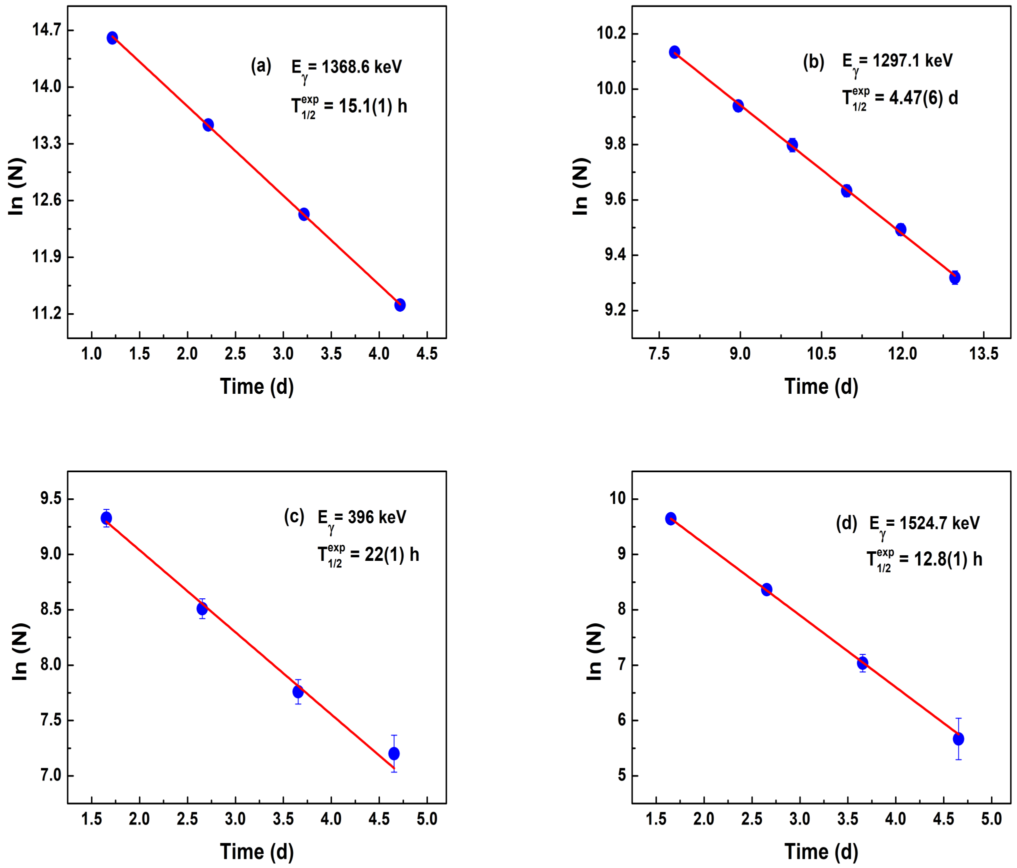

Figure 5.4: Decay curves (a) E_γ = 1386.6 keV of ^{24}Na, (b) E_γ = 1297.1 keV of ^{47}Ca, (c) E_γ = 396.9 keV of ^{43}K and (d) E_γ = 1524.7 keV of ^{42}K, where N are photopeak counts corresponding to the integration time of 3 h.

precise shape of the neutron energy distribution is not available in the present experiment. Moreover, in fast neutron-induced reactions, multiple reaction pathways can produce a particular isotope (see Table 5.3). Hence, a thermal neutron activation study would be desirable for quantitatively estimating the trace elements and/or rock composition. To understand the impact of long-lived activities, the spectrum of the irradiated Aut rock after $t_c \sim 30$ days was compared with the spectrum prior to the irradiation. The effect of the remnant activities is reflected in the enhancement in the background at low energies and in the presence of a few characteristic gammas (100 - 1300 keV) and can be seen in Figure 5.5.

Overall, the BWH rock spectrum shows the presence of Potassium neutron-induced reaction products, while Calcium products dominate that of the Aut sample. The Aut rock appears to have mostly short-lived activities. However, long-lived products like ^{54}Mn and ^{47}Ca can result in the enhanced background at $E < 1000$ keV. The high energy gamma rays from ^{24}Na need to be adequately shielded, as the sum peak can contribute to the background above 2 MeV, a region of interest for many NDBD studies.

Table 5.3: Observed neutron-induced reaction products in Aut and BWH rocks together with the threshold neutron energy E_{th} corresponding to $\sim 1\,\mu$b cross-section. The half-life ($T_{1/2}$) and prominent gamma rays (E_γ) are also listed.

Reaction channel	E_{th} (MeV)	$T_{1/2}$ (reference)	$T_{1/2}$ (measured)	E_γ (keV)
^{48}Ti(n,p)^{48}Sc	5	1.82 d	—	983.5, 1037.5, 1312.1
^{48}Ca(n,2n)^{47}Ca	10	4.54 d	4.47 (6) d	489.2, 807.9, 1297.1
^{24}Mg(n,p)^{24}Na, ^{27}Al(n,α)^{24}Na	5, 4.64	15 h	15.04 (5) h	1368.6, 2754.0
^{43}Ca(n,p)^{43}K	1.8	22.3 h	22 (1) h	373.8, 617.5
^{46}Ti(n,p)^{46}Sc	3	83.79 d	—	889.3, 1120.5
^{23}Na(n,2n)^{22}Na	13	2.60 y	—	511.0, 1274.5
^{39}K(n,2n)^{38}K	14.5	7.64 min	—	2167.5
^{41}K(n,p)^{41}Ar	3	1.82 h	—	1293.6
^{54}Fe(n,p)^{54}Mn	0.72	312 d	279 (68) d	835.0
^{56}Fe(n,p)^{56}Mn	4	2.58 h	—	846.8
^{43}Ca(n,n'p)^{42}K, ^{41}K(n,γ)^{42}K	12, 1	12.36 h	12.8 (1) h	1524.7

Table 5.4: Saturated activity A_∞ per unit mass for the prominent reaction products. The E_{coin}, emitted in coincidence with E_γ, which has been considered for the summing corrections, are also listed.

Nuclide	E_γ (keV)	E_{coin} (keV)	A_∞ ($E_p = 12$ MeV) (Bq/g)	A_∞ ($E_p = 22$ MeV) (Bq/g)
^{22}Na	1274.5	511.0	—	9 (2)
^{24}Na	1368.6 2754.0	2754.0 1368.6	336 (14)	6536 (299)
^{42}K	1524.6	—	4.6 (6)	62 (13)
^{43}K	617.5	372.8	0.52 (8)	18 (1)
^{47}Ca	1297.1	—	—	54 (3)

5.4 Summary

A detailed comparison of neutron-induced activity in Aut and BWH rock samples has been conducted. The low energy neutron background at both sites is expected to be similar. Radiogenic neutron flux is dominated by ^{238}U to be around 3×10^{-6} n cm^{-2} s^{-1}, which is equivalent to other underground laboratories. The fast neutron activation studies of both Aut and BWH rock samples have revealed mostly short-lived and few long-lived activities. The indicated presence of long-lived isotopes like ^{54}Mn (0.855 y) and ^{22}Na (2.60 y) can contribute to the enhanced background in energy region below 1500 keV, which could be a

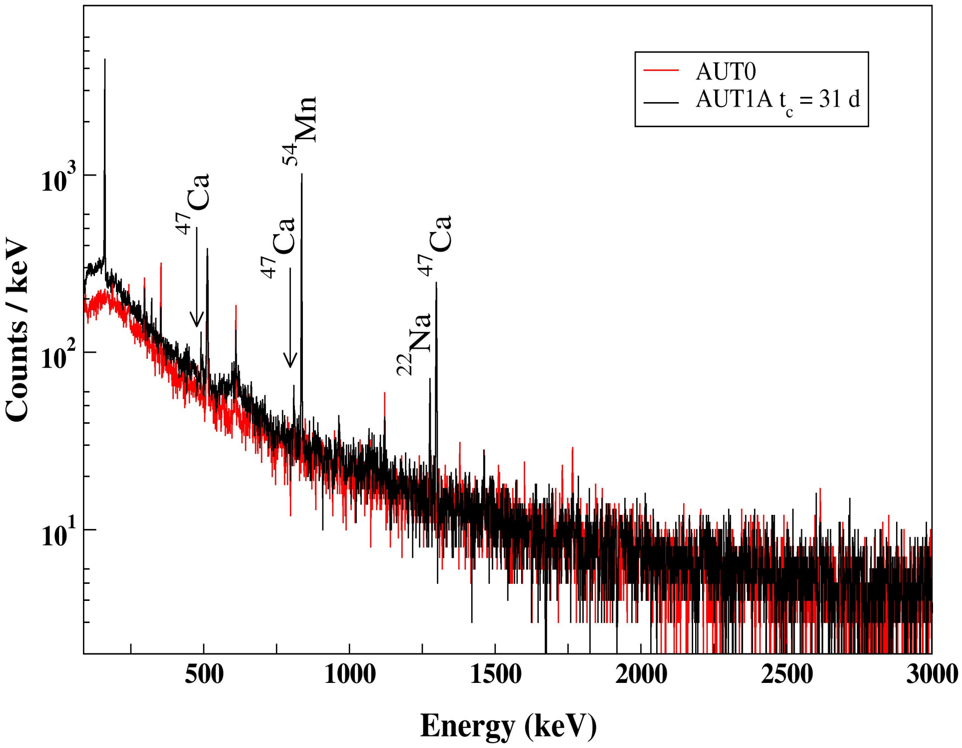

Figure 5.5: Comparison of gamma ray spectra of the irradiated ($E_p = 22\,\mathrm{MeV}$) AUT1A (black line) after $t_c = 31\,\mathrm{d}$ and pristine AUT0 (red line) samples. Note that AUT1A (10.6 g) has a smaller mass than AUT0 (27.5 g). Both spectra are normalised to $t = 1\,\mathrm{d}$.

dominating background for dark matter experiments. However, no observation of gamma ray energies at $E > 2\,\mathrm{MeV}$, a region of interest for many double beta decay isotopes, is desirable to achieve the required sensitivity. The estimation of neutron-induced background will be helpful in the design of radiation shielding for the laboratory at the underground site.

Chapter 6

Summary and Future Outlook

6.1 Summary

In summary, this thesis deals with the low background studies for environmental and rare decay investigations. The fact that the studies related to natural radioactivity, rare nuclear decays (e.g., $\alpha/\beta/2\nu\beta\beta$), neutrinoless double beta decay ($0\nu\beta\beta$), the interaction of dark matter particles, etc., involve low-level radiation background settings and underground facilities to investigate their nature and origin. Understanding the underlying physics of these processes is essential for probing the new physics beyond the standard model. The development of dedicated low background measurement setups plays a crucial role in investigating rare event processes to adequate sensitivity levels. While background reduction is necessary, it is imperative to quantify all potential sources of radiation background around the measurement setup, which are specific to the experimental site. To exploit the potential of low background settings for rare decay studies, efforts are underway to set up an underground laboratory in India for neutrinoless double beta decay, dark matter, etc. An underground laboratory, Jaduguda Underground Science Laboratory (JUSL), as of now, which is being utilized for rare event studies, is located inside a mine at 555 m depth at Jaduguda in Jharkhand, India. In the recent past, a site search for the India-based Neutrino Observatory (INO) hinted at possibilities of an underground lab in Bodi West Hills (BWH) of Theni District in the state of Tamil Nadu in South India.

Recently, feasibility studies for rare event experiments have been initiated in North India to search for a potential site for setting up a moderate underground laboratory in the mountains of Himachal Pradesh. In order to qualify a site for such a laboratory, comprehensive knowledge of the nature and extent of the radiation environment is demanded to assess the background levels, which is crucial for the sensitivity of the experiment. The improvement in the background reduction can lead to a considerable gain in experimental sensitivity. In order to complement an underground laboratory, several dedicated low background facilities are required for the screening of materials that may be used for background reduction in targeted experiments. In this thesis, various aspects of radiation background and feasibility studies relevant to rare event searches using single or combinations of low background HPGe spectrometers have been carried out.

A low background setup ILM (IIT Ropar Low-background Measurement setup) above ground is being set up at IIT Ropar in India, to investigate radiation background and feasibility studies relevant to rare decay studies. In this thesis, the development of ILM-0, a demonstrator of ILM, is presented. The setup consists of a carbon-loaded low background cryocooled HPGe detector coupled with a NIM/VME-based data acquisition system. A suite of experimental measurements has been performed using point-like gamma sources in a wide energy range of 80-1408 keV for performance tests and characterization of ILM-0. Additionally, Monte Carlo simulation studies have been performed using the GEANT4 package to estimate the photopeak efficiency of the HPGe detector employed in the ILM-0 setup. A preliminary detector model has been developed with an average relative deviation of ~10% as compared with the experimental data. The present setup has shown improved measurement sensitivity in counting environmental samples and quantifying radionuclides in a shorter duration. This suggests the capabilities of ILM-0 for high-quality environmental measurements by investigating the specific activities and their variation in soil/rock samples.

Investigations on rare α/β decays and other decay modes of DBD ($ECEC/\beta^+EC/\beta^+\beta^+$) are possible for a few nuclei with high discovery potential. These searches have recently gained much attention due to the steady improvement in sensitivity in increasingly low background conditions. Feasibility studies have been performed for ^{96}Zr β decay and positron DBD processes using a combination of 2/4 HPGe detectors ($\sim$ 33% R.E.) to optimize the source-detectors configuration for rare decay experiments. A simulation program, 4HPGeSim, has been developed using GEANT4 to optimize mass efficiency product (Mϵ_c). The value of Mϵ_c has been estimated using a setup of 4 HPGe detectors with extended sources in a compact geometry for 568-1091 keV gamma ray pair in the ^{96}Nb decay cascade. Results suggest that ~70 g of 50% enriched source will yield mass efficiency of ~12-20 g-% for 568-1091 keV gamma ray pair in the ^{96}Nb decay cascade, comparable to that of Finch *et al.* [4]. Further, the feasibility study of positron double beta decay modes involving simultaneous emission of 2/4 gamma rays of 511 keV in ^{112}Sn (EC-β^+) and ^{106}Cd ($\beta^+\beta^+$) has been performed using a coincidence setup of two HPGe detectors. Simulations for coincident detection efficiency (ϵ_c) of 511 keV gamma rays with two HPGe detectors have been carried out using GEANT4 for different sources geometries to optimize the mass efficiency. The ambient background of the two detector setup with moderate Pb shielding was measured in coincidence mode at sea level. It has been observed that the coincidence detection of the 511 keV pair significantly improves the background in the region of interest. The sensitivity for $T_{1/2}^{\beta^+\beta^+}$ (^{106}Cd) and $T_{1/2}^{EC-\beta^+}$ (^{112}Sn) is estimated to be $\sim 10^{19}$ - 10^{20} y from the background measurements with ~40 g of ^{nat}Sn for 1 y of measurement time with enriched samples (90%).

Mitigation of radiation background is of paramount importance for rare event studies e.g., double beta decay, dark matter, etc. Additionally, understanding the ambient background of the site originating from the surrounding rocks is one of the crucial factors. Efforts are underway in India to set up an underground laboratory for conducting low background experiments. The radiopurity studies of a rock sample from the potential laboratory site near the Aut tunnel of Himachal Pradesh (India) have been carried out using the low background experimental setup (TiLES) [2] at TIFR, Mumbai. The measured specific activities of trace impurities ^{232}Th and ^{238}U in the Aut rock are found to be 0.50 (6) and 8.2 (3) mBq/g, respectively. It has been found that the Aut rock appears to have a lesser amount of ^{232}Th and a somewhat higher amount of ^{238}U as compared with BWH rock. The concentration of ^{40}K in Aut rock was lower by a factor of $\sim$ 1000 as compared to the BWH rock sample. It is noted that the Aut rock trace impurity concentrations are considerably lower than the respective worldwide average values. This analysis suggests that the ambient gamma ray background at the Aut site is found to be lower than the BWH site [129], which indicates this site's suitability for an underground laboratory.

Besides the gamma background, the neutron background can also be a limiting factor for the low background experiments to achieve desirable sensitivity. To assess the neutron-induced long-lived activities, fast neutron activation experiments have been carried out on both Aut and BWH rock samples at BARC-TIFR Pelletron Linac Facility, Mumbai [5]. In the present work, the neutron activation analysis of Aut rock revealed mostly short-lived activity. The fast neutron activation studies of both Aut and BWH rock samples have indicated the presence of long-lived activities like ^{54}Mn (0.855 y) and ^{22}Na (2.60 y). The resultant gamma ray energies were lower than 1500 keV, and no significant long-lived contributions at $E > 2$ MeV were observed. The low energy neutron flux arising due to spontaneous fission and (α,n) reactions, dominated by ^{238}U, is expected to be around 3×10^{-6} $\mathrm{n\,cm^{-2}\,s^{-1}}$, which is similar to other underground laboratories [54]. On this basis, it may be concluded that the Aut site is expected to have lower ambient radiation background than the BWH, while the low-energy neutron background is expected to be similar. From radioactive background investigations, Aut is a favorable site for building an underground laboratory.

6.2 Future outlook

As has been mentioned in the present work, ultra-low background levels are essential to enhance the counting sensitivity relevant to rare decay searches. It can be inferred that the sensitivity of ILM-0 with the present shielding configuration is adequate for counting environmental samples. However, for further improvement in the background for rare event studies, augmenting the present setup with low-activity Pb (10-15 cm) shielding can mitigate the dominant background of the primordial activities from the chains of U, Th, and ^{40}K. In addition, low-activity Cu (5-10 cm) can attenuate the X-rays from the outer Pb shield adequately. Further, the gamma ray background arising from the low energy (< 10 MeV) neutron flux can be attenuated effectively to 90% by the implementation of a neutron shield using a combination of High-Density Polyethylene (HDPE) and Boron loaded rubber. It may be pointed out that surface laboratories are primarily dominated by cosmic-ray muons and their secondary products, such as; neutrons, gammas, and cosmogenic isotopes. Deploying additional cosmic muon veto systems can further improve the counting sensitivity with a background reduction of about 50% in the present setup. The overall improvement in background level is expected to be about an order of magnitude and adequate to estimate low-level samples relevant to rare decay searches.

To reduce the overall modeling uncertainty below 5%, a Monte Carlo simulation needs to be optimized by detailed measurements carried out with a point and extended geometry samples over a wide energy range. Adopting coincidence counting techniques along with active and passive background reduction strategies can significantly improve the signal-to-noise ratio. Coincidence measurements will be appropriate for studying nuclides decaying through a cascade of successive photon emissions.

In a 4-detector coincidence setup, the detector configurations with larger solid angles are required to reduce the scattering/escaping of gamma rays from the sides and gaps between the detectors. With the present source-detector configuration, the simulation results clearly highlight the requirement of enriching samples (>50%) to achieve statistically significant measurements. The half-life sensitivity with enriched ^{112}Sn can be improved from the present best limits by deploying the coincidence setup of 2 detectors in an underground laboratory at a moderate depth. However, for ^{106}Cd, further measurements to improve the signal-to-noise ratio are essential. It is suggested that the additional shielding and cosmic veto could substantially improve the sensitivity with a background reduction of about 50% in the present two HPGe detector setups at moderate depth to probe EC-β^+/ $\beta^+\beta^+$.

For ambient radioactivity studies, multi-stage gamma ray decay cascades can be addressed within the GEANT4 simulation, e.g., decay event generator. The generated cascade should be realistic according to the decay scheme of the chosen isotope. Additionally, the correlations between gamma rays should be considered to correctly determine the detection efficiency for each gamma line. The analysis of radiopurity measurements suggests measuring rock samples in powdered form to ensure the homogeneity of a finite sample size towards the face of the detector. In order to study the composition of rock samples, analytical methods, such as; scanning electron microscopy with energy dispersive x-ray analysis (SEM-EDX) and Inductively Coupled Plasma Mass Spectrometry (ICPMS), can be performed. The ICPMS is a highly sensitive complementary method to gamma ray spectroscopy often utilized to obtain quantitative information on lower concentrations of impurities in various materials of importance to rare decay experiments. The measurements of ambient gamma, cosmic-ray muons and residual neutron background fluxes can be carried out inside the Aut tunnel to perform rare event searches. In neutron activation results, the formation of long-lived radionuclides in the low background experiments is undesirable. The background events from the high energy gamma rays or pile up from low energy gamma rays may affect the sensitivity of these experiments to rare event searches. In addition, the activation of materials to be used in the detector setup and components can also be studied. Further, the inputs from experimental radiogenic and cosmogenic backgrounds provide a crucial input to perform detailed Monte Carlo simulations and understand their contribution to the background in the ROI. The simulation model is necessary to investigate the best shielding combination and an optimal shielding configuration to reduce the dominant sources of background effectively.

Bibliography

[1] Joseph A. Formaggio and C.J. Martoff. BACKGROUNDS TO SENSITIVE EXPERIMENTS UNDERGROUND. *Annual Review of Nuclear and Particle Science*, 54(1):361–412, 2004.

[2] N. Dokania, V. Singh, S. Mathimalar, V. Nanal, et al. Characterization and modeling of a low background HPGe detector. *Nucl. Instrum. Meth. A*, 745:119–127, 2014.

[3] National nuclear data center. Last accessed: 2022-02-21.

[4] S.W. Finch and W. Tornow. Search for the β decay of ^{96}Zr. *Nucl. Instrum. Meth. A*, 806:70–74, 2016.

[5] S. Paul, G.S. Sahoo, S.P. Tripathy, S.C. Sharma, et al. Measurement of neutron spectra generated from bombardment of 4 to 24 MeV protons on a thick ^{9}Be target and estimation of neutron yields. *Review of Scientific Instruments*, 85(6):063501, 2014.

[6] M.E. Medhat, Nilgun Demir, Urkiye Akar Tarim, and Orhan Gurler. Calculation of gamma-ray mass attenuation coefficients of some egyptian soil samples using monte carlo methods. *Radiation Effects and Defects in Solids*, 169(8):706–714, 2014.

[7] J. Sedlet. Historical perspectives on environmental radioactivity measurements. *Trans. Am. Nucl. Soc.;(United States)*, 54(CONF-870601-), 1987.

[8] A.B. MacKenzie. Environmental radioactivity: experience from the 20th century—trends and issues for the 21st century. *Science of the Total Environment*, 249(1-3):313–329, 2000.

[9] United nation. Scientific committee on the effects of atomic radiation. *Sources and Effects of Ionizing Radiation: UNSCEAR 2000 Report to the General Assembly, with Scientific Annexes.* UN, 2000.

[10] World Health Organization. *WHO handbook on indoor radon: a public health perspective.* World Health Organization, 2009.

[11] T. Frosio, P. Bertreix, M. Magistris, N. Menaa, et al. An enhanced characterization process for the elimination of very low level radioactive waste in particle accelerators. *Applied Radiation and Isotopes*, 166:109312, 2020.

[12] J. Bezuidenhout. The investigation of natural radionuclides as tracers for monitoring sediment processes. *Journal of Applied Geophysics*, 181:104135, 2020.

[13] X. Hou. Radioanalysis of ultra-low level radionuclides for environmental tracer studies and decommissioning of nuclear facilities. *Journal of Radioanalytical and Nuclear Chemistry*, 322(3):1217–1245, 2019.

[14] M. Köhler, D. Degering, M. Laubenstein, P. Quirin, et al. A new low-level γ-ray spectrometry system for environmental radioactivity at the underground laboratory Felsenkeller. *Applied Radiation and Isotopes*, 67(5):736–740, 2009. 5th International Conference on Radionuclide Metrology - Low-Level Radioactivity Measurement Techniques ICRM-LLRMT'08.

[15] T. Cresswell, M. Metian, Nicholas S. Fisher, S. Charmasson, et al. Exploring New Frontiers in Marine Radioisotope Tracing – Adapting to New Opportunities and Challenges. *Frontiers in Marine Science*, 7, 2020.

[16] Marios J. Anagnostakis. Environmental radioactivity measurements and applications–difficulties, current status and future trends. *Radiation Physics and Chemistry*, 116:3–7, 2015.

[17] Pavel P. Povinec. Ultra-sensitive radionuclide analyses: new frontiers in radioanalytics. *Journal of Radioanalytical and Nuclear Chemistry*, 322(3):1247–1255, 2019.

[18] Yu. S. Tsyganov and S.V. Barinova. Low-Background Techniques in Nuclear Physics. *Physics of Particles and Nuclei Letters*, 16(5):542–551, 2019.

[19] Matthias Laubenstein and Ian Lawson. Low Background Radiation Detection Techniques and Mitigation of Radioactive Backgrounds. *Frontiers in Physics*, 8:506, 2020.

[20] Michele Maltoni et al. Solar neutrinos and neutrino physics. *The European Physical Journal A*, 52(4):1–16, 2016.

[21] A. B. Aleksandrov, A. .B Dashkina, N. S. Konovalova, et al. Search for weakly interacting massive dark matter particles: state of the art and prospects. *Physics-Uspekhi*, 64(9):861–889, 2021.

[22] Michelle J Dolinski, Alan W.P. Poon, and Werner Rodejohann. Neutrinoless double-beta decay: Status and prospects. *Annual Review of Nuclear and Particle Science*, 69(1), 2019.

[23] P. Belli, R. Bernabei, F.A. Danevich, A. Incicchitti, and V.I. Tretyak. Experimental searches for rare alpha and beta decays. *The European Physical Journal A*, 55(8):1–43, 2019.

[24] I. Barabanov, S. Belogurov, L. Bezrukov, et al. Cosmogenic activation of germanium and its reduction for low background experiments. *Nuclear Instruments and Methods in Physics Research Section B: Beam Interactions with Materials and Atoms*, 251(1):115–120, 2006.

[25] D.-M. Mei, Z.-B. Yin, and S.R. Elliott. Cosmogenic production as a background in searching for rare physics processes. *Astroparticle Physics*, 31(6):417–420, 2009.

[26] S. Abe, S. Enomoto, K. Furuno, et al. Production of radioactive isotopes through cosmic muon spallation in kamland. *Phys. Rev. C*, 81:025807, 2010.

[27] K. Hagiwara et al. Review of particle properties. *Phys. Rev. D*, 66:010001, 2002.

[28] Dongming Mei and A. Hime. Muon-induced background study for underground laboratories. *Phys. Rev. D*, 73:053004, 2006.

[29] A. Bassignani, B.B. Bam, G. Colombo, et al. Review of long term radon studies at the gran sasso underground laboratory. *Radiation Measurements*, 25(1):557–560, 1995. Nuclear Tracks in Solids.

[30] K.-H. Ackermann, M. Agostini, and others. The GERDA experiment for the search of $0\nu\beta\beta$ decay in ^{76}Ge. *Eur. Phys. J. C*, 73(3):2330, 2013.

[31] Nicolas Abgrall, Estanislao Aguayo, Frank T. Avignone, et al. The Majorana Demonstrator neutrinoless double-beta decay experiment. *Advances in High Energy Physics*, 2014, 2014.

[32] F.M. Fränkle, A. Schaller, K. Blaum, et al. KATRIN background due to surface radioimpurities. *Astroparticle Physics*, 138:102686, 2022.

[33] F. Alessandria, E. Andreotti, R. Ardito, et al. CUORE crystal validation runs: Results on radioactive contamination and extrapolation to CUORE background. *Astroparticle Physics*, 35(12):839–849, 2012.

[34] A. Gando, Y. Gando, H. Hanakago, et al. Measurement of the double-β decay half-life of ^{136}Xe with the KamLAND-Zen experiment. *Phys. Rev. C*, 85:045504, 2012.

[35] D. Budjáš, W. Hampel, M. Heisel, et al. Highly Sensitive Gamma-Spectrometers of GERDA for Material Screening: Part 2, 2008.

[36] P. Agnes, L. Agostino, I. F. M. Albuquerque, et al. Results from the first use of low radioactivity argon in a dark matter search. *Phys. Rev. D*, 93:081101, 2016.

[37] E. Aprile, K. Abe, F. Agostini, et al. Material radiopurity control in the XENONnT experiment. *The European Physical Journal C*, 82(7):1–21, 2022.

[38] H. Simgen. Radon assay and purification techniques. In *AIP Conference Proceedings*, volume 1549, pages 102–107. American Institute of Physics, 2013.

[39] K. Pushkin, C. Akerlof, D. Anbajagane, J. Armstrong, et al. Study of radon reduction in gases for rare event search experiments. *Nuclear Instruments and Methods in Physics Research Section A: Accelerators, Spectrometers, Detectors and Associated Equipment*, 903:267–276, 2018.

[40] A. Cagniant, G. Le Petit, P. Gross, G. Douysset, et al. Improvements of low-level radioxenon detection sensitivity by a state-of-the art coincidence setup. *Applied Radiation and Isotopes*, 87:48–52, 2014.

[41] Matthew A. Goodwin, Patrick H. Regan, Steven J. Bell, R. Britton, et al. Enhancing the detection sensitivity of a high-resolution $\beta - \gamma$ coincidence spectrometer. *Journal of Environmental Radioactivity*, 250:106915, 2022.

[42] C. Brofferio, O. Cremonesi, and S. Dell'Oro. Neutrinoless Double Beta Decay Experiments With TeO_2 Low-Temperature Detectors. *Frontiers in Physics*, 7, 2019.

[43] Frank T. Avignone III and Steven R. Elliott. The Search for Double Beta Decay with Germanium Detectors: Past, Present, and Future. *Frontiers in Physics*, 7:6, 2019.

[44] Alexander Barabash. Precise Half-Life Values for Two-Neutrino Double-β Decay: 2020 Review. *Universe*, 6(10), 2020.

[45] Pierluigi Belli, Rita Bernabei, et al. Double Beta Decay to Excited States of Daughter Nuclei. *Universe*, 6(12), 2020.

[46] Pierluigi Belli, Rita Bernabei, and Vincenzo Caracciolo. Status and Perspectives of 2ϵ, $\epsilon\beta^+$ and $2\beta^+$ Decays. *Particles*, 4(2):241–274, 2021.

[47] M. Agostini, G. Araujo, A.M. Bakalyarov, M. Balata, I. Barabanov, L. Baudis, C. Bauer, E. Bellotti, S. Belogurov, A. Bettini, et al. Pulse shape analysis in GERDA Phase II. *The European Physical Journal C*, 82(4):1–16, 2022.

[48] L. Gironi. Pulse shape analysis with scintillating bolometers. *Nuclear Instruments and Methods in Physics Research Section A: Accelerators, Spectrometers, Detectors and Associated Equipment*, 718:546–549, 2013. Proceedings of the 12th Pisa Meeting on Advanced Detectors.

[49] A.S. Barabash, A. Basharina-Freshville, S. Blot, et al. Calorimeter development for the SuperNEMO double beta decay experiment. *Nuclear Instruments and Methods in Physics Research Section A: Accelerators, Spectrometers, Detectors and Associated Equipment*, 868:98–108, 2017.

[50] L. Lewandowski, P. Reiter, B. Birkenbach, B. Bruyneel, et al. Pulse-Shape Analysis and position resolution in highly segmented HPGe AGATA detectors. *The European Physical Journal A*, 55(5):1–13, 2019.

[51] Dariusz Malczewski, Jan Kisiel, and Jerzy Dorda. Gamma background measurements in the Boulby Underground Laboratory. *Journal of Radioanalytical and Nuclear Chemistry*, 298(3):1483–1489, 2013.

[52] S. Thakur, A. Mazumdar, N. Jangid, V. Vatsa, et al. Radiopurity studies of a rock sample from the Aut region. *Nuclear Instruments and Methods in Physics Research Section A: Accelerators, Spectrometers, Detectors and Associated Equipment*, page 166892, 2022.

[53] V. Gostilo, A. Sokolov, S. Pohuliai, and J. Joutsenvaara. Characterisation of the natural gamma-ray background in the underground Callio Lab facility. *Applied Radiation and Isotopes*, 156:108987, 2020.

[54] Dariusz Malczewski et al. Gamma background measurements in the Gran Sasso National Laboratory. *Journal of Radioanalytical and Nuclear Chemistry*, 295(1):749–754, 2013.

[55] Dariusz Malczewski, Jan Kisiel, and Jerzy Dorda. Gamma background measurements in the Laboratoire Souterrain de Modane. *Journal of Radioanalytical and Nuclear Chemistry*, 292(2):751–756, 2012.

[56] D.S. Akerib, C.W. Akerlof, S.K. Alsum, et al. Measurement of the gamma ray background in the Davis cavern at the Sanford Underground Research Facility. *Astroparticle Physics*, 116:102391, 2020.

[57] Zhi Zeng, Jian Su, Hao Ma, Hengguan Yi, et al. Environmental gamma background measurements in china jinping underground laboratory. *Journal of Radioanalytical and Nuclear Chemistry*, 301(2):443–450, 2014.

[58] Sayan Ghosh, Shubham Dutta, Naba Kumar Mondal, and Satyajit Saha. Measurements and simulation of background radiation for rare event search experiments at an underground laboratory. *Journal of Physics: Conference Series*, 2156(1):012168, 2021.

[59] S. Sharma and M. Saha Sarkar. Measurement and simulation of gamma-ray background in a low energy accelerator facility. *Journal of Instrumentation*, 15(09):T09003–T09003, 2020.

[60] Oliviero Cremonesi and Maura Pavan. Challenges in double beta decay. *Advances in High Energy Physics*, 2014, 2014.

[61] M. Agostini, G. R. Araujo, et al. Final Results of GERDA on the Search for Neutrinoless Double-β Decay. *Phys. Rev. Lett.*, 125:252502, 2020.

[62] D. Q. Adams, C. Alduino, et al. Improved Limit on Neutrinoless Double-Beta Decay in ^{130}Te with CUORE. *Phys. Rev. Lett.*, 124:122501, 2020.

[63] D. S. Akerib, C. W. Akerlof, S. K. Alsum, H. M. Araújo, et al. Projected WIMP sensitivity of the LUX-ZEPLIN dark matter experiment. *Phys. Rev. D*, 101:052002, 2020.

[64] R. Ajaj, P.-A. Amaudruz, G. R. Araujo, M. Baldwin, et al. Search for dark matter with a 231-day exposure of liquid argon using DEAP-3600 at SNOLAB. *Phys. Rev. D*, 100:022004, 2019.

[65] P. Agnes, I. F. M. Albuquerque, T. Alexander, A. K. Alton, et al. DarkSide-50 532-day dark matter search with low-radioactivity argon. *Phys. Rev. D*, 98:102006, 2018.

[66] E. Aprile et al. Dark Matter Search Results from a One Ton-Year Exposure of XENON1T. *Physical Review Letters*, 121:111302, 2018.

[67] G. Heusser, M. Laubenstein, and H. Neder. Low-level germanium gamma-ray spectrometry at the μbq/kg level and future developments towards higher sensitivity. In P.P. Povinec and J.A. Sanchez-Cabeza, editors, *Radionuclides in the Environment*, volume 8 of *Radioactivity in the Environment*, pages 495–510. Elsevier, 2006.

[68] T.M. Semkow, P.P. Parekh, C.D. Schwenker, et al. Low-background gamma spectrometry for environmental radioactivity. *Applied Radiation and Isotopes*, 57(2):213–223, 2002.

[69] P.P. Povinec, J.-F. Comanducci, and I. Levy-Palomo. IAEA-MEL's underground counting laboratory in Monaco—background characteristics of HPGe detectors with anti-cosmic shielding. *Applied Radiation and Isotopes*, 61(2):85–93, 2004. Low Level Radionuclide Measurement Techniques - ICRM.

[70] S. Neumaier, M. Wojcik, H. Dombrowski, and D. Arnold. Improvements of a low-level gamma-ray spectrometry system at the underground laboratory "UDO". *Applied Radiation and Isotopes*, 67(5):726–730, 2009. 5th International Conference on Radionuclide Metrology - Low-Level Radioactivity Measurement Techniques ICRM-LLRMT'08.

[71] Y. Hamajima and K. Komura. Background components of Ge detectors in Ogoya underground laboratory. *Applied Radiation and Isotopes*, 61(2):179–183, 2004. Low Level Radionuclide Measurement Techniques - ICRM.

[72] M. Laubenstein, M. Hult, J. Gasparro, et al. Underground measurements of radioactivity. *Applied Radiation and Isotopes*, 61(2):167–172, 2004. Low Level Radionuclide Measurement Techniques - ICRM.

[73] Holger Gastrich, Claus Gößling, Reiner Klingenberg, Kevin Kröninger, et al. The Dortmund Low Background Facility — Low-background gamma ray spectrometry with an artificial overburden. *Applied Radiation and Isotopes*, 112:165–176, 2016.

[74] L.R. Greenwood, M.G. Cantaloub, J.L. Burnett, A.W. Myers, et al. Low-background gamma-ray spectrometry for the international monitoring system. *Applied Radiation and Isotopes*, 126:240–242, 2017. Proceedings of the 7th International Conference on Radionuclide Metrology – Low-Level Radioactivity Measurement Techniques.

[75] G. Gupta, N. Dokania, H. Krishnamoorthy, A. Garai, et al. Improvements to Tifr Low background Experimental Setup (TiLES). *DAE Symp. Nucl. Phys.*, 61:1026–1027, 2016.

[76] V. Nanal. Is neutrino its own antiparticle? *Current Science*, 112:1375–1380, 2017.

[77] N. Dokania, V. Nanal, G. Gupta, et al. New limit for the half-life of double beta decay of ^{94}Zr to the first excited state of ^{94}Mo. *The European Physical Journal A*, 53(4):1–7, 2017.

[78] Particle Data Group, P A Zyla, et al. Review of Particle Physics. *Progress of Theoretical and Experimental Physics*, 2020(8), 08 2020. 083C01.

[79] M. Sajjad Athar, Steven W. Barwick, Thomas Brunner, et al. Status and perspectives of neutrino physics. *Progress in Particle and Nuclear Physics*, page 103947, 2022.

[80] J. Göggelmann, A .and Jochum, L. Gastaldo, F. Mantegazzini, A. Barth, and R. Hammann. Study of naturally occurring radionuclides in the ECHo set-up. *The European Physical Journal C*, 82(2):139, 2022.

[81] R. Matsumoto, K. Abe, Y. Hayato, K. Hiraide, et al. Search for proton decay via $p \to \mu^+ K^0$ in 0.37 megaton-years exposure of Super-Kamiokande. *Phys. Rev. D*, 106:072003, 2022.

[82] Antonio Caciolli and on behalf of the LUNA collaboration. Nuclear Astrophysics in underground laboratories: the LUNA experiment. *Journal of Physics: Conference Series*, 1610(1):012002, 2020.

[83] M. Goeppert-Mayer. Double Beta-Disintegration. *Phys. Rev.*, 48:512–516, 1935.

[84] Ettore Majorana. Teoria simmetrica dell'elettrone e del positrone. *Il Nuovo Cimento*, 14(4):171–184, 1937.

[85] Giulio Racah. Sulla Simmetria Tra Particelle e Antiparticelle. *Il Nuovo Cimento*, 14(7):322–328, 1937.

[86] S. R. Elliott, A. A. Hahn, and M. K. Moe. Direct evidence for two-neutrino double-beta decay in ^{82}Se. *Phys. Rev. Lett.*, 59:2020–2023, 1987.

[87] S. Abe, S. Asami, M. Eizuka, S. Futagi, et al. Search for the Majorana Nature of Neutrinos in the Inverted Mass Ordering Region with KamLAND-Zen. *Phys. Rev. Lett.*, 130:051801, 2023.

[88] N. Abgrall, A. Abramov, N. Abrosimov, I. Abt, M. Agostini, M. Agartioglu, A. Ajjaq, S.I. Alvis, F.T. Avignone III, X. Bai, et al. The large enriched germanium experiment for neutrinoless double beta decay (LEGEND). In *AIP Conference Proceedings*, volume 1894, page 020027. AIP Publishing LLC, 2017.

[89] I. J. Arnquist, F. T. Avignone, A. S. Barabash, et al. Final Result of the MAJORANA DEMONSTRATOR's Search for Neutrinoless Double-β Decay in ^{76}Ge, 2022.

[90] Frank F. Deppisch, Lukas Graf, Werner Rodejohann, and Xun-Jie Xu. Neutrino self-interactions and double beta decay. *Phys. Rev. D*, 102:051701, 2020.

[91] Frank F. Deppisch, Lukas Graf, and Fedor Šimkovic. Searching for New Physics in Two-Neutrino Double Beta Decay. *Phys. Rev. Lett.*, 125:171801, 2020.

[92] J. B. Albert, P. S. Barbeau, D. Beck, et al. First search for Lorentz and CPT violation in double beta decay with EXO-200. *Phys. Rev. D*, 93:072001, 2016.

[93] O. Azzolini, J. W. Beeman, F. Bellini, et al. First search for Lorentz violation in double beta decay with scintillating calorimeters. *Phys. Rev. D*, 100:092002, 2019.

[94] R. Arnold, C. Augier, A.S. Barabash, A. Basharina-Freshville, et al. Detailed studies of ^{100}Mo two-neutrino double beta decay in NEMO-3. *The European Physical Journal C*, 79(5):1–11, 2019.

[95] P. K. Rath, A. Kumar, R. Gautam, R. Chandra, P. K. Raina, and B. M. Dixit. Nuclear transition matrix elements for neutrinoless double-β decay of ^{76}Ge within mechanisms involving sterile neutrinos, Majorons and composite neutrinos. *International Journal of Modern Physics E*, 30(01):2150004, 2021.

[96] A. S. Barabash. Double beta decay to the excited states: Review. *AIP Conf. Proc.*, 1894(1):020002, 2017.

[97] K. Blaum, S. Eliseev, F. A. Danevich, V. I. Tretyak, Sergey Kovalenko, M. I. Krivoruchenko, Yu. N. Novikov, and J. Suhonen. Neutrinoless double-electron capture. *Rev. Mod. Phys.*, 92:045007, 2020.

[98] D. Q. Adams, C. Alduino, K. Alfonso, F. T. Avignone, et al. Search for neutrinoless β^+EC decay of ^{120}Te with CUORE. *Phys. Rev. C*, 105:065504, 2022.

[99] O.G. Polischuk, P. Belli, R. Bernabei, V.B. Brudanin, et al. New limit on two neutrino electron capture with positron emission in 106cd. In *AIP Conference Proceedings*, volume 2165, page 020020. AIP Publishing LLC, 2019.

[100] E. Aprile, J. Aalbers, F. Agostini, M. Alfonsi, et al. Observation of two-neutrino double electron capture in ^{124}Xe with XENON1T. *Nature*, 568(7753):532–535, 2019.

[101] E. Aprile, K. Abe, F. Agostini, S. Ahmed Maouloud, et al. Double-weak decays of ^{124}Xe and ^{136}Xe in the XENON1T and XENONnT experiments. *Phys. Rev. C*, 106:024328, 2022.

[102] A.S. Barabash, V.V. Kuzminov, V.M. Lobashev, V.M. Novikov, B.M. Ovchinnikov, and A.A. Pomansky. Results of the experiment on the search for double beta decay of ^{136}Xe, ^{134}Xe and ^{124}Xe. *Physics Letters B*, 223(2):273–276, 1989.

[103] Matthias Laubenstein. Screening of materials with high purity germanium detectors at the Laboratori Nazionali del Gran Sasso. *International Journal of Modern Physics A*, 32(30):1743002, 2017.

[104] L. Mikaélyan. Proc. Int. Conf. "Neutrino 77,", 1978.

[105] Eric B. Norman and Dawn M. Meekhof. New limits on the double beta decay half-lives of ^{94}Zr, ^{96}Zr, ^{116}Cd and ^{124}Sn. *Physics Letters B*, 195(2):126 – 129, 1987.

[106] A. S. Barabash. A possibility for experimentally observing two-neutrino double beta decay. *Soviet Journal of Experimental and Theoretical Physics Letters*, 51:207, February 1990.

[107] A.A. Vasenko, I.V. Kirpichnikov, et al. New results in the ITEP/YePI double beta-decay experiment with enriched germanium detectors. *Modern Physics Letters A*, 5(17):1299–1306, 1990.

[108] C. Arpesella, A.S. Barabash, E. Bellotti, C. Brofferio, E. Fiorini, P.P. Sverzellati, and V.I. Umatov. Search for $\beta\beta$ decay of ^{96}Zr and ^{150}Nd to excited states of ^{96}Mo and ^{150}Sm. *EPL (Europhysics Letters)*, 27(1):29, 1994.

[109] A. S. Barabash, R. Gurriarán, F. Hubert, Ph Hubert, J. L. Reyss, J. Suhonen, and V. I. Umatov. Investigation of the $\beta\beta$ decay of ^{96}Zr to excited states in ^{96}Mo. *Journal of Physics G: Nuclear and Particle Physics*, 22(4):487–496, 1996.

[110] S.W. Finch and W. Tornow. Search for two-neutrino double-β decay of ^{96}Zr to excited states of ^{96}Mo. *Phys. Rev. C*, 92(4):045501, 2015.

[111] N. Dokania, D. Degering, B. Lehnert, V. Nanal, and K. Zuber. An improved half-life limit of the double beta decay of ^{94}Zr into the excited state of ^{94}Mo. *Journal of Physics G: Nuclear and Particle Physics*, 45(7):075104, 2018.

[112] A.S. Barabash, Ph. Hubert, A. Nachab, S.I. Konovalov, et al. Search for β^+EC and ECEC processes in ^{112}Sn and $\beta^-\beta^-$ decay of ^{124}Sn to the excited states of ^{124}Te. *Nuclear Physics A*, 807(3):269–281, 2008.

[113] V. Nanal. Search for neutrinoless double beta decay in ^{124}Sn. *EPJ Web of Conferences*, 66:08005, 2014.

[114] A. S. Barabash, Ph. Hubert, Ch. Marquet, A. Nachab, S. I. Konovalov, F. Perrot, F. Piquemal, and V. Umatov. Improved limits on β^+EC and ECEC processes in ^{112}Sn. *Phys. Rev. C*, 83:045503, 2011.

[115] I. J. Arnquist, F. T. Avignone, A. S. Barabash, C. J. Barton, et al. Search for double-β decay of ^{76}Ge to excited states of ^{76}Se with the MAJORANA DEMONSTRATOR. *Phys. Rev. C*, 103:015501, 2021.

[116] D.Q. Adams, C. Alduino, K. Alfonso, F.T. III Avignone, et al. Search for double-beta decay of ^{130}Te to the 0^+ states of ^{130}Xe with CUORE. *The European Physical Journal C*, 81(7):567, 2021.

[117] P. Belli, R. Bernabei, R.S. Boiko, F. Cappella, et al. First search for 2ϵ and $\epsilon\beta^+$ processes in ^{168}Yb. *Nuclear Physics A*, 990:64–78, 2019.

[118] P. Belli, R. Bernabei, R. S. Boiko, F. Cappella, et al. First search for 2ϵ and $\epsilon\beta^+$ decay of ^{162}Er and new limit on $2\beta^+$ decay of ^{170}Er to the first excited level of ^{170}Yb. *Journal of Physics G: Nuclear and Particle Physics*, 45(9):095101, 2018.

[119] F.A. Danevich, M. Hult, D.V. Kasperovych, G.P. Kovtun, et al. First search for 2ϵ and $\epsilon\beta^+$ decay of ^{174}Hf. *Nuclear Physics A*, 996:121703, 2020.

[120] V. I. Tretyak. Beta decays in investigations and searches for rare effects. In *AIP Conference Proceedings*, volume 1894, page 020026. AIP Publishing LLC, 2017.

[121] E. Ferri, D. Bagliani, M. Biasotti, G. Ceruti, et al. The Status of the MARE Experiment with ^{187}Re and ^{163}Ho Isotopes. *Physics Procedia*, 61:227–231, 2015. 13th International Conference on Topics in Astroparticle and Underground Physics, TAUP 2013.

[122] V. A. Zheltonozhsky, A. M. Savrasov, N. V. Strilchuk, and V. I. Tretyak. Precise measurement of energy of the first excited state of ^{115}Sn ($E_{exc} \simeq 497.3$ keV). *Europhysics Letters*, 121(1):12001, 2018.

[123] Erica Andreotti, Mikael Hult, Raquel González de Orduña, Gerd Marissens, et al. Half-life of the β decay ^{115}In$(9/2^+) \rightarrow ^{115}Sn(3/2^+)$. *Phys. Rev. C*, 84:044605, 2011.

[124] P. Belli, R. Bernabei, N. Bukilic, F. Cappella, et al. Investigation of β decay of ^{113}Cd. *Phys. Rev. C*, 76:064603, 2007.

[125] A. Bakalyarov, A. Balysh, A. S. Barabash, P. Beneš, et al. Improved limits on β^- and $\beta^-\beta^-$ decays of ^{48}Ca. *Journal of Experimental and Theoretical Physics Letters*, 76:545–547, 2002.

[126] R. Arnold, C. Augier, A. M. Bakalyarov, J. D. Baker, et al. Measurement of the double-beta decay half-life and search for the neutrinoless double-beta decay of ^{48}Ca with the NEMO-3 detector. *Phys. Rev. D*, 93:112008, 2016.

[127] S. Agostinelli et al. Geant4—a simulation toolkit. *Nucl. Instrum. Meth. A*, 506(3):250–303, 2003.

[128] Rene Brun and Fons Rademakers. Root — an object oriented data analysis framework. *Nucl. Instrum. Meth. A*, 389(1):81–86, 1997. New Computing Techniques in Physics Research V.

[129] N. Dokania, V. Singh, S. Mathimalar, A. Garai, et al. Estimation of low energy neutron flux ($E_n \leq 15$ MeV) in India-based Neutrino Observatory cavern using Monte Carlo techniques. *Journal of Instrumentation*, 10(12):T12005–T12005, 2015.

[130] Jonas Boson et al. A detailed investigation of HPGe detector response for improved Monte Carlo efficiency calculations. *Nucl. Instrum. Meth. A*, 587(2):304–314, 2008.

[131] Michal Koleska, Ladislav Viererbl, and Milan Marek. Development of the MCNPX model for the portable HPGe detector. *Radiation Physics and Chemistry*, 104:351–354, 2014. 1st International Conference on Dosimetry and its Applications.

[132] G. Gupta et al. Modeling of an electrically cooled HPGe detector. *DAE Symposium on Nuclear Physics*, 63:1142–1143, 2018.

[133] Linux advanced multiparameter sysytem (LAMPS). `https://www.tifr.res.in/~pell/lamps.html`. Last accessed: 2022-02-21.

[134] IEEE Standard Test Procedures for Germanium Gamma-Ray Detectors. Technical report.

[135] G.R. Gilmore. *Practical Gamma Ray Spectrometry.* John Wiley & Sons, New York U.S.A, 2008.

[136] American National Standard for Calibration and Use of Germanium Spectrometers for the Measurement of Gamma-Ray Emission Rates of Radionuclides. Technical report.

[137] Y. Mei-Woo. Determination Performance Of Gamma Spectrometry Co-Axial HPGE Detector In Radiochemistry And Environment Group, Nuclear Malaysia., 2014.

[138] D Budjás et al. Gamma-ray spectrometry of ultra low levels of radioactivity within the material screening program for the GERDA experiment. *Applied Radiation and Isotopes*, 67(5):755—758, 2009.

[139] A. Aguilar-Arevalo et al. Characterization of germanium detectors for the first underground laboratory in Mexico. *Journal of Instrumentation*, 15(11):P11014–P11014, 2020.

[140] Lloyd A. Currie. Limits for qualitative detection and quantitative determination. Application to radiochemistry. *Analytical Chemistry*, 40(3):586–593, 1968.

[141] H. Heiskanen, M.T. Mustonen, and J. Suhonen. Theoretical half-life for beta decay of Zr-96. *J. Phys. G*, 34:837–843, 2007.

[142] M. Alanssari et al. Single and Double Beta-Decay Q Values among the Triplet ^{96}Zr, ^{96}Nb, and ^{96}Mo. *Phys. Rev. Lett.*, 116(7):072501, 2016.

[143] Adam J. Mayer, M. Wieser, M. Alanssari, D. Frekers, W. Matthews, J. Dilling, and R. I. Thompson. Isotope abundance measurement of the half-life of the $\beta\beta$-decaying nucleus ^{96}Zr from a 2.68 gyr zircon sample. *Phys. Rev. C*, 98:024617, 2018.

[144] Glenn F. Knoll. *Radiation Detection and Measurement.* John Wiley & Sons, New York U.S.A, 2009.

[145] M. F. Kidd, J. H. Esterline, S. W. Finch, and W. Tornow. Two-neutrino double-β decay of ^{150}Nd to excited final states in ^{150}Sm. *Phys. Rev. C*, 90:055501, 2014.

[146] S. Banik et al. Simulation of neutron background for a dark matter search experiment at JUSL. *Journal of Instrumentation*, 16(06):P06022, 2021.

[147] P. Belli, R. Bernabei, V. B. Brudanin, F. Cappella, et al. Search for 2β decay of ^{106}Cd with an enriched ^{106}CdWO$_4$ crystal scintillator in coincidence with four HPGe detectors. *Phys. Rev. C*, 93:045502, 2016.

[148] Y. Farzan and M. Tortola. Neutrino oscillations and Non-Standard Interactions. *Frontiers in Physics*, 6:10, 2018.

[149] Leszek Roszkowski et al. WIMP dark matter candidates and searches—current status and future prospects. *Reports on Progress in Physics*, 81(6):066201, 2018.

[150] Igor Ostrovskiy and Kevin O'Sullivan. Search for neutrinoless double beta decay. *Modern Physics Letters A*, 31(18):1630017, 2016.

[151] Naba K Mondal. India-based neutrino observatory (INO). *The European Physical Journal Plus*, 127(9):1–6, 2012.

[152] S. Thakur, A. Mazumdar, R. Shah, V. Vatsa, et al. Background Estimation Studies for Positron Double Beta Decay. *arXiv preprint arXiv:2111.08825*, 2021.

[153] A. Bettini. The world deep underground laboratories. *The European Physical Journal Plus*, 127(9):1–11, 2012.

[154] D.-M. Mei, S. R. Elliott, A. Hime, V. Gehman, and K. Kazkaz. Neutron inelastic scattering processes as a background for double-β decay experiments. *Phys. Rev. C*, 77:054614, 2008.

[155] S. R. Elliott, V. E. Guiseppe, B. H. LaRoque, R. A. Johnson, and S. G. Mashnik. Fast-neutron activation of long-lived isotopes in enriched ge. *Phys. Rev. C*, 82:054610, 2010.

[156] N. Dokania, V. Singh, S. Mathimalar, C. Ghosh, et al. Study of neutron-induced background and its effect on the search of $0\nu\beta\beta$ decay in ^{124}Sn. *Journal of Instrumentation*, 9(11):P11002–P11002, 2014.

[157] D.A. Brown et al. ENDF/B-VIII.0: The 8th Major Release of the Nuclear Reaction Data Library with CIELO-project Cross Sections, New Standards and Thermal Scattering Data. *Nuclear Data Sheets*, 148:1–142, 2018. Special Issue on Nuclear Reaction Data.

Nuclear Inst. and Methods in Physics Research, A 1038 (2022) 166892

Contents lists available at ScienceDirect

Nuclear Inst. and Methods in Physics Research, A

journal homepage: www.elsevier.com/locate/nima

Radiopurity studies of a rock sample from the Aut region

Swati Thakur [a], A. Mazumdar [b], Nishant Jangid [c], V. Vatsa [d,e], M.S. Pose [c], S. Mallikarjunachary [c], S. Pal [f], V. Nanal [c,*], R.G. Pillay [a], P.K. Raina [a], Pushpendra P. Singh [a], S.K. Dhiman [g]

[a] Department of Physics, Indian Institute of Technology Ropar, Rupnagar, Punjab 140001, India
[b] TIF-AWaDH, Indian Institute of Technology Ropar, Rupnagar, Punjab 140001, India
[c] Department of Nuclear and Atomic Physics, Tata Institute of Fundamental Research, Mumbai 400005, India
[d] India-based Neutrino Observatory, Tata Institute of Fundamental Research, Mumbai 400005, India
[e] Homi Bhabha National Institute, Anushaktinagar, Mumbai 400094, India
[f] Pelletron Linac Facility, Tata Institute of Fundamental Research, Mumbai 400005, India
[g] Department of Physics, Himachal Pradesh University, Shimla 171005, India

ARTICLE INFO

Keywords:
Low background measurements
Gamma ray spectroscopy
Neutron activation studies

ABSTRACT

Efforts are underway to set up an underground laboratory in India for rare event studies like double beta decay, dark matter, etc. For such experiments, mitigation of radiation background is of paramount importance and understanding ambient background at the site, originating from the rock, is one of the crucial factors. With this motivation, the radiopurity studies of a rock sample from the potential laboratory site in the Aut tunnel of Himachal Pradesh (India) have been carried out using the TIFR low background experimental setup (TiLES). The concentration of ^{40}K in Aut rock is observed to be lower by a factor of ∼1000 as compared to the samples from BWH (Bodi West Hill), Tamil Nadu (India), current designated site for India-based Neutrino Observatory. The natural radioactive trace impurity ^{232}Th is lower in the Aut rock, while ^{238}U is somewhat higher than the BWH rock. Overall, the ambient gamma ray background at Aut is expected to be lower than the BWH, while ambient neutron background is expected to be similar. Further, to assess the neutron-induced long lived activity, fast neutron activation studies have been carried out on both the Aut and BWH rock samples at the Pelletron Linac Facility, Mumbai.

1. Introduction

Recently, experimental investigations of physics beyond the standard model, such as neutrino oscillations, neutrinoless double beta decay (NDBD), dark matter search, etc., have attracted much attention worldwide [1–3]. These studies for rare events demand stringent background levels. The ultimate background levels (N_{bkg}) achieved in the region of interest are 4.0 $\times 10^{-4}$ keV^{-1} kg^{-1} y^{-1} for KamLAND-Zen NDBD experiment [4] and 8.5 $\times 10^{-2}$ keV ee^{-1} kg^{-1} y^{-1} for XENON1T dark matter experiment [5]. It is important to note that minimizing the ambient background is a crucial aspect for rare event studies. Some of the major sources of the background radiation are cosmic rays, long-lived primordial radionuclides ($T_{1/2} \sim 10^8$ - 10^{10} y), cosmogenic radionuclides ($T_{1/2} \sim$ days - years) and neutron induced activity produced in and around the detector [3]. In order to suppress the cosmic muon background (by about 5–6 orders of magnitude), these experiments are located in underground laboratories, typically with a rock overburden of more than 500 m. In an underground laboratory, the ambient gamma and neutron background at the site and the background arising from penetrating (high energy) cosmic muons, can be the limiting factors for the sensitivity of the experiment.

The gamma ray background originates from natural radioactivity due to trace elements like ^{40}K, ^{232}Th, ^{235,238}U in the rock, and the neutron induced activities of the constituents of the rock. The concentrations of these trace elements, and subsequently the associated gamma/neutron backgrounds, are known to exhibit geographical variation, depending on local geological conditions. Amongst the natural gamma ray background, high energy gamma rays ($E \geq 2$ MeV) produced in the natural radioactivity chains of ^{238}U and ^{232}Th e.g. 2448 keV (^{214}Bi) and 2615 keV (^{208}Tl), respectively, are of significant concern. The neutron background is usually categorized in two parts -low energy neutrons ($E_n < 20$ MeV), originating from the spontaneous fission of uranium and (α, n) reactions in the rock, and very high energy neutrons ($E_n > 1$ GeV) produced by muon-induced interactions in the rocks or materials surrounding the detector. The flux of high energy neutrons is expected to be smaller by a factor of 10^2 - 10^3 as compared to the low energy neutrons [6]. The inelastic scattering of neutrons (n, n$'\gamma$) and neutron-capture (n, γ) with the detector and/or surrounding materials can also lead to the production of high energy

---

[*] Corresponding author.
E-mail address: nanal@tifr.res.in (V. Nanal).

https://doi.org/10.1016/j.nima.2022.166892
Received 22 February 2022; Received in revised form 17 May 2022; Accepted 17 May 2022

gamma rays. The neutron-activated reaction products can have wide-ranging half-lives (~ min to ~ years) and the contribution of long-lived activities is difficult to mitigate.

In India, driven by the interest in rare decay studies, a proposal for an underground laboratory has been initiated. A laboratory with about 1 km rock overburden is proposed in Bodi West Hills (BWH) of the Theni district in Tamil Nadu (Lat. North 9°57'47.65'' and Long. East 77°16'22.55'') [7]. Also, a small laboratory (approximately 5 m × 5 m × 2.2 m) has been set up at UCIL, Jaduguda, Jharkhand with a rock cover of 555 m inside an Uranium mine [8]. Another potential site with a reasonable rock overburden (~ 500 m) has been identified in the existing Aut tunnel, Himachal Pradesh (Lat. North 31.725° and Long. East 77.206°). The Aut rock is Dolomite type, while the BWH rock is Charnockite. To assess the feasibility of this site, the radiation background studies are important and hence the radiopurity studies of the Aut rock samples have been carried out. The concentrations of trace level natural radioactive elements are determined and are compared with the BWH rock sample data. Additionally, the neutron activation measurements have been performed for both Aut and BWH rock samples, with an emphasis to study long-lived activities.

The paper is organized as follows: Experimental details for the radiopurity and neutron activation measurements are described in Section 2. The analysis of the radiopurity measurements and the estimation of trace level radioimpurities are discussed in Section 3.1. The results of the neutron induced activities are presented in Section 3.2. Finally, the results are summarised in Section 4.

2. Experimental details

The rock samples used in the present study were collected from the Aut tunnel (from the location of the proposed laboratory site) and the BWH site. The latter sample was bored from a depth of ~ 30 m. The densities of the Aut rock sample and the BWH rock were measured to be ~ 2.93 g/cm^3 and ~ 2.89 g/cm^3, respectively. The gamma ray spectra were measured using two low background counting setups at TIFR (Mumbai) at sea level - TiLES (TIFR Low background Experimental Setup) [9] and a coincidence setup of two low background HPGe detectors (D1-D2) [10]. Neutron activation studies were performed at the fast neutron irradiation setup at the Pelletron Linac Facility (PLF), Mumbai.

2.1. Low background counting setups

The TiLES consists of a ~ 70% relative efficiency high-purity Germanium (HPGe) detector (ORTEC, Model no GEM75-95-LB-C-HJ) in a passive shielding of 10 cm thick low activity Pb (< 0.3 Bq/kg of ^{210}Pb) and 5 cm oxygen-free high thermal conductivity Cu. The setup has a provision to further reduce the ambient background by employing a cosmic muon veto and continuous dry nitrogen flushing. However, the cosmic muon veto and dry nitrogen flushing were not used for the present measurements as the samples had sufficiently high activity compared to the ambient background as well as to facilitate frequent sample changes. The D1-D2 coincidence setup consists of two identical low background cryocooled HPGe detectors (ORTEC, Model no GEM30P4-83-RB). Both detectors have ~ 33% relative efficiency and have a carbon fiber housing with a 0.9 mm thick front window. The D1-D2 detectors are mounted in a close geometry, facing each other at a distance of about 2.5 cm, surrounded by two layers of passive shielding with 5 cm thick low activity lead (< 0.3 Bq/kg of ^{210}Pb) inside and 5 cm thick (< 21 Bq/kg of ^{210}Pb) outside. As both D1 and D2 are expected to be identical, the optimized geometry of D1 [11] was adopted for simulation of the photopeak efficiency of both the detectors (D1 and D2).

Data were recorded using 14-bit, 100 MHz CAEN 6724 series commercial digitizers using the trapezoidal filter for pulse height determination. The digital parameters were optimized to achieve the best energy resolution. For both setups, the optimum trapezoidal filter settings, namely, input signal decay time (T_{decay}), trapezoidal rise time (T_{rise}) and trapezoidal flat top time ($T_{flattop}$) were set at 50 μs, 5.5 μs and 1.3 μs, respectively. The typical resolution at 1460 keV was ~ 2.6 keV in TiLES and ~ 3.5 keV for D2. The data were analyzed offline using ROOT [12] and LAMPS [13] software. The energy calibration was obtained using standard gamma ray sources prior to the measurement and were monitored with known background lines over an energy range of 120–2615 keV. The observed drifts were less than 1 keV over an extended period of one year. The dead time was monitored with a standard 10 Hz pulser and was found to be negligible (< 0.1%). Fig. 1 shows the background measured in TiLES (with the perspex sample mounting plate) for a total duration of 69 d, acquired at different times over a period of about 7 months.

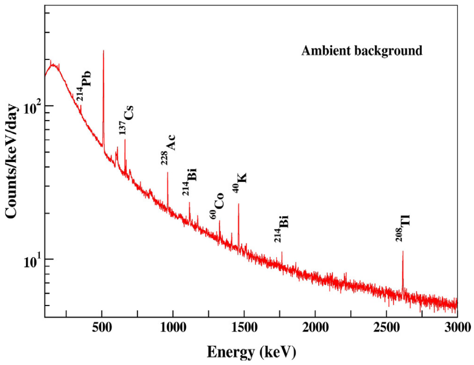

Fig. 1. A typical gamma ray spectrum of the ambient background in the TiLES, where the prominent gamma rays are labelled (counting time $t = 69$ d).

For radiopurity measurements both the Aut and BWH rock samples were mounted on the sample plate at $d \sim 10$ mm from the face of the detector in TiLES. The details of the samples, namely, mass and counting time are given in Table 1. The photopeak efficiencies (ϵ) for various gamma rays in each rock sample were obtained using GEANT4 based simulation program [14] for respective counting configurations. Since the rocks were of irregular shape, the geometry of the sample was simulated by approximating the closest regular shapes corresponding to the sample volume. The gamma rays were assumed to originate from trace impurities uniformly distributed within the sample. For each energy, 10^6 (1 M) gamma rays were generated within the sample isotropically and consequently statistical errors in simulated photopeak efficiencies were negligible (< 1%). Further, the uncertainties in the detection efficiency due to variation in rock dimensions about mean values were estimated. Since the largest linear dimension of both samples were smaller than the detector crystal size, only the variation in thickness is expected to have a pronounced effect on the efficiency. The thickness variation over the sample size was found to be 8.1–8.6 mm for AUT0 and 9–12 mm for BWH0. In simulation, different shapes were generated corresponding to different thicknesses, by appropriately modifying the cross sectional area to keep the volume constant. The ϵ_γ is taken as average value of ϵ for different shapes, while the error in the efficiency is calculated as $(\epsilon_{max} - \epsilon_{min})/2$. The overall observed spread in efficiency due to shape variation was $< \pm 5\%$, for the energy range of interest ($E_\gamma = 186 - 2615$ keV). Another important aspect that needs to be taken into consideration, especially for close counting geometry, is the coincident summing of multiple gamma rays in the decay cascade. While detailed simulations are essential for multi-stage decay cascades, a simple estimation can be done for a two gamma cascade $2 \xrightarrow{\gamma_2} 1 \xrightarrow{\gamma_1} 0$. If ϵ_i^{tot} is the total detection probability of γ_i (i.e. Compton

Table 1
Details of the rock samples for radiopurity study in TiLES.

Sample	Type	Mass (g)	Counting time (d)
BWH0	Charnockite	32.2	24.9
AUT0	Dolomite	27.5	23.4

and photopeak), then the loss due to the coincident summing (I_1^{sum}, I_2^{sum}) to the intensity of γ_1 and γ_2 ($I_{\gamma 1}$ and $I_{\gamma 2}$, respectively) can be estimated as

$$\begin{aligned} I_1^{sum} &= \epsilon_2^{tot} \cdot p_1 \cdot p_2 \cdot f_2 \\ I_2^{sum} &= \epsilon_1^{tot} \cdot p_1 \cdot p_2 \cdot f_2 \end{aligned} \quad (1)$$

where p_1 and p_2 are the gamma decay probabilities of levels 1 and 2, respectively and f_2 is the feeding fraction for the level 2. The effective net intensity for γ_i can be written as

$$I_i^{net} = I_{\gamma i} - I_i^{sum} \quad (2)$$

Here, both gamma rays are assumed to be emitted isotropically, neglecting angular correlations. It is evident that the coincident summing probability of 3 or more gamma rays is insignificant. However, the complex decay cascades with multiple parallel decay branches are not considered for estimating elemental concentration. It should be mentioned that the systematic errors in the simulated efficiencies of the optimized models for TiLES and D1/D2 are 5% and 8%, respectively. Total uncertainties quoted include all contributions, namely, statistical, systematic (due to detector modelling) and coincident summing.

2.2. Neutron activation

For neutron activation measurements, fast neutrons having a broad energy range up to ∼ 20 MeV were produced at the irradiation setup of the Pelletron Linac Facility, Mumbai, using ^{9}Be(p,n)^{9}B reaction ($Q = -1.85$ MeV) with ∼ 5 mm thick ^{9}Be target [15]. The maximum proton beam energy (22 MeV) was chosen to cover the energy range of neutron spectra originating from fission and (α, n) reactions in the rocks [16]. Irradiation at lower proton beam energy (12 MeV) was carried out for independent verification of some of the channels by comparison of relative yields. Although the primary interest in the present work was to study the Aut rock samples, neutron activation for BWH rock was also carried out for comparison at one energy. The neutron flux was estimated using the ^{56}Fe(n,p)^{56}Mn reaction [17]. For this purpose, the ^{nat}Fe foils (∼ 4.5 – 10 mg/cm^2) were placed in front and back of the rock samples during each irradiation. The activity of ^{56}Mn in the irradiated iron foils was extracted from the yield of 846.8 keV gamma ray, which was measured with the D2 or TiLES. The yield for 846.8 keV was corrected for losses due to coincident summing in the detector with 1810.7 keV (I_γ = 26.9%) or 2113.1 keV (I_γ = 14.2%). The corrections due to coincident summing from other low intensity gamma rays (branching ratio < 1.5%) are found to be negligible. The energy averaged neutron flux $\langle \phi_n \rangle$ is obtained using relation

$$\langle \phi_n \rangle = \frac{\sum_{E_n} \sigma(E_n)\phi_n(E_n) dE_n}{\sum_{E_n} \sigma(E_n) dE_n} \quad (3)$$

where $\sigma(E_n)$ is the neutron induced reaction cross section and $\phi_n(E_n)$ is the neutron flux per unit energy at E_n. The numerator is derived from the measured ^{56}Mn activity with appropriate corrections for the decay during irradiation and cooldown time. The cross sections for the ^{56}Fe(n,p)^{56}Mn reaction were taken from the ENDF/B-VIII.0 library [18]. The error in $\langle \phi_n \rangle$ is largely limited by the statistical error in extracting the yield of 846.8 keV gamma ray. It should be noted that the uncertainties in the neutron cross sections have not been considered in the final errors. Table 2 gives the details of the rock samples and irradiation (average proton beam current, irradiation time t_{irr}, etc.)

Table 2
Details of the irradiation of rock samples together with maximum neutron energy (E_n) and estimated energy averaged neutron flux.

Sample	Mass (g)	E_p (MeV)	$\langle I \rangle$ (nA)	t_{irr} (h)	E_n (MeV)	$\langle \phi_n \rangle$ (10^6 n cm^{-2} s^{-1} MeV^{-1})
AUT1A	10.6	22	136	15.5	19.9	1.9 (2)
AUT4E	6.7	12	148	16.0	9.9	0.51 (4)
BWH2B	5.5					

The irradiated rock samples and iron foils were removed from the irradiation setup after a sufficient cool-down time t_c (≥ 1–2 hr). Hence, some of the short-lived activities could not be measured. The offline counting of the irradiated rock samples was carried out in a close geometry in both setups and reaction products were identified by their characteristic gamma rays. In case of low energy irradiation, where both BWH and Aut rock samples were irradiated simultaneously for optimal use of the beam time, priority for counting in the off-line setups was given to the irradiated Aut samples. Spectra of rock samples were recorded at different cool-down times (t_c) to track activities with varying half-lives, namely, ∼ mins to few ∼ days. The D1-D2 setup was mainly used for detection of coincident gamma rays for confirmation of the nuclide identification.

3. Analysis and results

3.1. Radiopurity measurements

A comparison of gamma ray spectra of the AUT0 and BWH0 rock samples in TiLES is shown in Fig. 2 along with the ambient background. Both the rock spectra are clearly dominated by gamma lines from the ^{238}U and ^{232}Th decay chains, as compared to the ambient background. The high energy gamma rays from ^{208}Tl (end product in ^{232}Th decay chain) - 2614.5 keV (I_γ = 99.75%) are of particular concern. A sum energy peak at 3197.7 keV, arising from the coincident summing of 2614.5 and 583.2 keV is clearly visible in the BWH0 spectrum, but not observed in the AUT0 spectrum. The BWH0 also shows a strong peak at 1460.8 keV, indicating large amount of ^{40}K in the rock. This also results in significantly enhanced background at lower energies, $E < 1500$ keV, for the BWH0 as compared to the AUT0.

Although many gamma rays from ^{232}Th and ^{238}U decay chains are visible, not all could be considered for trace impurity analysis. Some of the gamma rays are mixed from different radionuclides - for example, the observed gamma line at 242.6 keV has contribution from ^{214}Pb in ^{238}U decay chain (242.0 keV) and ^{224}Ra in ^{232}Th decay chain (241.9 keV), similarly for 351.9 keV (^{214}Pb, ^{211}Bi), 185.9 keV (^{226}Ra, ^{235}U) etc. Hence, only those gamma rays which could be unambiguously assigned to a particular nuclide were considered in further analysis. Further, a subset was selected from coincident summing corrections as explained earlier. To extract the peak area, the photopeaks of interest were fitted with a gaussian + background (second order polynomial). The specific activity, that is, activity per unit mass $A_E(\gamma)$ corresponding to a given transition of the radionuclide was determined using

$$A_E(\gamma) = \frac{N_{obs}}{I_\gamma^{net} . \epsilon_\gamma . m . t} \quad (4)$$

where N_{obs} is the net observed counts in the photopeak after correcting for the ambient background, I_γ^{net} is the branching ratio of the gamma ray after summing correction, ϵ_γ is the photopeak detection efficiency computed using GEANT4 simulation [9], m is the mass of the sample and t is the counting time. The I_γ was corrected for coincident summing estimate of 2 gamma cascades, as explained earlier. However, the coincident summing is neglected if summing correction is significantly less than the statistical error. In the cases where no measurable activity could be observed above the ambient background (at the present

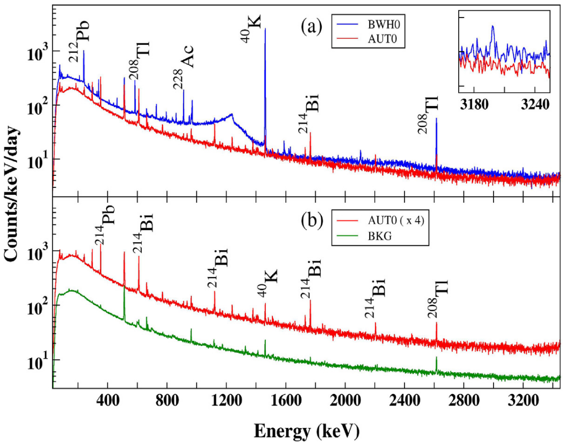

Fig. 2. Gamma ray spectra measured in TiLES for (a) AUT0 (red line) and BWH0 (blue line), (b) ambient background (green line) and AUT0, scaled by an arbitrary factor of 4 for better visualisation. The inset in top panel shows the presence of the sum energy peak at 3197.7 keV in the BWH rock.

Table 3
Observed specific activities for different radionuclides in the AUT0 and BWH0 rocks.

Parent radionuclide	Daughter radionuclide	E_γ	AUT		BWH	
		(keV)	A_E (mBq/g)	$\langle A_E \rangle$ (mBq/g)	A_E (mBq/g)	$\langle A_E \rangle$ (mBq/g)
^{40}K		1460.8	<1	<1	1064 (68)	1064 (68)
^{232}Th	^{212}Pb	238.6	0.50 (7)	0.50 (6)	15 (1)	14.7 (6)
	^{228}Ac	911.2	0.5 (2)		15 (1)	
		969.0	–		14 (1)	
^{238}U	^{214}Pb	295.3	8.2 (5)	8.2 (3)	1.2 (2)	1.2 (1)
	^{214}Bi	609.3	7.7 (4)		1.5 (2)	
		1120.3	8.1 (5)		–	
		1377.7	12 (2)		–	
		1729.6	13 (2)		–	
		1764.5	7.8 (7)		0.9(3)	
		1847.5	14 (3)		–	
		2204.1	10 (1)		–	

Table 4
Trace radioimpurity concentrations in AUT0 and BWH0 rocks.

Sample	Parent radionuclide	Concentration (ppb)
AUT0	^{40}K	<2
	^{232}Th	12 (1)
	^{238}U	60 (2)
BWH0	^{40}K	2179 (139)
	^{232}Th	338 (14)
	^{238}U	9 (1)

sensitivity of the setup), the upper limit on the specific activity (L_A) was estimated from the minimum detectable counts (L_D) using Currie's method [19] as

$$L_A = \frac{L_D}{I_\gamma . \epsilon_\gamma . m.t} \tag{5}$$

where $L_D = 4.65\ \sigma_B + 2.7$ and σ_B is the standard deviation in the background counts. The extracted specific activities for the AUT0 and BWH0 samples are listed in Table 3. Due to its small isotopic abundance, the concentration of ^{235}U could not be determined in the present work.

The mean specific activity ($\langle A_E \rangle$) is obtained by weighted average over measured specific activities of different gamma rays/daughter nuclides in the given decay chain. In order to extract the concentrations of the parent radionuclides (^{232}Th and ^{238}U), the data were analyzed under the assumption of secular equilibrium within samples. The atomic fraction F_E of the trace radioimpurity in the rock sample was computed using

$$F_E\,(ppb) = \frac{A_E . M}{\lambda . N_A} 10^6 \tag{6}$$

where M is the molar mass (in g/mole), λ is the decay constant (in s^{-1}) and N_A is Avogadro's number.

For the BWH0 sample, the molar mass was determined from the rock composition obtained from the Secondary Ion Mass Spectroscopy (SIMS) results reported in Ref. [16]. Further, in the case of the AUT0 sample, since the rock composition was not available, the molar mass was assumed to be identical to that of the BWH0. This is a reasonable assumption as the molar mass is not expected to vary significantly for different types of rocks. The concentrations of the trace radioimpurities for both the rock samples are listed in Table 4.

From the comparison of trace element concentrations in AUT0 and BWH0 in Table 4, it is evident that the ^{40}K content in the AUT0 is significantly lower by a factor of ∼1000. The content of ^{232}Th is also lower in the AUT0 by a factor of ∼28, whilst that for the ^{238}U is higher by a factor of ∼7. The concentrations of ^{40}K and ^{232}Th in the BWH0 rock obtained in the present study are similar to earlier

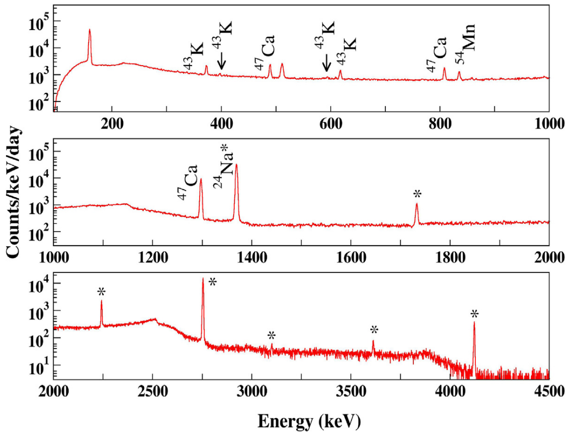

Fig. 3. Gamma ray spectrum of the irradiated AUT1A rock ($E_p = 22$ MeV) after $t_c = 5$ d. Various ^{24}Na gamma rays and associated single/double escape peaks are indicated (*).

reported values [16], namely, 2520 ppb (by SIMS) and 224 ppb (by Inductively Coupled Plasma Mass Spectroscopy i.e. ICPMS), respectively. However, for ^{238}U the present value is significantly lower than that reported with ICPMS, namely 60 ppb [16]. It should be pointed out that radiopurity measurements reflect average over a larger finite sample size as compared to the ICPMS. Hence, the observed difference may arise due to the non-homogeneous distribution of radionuclides within the rock. The variation in trace impurity content was also probed by measurements on different BWH/Aut samples from the same location. While no differences were observed in the spectra at the measured level of sensitivity for three different Aut rock samples ($t \sim 2$ weeks), two BWH rock samples showed $\sim 33\%$ and $\sim 17\%$ variation for ^{232}Th and ^{40}K, respectively.

As a result of lower levels of ^{40}K and ^{232}Th in AUT0, the yield of the high energy gamma rays of 1460.8 keV and 2614.5 keV is significantly reduced as compared to the BWH0. The higher ^{232}Th content in BWH0 is also reflected in the presence of 3197.7 keV gamma ray (see inset of Fig. 2). The presence of high energy gamma rays and the corresponding Compton background leads to an overall enhancement in background at lower energies, i.e. in the region of interest relevant to low background experiments ($E \sim 2$ MeV). Thus, the smaller ^{232}Th content in the Aut rock appears to be advantageous.

The observed specific activities in the AUT0 (see Table 3) can be compared with those at the well established underground facility LNGS, which also has dolomitic limestone rock as well as the worldwide average. The measured average specific activities in LNGS [20] are 26 (2) mBq/g for ^{40}K, 1.5 (1.0) mBq/g for ^{232}Th and 1.8 (1.0) mBq/g for ^{238}U. Thus, the Aut rock appears to have lower levels of both ^{40}K and ^{232}Th, while ^{238}U content is somewhat higher. It is important to note that the trace radioactive element content in Aut rock is significantly lower than the worldwide average, namely, 400, 30 and 35 mBq/g for ^{40}K, ^{232}Th and ^{238}U, respectively [21]. The neutron flux at the BWH site is estimated to be 2.76 (47) $\times 10^{-6}$ n cm^{-2} s^{-1} with 60 ppb for ^{238}U and 224 ppb of ^{232}Th [16] trace impurities in the rock. The low energy neutron flux produced by spontaneous fission and (α,n) reactions in the rocks is dominated by ^{238}U. The measured concentration of ^{238}U in the AUT0, 60 (2) ppb, is similar to that used for the neutron flux estimation at the BWH site (namely, 60 ppb). Consequently, the expected neutron flux at the Aut site will be similar to that for the BWH site, i.e., $\sim 3 \times 10^{-6}$ n cm^{-2} s^{-1}. It should be noted that this estimate is comparable to other underground laboratories, although concrete wall contributions will have to be taken into consideration at the actual site. Thus, Aut site is expected to have a overall lower gamma ray background and similar neutron background as compared to the BWH and subsequently appears to be a suitable site for laboratory from radioactive background considerations.

3.2. Neutron activation measurements

Figs. 3 and 4 show gamma ray spectra of the irradiated rocks at $E_p = 22$ and 12 MeV, respectively. Various observed reaction channels such as (n, γ), (n,p), (n, α), and (n,2n) are listed in Table 5 together with respective $T_{1/2}$ and prominent gamma rays. The threshold neutron energy E_{th} corresponding to $\sim 1\,\mu$b cross section is also listed in the table.

In the AUT1A spectrum, the dominant contribution at small t_c (i.e. $\lesssim$2–3 days) comes from the ^{24}Na activity ($T_{1/2} = 15$ h). The high energy gamma rays, namely, 1368.6 keV and 2754.0 keV, and the respective single/double escape peaks are clearly visible in the figure. It is important to note that the associated Compton background also leads to the enhancement of the low energy background. The ^{24}Na can be formed either via ^{23}Na(n, γ) or ^{24}Mg(n,p) or ^{27}Al(n, α). With fast neutrons, ^{23}Na(n, γ) is less probable as compared to ^{24}Mg(n,p) or ^{27}Al(n, α). However, the relative contributions of these two channels will depend on the actual rock composition, namely, Al/Mg content. It is seen that the BWH rock contains more aluminum than magnesium (from the SIMS data). The Aut rock also shows the presence of ^{42,43}K and ^{47}Ca originating from the Calcium isotopes, which is present in dolomite rock. These reaction products are relatively short-lived ($T_{1/2} \leq$ few days) and give rise to low energy gamma rays, $E_\gamma < 1300$ keV, during the decay. The long-lived activities ^{22}Na ($T_{1/2}$ = 2.6 y) and ^{54}Mn ($T_{1/2}$ = 0.855 y) were measured after sufficiently long cool-down time, which ensured that dominant short-lived products have diminished. Further, identification of long-lived activities ^{22}Na and ^{46}Sc were confirmed by the detection of coincident gamma rays in the decay cascade in D1-D2 setup. The measured half-life of the reaction products were found to be in good agreement with the reference values [22]. Fig. 5 shows typical decay curves for a couple of reaction products in the AUT1A sample ($E_p = 22$ MeV).

From the measured yield of the characteristic gamma ray during time t_1 to t_2, the saturated activity A_∞ [23] (for $t_{irr} \rightarrow \infty$) can be obtained as

$$A_\infty = \frac{\lambda N_{obs}}{\epsilon_\gamma I_\gamma^{net}(1 - e^{-\lambda t_{irr}})e^{\lambda t_{irr}}(e^{-\lambda t_1} - e^{-\lambda t_2})} \tag{7}$$

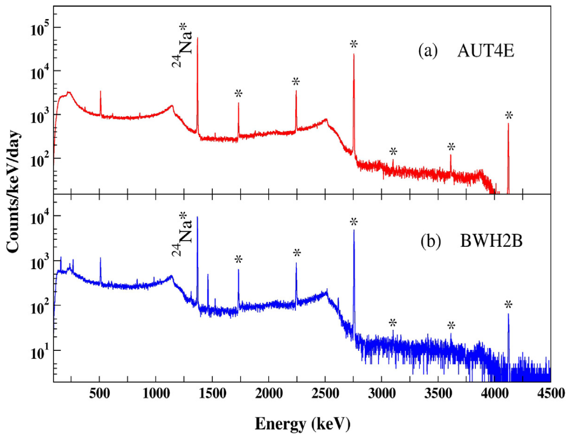

Fig. 4. Gamma ray spectra of the irradiated ($E_p = 12$ MeV) rock samples after $t_c = 1.7$ d, (a) AUT4E in TiLES and (b) BWH2B in D1. The * mark has same meaning as in Fig. 3.

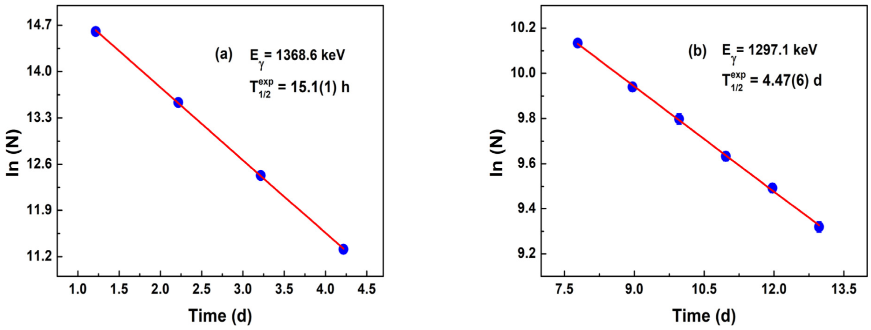

Fig. 5. Decay curves (a) $E_\gamma = 1386.6$ keV of ^{24}Na and (b) $E_\gamma = 1297.1$ keV of ^{47}Ca, where N are photopeak counts corresponding to integration time of 3 h and 24 h for (a) and (b), respectively. Errors are smaller than the symbol size.

Table 5
Observed neutron-induced reaction products in Aut and BWH rocks together with the threshold neutron energy E_{th} corresponding to ∼1 μb cross section. The half-life ($T_{1/2}$) and prominent gamma rays (E_γ) are also listed.

Reaction channel	E_{th} (MeV)	$T_{1/2}$ (reference)	$T_{1/2}$ (measured)	E_γ (keV)
^{48}Ti(n,p)^{48}Sc	5	1.82 d	–	983.5, 1037.5, 1312.1
^{48}Ca(n,2n)^{47}Ca	10	4.54 d	4.47 (6) d	489.2, 807.9, 1297.1
^{24}Mg(n,p)^{24}Na,^{27}Al(n, α)^{24}Na	5, 4.64	15 h	15.04 (5) h	1368.6, 2754.0
^{43}Ca(n,p)^{43}K	1.8	22.3 h	22 (1) h	373.8, 617.5
^{46}Ti(n,p)^{46}Sc	3	83.79 d	–	889.3, 1120.5
^{23}Na(n,2n)^{22}Na	13	2.60 y	–	511.0, 1274.5
^{39}K(n,2n)^{38}K	14.5	7.64 min	–	2167.5
^{41}K(n,p)^{41}Ar	3	1.82 h	–	1293.6
^{54}Fe(n,p)^{54}Mn	0.72	312 d	279 (68) d	835.0
^{56}Fe(n,p)^{56}Mn	4	2.58 h	–	846.8
^{43}Ca(n,n'p)^{42}K,^{41}K(n, γ)^{42}K	12, 1	12.36 h	12.8 (1) h	1524.7

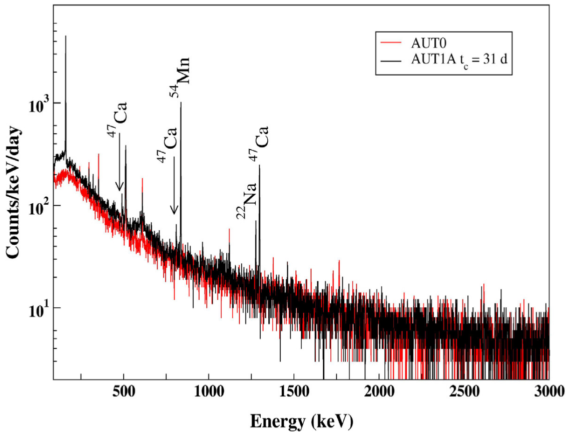

Fig. 6. Comparison of gamma ray spectra of the irradiated ($E_p = 22$ MeV) AUT1A (black line) after $t_c = 31$ d and pristine AUT0 (red line) samples. Note that AUT1A (10.6 g) has smaller mass than AUT0 (27.5 g).

Table 6
Saturated activity A_∞ per unit mass for the prominent reaction products. The E_{coin}, emitted in coincidence with E_γ, which has been considered for the summing corrections are also listed.

Nuclide	E_γ (keV)	E_{coin} (keV)	A_∞ (E_p = 12 MeV) (Bq/g)	A_∞ (E_p = 22 MeV) (Bq/g)
^{22}Na	1274.5	511.0	–	9 (2)
^{24}Na	1368.6 2754.0	2754.0 1368.6	336 (14)	6536 (299)
^{42}K	1524.6	–	4.6 (6)	62 (13)
^{43}K	617.5	372.8	0.52 (8)	18 (1)
^{47}Ca	1297.1	–	–	54 (3)

The saturated activity A_∞ per unit mass has been estimated for the prominent reaction products in the Aut rock and are presented in Table 6. The coincident summing corrections have been taken into consideration as samples were counted in the close geometry (see eq. (2)) and were found to be around 10–16% for the nuclides ^{22}Na, ^{24}Na and ^{43}K. The nuclides ^{22}Na and ^{47}Ca are absent in the AUT4E sample, which is irradiated at lower energy ($E_p = 12$ MeV). This is expected as both these nuclides are produced via (n, 2n) reaction which have higher threshold energies and hence require $E_n > 10$ MeV. The differences in the A_∞ per unit mass at $E_p = 12$ and 22 MeV correspond to contribution from high energy neutrons (i.e. $E_n \sim 10$–20 MeV) and can also be estimated from Table 6. It is evident that production of both ^{24}Na and ^{42,43}K is dominated by the high energy neutrons.

It should be mentioned that it is not possible to extract the concentration of the parent nuclides since the precise shape of the neutron energy distribution is not available in the present experiment. Moreover, in fast neutron induced reactions, multiple reaction pathways can lead to the production of a particular isotope (see Table 5). Hence, a thermal neutron activation study would be desirable for quantitative estimation of the trace elements and/or rock composition.

To understand the impact of long-lived activities, the spectrum of the irradiated Aut rock after $t_c \sim 30$ d was compared with the spectrum prior to the irradiation. The effect of the remnant activities is reflected in the enhancement in the background at low energies as well as in the presence of few characteristic gammas (100–1300 keV) and can be seen in Fig. 6.

Overall, the BWH rock spectrum shows the presence of Potassium neutron induced reaction products, while that for Aut sample is dominated by Calcium products. The Aut rock appears to have mostly short-lived activities. However, long-lived products like ^{54}Mn and ^{47}Ca can result in the enhanced background at $E < 1000$ keV. The high energy gamma rays from ^{24}Na need to be adequately shielded, as sum peak can contribute to the background above 2 MeV, which is region of interest for many NDBD studies.

4. Summary

The radiopurity studies of a rock sample from the potential underground laboratory site in the Aut tunnel have been carried out using the TiLES. The concentration of ^{40}K in Aut rock is observed to be lower by a factor of ∼1000 as compared to the BWH rock sample. The measured specific activities of trace impurities ^{232}Th and ^{238}U in the Aut rock are 0.50 (6) and 8.2 (3) mBq/g, respectively. In comparison with BWH rock, the Aut rock appears to have lesser amount of ^{232}Th and somewhat higher amount of ^{238}U. It is important to note that Aut rock trace impurity concentrations are considerably lower than the respective worldwide average values. The low energy neutron flux arising due to spontaneous fission and (α,n) reactions, dominated by ^{238}U, is expected to be around 3×10^{-6} n cm^{-2} s^{-1}, which is similar to other underground laboratories. The fast neutron activation studies of both Aut and BWH rock samples have indicated presence of long lived activities like ^{54}Mn (0.855 y) and ^{22}Na (2.60 y), but the resultant gamma ray energies are lower than 1500 keV and no significant contributions at $E > 2$ MeV are observed. Overall, the ambient gamma ray background at Aut is expected to be lower than the BWH, while the low energy neutron background is expected to be similar. Hence, the Aut appears to be a suitable site for laboratory from radioactive background considerations.

Declaration of competing interest

The authors declare that they have no known competing financial interests or personal relationships that could have appeared to influence the work reported in this paper.

Acknowledgments

We are grateful to Project Director, NHAI, Pandoh-Aut-Takoli Tunnels section for helping us to collect the rock samples from the AUT tunnel (T02-02) at Mandi-Kullu National Highways. We thank Mr. K.V. Divekar for assistance during the measurements, the PLF staff for the smooth operation of the machine and the target lab staff for preparation of Fe foils. This work is supported by the Department of Atomic Energy, Government of India (GoI), under Project No. RTI4002. S. Thakur acknowledges the Ministry of Education, GoI, for Ph.D. research fellowship, and TIFR for supporting the visit related to this work.

References

[1] Y. Farzan, M. Tortola, Neutrino oscillations and Non-Standard Interactions, Front. Phys. 6 (2018) 10, http://dx.doi.org/10.3389/fphy.2018.00010.

[2] R. Leszek, et al., WIMP dark matter candidates and searches–current status and future prospects, Rep. Progr. Phys. 81 (6) (2018) 066201, http://dx.doi.org/10.1088/1361-6633/aab913.

[3] M.J. Dolinski, et al., Neutrinoless double-beta decay: Status and prospects, Ann. Rev. Nucl. Particle Sci. 69 (1) (2019) 219–251, http://dx.doi.org/10.1146/annurev-nucl-101918-023407.

[4] I. Ostrovskiy, K. O'Sullivan, Search for neutrinoless double beta decay, Modern Phys. Lett. A 31 (18) (2016) 1630017, http://dx.doi.org/10.1142/S0217732316300172.

[5] E. Aprile, et al., Dark Matter Search Results from a One Ton-Year Exposure of XENON1T, Phys. Rev. Lett. 121 (2018) 111302, http://dx.doi.org/10.1103/PhysRevLett.121.111302.

[6] D.-M. Mei, A. Hime, Muon-induced background study for underground laboratories, Phys. Rev. D 73 (2006) 053004, http://dx.doi.org/10.1103/PhysRevD.73.053004.

[7] N.K. Mondal, India-Based Neutrino Observatory (INO), Eur. Phys. J. Plus 127 (9) (2012) 1–6, http://dx.doi.org/10.1140/epjp/i2012-12106-y.

[8] S. Banik, et al., Simulation of neutron background for a dark matter search experiment at JUSL, J. Instrum. 16 (06) (2021) P06022, http://dx.doi.org/10.1088/1748-0221/16/06/p06022.

[9] N. Dokania, et al., Characterization and modelling of a low background HPGe detector, Nucl. Instrum. Methods Phys. Res. A 745 (2014) 119–127, http://dx.doi.org/10.1016/j.nima.2014.01.064.

[10] S. Thakur, et al., Background Estimation Studies for Positron Double Beta Decay, 2021, ArXiv:2111.08825 Physics.Ins-Det.

[11] G. Gupta, et al., Modelling of an electrically cooled HPGe detector, in: DAE Symposium on Nuclear Physics, Vol. 63, 2018, pp. 1142–1143.

[12] B. Rene, R. Fons, ROOT — An object oriented data analysis framework, Nucl. Instrum. Methods Phys. Res. A 389 (1) (1997) 81–86, http://dx.doi.org/10.1016/S0168-9002(97)00048-X, New Computing Techniques in Physics Research V.

[13] Linux advanced multiparameter sysytem (LAMPS), 2022, https://www.tifr.res.in/∼pell/lamps.html (Last Accessed: 21 Feb 2022).

[14] S. Agostinelli, et al., Geant4—a simulation toolkit, Nucl. Instrum. Methods Phys. Res. A 506 (3) (2003) 250–303, http://dx.doi.org/10.1016/S0168-9002(03)01368-8.

[15] S. Paul, et al., Measurement of neutron spectra generated from bombardment of 4 to 24 MeV protons on a thick ^{9}Be target and estimation of neutron yields, Rev. Sci. Instrum. 85 (6) (2014) 063501, http://dx.doi.org/10.1063/1.4880202.

[16] N. Dokania, et al., Estimation of low energy neutron flux ($E_n \leq 15$ MeV) in India-based Neutrino Observatory cavern using Monte Carlo techniques, J. Instrum. 10 (12) (2015) T12005, http://dx.doi.org/10.1088/1748-0221/10/12/t12005.

[17] N. Dokania, et al., Study of neutron-induced background and its effect on the search of $0\nu\beta\beta$ decay in ^{124}Sn, J. Instrum. 9 (11) (2014) P11002, http://dx.doi.org/10.1088/1748-0221/9/11/p11002.

[18] D. Brown, et al., ENDF/B-VIII.0: The 8th Major Release of the Nuclear Reaction Data Library with CIELO-project Cross Sections, New Standards and Thermal Scattering Data, Nucl. Data Sheets 148 (2018) 1–142, http://dx.doi.org/10.1016/j.nds.2018.02.001, Special Issue on Nuclear Reaction Data.

[19] L.A. Currie, Limits for qualitative detection and quantitative determination. application to radiochemistry, Anal. Chem. 40 (3) (1968) 586–593, http://dx.doi.org/10.1021/ac60259a007.

[20] D. Malczewski, et al., Gamma background measurements in the Gran Sasso National Laboratory, J. Radioanal. Nucl. Chem. 295 (1) (2013) 749–754, http://dx.doi.org/10.1007/s10967-012-1990-9.

[21] UNSCEAR, Sources and Effects of Ionizing Radiation, United Nations Scientific Committee on the Effects of Atomic Radiation 2000 Report, Vol. I, United Nations, 2000.

[22] National nuclear data center, 2022, URL http://www.nndc.bnl.gov (Last Accessed: 21 Feb 2022).

[23] G.F. Knoll, Radiation Detection and Measurement, John Wiley & Sons, New York U.S.A, 2009.

IL NUOVO CIMENTO **45 C** (2022) 24
DOI 10.1393/ncc/i2022-22024-9

Colloquia: SoUP 2021

Simulation studies for source optimization in ^{96}Zr β decay

S. Thakur(1), V. Nanal(2)(*), Pushpendra P. Singh(1), R. G. Pillay(1),
H. Krishnamoorthy(3)(4), A. Mazumdar(3)(4), A. Reza(2), P. K. Raina(1)
and V. Vatsa(3)(4)

(1) *Department of Physics, Indian Institute of Technology Ropar*
Rupnagar, 140001, Punjab, India
(2) *Department of Nuclear and Atomic Physics, TIFR - Mumbai, 400005, India*
(3) *India Neutrino Observatory, Tata Institute Fundamental Research*
Mumbai, 400005, India
(4) *Homi Bhabha National Institute - Mumbai, 400094, India*

received 4 November 2021

Summary. — The single β decay of ^{96}Zr to the ground state of ^{96}Nb is spin forbidden and poses a great experimental challenge. The β decay of ^{96}Zr can be studied via coincident detection of de-exciting gamma rays in ^{96}Mo, which is the end product of ^{96}Nb β decay. Simulations are done with four high purity Ge (HPGe) detector setup ($\sim 33\%$ relative efficiency each) to optimize the source configuration. The results suggest that ~ 70 g of 50% enriched ^{96}Zr will yield sensitivity comparable to the reported results.

1. – Introduction

The ^{96}Zr is one of the two double β decay (DBD) candidates, where single β decay is spin forbidden and competes with $\beta\beta$ decay. For ^{96}Zr, $Q_{\beta\beta}$ (Q-value) is 3.35 MeV and reported limit for $T_{1/2}$ (half-life) is 3.1×10^{20} yr [1] from DBD to excited states of ^{96}Mo. A schematic representation of β decays of ^{96}Zr and ^{96}Nb is shown in fig. 1 together with prominent gamma decay cascades. There have been several attempts to measure the half-life for ^{96}Zr β decay [2-4] and the best limit is given as $T_{1/2} \geq 6.2 \times 10^{19}$ yr [5].

Given the relatively small natural isotopic abundance of ^{96}Zr (2.8 %), one of the major challenges in a rare β decay study is to improve the sensitivity, which primarily involves the reduction of background to achieve a better signal to noise ratio. Recently, an improved lower limit for $T_{1/2}$ of DBD of ^{94}Zr to excited states of ^{94}Mo has been reported using low background setup TiLES [6]. In the present work, a feasibility study of the ^{96}Zr β decay through ^{96}Mo gamma ray cascade using a low background setup of four detectors

---

(*) E-mail: `nanal@tifr.res.in`

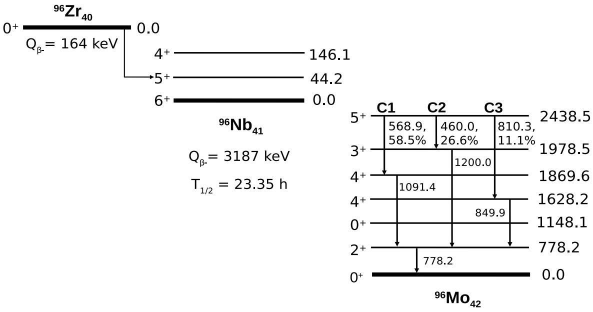

Fig. 1. – A schematic representation of β decay in ^{96}Zr and ^{96}Nb (energy values are in keV) [7].

is carried out employing the coincidence technique for background reduction. A setup of four identical HPGe detectors, with the relative efficiency of about 33%, arranged in a plane, is considered in the present study (see fig. 2). The source foil configuration and mounting geometry are optimized for maximizing the coincidence detection efficiency. The ^{96}Zr is considered to be distributed in ^{nat}Zr matrix. The results are compared with coincidence measurements of Finch *et al.* [4] with a two detector setup.

2. – Simulation and analysis

A simulation program 4HPGeSim has been developed using GEANT4 (v10.05) [8]. Figure 2 shows source and detector configuration. The geometry of the 4 HPGe detectors is taken to be similar to that of the CRADLE detector at TIFR [9], having carbon fiber housing and 0.9 mm thick front window. The source is taken to be ^{nat}Zr and effect of isotopic enrichment are taken care of by appropriately scaling the number of events generated with the desired fraction (f) while retaining the natural material properties for the source.

Two randomly oriented gamma rays from a chosen cascade (see fig. 1) are generated at a given vertex, which is uniformly distributed within the source and detected in the HPGe detectors. The dimensions of box-shaped source plates (consequently, the source mass) and their positioning are varied to find the optimum configuration to maximize mass efficiency (Mϵ_c) - the product of the source mass and the coincidence photopeak efficiency. The total energy deposited in each detector (E$_{dep}$) is folded by a Gaussian function to account for the detector resolution and the energy detected (E$_{det}$) is recorded. Simulation

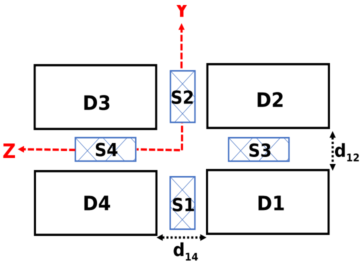

Fig. 2. – A schematic view of source - detector configuration employed in simulation.

outputs are stored and analyzed in ROOT [10] for ~1 M events. The photopeak area (N_i) is extracted by fitting a sum of Gaussian peaks with a quadratic background in single and coincidence spectra. The efficiency ϵ_i of detector i is given by

$$\epsilon_i = N_i/N_{gen}, \tag{1}$$

where, N_{gen} are the total generated events. The coincidence counts (N_{coin}) in the region of interest are extracted from the two dimensional correlation plots of E_i vs E_j (see fig. 3(a)). The net coincidence counts $N_{c,ij}$ are obtained after proper background and underlying Compton chance coincidence correction. The coincidence efficiency for D1-D4 and D1-D2 sets are computed as

$$\epsilon_{c,ij} = N_{c,ij}/N_{gen}. \tag{2}$$

Further, $\gamma_i - \gamma_j$ (γ_i in D4 and γ_j in D1) and $\gamma_j - \gamma_i$ (γ_j in D4 and γ_i in D1) combinations are taken into account while defining the total coincidence efficiency ϵ_c. In a rare decay experiment, the net expected event rate is often quoted in terms of Mϵ_c, defined as

$$M\epsilon_c = fM_0\epsilon_c, \tag{3}$$

where M_0 is the total mass of the source, f is the isotopic fraction. It should be pointed out that with increasing thickness, the attenuation of emitted gamma rays within the source becomes increasingly important. Hence, the source geometry needs to be optimized to maximize Mϵ_c. Initially, Mϵ_c is optimized for a two detector setup D1-D4 (front source) and D1-D2 (side source). For the front source, thickness t is varied, keeping the cross-sectional area of ($l \times w$) constant. For the side source, both thickness t and width w are varied, keeping l constant and the effect of variation of l is investigated separately. Distance between detectors d_{12}/d_{14} is fixed at $t + 10$ mm.

3. – Results and discussion

Amongst all 3 possible $\gamma - \gamma$ combinations in the most dominant cascade C1 (see fig. 1), 568–1091 keV pair is expected to give a cleaner identification of the decay branch. Hence the source geometry optimization has been done for this pair. For side source, it is observed that both singles and coincidence efficiencies show weak dependence on the source width. As no significant gain in $M\epsilon_c$ was observed for $w > 30$ mm, w_{opt} is taken to be 30 mm. The optimal source length (l_{opt}) is taken to be 55 mm same as the crystal length. The Mϵ_c for 568-1091 keV gamma pair are plotted as a function of source thickness in fig. 3(b) for front and side sources. As expected, for the given mass of the source, the side configuration yields lower efficiency (~half) as compared to the front source. For 778–1091 keV pair, as energy is higher, the optimal thickness is somewhat higher than 10 mm. Although the highest Mϵ_c is observed for the 568–778 keV pair, the background in the relevant region will be a crucial factor in the actual experiment. The optimal source dimensions for 2 detector setup are 55 mm×55 mm×10 mm and 55 mm×30 mm×10 mm for front and side source, respectively. These are used in optimizing the 4 detector setup. To compare the present $M\epsilon_c^{opt}$ with the earlier measurement of Finch et al. [4], $M\epsilon_c$ is estimated for 568-1091 keV gamma ray pair for the reference source-detector geometry. Two coaxial HPGe detectors with ~88 mm diameter (dia) and ~50 mm length, having 2.54 mm thick magnesium front window are mounted

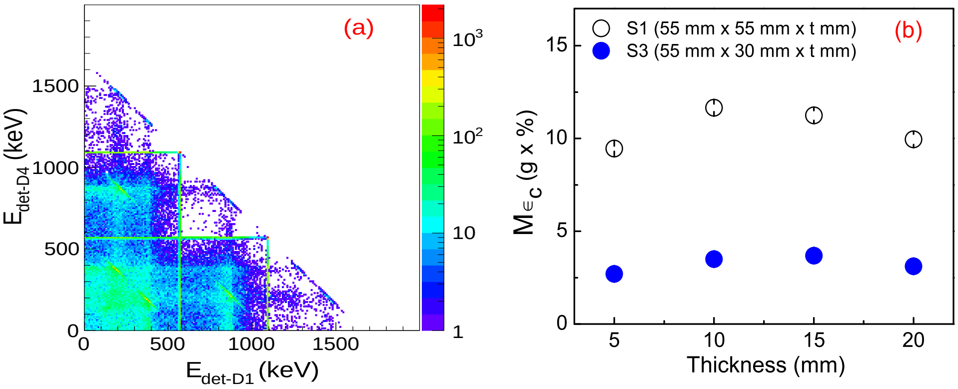

Fig. 3. – (a) Simulated 2D spectrum of the detected energy in D1 and D4, (b) Simulated $M\epsilon_c$ for 568-1091 keV gamma rays as a function t for both front (S1) and side (S3) Zr sources.

face to face at a distance (d) of 12 mm. A cylindrical source of mass ~36.8 g with ~50 % enrichment and ~60 mm dia×2 mm size is considered, giving $M_{ref} \sim 18$ g of ^{96}Zr. As it can be seen from table I, a significantly large quantity of the Zr source will be needed to achieve $M\epsilon_c$ similar to earlier measurement with present set of detectors. It should be mentioned that the measured best reported limit so far on $T_{1/2}$ of ^{96}Zr employed about 19 g of ZrO_2 powder with 57.3 % enrichment for singles gamma ray measurements, resulting in $M\epsilon$ of ~37 g-% [2].

For the four detector setup, the total mass is configured in four sources - S1+S2 (front sources) and S3+S4 (side sources). Initially, the respective optimum source dimensions obtained in the two detector geometry for the front (55 mm×55 mm) and side sources (55 mm×30 mm) are employed and sources are positioned symmetrically w.r.t detector crystal for better solid angle coverage. It may be noted that reducing thickness t from 10 mm to 5 mm, permits $d_{14} = 7$ mm, which yields ~60 % gain in ϵ_c. Thus, even though there is a mass decrease of 50 %, only ~20 % decrease is observed in the total $M\epsilon_c$. The four detector configuration with t = 5 mm for front and side sources will result in 70 % higher $M\epsilon_c$ (see table I), but still considerably large mass ~152 g of ^{96}Zr will be needed. Hence, further mass optimization needs to be considered.

As mentioned earlier, dominant contribution comes from sources in the front. So in the first step, only front sources S1 and S2 are employed and the cross-sectional area of the source ($l \times w$) is varied, maintaining $t_0 = 5$ mm and d = 7 mm to obtain the optimal front source mass (M_f). In the second step, a fraction of M_f (30-60 %) is distributed as side sources S3 and S4. Similar to the first case, t_0 and d are kept as 5 mm and

Table I. – *A comparison of $M\epsilon_c$ (568-1091) for D1-D4 and ref.* [4] *setup* ($f = 50\,\%$).

Crystal size	Front window (mm)	Source size	d (mm)	ϵ_c %	M (g)	$M\epsilon_c$ (g-%)
88 mm (dia)×50 mm	2.54	60 mm (dia)×2 mm	12	0.65	18	12
55 mm (dia)×55 mm	0.90	55 mm×55 mm×2 mm	12	0.12	20	2

Table II. – *$M\epsilon_c(\gamma_1, \gamma_2)$ in optimal source configuration ($M_{eff} \sim 72$ g) in 4 detector geometry.*

Eγ (keV)	ϵ_c (%)	Mϵ_c (g-%)
568, 1091	0.216	15.4
568, 778	0.279	20.0
778, 1091	0.172	12.3

7 mm, respectively, and ($l \times w$) is varied keeping M$_f$ fixed ($l <$ crystal length, to avoid edge effects). The optimal configuration for t = 5 mm is obtained as $M_{eff} \sim 72$ g with M$_s \sim 40$ % of M$_f$. The cross-sectional dimensions (l_{opt}, w_{opt}) are 40 mm×40 mm for the front source and 30 mm×20 mm for the side source. The M$\epsilon_c(\gamma_1, \gamma_2)$ in Zr matrix with ~ 50 % enrichment for the optimal source configuration are given in table II. Although higher granularity in the four detector setup is expected to improve the background and reduce the pileup, these effects cannot be quantified at this stage.

4. – Conclusion

Simulation studies are carried out for estimation of mass efficiency (Mϵ_c) for β decay measurements in ^{96}Zr. The optimization of Mϵ_c is done for four HPGe detector (~ 33 % relative efficiency each) setup with extended sources in a close geometry for 568-1091 keV gamma ray pair in the ^{96}Nb decay cascade. It is shown that for ^{96}Zr β decay, even in a four detector configuration, a significantly larger source mass is required to achieve the reported sensitivity. Present simulations for a four detector setup show the optimal source configuration to be 5 mm thick foils with a cross-sectional area of 40 mm×40 mm for front sources and 30 mm×20 mm for side sources. This corresponds to about 72 g of effective mass with 50 % enrichment and can yield Mϵ_c of $\sim$12-20 g-% for different gamma ray pairs, which is slightly better than the coincidence measurement reported earlier.

* * *

This work is supported by the Department of Atomic Energy, Government of India (GoI), under Project No. 12-R&DTFR-5.02-0300. S. Thakur acknowledges the Ministry of Education, GOI, for PhD research fellowship, and TIFR for supporting the visit related to this work.

REFERENCES

[1] Finch S. W. *et al.*, *Phys. Rev. C*, **92** (2015) 045501.
[2] Arpesella C. *et al.*, *Europhys. Lett.*, **27** (1994) 29.
[3] Barabash A. S. *et al.*, *J. Phys. G: Nucl. Part. Phys.*, **22** (1996) 487.
[4] Finch S. W. *et al.*, *Nucl. Instrum. Methods A*, **806** (2016) 70.
[5] Mayer A. J. *et al.*, *Phys. Rev. C*, **98** (2018) 024617.
[6] Dokania N. *et al.*, *Eur. Phys. J. A*, **53** (2017) 270.
[7] `https://www.nndc.bnl.gov/`.
[8] Agostinelli S. *et al.*, *Nucl. Instrum. Methods A*, **506** (2003) 250.
[9] Gupta G. *et al.*, *DAE-BRNS Symp. Nucl. Phys.*, **63** (1142) 2018.
[10] Brun R. *et al.*, *Nucl. Instrum. Methods A*, **389** (1997) 81.

Background Estimation Studies for Positron Double Beta Decay

Swati Thakur[1], A. Mazumdar[2,3], R. Shah[2,3], V. Vatsa[2,3], V. Nanal *[4], M.S. Pose[4], Pushpendra P. Singh[1], P.K. Raina[1], and R.G. Pillay[1]

[1] *Department of Physics, Indian Institute of Technology Ropar, Rupnagar Punjab - 140001, India*
[2] *India-based Neutrino Observatory, Tata Institute of Fundamental Research, Mumbai - 400005, India*
[3] *Homi Bhabha National Institute, Anushaktinagar, Mumbai - 400094, India*
[4] *Department of Nuclear and Atomic Physics, Tata Institute of Fundamental Research, Mumbai - 400005, India*

Abstract

The study of neutrinoless double beta decay has attracted much attention as it can provide valuable information about the mass and the nature of the neutrino. The double beta decay (DBD) itself is also of interest in nuclear physics. While DBD has been observed in about a dozen nuclei, the positron double beta decay ($\beta^+\beta^+$/EC-β^+) continues to be an elusive. An important signature for $\beta^+\beta^+$ decay is the simultaneous emission of four 511 keV gamma rays and the coincident detection of these gamma rays can improve the measurement sensitivity. This paper presents an estimation of sensitivity for EC-β^+ and $\beta^+\beta^+$ employing coincidence measurement with two high purity Ge (HPGe) detectors. Simulations for coincident detection efficiency (ϵ_c) of 511 keV gamma rays with two HPGe detectors have been carried out using GEANT4 for different source geometries to optimize the mass efficiency product (Mϵ_c). The source of size $55\,mm \times 55\,mm \times 5\,mm$ (thickness) sandwiched between the front faces of the detectors were found to be optimal for 2 pairs of 511 keV gamma rays in the present detector setup. The coincident background is estimated at the sea level with moderate Pb shielding. With this setup, the sensitivity for T$_{1/2}$ measurement of EC-β^+ in ^{112}Sn and $\beta^+\beta^+$ in ^{106}Cd is estimated to be $\sim 10^{19}$ - 10^{20} y for 1 y of measurement time.

1 Introduction

Recent neutrino oscillation experiments have boosted the worldwide interest in the search for neutrinoless double beta decay (NDBD) with increased sensitivity [1]. The neutrinoless double beta decay provides a unique probe to study the mass and nature of the neutrino. Double beta decay (DBD) is a second-order allowed process in the Standard Model and $\beta^-\beta^-$ decay mode has been detected in several nuclei. However, positron decay modes are hindered due to lower effective Q value [2] and experimental search for $\beta^+\beta^+$/EC-β^+ continues to be elusive. An important experimental signature of the decay modes involving positrons like EC-β^+ and $\beta^+\beta^+$ is the simultaneous emission of pair(s) of 511 keV gamma rays. Hence, the coincident detection of 511 keV gamma rays can significantly improve the measurement sensitivity. However, since 511 keV gamma rays can also originate from many other processes, it is important to understand and discriminate against the background originating from trace impurities in the source, detector and surrounding materials and as well as from cosmic muon induced reactions. The present work aims to estimate the sensitivity of the half-life measurement for positron DBD modes using a coincidence

---

*nanal@tifr.res.in

setup. In the first part, simulations are done to optimize the source-detector configuration to maximize the mass efficiency product ($M\epsilon_c$). In the second part, background measurements are carried out using a coincidence setup of two high purity Ge (HPGe) detectors ($\sim$ 33%) with moderate lead shielding. Both ambient background and background with natural tin (^{nat}Sn) sample of mass $\sim$40 g were measured. The background in the coincidence setup, especially in the region of interest around 511 keV is compared with that from the low background counting setup TiLES [3]. The sensitivity for $T_{1/2}$ measurement of EC-β^+ in ^{112}Sn and $\beta^+\beta^+$ in ^{106}Cd is estimated using the measured background and simulated coincidence efficiency. Measures for improvement in the background are also discussed.

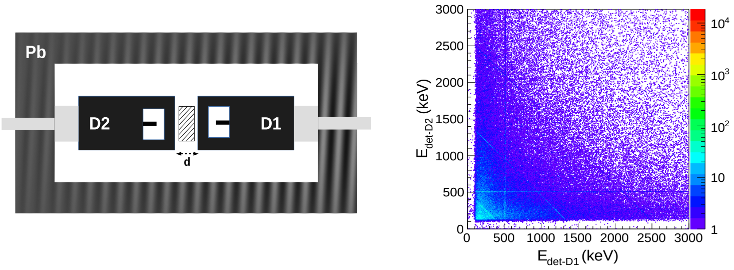

Figure 1: a) A schematic view of D1-D2 coincidence setup and b) Coincident energy spectra of D1-D2 for ambient background (t = 27.0 d).

2 Experimental details

For background measurements in coincidence, a simple setup with two identical low background cryo-cooled HPGe detectors is made at TIFR, Mumbai. Both detectors D1 and D2 (Ortec make) have carbon fiber housing with 0.9 mm thick front window, and $\sim$33 % relative efficiency each. Detectors are mounted in a close geometry with a face-to-face distance of about 2 cm as shown in Figure 1(a). The detailed measurements were carried out with detector D1 using mono-energetic point+volume sources, and an optimized geometrical model of the detector was obtained [4]. The same geometry is adopted for both D1 and D2 in the present simulations. This two detector setup is surrounded by a passive shield of 5 cm thick low activity lead ($<$0.3 Bq/kg) in all directions. Additionally, 5 cm thick lead ($<$ 21 Bq/kg) is added on both the sides. The setup also has a provision for cosmic muon veto in the future.

Data were acquired using CAEN DT6724 digitizer (14-bit, 100 MS/s) and recorded separately (time stamp and energy) for each detector on an event by event basis. The coincident spectra were generated using offline analysis. The dead time was monitored with a standard 10 Hz pulser, and was found to be negligible ($<$ 0.1 %). The resolution of the detector was $\sim$3 keV at 1332 keV. The ambient background was recorded for $\sim$ 27 d, at different times over the period of about 10 months. No measurable drifts were observed in the data. The ^{nat}Sn sample of mass 38.8990 g, in the form of granules (7N purity, Alfa aesar) with an approximate overall size $30\,mm \times 39\,mm \times 6.5\,mm$, was counted in close geometry for t = 77.8 d. Figure 1(b) shows a typical 2-dimensional plot of E_{D1} vs E_{D2} for the ambient background. Correlated 511 keV lines and high energy background lines (1460, 2615 keV) are clearly visible.

The coincidence efficiency (ϵ_c) of D1-D2 detectors for ^{nat}Sn and ^{nat}Cd foils was obtained using a GEANT4 [5] simulation program. A total of 10^6 events of 2 (1) correlated pairs of 511 keV gamma rays were generated at a given vertex for $\beta^+\beta^+$ (EC-β^+). In rare decay search experiments like $\beta^+\beta^+$, the mass efficiency product ($M\epsilon_c$) needs to be maximized. Hence, the source size and mounting geometry were optimized for the present detector setup. Details of simulation and source optimization procedure are given in Ref. [6]. It was found that 55 mm×55 mm source of 10 mm thickness yields maximum $M\epsilon_c$. However, with a 5 mm thick source, the detectors can be moved closer (d = 7 mm) and consequently decrease in $M\epsilon_c$ is only $\sim 20\,\%$ even if M is reduced by $50\,\%$. This is preferable as the inherent background scales with the mass of the source. Hence, the optimal source geometry is chosen to be $55\,mm \times 55\,mm \times 5\,mm$ foil sandwiched between front faces of detectors, with separation between detectors d = 7 mm. The simulated values of ϵ_c are given in Table 1.

3 Data analysis and results

The coincidence was performed using an offline C++ based algorithms developed in ROOT [7]. The coincidence time window was set to $\pm 1\,\mu$s to ensure that all coincident events are collected, and the output was written in a ROOT Tree. The data were analyzed using LAMPS [8]. Figure 2 shows a comparison of the ambient background of D1 in singles and coincidence. It is evident that the coincidence yields significant improvement in the background. In fact, only 511 keV peak survives in the background, albeit with much reduced intensity. The sum energy spectrum ($E_{sum} = E_{D1}+E_{D2}$) is also shown for comparison. It can be seen that while high energy gamma rays like 1460 keV (^{40}K) and 2615 keV (^{208}Tl, originating from ^{232}Th) are visible in sum energy, the overall background is reduced by an order of magnitude.

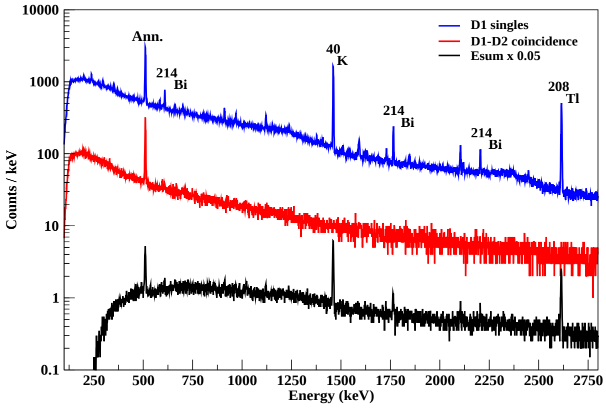

Figure 2: A comparison of the ambient background in D1 - singles and coincidence with D2 (i.e. $E_{D2} > 0$). Sum energy spectrum $E_{sum} = E_{D1}+E_{D2}$, scaled by an arbitrary factor of 0.05 for better visibility, is also shown for comparison. All spectra have been time normalized to t = 7 d.

For both ambient background and ^{nat}Sn sample, analysis to extract counts in the region of interest (ROI) near 511 keV was done in an identical manner. The chance correction from the time spectrum was found to be negligible. The coincident 511-511 keV events were suitably corrected for underlying Compton chance coincidence. The prompt gated D1 spectrum was generated for the photopeak region (511 ± 5 keV) in D2, while the chance gated spectrum was generated from 5 keV window on the left and right of the photopeak in D2. The observed counts in the ROI for ambient background (i.e., without the sample) are 3 ± 1 cts/d, which is equivalent to 1271 ± 297 cts/y. It should be mentioned that the observed singles count rate for 511 keV gamma ray in low background setup TiLES [3], is 680 ± 20 cts/d, which clearly emphasizes improvement with coincident detection. However, higher statistics will be required to study 1022 - 1022 keV correlations. In presence of ^{nat}Sn (~ 40 g), the background in the ROI was enhanced to 1919 ± 211 cts/y, giving the excess of 2 ± 1 cts/(keV.g.y) with ^{nat}Sn.

In the absence of a positive signal, based on the present background, a lower limit on the half-life can be estimated as:

$$T_{1/2} > \frac{ln2 * N_A * \epsilon_c * a}{w * k_{CL}} \sqrt{\frac{M * t}{N_{bkg} * \Delta E}} \tag{1}$$

where N_A is Avogadro's number, ϵ_c is the coincidence detection efficiency of a gamma ray, a is the isotopic abundance of sample, W is the molar mass of sample, M is the sample mass, t is the time of measurement (in y), N_{bkg} is the background index (in cts/(keV.g.y)), ΔE is the energy window defining the signal region of D1-D2 setup and k_{CL} is the number of standard deviations corresponding to a given confidence interval (C.L.). If one considers only the background from the source, N$_{bkg}$ is estimated to be 2 ± 1 cts/(keV.g.y) from the tin data. As mentioned in previous section, the ϵ_c is obtained from simulations for an optimal source geometry ($55\,mm \times 55\,mm \times 5\,mm$). Using the simulated ϵ_c, the $T_{1/2}$ sensitivity of the present D1-D2 coincidence setup for EC-β^+ in ^{112}Sn and $\beta^+\beta^+$ in ^{106}Cd has been estimated for different enrichment fractions and listed in Table 1.

Table 1: The projected sensitivity for the half-life (T$_{1/2}$) of the present D1-D2 coincidence setup for ^{112}Sn (EC-β^+) and ^{106}Cd ($\beta^+\beta^+$) for t_{data} = 1 y. The isotopic abundance (a), total mass (M_0) and coincidence efficiency (ϵ_c) are also listed.

Source	a (%)	ϵ_c (%)	M_0 (g)	T$_{1/2}$ (68% C.L.) (y)	T$_{1/2}$ (90% C.L.) (y)
^{106}Cd	50	1.04	130	5.5×10^{19}	3.4×10^{19}
^{106}Cd	90	1.04	130	1.0×10^{20}	6.2×10^{19}
^{112}Sn	50	0.64	110	2.9×10^{19}	1.8×10^{19}
^{112}Sn	90	0.64	110	5.4×10^{19}	3.3×10^{19}

The ambient background has contributions from trace radioactive impurities, natural radioactive chains and cosmic muons as well as muon induced reactions. The external background can be minimized with suitable shielding. A moderate rock cover of ~500 m would suppress the muon flux by ~4 orders of magnitude [9]. Thus, the inherent background from the source (trace impurities, neutron induced reactions) will be a limiting factor and hence the same has been used in the present estimation. Nevertheless, it is important to reduce overall background. The use of larger detectors with an annular anti-compton shield would also improve the coincidence efficiency and reduce background [10]. In the present setup, it is proposed to augment the shielding by adding an active veto for muon and increasing passive shield thickness.

The present best limits for $T_{1/2}^{\beta^+\beta^+}$ (^{106}Cd) and $T_{1/2}^{EC-\beta^+}$ (^{112}Sn) are 2.3×10^{21} y [11] and 9.7×10^{19} y [12], respectively. From Table 1, it can be seen that an improvement in the background index by about a factor of 5, will be suitable to yield an improved limit for ^{112}Sn, while for ^{106}Cd further measures to improve signal to noise ratio are essential.

4 Conclusion

The feasibility study of positron double beta decay modes is presented for ^{112}Sn (EC-β^+) and ^{106}Cd ($\beta^+\beta^+$) using a coincidence setup of 2 HPGe detectors. The coincident detection efficiency of 511 keV gamma rays for source foil sandwiched between the detectors has been estimated using GEANT4. The source of size $55\,mm \times 55\,mm \times 5\,mm$ (thickness) was found to be optimal for 2 pairs of 511 keV gamma rays. The ambient background of the 2 detector setup with moderate Pb shielding is measured in coincidence mode at sea level. The coincident detection of 511 keV pair yields a significant improvement in the background in the region of interest. From background measurements with ~40 g of ^{nat}Sn, the sensitivity for $T_{1/2}^{\beta^+\beta^+}$ (^{106}Cd) and $T_{1/2}^{EC-\beta^+}$ (^{112}Sn) are estimated to be ~10^{19} - 10^{20} y for 1 y of measurement time with enriched samples. Thus, coincidence measurements with the present two HPGe detector setup at moderate depth can be used to probe EC-β^+/ $\beta^+\beta^+$.

Acknowledgement

We thank Mr. S. Mallikarjunachary and Mr. K.V. Divekar for the assistance with measurements. This work is supported by the Department of Atomic Energy, Government of India (GoI), under Project No. RTI4002. Swati Thakur acknowledges the Ministry of Education, GoI, for PhD research fellowship.

References

[1] M. J. Dolinski *et. al.* Annu. Rev. Nucl. Part. Sci. **69**, 219 (2019).

[2] P. Belli *et. al.* Particles **4**, 241 (2021).

[3] N. Dokania *et. al.* Nucl. Instrum. Meth. A **745**, 119 (2014).

[4] G. Gupta *et. al.* DAE-BRNS Symp. Nucl. Phys. **63**, 1142 (2018).

[5] S. Agostinelli *et. al.* Nucl. Instrum. Meth. A **506**, 250 (2003).

[6] S. Thakur *et. al.* arXiv 2110.02171 (2021).

[7] R. Brun *et. al.* Nucl. Instrum. Meth. A **389**, 81 (1997).

[8] https://www.tifr.res.in/∼pell/lamps.html

[9] M. K. Sharan *et. al.* Nucl. Instrum. Meth. A **994**, 165083 (2021).

[10] S.W. Finch *et. al.* Nucl. Instrum. Meth. A **806**, 70 (2016).

[11] P. Belli *et. al.* Phys. Rev. C **93**, 045502 (2016).

[12] A. S. Barabash *et. al.* Phys. Rev. C **83**, 045503 (2011).

Neutron induced activation studies for low background experiments

S. Thakur[1],* A. Mazumdar[2,3],† V. Vatsa[2,3], M.S. Pose[4], S. Mallikarjunachary[4],
S. Pal[5], V. Nanal[4], P.P. Singh[1], R.G. Pillay[1], and P.K. Raina[1]
[1]*Department of Physics, Indian Institute of Technology Ropar, Rupnagar, Punjab - 140001, INDIA*
[2]*INO, Tata Institute of Fundamental Research, Mumbai - 400005, INDIA*
[3]*HBNI, Anushaktinagar, Mumbai - 400094, INDIA*
[4]*DNAP, Tata Institute of Fundamental Research, Mumbai - 400005, INDIA and*
[5]*PLF, Tata Institute of Fundamental Research, Mumbai - 400005, INDIA*

Introduction

Underground locations are preferred for rare event studies like neutrinoless double beta decay (NDBD) and dark matter (DM). The ambient background at these locations can significantly affect the sensitivity of the experiment. The present work, for the first time, reports the neutron activation studies of the rock samples collected from Aut in Himachal Pradesh. Neutron induced reactions were studied with an emphasis on long-lived activities, which can be a limiting factor for low background experiments.

Experiment & Data Analysis

The neutron activation experiment was performed at the neutron irradiation setup of the Pelletron Linac Facility, Mumbai [1]. Proton beams of E_p = 12 and 22 MeV were used on ^{9}Be target to generate neutrons of broad energy range upto E_{max} = 9.9 and 19.9 MeV, respectively via the ^{9}Be(p,n)^{9}B reaction (Q = -1.85 MeV). Table I gives the details of the irradiation and samples. The energy integrated neutron flux was estimated to be $\sim 10^6$ n cm^{-2} s^{-1}, using ^{56}Fe(n,p)^{56}Mn reaction. The irradiated rock samples and iron foils were counted offline in low background counting setups at TIFR - TiLES [2] and CRADLE [3], in a close geometry and after a sufficient cooldown time t_c ($\geq$ 1-2 hr). In both the setups data was recorded using a commercial CAEN N6724 digitizer (14-bit, 100 MS/s).

TABLE I: Details of sample irradiation

Sample	Mass (g)	E_{beam} (MeV)	$T_{irradiation}$ (hr)	$< I >$ (nA)
AUT1A	10.6220	22	15.5	136
AUT4E	6.6985	12	16.0	148
BWH2A	8.2211	22	5.2	167
BWH2B	5.4729	12	16.0	148

The gamma ray spectra were analyzed using LAMPS [4]. A typical spectrum of the irradiated Aut rock sample (E=22 MeV) is shown in Fig. 1 after the t_c of 5 d, where various gamma rays of activated products ($T_{1/2} \sim$ few days) are visible.

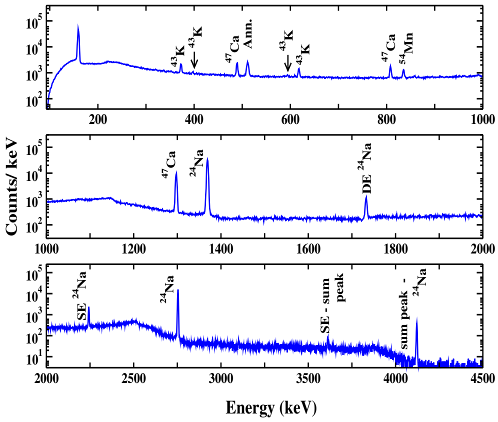

FIG. 1: Gamma ray spectrum of AUT1A, irradiated at 22 MeV, after a t_c of 5 d (t = 1 d).

Reaction products were identified by characteristic gamma rays and half-life tracking was done for the verification. Further, in the

---

*Electronic address: `swatithakur1520@gmail.com`

†Present address: TIF - AWaDH, IIT Ropar, Rupnagar, Punjab - 140001, INDIA

case of multiple gamma rays of the same nuclide, relative branching ratios were checked. Products arising from (n,p), (n,α), (n,γ) and (n,2n) reactions are visible and are listed in Table II. Irradiation at two different incident energies provides an independent check for the yield of the observed products on neutron energy.

TABLE II: Observed products and gamma rays

Channel	E_γ	$T_{1/2}$
^{43}Ca(n,p)^{43}K	372.8, 617.5	22.3 h
^{54}Fe(n,p)^{54}Mn	835.0	312.2 d
^{56}Fe(n,p)^{56}Mn	846.5	2.58 h
^{41}K(n,γ)^{42}K	1524.7	12.36 h
^{48}Ca(n,2n)^{47}Ca	489.2, 807.9, 1297.1	4.54 d
^{24}Mg(n,p)^{24}Na	1368.6, 2754.0	14.96 h
^{23}Na(n,2n)^{22}Na	1274.5	2.60 y

The source of the observed peak at 159.2 keV could not be clearly identified. It can originate either from ^{117m}Sn (E_γ= 158.6 keV, $T_{1/2}$ = 13.76 d) or ^{47}Sc, which is produced via β-decay of ^{47}Ca (E_γ= 159.4 keV, $T_{1/2}$ = 3.35 d). The observed lifetime is not consistent with either.

In order to assess the impact of the long-lived neutron induced activity on the residual background, a comparison of the gamma ray spectra of the Aut rock samples before and after irradiation was carried out. Fig. 2 shows the gamma ray spectrum of the AUT1A (10.6220 g, t_c = 31 d) together with that for AUTB (27.5430 g) prior to neutron activation. It should be noted that a few gamma rays upto 1300 keV, corresponding to neutron induced reaction products, are still visible after fairly long cooldown t_c = 31 d and corresponding Compton tails lead to the enhanced low energy background. The gamma rays belonging to natural radioactive decay chains (from the rock and the ambient background) are also indicated (*) in the spectra. No significant differences are visible at E > 1500 keV, although the statistics are very poor.

A comparison of Aut rock background with that of INO laboratory site at Bodi West Hill (BWH) [5] is of interest and hence neutron activation was also carried out on the BWH samples. The BWH rock is known to have higher levels of potassium. The presence of high energy gamma ray 2167.5 keV ($t_c \sim$ 42 m) in the spectrum of the irradiated BWH rock sample, may originate from ^{39}K(n,2n)^{38}K reaction.

In summary, neutron activation studies of Aut rock have revealed mostly short-lived activity. However, long-lived products like ^{54}Mn and ^{47}Ca can result in the enhanced background at E < 1000 keV. A detailed comparison of neutron induced activity in BWH (INO) and Aut rock samples will be presented.

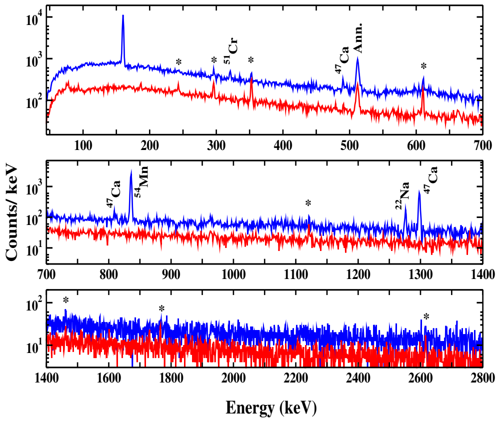

FIG. 2: Gamma ray spectra of the AUT1A (blue line, $t_c = 31$ d, scaled by a factor of 2.5 for better visualization) and AUTB (red line), (t = 1 d).

Acknowledgments

We thank the PLF staff, target lab staff and Mr. K.V. Divekar for assistance during the experiment. This work is supported by the Department of Atomic Energy (GoI), under Project No. 12-R&DTFR-5.02-0300.

References

[1] S. Paul *et. al.* Rev. Sci. Instru. **85**, 063501 (2014).
[2] N. Dokania *et. al.* NIM A **745**, 119 (2014).
[3] G. Gupta *et. al.* DAE Symp. Nucl. Phys. **63**, 1142 (2018).
[4] http://www.tifr.res.in/~pell/lamps.html
[5] N. Dokania *et. al.* JINST **10**, T12005 (2015).

Performance study of low background co-axial HPGe detector

S. Thakur[1],* H. Krishnamoorthy[2,3], V. Nanal[4],
Pushpendra P. Singh[1], and R.G. Pillay[1]
[1]*Indian Institute of Technology Ropar,Rupnagar - 1410001,Punjab INDIA*
[2]*INO, Tata Institute of Fundamental Research, Mumbai - 400005, INDIA*
[3]*Homi Bhabha Atomic Research Centre, Mumbai - 400094, INDIA and*
[4]*DNAP, Tata Institute of Fundamental Research, Mumbai - 400005, INDIA*

Introduction

The gamma-ray spectroscopy using high-purity germanium (HPGe) detector is a useful tool for nuclear structure studies. In rare decay studies like neutrinoless double beta decay or search for dark matter, the minimization of background is essential. Hence, identification of the radiative impurities in the detector as well as surrounding elements and elimination of the same to the extent possible, is highly desirable. In such low background measurements, samples often need to be counted in a close geometry to maximise the counting efficiency [1]. Therefore, it is necessary to understand the detector performance over a range of energies and for different counting geometries. A dedicated low background HPGe detector is being setup at IIT Ropar. This setup aims to perform measurements relevant for rare decay studies like *Tin.Tin* [2]. This paper reports the preliminary results of the characterization of the cryocooled HPGe detector installed at NuStaR Lab of IIT Ropar.

Experimental details and Setup

The HPGe detector is ORTEC make, GEM Series (GEM30P4-83-RB), coaxial, p-type, low-background crystal with a carbon fibre body. The detector is electrically cooled, making it suitable for usage at remote underground locations. The nominal dimensions of the detector, given by the manufacturer are : diameter -62 mm, length - 46 mm and carbon window thickness 0.9 mm. The detector is designed for relative efficiency of 35%. In order to make an equivalent detector model, it is essential to determine the detailed detector geometry including dead layers. A scanning table has been designed and fabricated to facilitate the radial, lateral and distance scans with collimated sources. A picture of the setup is shown in Fig 1. The sealed disk type gamma-ray sources ^{109}Cd, ^{57}Co, ^{60}Co, ^{54}Mn, ^{133}Ba and ^{137}Cs have been used for initial measurements.

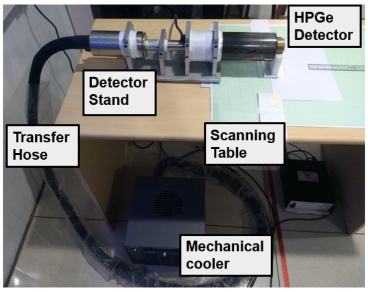

FIG. 1: IIT Ropar Low-background Measurement Infrastructure (ILMI)

The data was acquired using MAESTRO (ORTEC) software and analyzed in ROOT[3] and LAMPS [4].

Data Analysis and Results

A typical gamma-ray spectrum with ^{60}Co source is shown in Fig. 2 (top panel). The figure also shows efficiency as a function of energy (bottom panel) at d=25 cm. For 1332 keV, the measured resolution of 1.81 keV and the Relative efficiency of 33% at 25 cm distance are consistent with manufacturer's values.

---

*Electronic address: `2017phz0004@iitrpr.ac.in`

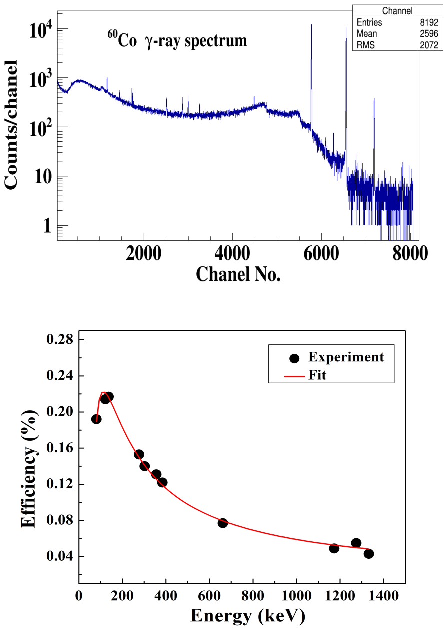

FIG. 2: Energy resolution and photopeak efficiency at d=25 cm.

The distance scan has been done with multiple sources in the range of 5-30 cm, in 5 cm steps and data are shown in Fig. 3. measured data are also compared with the efficiency obtained from simulations using GEANT4 [5]. The detector geometry is taken from the manufacturer's values. The simulated efficiency data is also shown in Fig. 3 (solid line). It can be seen that the simulations somewhat overestimates the data, particularly at low energy. The simulated relative efficiency for 1332 keV at 25 cm is 40%, which is about 10% higher than the measured value.

In the low energy region, the detection efficiency is strongly affected by the presence of the dead layer. For the front dead layer thickness (t) estimation, spectra with ^{57}Co (122 keV) was recorded with two collimators : one with ∼ 1 mm straight through hole (C_0) and the other with ∼ 1 mm through hole at 30^0 angle (C_{30}). A horizontal scan was also made on the top surface of detector in steps of ±5 mm using both these collimators. From the measured photopeak yields Y(C_0) and Y(C_{30}) of 122 keV gamma ray with collimator C_0 and C_{30}, respectively, the front dead layer thickness is evaluated as

$$\frac{Y(C_0)}{Y(C_{30})} = \frac{e^{(-\sum_i \mu_i x_i)} e^{(-\mu_{Ge} t)}}{e^{(-\sum_i 1.15\mu_i x_i)} e^{(-1.15\mu_{Ge} t)}} \tag{1}$$

where μ_i and x_i are the attenuation coefficient and path length of absorber windows (Al and C). In the central region of the detector t is found to be 0.090±0.003 mm.

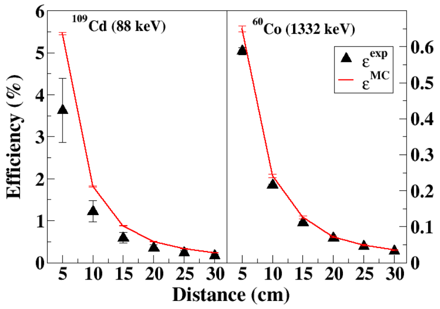

FIG. 3: Efficiency data (experiment and simulation) for distance scan using 88 keV and 1332 keV gamma rays.

Summary

An electrically cooled HPGe detector is setup at IIT Ropar for low background measurements. Simulations are carried out with Geant4 using manufacturer supplied geometry and results are found to be about 10% higher than the data. Further optimization of the detector geometry is in progress and results will be reported.

Acknowledgments

We thank IIT Ropar and TIFR, Mumbai for providing the support for the fabrication of the setup.

References

[1] N. Dokania *et al.*, NIM A **745**, 119 (2014).
[2] V. Nanal, Eur. Phys. J. Conf. **66**, 08005 (2014).
[3] https://root.cern.ch
[4] www.tifr.res.in/∼pell/lamps.html
[5] https://geant4.web.cern.ch